OPTICAL MEASUREMENTS ON A STABILISED LINEAR PINCHED DISCHARGE

by

THOMAS ANTHONY HALL

A Thesis submitted for the degree
of Doctor of Philosophy of
the University of London

January 1968

Physics Department
Imperial College of Science and Technology

Abstract

In this thesis we discuss a new method for measuring magnetic field in a plasma, using the Zeeman effect on the spectral emission lines. An analysis of the instrument is given, and some results, obtained with it, are presented. These results were obtained on a B_Z stabilised linear pinched discharge and they show that, under certain conditions, appreciable field compression is experienced. The accuracy of these results is discussed and a comparison is made with those taken with a conventional magnetic probe. These show good agreement with the Zeeman effect instrument.

The second part of this thesis presents a method for obtaining time resolved electron density distributions. A Mach-Zehnder interferometer is used for this purpose, in conjunction with a ruby laser light source and the construction of these are described. Results obtained with this apparatus are presented for the same conditions used in the first part and a definite correlation is established between the two sets of results.

A simple model of the B_Z stabilized pinch is proposed, in which it is attempted to explain these two sets of experimental

results. The snowplough model of the unstabilised linear pinch is used as a basis for this model and some further assumptions are made to take account of the stabilising field. The experimental results, on the whole, tend to give higher values of compression than this model predicts. However, a modification to the simple snowplough model reduces this discrepancy considerably. In conclusion, suggestions are made that would explain the remaining difference.

CONTENTS

Page

Page

Chapter I

The Stabilised Linear Pinched Discharge

1.1 Introduction

A linear pinched discharge tube with a pulsed stabilising magnetic field has been constructed by A. E. Dangor. The discharge has been studied by Dangor (1964), Troughton (1965) and Roberts (1967). This thesis represents an extension of the work carried out by these three authors and is concerned primarily with the interactions between the plasma and a stabilising magnetic field. The effect that the stabilising magnetic field has on the discharge is considerable, as is readily apparent from the discharge current traces that have been obtained (Fig 1.1). The effect which the discharge has on the magnetic field is not nearly so apparent. Here, the small kink in the stabilising magnetic field current, shown in this figure, is a result of the discharge and is indicative of the fact that the stabilising field is being compressed by the collapsing plasma. To obtain more quantitative results it is necessary to measure the magnetic field directly. Before describing how this has been done, together with some other correlated measurements, it is necessary to describe more fully the discharge tube and the work that has been carried out up until the present.

1.2 The Stabilised Linear Pinched Discharge

The discharge tube basically consists of two stainless steel electrodes held 40 cm apart in a pyrex tube. The tube itself is 90 cm long, thus allowing the end plates of the tube to be well away from the

Fig 1.1 Current Traces of the Disharge Tube and Magnetic Field.

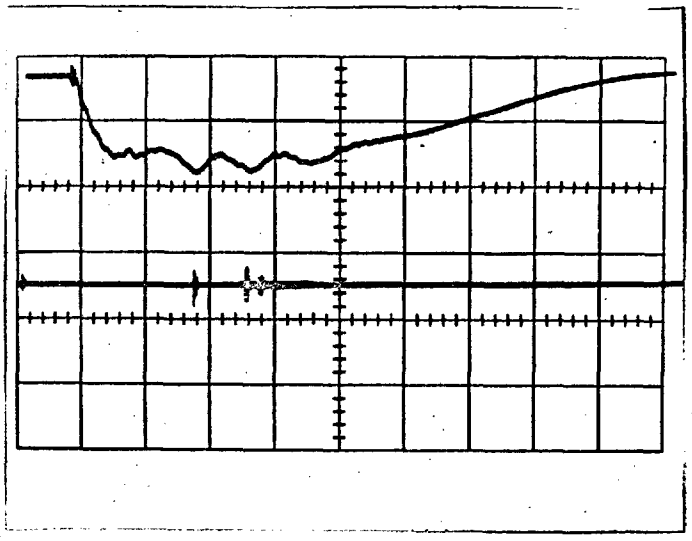

Discharge Tube Bank
Voltage =2 KV.

Mag. Field Bank
Voltage = 0 KV

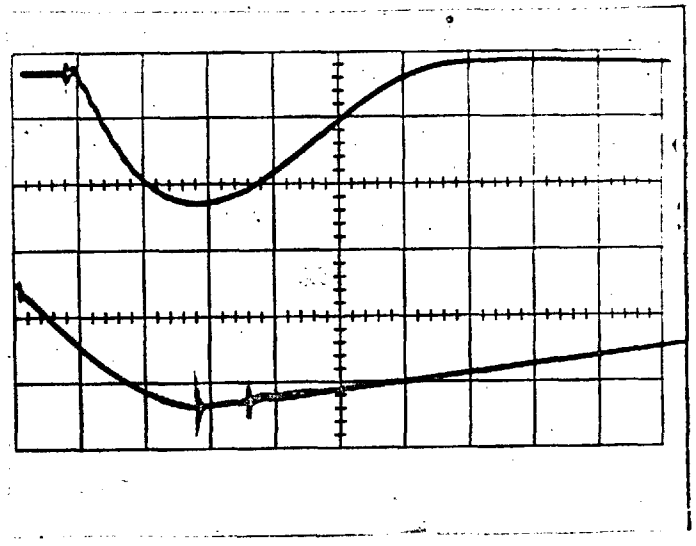

Discharge Tube
Voltage = 2 KV

Mag. Field Bank
Voltage = 1 KV

Upper Traces 20μsec/div.
Lower Traces .2msec/div.

discharge and hence from the region where the magnetic field is strongest. As it was originally constructed, the electrodes were held in position on the end of stainless steel tubes screwed to the end plates of the discharge tube. Current return is provided for by 120 brass wires, evenly spaced around the tube. Copper gauze, which is the more usual method of providing the return conductor, is not suitable in this case because of the azimuthal currents that will occur when the magnetic field is produced. Current feed to the tube is by 20 coaxial cables, connected in parallel, from a capacitor bank of 1080 μf which is capable of being charged up to 5 K volts. The charge on the capacitor bank is held off by means of a single pressurised spark gap which is triggered by discharging a capacitor, of 0.002 μf charged up to 20 KV, between one electrode and a centre pin. The peak discharge current which can be produced by this arrangement is in the order of 100,000 amps. The discharge is very nearly critically damped and has a half period of somewhat greater than 100 μsec depending to some extent on the conditions.

The discharge tube was pumped continuously. This continuous flushing system tends to keep the impurity level at an acceptable level for the device.

The pressure within the tube was monitored both by a pirani gauge and a 'vacustat', the latter always being used to set the final pressure.

The stabilising magnetic field was produced by a single layer coil consisting of 30 turns of ½" x ¼" copper bar wound such that the coil had an internal diameter of 14 cm and a length of 50 cm. The windings of the coil were spaced slightly non-uniformly, being closer

together at the ends than in the middle, in order to produce a more uniform magnetic field.

The magnetic field was produced by discharging a 2160 μF capacitor bank through the coil. The capacitors, each having a capacity of 27 μf, are arranged in groups of four, each group being served by one spark gap. The spark gaps were a six electrode type developed by Dangor and Wheeler (unpublished) and work reliably both when operated simply and when operated with the crowbarring mechanism. The magnetic field and crowbar spark gaps were triggered by means of two other spark gaps working at 30 KV.

The maximum value of magnetic field that can be produced by this arrangement is approximately 33 K gauss, and its natural period is 2 msec. Crowbarring maintains the magnetic field constant to better than 5% during the time of the discharge.

A block diagram of the electronic system is shown, in modified form, in Chapter 9. A 70 volt pulse generated by the 'trigger strip' was delayed by a two channel timing unit, one output from which is used, after amplification, to trigger a large thyratron. The output from the thyratron is fed into a 1 : 4 transformer, the output from which is used to provide a spark to trigger the magnetic field. The other channel of the first pulse delay unit is further delayed by a second, single channel, long period delay unit. The output pulse from this unit is used to drive a third delay unit which had five separate channels. One channel was used to drive a thyratron which in turn produced a spark to trigger the crowbar spark gap, another channel drives the discharge

tube spark gap, and a third was used to trigger an oscilloscope.

1.3 Diagnostics so Far Conducted on the Discharge

Apart from preliminary measurements such as framing camera photographs and current and voltage characteristics, Dangor has carried out fairly extensive measurements of the electron density within the plasma under many conditions. He used a Fabry-Perot and Mach-Zehnder systems with a He-Ne laser to obtain accurate values of density when viewed axially down the tube. Roberts carried out a determination of the electron temperature on the plasma, using the line spectra emitted by it. These measurements were mostly confined to conditions where there was no stabilising magnetic field, although a few measurements that were taken with the field indicated that T_e did not vary very greatly as the conditions were varied.

Also, measurement of the electron temperature was carried out by Troughton who used an argon ion laser operating at 4880 Å to measure resonant absorption within the plasma. This method yields a very accurate measurement of the temperature, provided the temperature lies between the limits set by the first and second ionisation potentials. Troughton carried out measurements under many conditions including situations where there was a stabilising magnetic field. His results confirmed those of Roberts in that the variation in temperature with various conditions was not great.

To summarise, we can thus see that a plasma was available which could be operated with or without a stabilising magnetic field. Under practically all conditions of interest the electron density and the electron temperature

were known. When there was no stabilising magnetic field the results could be shown to agree reasonably well with what was predicted by the shock model for a collapsing plasma sheath. Finally, the influence that the stabilising magnetic field has, has been found to be very great.

A logical extension of this work is thus a study of the discharge when there is a stabilising magnetic field present and effect of the field upon it.

1.4 The Work to be Presented in this Thesis

An experimental study of the interaction of a plasma and a magnetic field in this configuration naturally leads one to examine the possibility of measuring the increase in the magnetic field as the plasma sheath collapses. This magnetic field trapping is a useful and convenient way in which the interaction may be estimated. The primary objective of this thesis thus involves a measurement of this quantity.

The second chapter concerns itself with, essentially, a review of various methods for measuring the magnetic field and reasons why a particular method was used. Having decided upon the method, the third and fourth chapters are concerned with different aspects of the theory behind this method. The third chapter is devoted solely to a fairly complete study of the Fizeau interferometer which is shown to have several features which are particularly attractive in the present instant, and also in any situation where a high dispersion is required.

Chapter 5 consists of a description of the instrument and its method of operation, together with any ancillary work that is necessary in order

to obtain quantitative results. The chapter is concluded by presenting some results obtained with the instrument and a brief discussion of them.

A more usual method that is used to measure magnetic fields is the simple coil probe, and although this has the disadvantage of actually disturbing the plasma, it was considered useful as a supplementary measure and worth including in the thesis. Its worthiness for inclusion lies not only as a check for the Zeeman instrument but also in that a comparison of the two sets of results will give some idea of just how much the plasma is affected by the presence of the probe.

If an attempt is made to correlate the results obtained with some physical model, it becomes obvious that more information is required about the plasma in the collapsing stages. Information that would be particularly useful would concern the structure of the collapsing front. To this end, it was decided to obtain electron density 'maps' of the plasma prior to and at the pinch. Several systems for obtaining such a 'map' are considered in chapter 8; the most suitable system, a Mach-Zehnder interferometer, is discussed at reasonable length. The light source used to obtain the interferograms was a 'Q-spoiled' ruby laser. The theory, construction and performance are presented rather briefly in chapter 7. Chapter 9 is concerned with the results that have been obtained with the Mach-Zehnder.

In chapter 10 is presented a very brief survey of the physical models which have been used to explain the pinch effect. A particular model is chosen and adapted to include the effect of the trapped magnetic field and the predictions made by this model are propounded.

The conclusions drawn at the end of the thesis fall into two parts. Firstly, a critical analysis of experimental methods used in this thesis is put forward with suggestions for improvement, should the experiments be extended. Secondly, a discussion of the agreement between experiment and theory is presented together with some proposals for future work.

References

Dangor, A.E. Thesis (to be published).

Roberts, D.E. Thesis, University of London, 1967.

Troughton, J. Thesis (to be published).

Chapter 2

Methods of Measuring Magnetic Fields

2.1 Introduction

This chapter is concerned with the various methods which are available for measuring magnetic fields. These methods can be separated into, basically, two distinct classes.

The first class consists of those devices which require that some physical object be placed at the point where the field is required to be measured. The effect produced by the magnetic field on the object is then recorded. The simplest of these devices is a coil, but other devices are used, such as those which work on the principles of magnetostriction and the Hall effect, Frayne (1963).

The second class utilizes the effect of the magnetic field on the atoms and ions within the plasma. This effect produced by the magnetic field results in changes in radiation emitted or absorbed by the plasma. This second class can be subdivided again, quite naturally, into two parts. The first part includes those methods which require that radiation be directed into the plasma, the Faraday and Voigt effects (see Jenkins and White) fall into this category. The second part consists of radiation emitted from the plasma. These devices rely on the Zeeman or Paschen-Back effects; the latter only when very high fields are encountered.

2.2 Probe Devices

The use of magnetic coil probes is a sensitive method of measuring changes in magnetic fields, since in the majority of plasma physics experiments the plasmas are of a transient nature. However, these probes involve two disadvantages. Firstly, the probe is likely to disturb the plasma. For the discharge on which the measurements are to be taken this is particularly true, since at the time of peak compression the discharge is only approximately 1 cm in diameter, and it was found impractical to construct probes with an overall diameter of less than about 4 mm. The second limitation is a result of Lenz's Law, for in order to record the output voltage from the probe, some current must inevitably flow. This current will then produce a magnetic field in opposition to the field to be measured, thus reducing the observed signal. This second limitation is not nearly so restricting as the first since it can be allowed for, with relative ease and reasonable accuracy, in the mathematics.

A simplified theory concerning the operation of magnetic coil probes is attempted in chapter 6 but a more complete theory is given by P. G. Frayne (1963)

It has been implied in the last few paragraphs that it is necessary to place a coil within the plasma in order to gain any information from it. This is not strictly true, since, in the

case of a plasma device, considerable information may be obtained by simply wrapping the coil around the outside of the tube. This arrangement will obviously not give spacially resolved values of the magnetic field, but in certain circumstances when the mechanisms involved in the discharge are well understood, these can be inferred.

As has been mentioned earlier, there are several other possible probe devices, the two most important ones being those based on magnetostriction and the Hall effect. Devices of these types are produced commercially and the theory can be found in most text books. These devices are beyond the scope of this thesis; this short paragraph has only been included for the sake of completeness. It is worth noting, however, that they suffer from the same disadvantage as magnetic coils, although to a lesser degree in the case of the Hall effect devices which can be made extremely small.

2.3 Non Perturbing Methods

a) The Faraday and Voigt Effects

The Faraday and Voigt effects are closely related phenomena. The Voigt effect bears a similar relationship to the Faraday effect as does the transverse Zeeman effect to the longitudinal Zeeman effect. Since there is this close relationship between the two phenomena, it would be superfluous to discuss both. The following discussion deals with the Faraday effect although with minor changes could equally apply to the Voigt effect.

If we consider the propagation of an electromagnetic wave through a homogeneous plasma, then, in the presence of a steady magnetic field in the direction of propagation, it is found that there is a coupling between two orthogonal states of polarisation. Physically the results of this can most easily be seen by considering that any plane polarised wave can be said to be the resultant of two contra-rotating circularly polarised components. It is then found (Denisse and Delcroix) that the refractive indices for the two components are different. The dielectric constants are given by

$$\varepsilon_1 = 1 - \frac{\omega_o^2}{(\omega+\omega_L)(\omega+\Omega_L)}$$

and $$\varepsilon_2 = 1 - \frac{\omega_o^2}{(\omega+\omega_L)(\omega-\Omega_L)}$$

when $\omega >> \omega_L, \Omega_L$

where ω is the frequency of the propagated wave and ω_L and Ω_L are the electron and ion gyromagnetic frequencies and ω_o is the plasma frequency.

In almost all cases $\omega_L >> \Omega_L$ since

$$\omega_L = \frac{q_e}{m_e} B$$

and $$\Omega_L = \frac{q_i}{m_i} B$$

and hence

$$\varepsilon_1 = 1 - \frac{\omega_o^2/\omega^2}{(1 - \omega_L/\omega)}$$

and $\varepsilon_2 = 1 - \frac{\omega_0^2/\omega^2}{(1 + \omega_L/\omega)}$

This difference in refractive indices results in, on emergence from the plasma, the two components having traversed different optical path lengths. This means that there is a phase change between the two components which results in the emergent plane polarised wave being rotated through an angle Θ. Where Θ is given by

$$\Theta = \frac{\pi d}{\lambda} \cdot \frac{\omega_0^2}{\omega^2} \cdot \frac{\omega_L/\omega}{(1 - \omega_L^2/\omega^2)}$$

where d is the physical path traversed and λ is the wavelength.

On the plasma device in question d ~ 40 cm and $n_e \sim 10^{17}$ electrons/cc and B ~ 10 K gauss then $\Theta = 0.5 \times 10^{-5}$ radians when $\lambda = 5000$ Å

Rotational changes of this order are not easily measured and involve very sophisticated techniques.

In arriving at the above formula the effect of ions or neutrals on the rotation has been neglected. This is only valid when radiation travelling through the plasma is well removed in wavelength from an emission line, then a considerable increase in the rotation occurs. This effect is usually known as resonance Faraday rotation. The mathematics involved in calculating the rotation in these is quite lengthy and will not be attempted here. It is sufficient to say that rotation is dependent upon the profile of the natural plasma radiation and whether it is shifted in wavelength from the probe

beam. The profile, width and shift of many spectral lines in Argon have been calculated by Griem (1965) but the calculated width is not in very good agreement with measured widths obtained, for example, by Jalufka (1966) and Roberts (1967). Moreover one cannot ascribe to the measured or calculated values of width an accuracy of generally better than ±30%. This leads to uncertainties in the value of the field associated with a particular rotation. There is a further difficulty involved, in that during the initial stages of the discharge whilst the driving current is still flowing then the theory is not truly valid,'Troughton.' This is particularly irritating when used on the stabilised Z pinch since any field compression that might occur, will do so before the current has stopped flowing.

Resonance Faraday rotation has been measured by Troughton at Imperial College using an argon ion laser on an argon plasma. Very great rotations (~ 100°) have been observed by him on the 4880 Å line emitted by the laser, although the values of the magnetic field obtained do not seem particularly satisfactory since they differ from the field measured in the absence of a plasma by as much as 100%

b) Zeeman Effect

The Zeeman effect at first sight appears to be the ideal method by which to measure magnetic fields. The Lande splitting factors are accurately known from spectroscopic data, (Moore 1949), and in consequence this could lead to a very reliable determination of magnetic fields. However, frequently the spectral lines emitted from the plasma are

broadened to such an extent that the line width far exceeds any splitting that may occur due to the Zeeman effect. In such a situation it is impossible to resolve the separate π or σ components and hence one must resort to some method which involves taking the small difference between two relatively large signals. This inevitably leads to problems of signal to noise ratio. Several methods for overcoming this difficulty are outlined later.

The essential requirements for measuring Zeeman shifts are

a) A dispersive system that is capable of fairly high dispersion.

b) An instrument which samples the wave form at two or three places.

Several possibilities exist for each of these requirements, producing very many combinations, but the best approach to the problem is to decide on which dispersive element to use and then find the most suitable sampling system

2.4 Possible Dispersive Elements

Table 2.1 shows several dispersive elements and some principle factors associated with them. A Prism spectrometer can be excluded immediately due to its very small dispersion and low light gathering power product. The light gathering power of a prism system has been shown by Jaquinot to be $3.4/\beta$ less than an equivalent Fabry Perot, where β is the angle subtended by the entrance slit at the prism. Jaquinot (1954) defines his equivalent Fabry Perot to be equal in area to the

area of the base of the prism. The angle β for most spectrometers is in the range of ·1 to ·01 radians thus giving the figures quoted in table 2.1.

The dispersion of a diffraction grating spectrometer is usually considerably higher than for a prism spectrometer, particularly when used in higher orders and could be quite suitable for this application. It has not, however, such a good light gathering power as the Fabry Perot, it being restricted by the same factor as for prism spectrometer. Values of β used with a diffraction grating are usually ~·1 radians although larger angles are possible if curved slits are employed. The use of curved slits in this application is somewhat impractical, as will be seen later when the sampling arrangements are discussed.

The arguments used for and against the diffraction grating apply equally to the echelon grating, since very high resolution is not of primary importance. In addition, since the echelon grating is used in very high orders, confusion is very likely considering spectra such as the argon spectrum which has a great number of emission lines. To avoid this order overlap confusion with the echelon and the diffraction grating a pre-dispenser would be required. This detracts somewhat from the advantage of simplicity that these two systems have.

The Fabry Perot interferometer has several advantages which

Table 2.1 Relative Merits of Various Dispensive Elements.

Dispersive Element	Dispersion	Resolution or Resolving Power	Light gathering power w.r.t. Fabry Perot
Prism	Normally very low 0.01-0.1 mm/Å Can be made higher but at expense of light gathering Power	Dependent mainly on dispersion ~1Å	30-100 times worse than Fabry Perot for an equivalant size (see text) but can be made high at the expense of resolution and dispersion.
Diffraction Grating	Large dispersion possible up to ~1 cm/Å	Dependent mainly on dispersion ~ 0.01Å	~ 30 times worse for equivalent size (see text)
Echelon Grating	Large	Very high ~ 10^6	Same as equivalent diffraction grating
Fabry-Perot Interferometer	Large	Very high on dispersion ~10^6 - 10^7	———
Fizeau Interferometer	Large up to 10 cm/Å	Slightly less than F.P. but indep. of dispersion ~10^6-10^7	2 - 5 times worse than Fabry Perot (see text)
Lummer Gehrcke Plate	Large	Very high	~ Fabry Perot

strongly commend its use in the present application. Firstly, its dispersion can easily be varied by adjusting the separation between the two reflecting surfaces. This is a relatively simple procedure and consequently the instrument could be made adaptable to almost all situations. The high light gathering power of a Fabry-Perot has been mentioned earlier when it was compared to a diffraction grating. This highly desirable characteristic is a result of the axial symetry possessed by the Fabry-Perot. This axial symetry, however, leads to a very serious disadvantage when one comes to consider the sampling arrangement that could be used in conjunction with the Fabry-Perot. Since the fringes produced are circular, a series of annular slits would be necessary in order to gather the total quantity of light from each fringe. The production of annular slits, which are variable in thickness and diameter would be an extremely difficult, if not impossible, task. To produce annular slits of fixed thickness and diameter is considerably less difficult, but this would necessitate extremely careful control over the plate separation of the Fabry-Perot.

At some loss in the light gathering power the slit arrangement may be simplified by angling the Fabry-Perot to the incident beam. Fringes produced by the angled Fabry-Perot are in fact arcs of large diameter fringes and if the incidence angle is great enough they may be considered as straight lines; this would lead to very great simplification of the sampling arrangement. If one plate of

the Fabry-Perot interferometer is tilted at a slight angle to the other, then, Fizeau fringes are produced. These fringes are straight and eminantly suitable to this application. There is of course some loss in light gathering power with respect to the Fabry-Perot but Burgess (1966) showed that this involves quite a useful saving over the equivalent grating. The Fizeau interferometer has two further advantages in that the dispersion is linear, and may be varied independently of the resolving power simply by varying the angle between the interferometer plates. This is not possible with a Fabry-Perot. The analysis of a Fizeau fringe system is rather more complex than for the Fabry-Perot, and this is discussed more fully in chapter 3.

2.5 Possible Sampling Arrangements

In general, it is necessary to monitor the intensity at three different points on the profile. If, however, the line profile is known, one can monitor at two points. In an optically thin, electron collision dominated plasma the line shape is dispersive and the width will be dependent upon the electron density and to a lesser degree on the temperature. Thus in order to use a two channel system it would be necessary to know the line widths at all times during the discharge. Alternatively, one can ensure that this width never becomes comparable to the instrument width in which case the effective width remains the same throughout the time of the discharge.

The first arrangement is the two slit method, and consists of two slits placed at a point on the line profile each measuring a different polarisation.

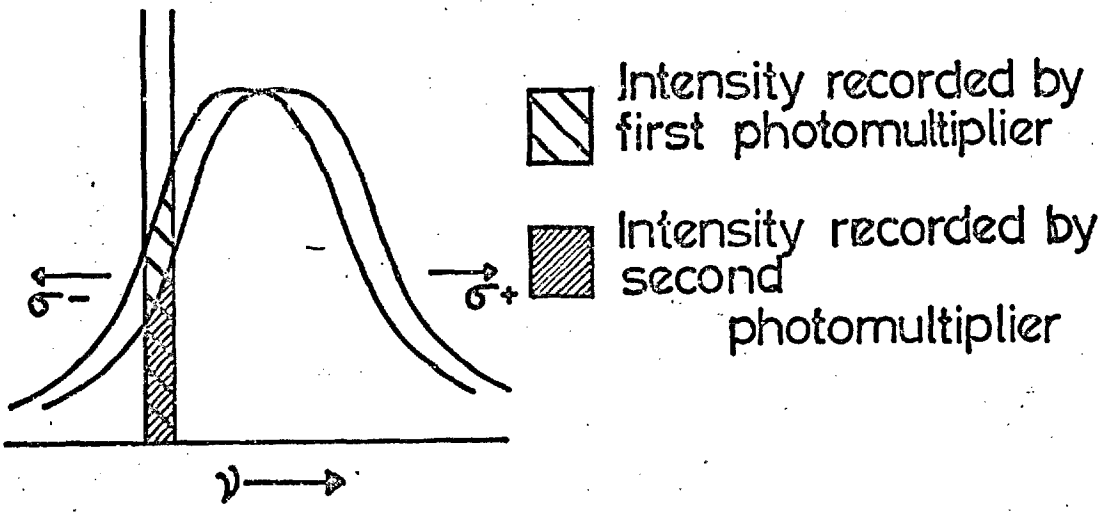

Fig 2.1 OPERATION TWO SLIT METHOD

Fig. 2.1 shows the different intensities recorded by the two photomultipliers. Taking the sum and difference of these two signals the magnetic field may be calculated. This is the arrangement that was adopted by Jahoda et alia (1963). Jahoda reported a very poor signal to noise ratio, which is not surprising considering the amount of light not used by this system.

A three slit arrangement was used by Hübner. This will yield magnetic field measurements without prior knowledge of the width and shape although relies on there being a portion of the line profile which is linear. This method suffers from the same defect, of poor use of available light, as did Jahoda's method.

A further method which can be used is a method utilizing a neutral density wedge. As each component of the line is shifted in opposite directions, the neutral density wedge may be so placed such that the intensity of one component transmitted through the wedge increases whilst the other component decreases. This method of measurement is somewhat better than those previously mentioned, in that it is capable of utilizing approximately 50% of the light.

The final method to be considered is comparable to the neutral wedge arrangement with regards to light utilisation. This sampling arrangement is much more versatile than the neutral density wedge system and is of relatively simple construction. It was for these reasons that this method was chosen. This method will be dealt with fully in Chapter 4 and will not be considered further at this juncture.

To summarise the section on the Zeeman effect we can see that the most attractive dispersive element is undoubtably the Fabry-Perot but the difficulty involved in the sampling arrangement leads us to consider other dispersive elements. The most promising of these is the Fizeau interferometer which, in conjunction with a relatively simple sampling arrangement, forms a convenient method for measuring magnetic fields in plasmas.

References

Burgess, D.D. Thesis, University of London, 1966.

Denisse and Delcroix, Plasma Waves, Interscience, 1963.

Frayne, P.G. Thesis, University of London, 1963.

Griem, H. Plasma Spectroscopy, 1964. (McGraw-Hill)

Hübner

Jahoda et al Physics Review 131, 1, 24, 1963
Jalufka et al Phys Rev Letters 16, 1073, 1966
Jenkins and White Fundamentals of Optics, Third Edition McGraw-Hill, 1957.

Moore, C. Atomic Energy Levels, 1949.

Roberts, D.E. Proc. Phys. Soc (in press)

Troughton, J. Thesis (to be published)

Chapter 3

3.1 General

The material presented in this chapter is a treatment of multiple beam Fizeau fringes. In chapter 2 consideration was given to various dispersers, and although it is not proposed to delve any more deeply into the suitability of the various grating devices, it should become more apparent by the end of the chapter as to the suitability of the Fizeau interferometer over the Fabry Perot.

An exact analytical description of multiple beam Fizeau fringes, which we will call in future wedge fringes, is not possible. Most of this chapter is based therefore on approximations which, in the most part, will be approximations to the Airy function. In this way analytic expressions can be obtained for various associated parameters, and criteria introduced which set the range of validity of these expressions.

In the latter part of this chapter we consider a slightly different approach to the problem by solving the equations numerically using an IBM 7090 computer. The reason for this is to see if the instrument can be used under conditions which lie outside those conditions set by the breakdown of the Airy sum.

3.2 Formation of Fizeau Fringes

The formation of wedge fringes has been discussed by several authors (Brossel 1947; Tolansky 1947), and consequently only a short account will be given here.

Fig 2.1 illustrates the formation of wedge fringes OA, OB are reflecting surfaces, usually aluminum or silver coatings on glass or quartz plates, at an angle θ. A ray is incident on the plates and after transmission through the plate OB strikes the plate OA at angle α. Most of the ray is reflected from OA and multiple reflections occur within the optical cavity. The p^{th} transmitted wave emerges from OA at an angle $\alpha + 2(p - 1)\theta$. Note that for simplicity the refraction at the quartz-air and quartz silver surfaces has been neglected. The dashed line OW_p represents the virtual position of the p^{th} transmitted wave front. It can clearly be seen from the diagram that the path between the directly transmitted wave and the p^{th} transmitted wave at the point P on the plates is given by

$$\Delta_p = PN_p - PN_1$$

$$= L (\sin \alpha_p - \sin \alpha)$$

The phase difference between these two rays is thus

$$\delta_p = \frac{2\pi}{\lambda} \Delta_p + 2(p - 1) \Phi$$

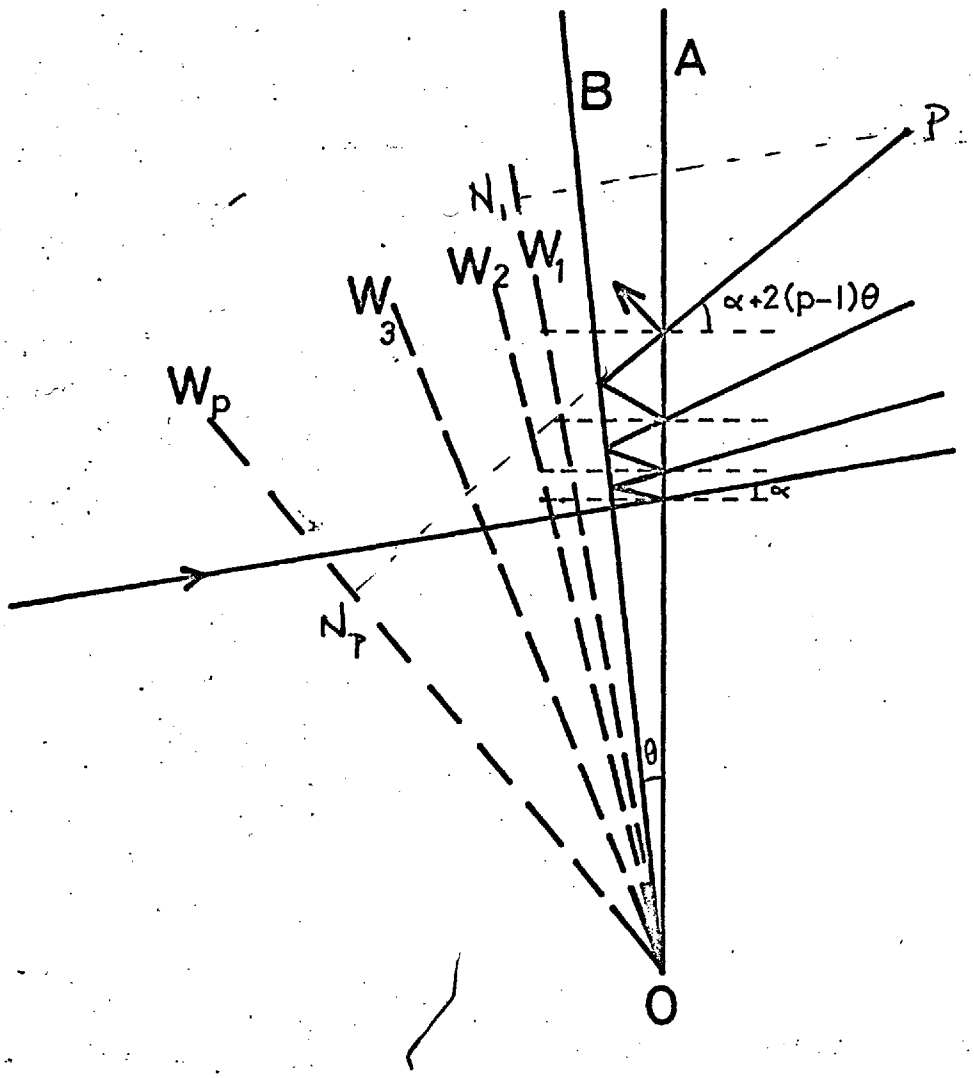

Fig 3.1 ILLUSTRATING THE FORMATION OF FIZEAU FRINGES

The term $2(p - 1)\Phi$ here represents the total phase change due to $2(p - 1)$ reflections, each one producing a phase change Φ, within the cavity. However this term is quite unnecessary in the understanding of wedge fringes and merely results in a shift of the fringes. For this reason it is not included in the following work.

If the distance between the two reflecting surfaces at P is t then

$$t = h \tan \theta$$

and $$\delta_p = \frac{2\pi t}{\lambda} \quad p \quad \frac{\Delta_p}{\tan \theta}$$

$$= \frac{2\pi t}{\lambda} \frac{1}{\tan \theta} \left\{ \sin \left[\alpha + 2(p - 1)\theta\right] - \sin \alpha \right\}$$

$$= \frac{2\pi t}{\lambda} \cdot 2 \cos \alpha \frac{\sin (p - 1)\theta}{\tan \theta} \left\{ \cos (p - 1)\theta - \tan \alpha \sin (p - 1)\theta \right\} \qquad - 3.1$$

Now the transmitted fronts can be described by

$$A_o tt' e^{i\delta_1}, A_o tt' r^2 e^{i\delta_2}, \ldots A_o tt' r^{2(p-1)} e^{i\delta p}$$

where A_o is the incident amplitude, t and t' are transmissions at the first and second surfaces respectively and r is the reflection at each surface (assumed to be the same)

The resultant amplitude at the point P is thus

$$A_p = A_o tt' \sum_{p=1}^{\infty} r^{2(p-1)} e^{i\delta p}$$

$$= A_o T \sum_{p=1}^{\infty} R^{(p-1)} e^{i\delta p}$$

and the corresponding intensity is

$$I_p = A_\delta^2 T^2 \left| \sum_{p=1}^{\infty} R^{(p-1)} e^{i\delta p} \right|^2 \qquad - 3.2$$

As stated at the beginning of this chapter, this expression has no analytic solution due to the rather involved form of δp. However, in all practical cases the angle Θ is small. We can therefore expand this relation in terms of Θ, and, neglecting all powers of Θ greater than 2 we obtain

$$\delta p = \frac{4\pi t}{\lambda} \left\{ p \cos \alpha - \frac{2p^3\Theta^2}{3} \cos \alpha - p^2\Theta \sin \alpha \right\} \qquad - 3.3$$

A similar result to this was obtained by Burgess as an extension of Brossel's work. Equation 3.3 differs from the corresponding equation for a Fabry Perot by the factor

$$\frac{4\pi t}{\lambda} \left\{ \frac{2p^3\Theta^2}{3} \cos \alpha + p^2\Theta \sin \alpha \right\}$$

The criterion used by Brossel that this correction should not affect wedge fringes being described by the Airy function, is that the last effective ray which contributes to the summation should not be retarded by more than $\lambda/2$. In other words, when α is non-zero,

$$\frac{4\pi t}{\lambda} \left\{ \frac{2p^3\Theta^2}{3} \cos \alpha + p^2\Theta \sin \alpha \right\} < \pi \qquad - 3.4$$

We will return to this criterion later but for the moment it is convenient to discuss some practical aspects of the wedge on the basis of it being described by the Airy function.

3.3a Fringe Spacing

Assuming the validity of the Airy summation, then symetrical uniformly spaced fringes occur across the interferometer. A maximum will occur for normal incidence when

$$n\lambda = 2t \qquad - 3.5$$

The next maximum will be given by

$$(n + 1)\lambda = 2(t + \Delta t)$$

therefore $\Delta t = x\Theta = \frac{\lambda}{2}$

$$\text{or} \quad x = \frac{\lambda}{2\Theta} \qquad - 3.6$$

where x is the fringe spacing.

We notice that the fringe spacing is only dependent upon the wedge angle Θ. As we shall see, this will enable the dispersion of the instrument to be varied without altering the resolving power.

3.3b Free Spectral Range (F.S.R.)

If in equation 3.4 we were to consider a change in wavelength which corresponds to a change of one order, instead of the change

in t which corresponds to this, then we obtain

$$\Delta\lambda_s = \frac{\lambda}{n-1} \simeq \frac{\lambda}{n} = \frac{\lambda^2}{2t} \qquad - 3.7$$

when $\Delta\lambda_s$ is called the free spectral range. The smallest value of $\Delta\lambda_s$ that will be required will be set by the doppler width of the line. The lowest temperatures likely to be encountered are about 10,000°Å and the doppler width at this temperature and at 5,000°Å is approximately 0.03 Å. Thus a free spectral range of 0.1 Å would be the smallest that would be required. This corresponds to a plate separation of about 1cm.

3.3c Dispersion

The wedge interferometer produces a linear dispersion which is given by

$$D = \frac{x}{\Delta\lambda_s} = \frac{t}{\lambda\theta} \qquad - 3.8$$

This can achieve very large values without too many practical difficulties being involved, for example with a plate separation of 1cm and with one fringe across 5cm diameter plates a dispersion of 2,500 mm/Å is obtained at 5,000 Å.

3.3d Half Width and Finesse of the Airy Function

There are three contributing factors to the total width of the instrument function. These can be expressed in terms of the finesse.

N_R is called the reflection finesse and is given by

$$N_R = \frac{\pi\sqrt{R}}{1-R} \qquad - 3.9$$

N_A was called the scanning finesse by Chabbal (1953) but a more suitable description is the aperture finesse. In this case, the finesse describes the contribution to the total line width of the finite angle of acceptance. If the maximum acceptance angle is α_{max} then

$$N_A = \frac{\lambda}{\alpha_{max}^2 t} \qquad - 3.10$$

The third contributing factor is due to imperfections in the plates. In the case of the Fabry-Perot these imperfections are attributable to three separate causes

1) Small defects in plates

2) Lack of Parallelism

3) Curvature of the plates

In the case of the Fizeau interferometer, however, only the first of these causes is applicable. If we assume a Gaussian distribution in defects with a mean deviation of λ/q then the surface defects finesse is given by

$$N_D = q/2$$

A much more complete description of the total finesse is given

by Chabbal.

The resultant finesse is given by

$$\frac{1}{N^2} = \frac{1}{N_R^2} + \frac{1}{N_D^2} + \frac{1}{N_A^2}$$

Thus the width of the profile is given by

$$w = \frac{\Delta\lambda_\Theta}{N}$$

The overall finesse of the instrument will determine to some extent the resolution which can be obtained with a practical interferometer. The aperture finesse, however, is important in two other respects concerning the breakdown of the Airy summation and the luminous throughput of the interferometer. This will be returned to in a later section.

3.3e Resolution

If we use a modified Rayleigh criterion that two lines are resolved when the saddle to peak intensity is $8/\pi^2$ then we see that the resolving power is (Mewe and De Vries, 1964)

$$P = 0.97 \frac{\lambda}{\Delta\lambda_\Theta}$$

$$\approx \frac{\lambda}{\Delta\lambda_\Theta} \qquad - 3.11$$

This can be expressed in terms of the finesse N_R

$$P = n N_R$$

$$= \frac{2\pi t\sqrt{R}}{\lambda(1-R)} \qquad - 3.12$$

We therefore find one of the great advantages of the wedge interferometer, i.e. that the dispersion may be altered without changing the ratio of dispersion to resolving power:-

$$D/P = \frac{2\theta(1-R)}{\lambda^2\pi\sqrt{R}} \qquad - 3.13$$

this is independent of t and hence by varying t the dispersion can be varied whilst keeping the above ratio constant.

3.4 Luminosity and Throughput of an Idealised Wedge with Respect to other Devices.

Burgess has shown that the luminosity of the wedge interferometer falls below that of an equivalent scanning Fabry-Perot by a factor of N_R when an ideal wedge is considered. However, the luminosity is not the most useful quantity to be considered since the final superiority or inferiority of the wedge can only be determined in terms of the signal to noise ratio at the detector. Furthermore a fair comparison is not gained by considering the luminosity of the two instruments since they are used in rather different ways. The scanning Fabry Perot rejects all wavelengths which are not included within the instrument function but accepts light from all parts of the plate. The wedge interferometer, on the other

hand, does not only accept wavelengths within the instrument function, but other wavelengths determined by conditions of the source, although it does not accept light from the whole area of the plates. It is therefore difficult to determine any precise criterion upon which to compare the two which is applicable to all equations. For the shift to width measuring instrument the free spectral range had to be adjusted until the width of the line under investigation was about $\frac{1}{6}$ of it. A larger fraction than this produced an error due to order overlap which changed too rapidly to be calculable. Thus the maximum throughput was about $\frac{1}{6}$ that of an equivalent Fabry-Perot. When measuring Zeeman shifts however the use of a three channel recording system obliviates any need for concern of order overlap and fig 4.5 shows the optimum operating conditions for the Zeeman instrument. We see from fig 4.5 the conditions of maximum sensitivity for shift to width ratios up to unity, varies slowly and that values of F.S.R./width which correspond to these optima lie between 2 and 3.

For an ideal wedge illuminated with monochromatic light, the ratio of the luminosities of the Fabry Perot and the wedge for small α is given by, following Burgess,

$$\frac{L_{FP}}{L_W} = \frac{1}{\frac{2}{\lambda}\int_{n\lambda-\frac{\lambda}{2}}^{n\lambda+\frac{\lambda}{2}} \frac{dt}{1+B\sin^2(\frac{2\pi t}{\lambda})}} \qquad - 3.14$$

where $B = \frac{4R}{(1-R)^2}$

$$\therefore \quad \frac{L_{FP}}{L_W} = \frac{1}{\sqrt{1+B}} \simeq \frac{1}{N_R}$$

If however the wedge is illuminated with a spectral line of width w then the resultant profile can be described in terms of the line profile and the Airy function. For the plasma on which this work has been done, the line profiles can be described best by a dispersive profile.

$$D(x) = \frac{1}{\pi w} \cdot \frac{1}{1+(\frac{x}{w})^2}$$

It is not necessary to convolute these two profiles if we remember that the Airy function can be represented by an infinite series of dispersive functions. The resultant profile now becomes

$$\frac{1}{1 + B^* \sin^2 \pi x}$$

where B* is given in terms of the new line width

$$B^* = \frac{4}{\pi^2 w^{*2}}$$

where $w^* = \frac{1 - R}{\pi \sqrt{R}} + w \simeq w$

Provided $\frac{1 - R}{\pi \sqrt{R}}$ is small.

Thus the ratio of throughputs will now be

$$\frac{T_{FP}}{T_W} = \frac{1}{\sqrt{1+B^*}}$$

$$= \frac{1}{\sqrt{1+\frac{4}{\pi^2 w^2}}} \qquad - 3.15$$

As we have seen for maximum sensitivity of the instrument w should lie between $\frac{1}{2}$ and $\frac{1}{3}$. Therefore, at worst, the throughput of the wedge falls below that of the Fabry Perot by a factor of 2.

3.5 The Instrument Function using the Airy Function

Up until now very little has been said concerning the effect of the finite solid angle of acceptance on the observed profile.

This new instrument profile can be shown to be similar to that used by Chabbal for the scanning Fabry-Perot except that in the wedge case the intensity is a function of x, rather than time. The profile is

$$I(x) = \int_0^{\alpha_m} \frac{2 \sin\alpha \, d\alpha}{1+B \sin^2(\frac{2\pi t}{\lambda} \cos \alpha)}$$

$$= -\frac{2\pi t}{\lambda} \frac{1}{(1+B)^{\frac{1}{2}}} \left[\tan^{-1}\left\{(1+B)^{\frac{1}{2}} \tan(\frac{2\pi t}{\lambda} \cos \alpha)\right\}\right]_0^{\alpha_m} \qquad - 3.16$$

Following Burgess, if we put

$$\frac{2\pi t}{\lambda} = \pi(n+e)$$

and $\frac{2\pi t}{\lambda} \cos \alpha_m \simeq \frac{2\pi t}{\lambda} (1 - \frac{\alpha_m^2}{2})$

$$= \pi(n+e) - \frac{\pi}{N_A}$$

where n is an integer and $0 < e < 1$

and N_A is as defined in equation 3.10

then

$$I(x) = \frac{\lambda}{2\pi t(1+B)^{\frac{1}{2}}} \left[\tan^{-1}\left\{(1+B)^{\frac{1}{2}} \tan \pi e\right\} - \tan^{-1}\left\{(1+B)^{\frac{1}{2}} \tan\left(\pi e - \frac{\pi}{N_A}\right)\right\}\right] \quad -3.17$$

differentiation of this equation with respect to e shows that the maximum occurs when

$$e = \frac{1}{2N_A}$$

$$= \frac{t\alpha m^2}{2\lambda} \quad - 3.18$$

When the Fizeau interferometer is being used to measure the shift to width ratio due to the stark effect this condition is of the utmost importance in so far as a systematic error may be introduced. This error is not nearly as important when the interferometer is used in the three channel, magnetic field measuring instrument, because the sensitive difference signal no longer depends on the accurate setting on the line centre (chapter 3).

3.6 Optimum Values of N_R and N_A

Chabbal has shown that the peak height of the transmitted profile maximises when

$$N_R = 1.15\ N_A \quad - 3.19$$

It was pointed out by Burgess that a more useful criterion is when the total intensity maximises. This results in

$$N_R = 1.02\ N_A \qquad - 3.20$$

The difference between the two is not critical however, because the luminosity varies very little over the range

$$0.9 < \frac{N_R}{N_A} < 1.5$$

as Chabbal points out.

2.7 Instrument Profile when the Airy Function is not Applicable.

The condition for the breakdown of the Airy summation is given by equation 3.4. As the angle α is reduced, 3.4 reduces to the less stringent requirement obtained by Brossel and Tolansky. However, it is desirable to keep the angle α as large as possible in order to increase the throughput of the instrument. This results in the Brossel criterion becoming inadequate as was pointed out by Burgess. Nevertheless, even in the present case the angle α will be small ($< 10^{-2}$ radians) with the consequence that condition 3.4 reduces to

$$\frac{4\pi t}{\lambda}\left[\frac{2p^3\theta^2}{3} + p^2\theta\alpha_m\right] < \pi \qquad - 3.21$$

A further restriction, which has been mentioned in section 2.3, results from the aperture finesse.

Since for optimum operating conditions

$$N_R \simeq N_A$$

and furthermore since

$$p \simeq 1.4\ N_R$$

then $$N_R = \frac{\lambda}{\alpha_{max}^2\ t} \qquad - 3.22$$

effectively sets another condition on the maximum values of α_{max} and t, because it is desirable that N_R be in the order of 20.

Conditions 3.22 and 3.21 can be represented graphically as in figs 3.2 and 3.3. Here graphs for various values of θ are plotted for α against t and various values of N_R are plotted for α against t.

From the graphs we see that if t is sufficiently large then the condition given in 3.21 is dominant. Conversly for small vlaues of θ then the aperture condition is more restrictive. This will necessitate the throughput of the instrument being reduced.

In fig 3.3 we see that as N_R is progressively increased, condition 3.21 becomes progressively more important with consequent restrictions on θ and t. This is generally undesirable.

The condition 2.21 sets a limit on when the normal incidence profile ceases to be describable by the Airy function. This is

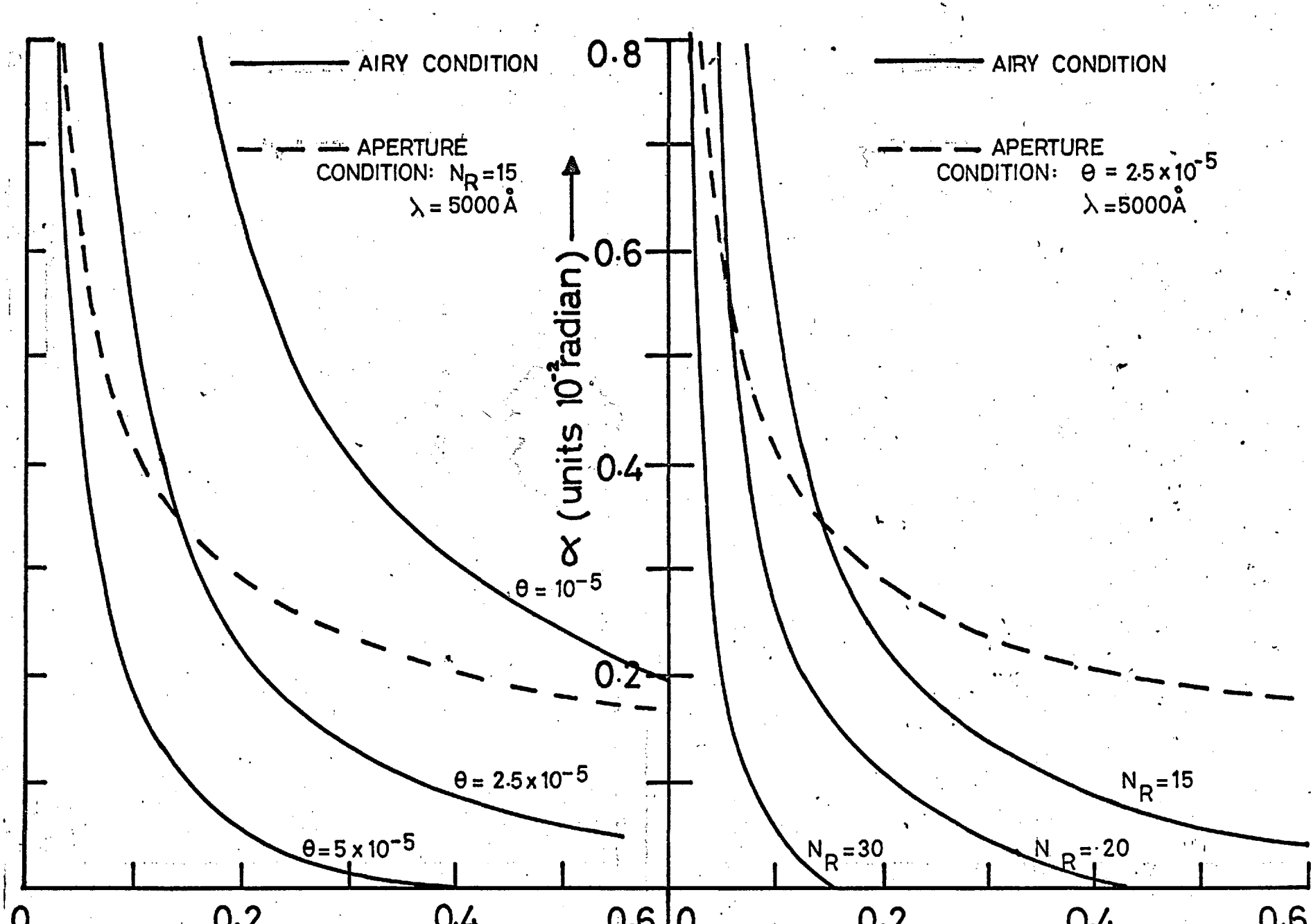
AIRY CONDITION
APERTURE CONDITION: N_R=15
λ = 5000 Å
θ = 10^{-5}
θ = 2.5 x 10^{-5}
θ = 5 x 10^{-5}
α (units 10^{-2} radian)
0.8
0.6
0.4
0.2
0
0.2
0.4
0.6
t in cm
AIRY CONDITION
APERTURE CONDITION: θ = 2.5 x 10^{-5}
λ = 5000Å
N_R=15
N_R=30
N_R=20
0
0.2
0.4
0.6
t in cm

Fig 3.2

Fig 3.3

a particularly arbitrary limit and may impose a more severe restriction than is necessary.

An exact analytic solution to the problem has not been found and resort must be made to numerical methods. Kinosita (1952) calculated the profile of a Fizeau fringe under the condition of normal incidence and for one value of R, θ and t. Kinosita's results were very restrictive in that he considered only normal incidence and this one condition. A computer program was written in order to ascertain firstly whether or not the limit set by Burgess is valid and secondly to find the effect of the acceptance angle on Kinosita's profile.

Equation 3.1 can be rewritten

$$\delta = \frac{2\pi t}{\lambda}\left[\frac{\sin 2(p-1)\theta \cos\alpha - 2\sin^2(p-1)\theta \sin\alpha}{\tan\theta}\right] \qquad - 2.22$$

An attempt was made to use this formula directly to calculate δ but unfortunately, it proved too prohibitive in time. However because both α and θ are always small, then both $\sin\alpha$, $\cos\alpha$ and $\tan\theta$ can be expanded, neglecting all terms of α and θ higher power than three. 3.22 becomes

$$\delta = \frac{2\pi t}{\lambda}\,\frac{\left[\sin 2(p-1)\theta.(1-\alpha^2/2) - 2\sin(p-1)\theta.(\alpha-\alpha^3/6)\right]}{\theta + \theta^3/3} \qquad - 3.23$$

For several angles of incidence, the intensity of the transmitted light was obtained using 3.23. These profiles were then numerically convolved to obtain the required final profile. This was compared with the profile obtained using equation 3.16.

It was assumed for this convolution that the intensity varied with α as a 'top hat' function; the intensity being zero when

$$-\alpha_{max} > \alpha > \alpha_{max}$$

and finite and constant within the range

$$-\alpha_{max} < \alpha < \alpha_{max}$$

This assumption will not be valid when very small angles of α_{max} are encountered, but since the primary aim of this calculation is to consider the effect of large α_{max}, the use of the 'top hat' function is justified.

3.8 Discussion of Computed Results

Fig 3.4, 3.5, 3.6 show the Fizeau instrument profile under various conditions. It has been assume din these calculations that we have a 'perfect' interferometer i.e. an interferometer with no absorption. The reflectivity is taken as 0.9 throughout. The intensity scales, although arbitrary, are consistent, in so far as the incident flux is normalised to take account of the

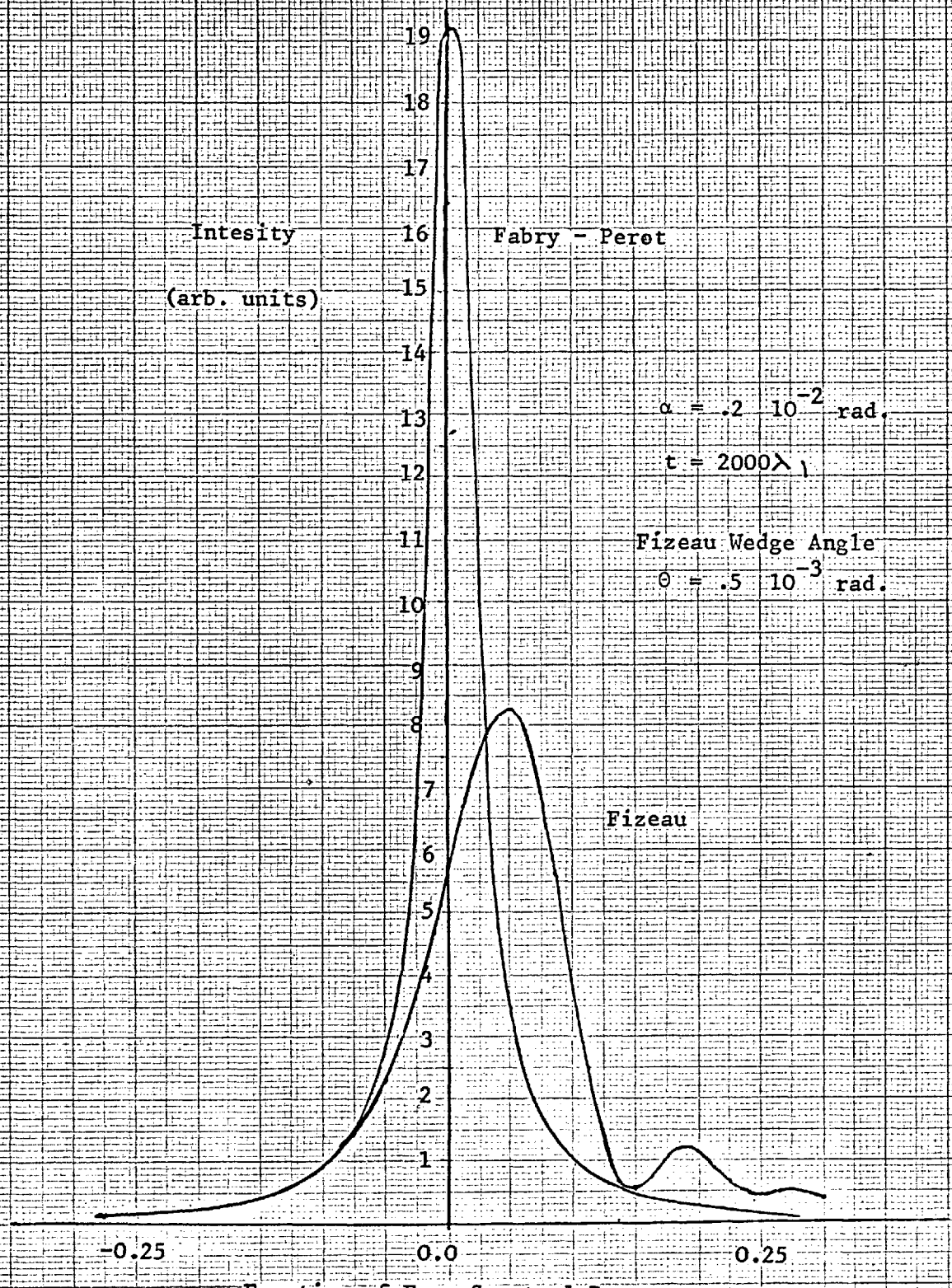

Fig. 3.4. Comparison between Fizeau and Fabry - Perot Instrument Functions.

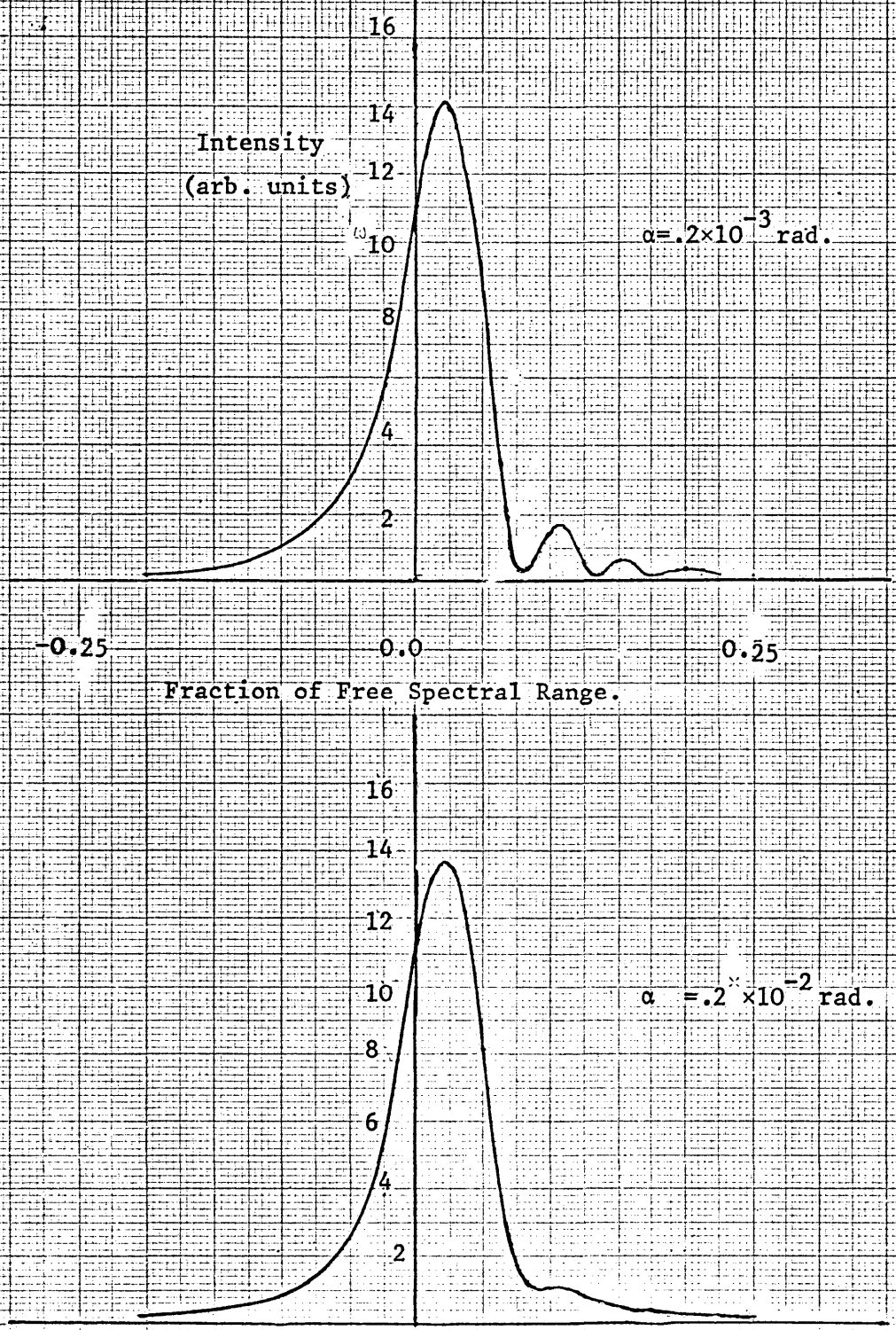

Fig.3.5 Fizeau Profile for Two Acceptance Angles.

$\theta = .2 \times 10^{-3}$ rad. $t = 2000\lambda$

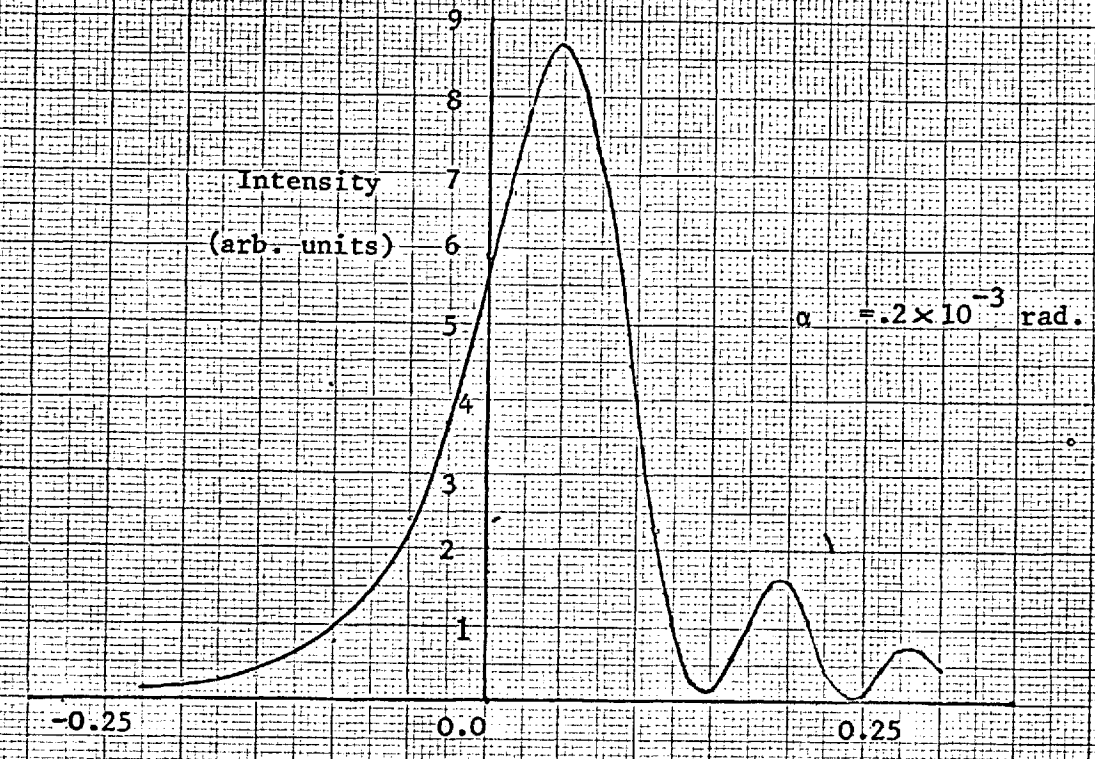

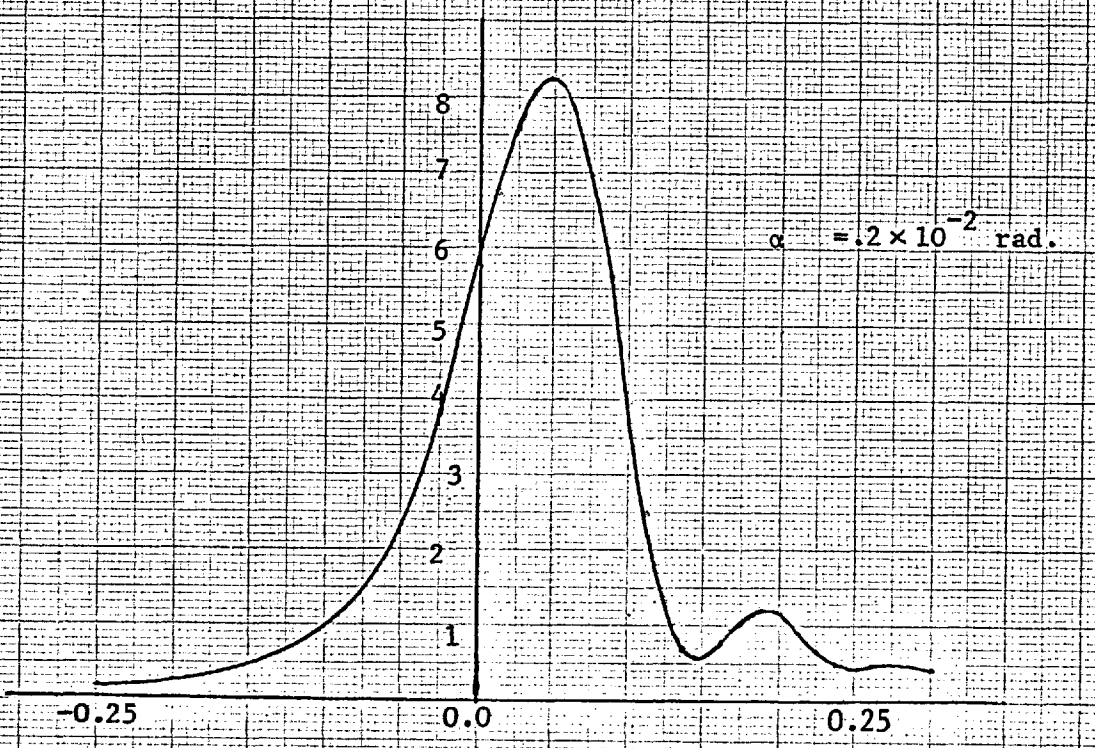

Fig. 3.6 Fizeau Profile for Two Acceptance Angles.

$\theta = .5 \ 10^{-3}$ $t = 2000 \ \lambda$

varying aperture sizes.

Thus, although the lower profile in fig 3.5 would normally be almost 10 times the intensity of the upper one, it is shown here after allowance for the larger source size.

We can see from the graphs that the effect of increasing θ is manifold

a) Peak height reduced

b) Width increased

c) Shift of Peak increased

d) Assymetry introduced, including the production of subsidiary maxima.

These four effects can be inferred from the single result obtained by Kinosita. As the angle θ is increased it is interesting to note the changes in the subsidiary maxima. The maxima not only increase in amplitude and number but their separation becomes greater.

The lower profiles in figs 3.5 and 3.6 show the effect of increasing the acceptance angle. Firstly we can see that increasing α within this range does not appreciably affect the width of the profile although its contribution to the Fabry-Perot instrument function would be appreciable.

$N_R \sim 30$

and

$N_A \sim 60$

From equation 3.19 we see that α would contribute ~20% of the width to the instrument function. In the case of the Fizeau instrument function, however, the effect of θ is so predominant that α only contributes ~4% to the width.

Although the effect on the width of increasing α is not great, it does have one striking property in that the subsidiary maxima are to some extent 'damped out'. This effect is particularly noticeable in fig 3.5 where the profile at large angle α is almost symetrical compared to the upper profile, despite the fact that the left hand side of the inequality, 3.21 is ~28! This is far in excess of this condition.

Apart from the effects of α mentioned above, the more obvious effect of a slight reduction in the normalised peak height is also experienced. Thus, increasing the angle α by 10 times in fig 3.5 results in the peak un-normalised intensity increasing by only 9.6.

The restriction on α for the Fizeau interferometer only applies in a direction at right angles to the fringe direction. In the case of the Fabry-Perot the restriction of N_A on α applies

in all directions, because of the circular symetry. However, for the purposes of these computations it has been assumed that α is increased in one direction only, so that a direct comparison between the two instruments can be obtained.

In conclusion we can see that under certain conditions it may be advantageous to use the Fizeau interferometer beyond the conditions set by 3.21. In this region the normal expressions for the finesse are not applicable; both N_A and N_R contribute little to the width directly. Furthermore low values of N_A are advantageous because of the increase in symetry that this entails, apart from the obvious advantages of increase in transmitted flux.

References

Brossel, J. Proc. Phys. Soc. 59, 224, 1947.

Burgess, D.D. Thesis, University of London, 1966.

Chabbal, R. Rech, J. Bellevue, 24, 138, 1953.

Kinosita, K. J. Phys. Soc. Japan 8, 219, 1953.

Mewe and De Vries Fijnhvizen Report (Instituut voor plasma-fysica) 64-17, 1964.

Tolansky Multiple Beam Interferometry, Pergamon, 1947.

Chapter 4.

Theory of Operation of Zeeman Shift Measuring Instrument

4.1 Introduction

Since the Zeeman splitting cannot be measured directly it is necessary to consider how the shift can be obtained from measured quantities. This chapter presents such a determination. The various assumptions, and their range of validity are then discussed, and for one particular assumption it is shown how the optimum operating conditions require that it is violated. Indication is then given as to how this problem is solved.

4.2 Theory of Instrument

Fig. 1 shows an arbitrary line profile obtained from the Fizeau interferometer. The edge of the beam splitter prism is adjusted so that it bisects the line profile. The aperture stop, A, is set on the minimum of the line profile. The aperture stop, C, is set near the edge of the beam splitter prism so that the light which enters photomultiplier C gives an effective measure of the line peak intensity.

Suppose the line profile is

$$\psi$$

then the voltage supplied by photomultiplier A is given by (see fig 4.1)

$$V_a = k_1 \int_o^a \psi dx$$

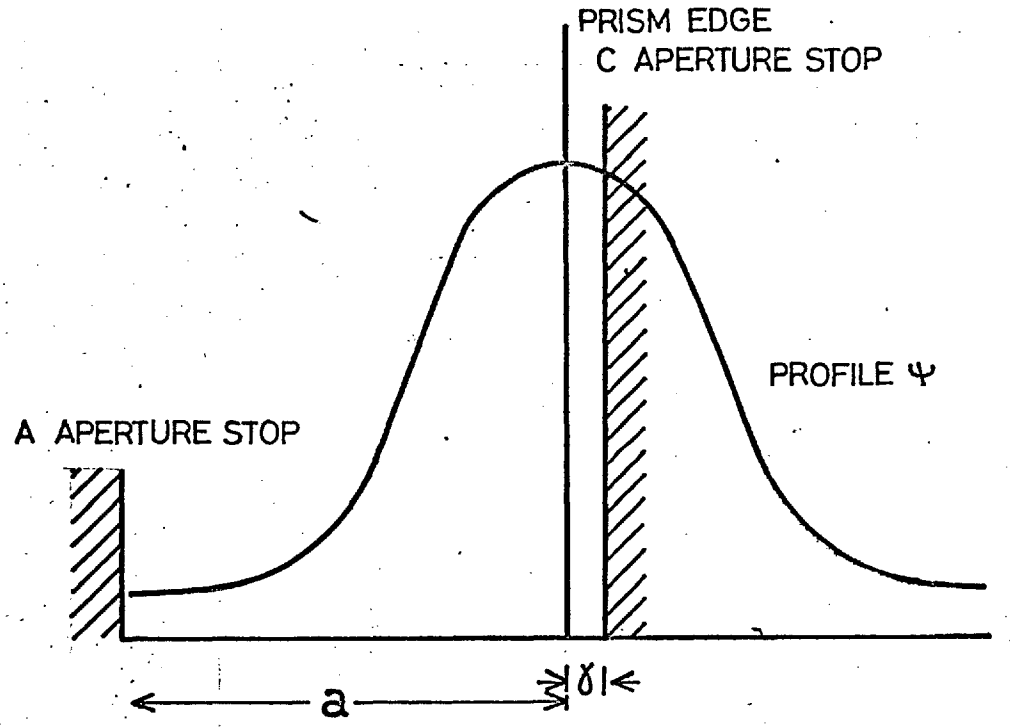

Fig 4.1 RELATIONSHIP OF PROFILE TO APERTURE STOPS AND PRISM EDGE FOR UNSHIFTED PROFILE

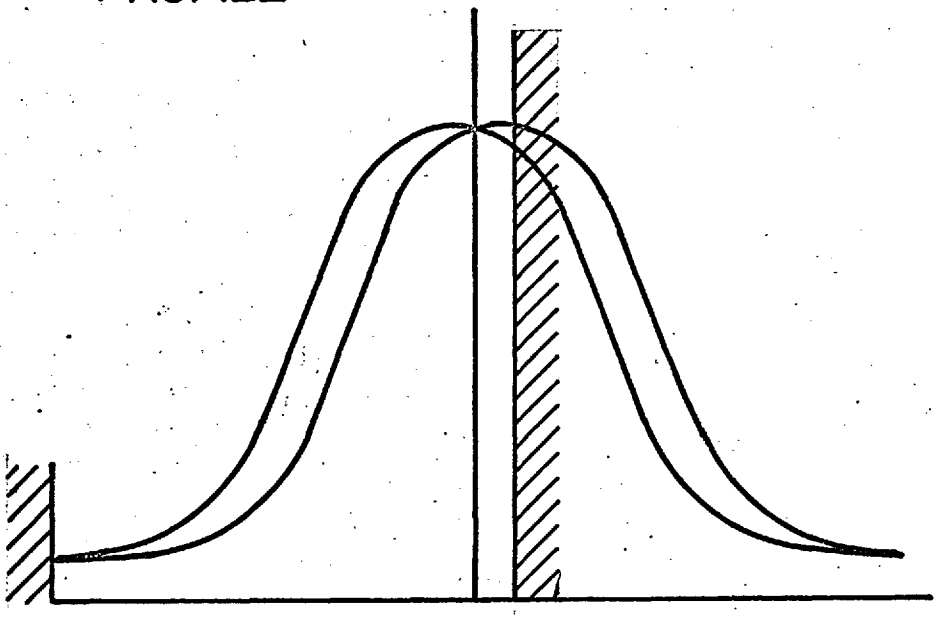

Fig 4.2 PROFILE SPLIT INTO TWO σ COMPONENTS SYMMETRICALLY ABOUT THE MEAN

It is arranged that initially $V_b = +V_a$

hence

$$V_b = +k_1 \int_o^a \psi dx$$

The voltage recorded by photomultiplier C will be

$$V_c = k_2 \int_o^\gamma \psi dx$$

This last equation implies that the profile is symetrical. This was shown to be the case by Roberts (1967) to a reasonable degree of accuracy (~5%), and is predicted by current stark broadening theory when $n_e \gtrsim 10^{15} cm.^{-3}$ When a magnetic field is applied this single line will split up into one or more pairs of components each with an identical profile but with different pairs having different intensities.

In the absence of a magnetic field we could have considered ψ as being composed of all these components being superimposed

$$\text{i.e.} \quad V_a = k_1 \left[A_1 \int_o^a \Phi dx + A_2 \int_o^a \Phi dx + A_3 \int_o^a \Phi dx + \cdots \right]$$

Similar equations can be written for V_b and V_c.

The splitting of each pair will be symetrical about the unperturbed wavelength but in general each pair will have a different splitting from any other pair, see fig. 4.2. Suppose that shifts of the σ components from the central position are δ_1, δ_2, δ_3 etc. and their amplitudes are A_1, A_2, A_3, respectively,

$$V_a' = k_1 \left[A_1 \int_{\delta 1}^{a+\delta_1} \Phi dx + A_2 \int_{\delta_2}^{a+\delta_2} \Phi dx + A_3 \int_{\delta 3}^{a+\delta_3} \Phi dx + \cdots \right] \qquad - 4.1$$

and similarly for V_b' and V_c'

$$V_b' = k_1 \left[A_1 \int_{-\delta_1}^{a-\delta_1} \Phi dx + A_2 \int_{-\delta_2}^{a-\delta_2} \Phi dx + A_3 \int_{-\delta_3}^{a-\delta_3} \Phi dx + \cdots\right] \quad - 4.2$$

$$V_c' = k_2 \left[A_1 \int_{\delta_1}^{\gamma+\delta_1} \Phi dx + A_2 \int_{\delta_2}^{\gamma+\delta_2} \Phi dx + A_3 \int_{\delta_3}^{\gamma+\delta_3} \Phi dx + \cdots\right] \quad - 4.3$$

V_c' is arrived at considering only the components shifted in one direction wheras experimentally V_c' is due to components shifted in both directions. Allowance is made for this in the determination of the ratio k_1/k_2 which will be considered later.

Subtracting equations 1 and 2 we obtain

$$V_b' - V_a' = k_1 \left[A_1 \left(\int_o^{\delta_1} \Phi dx - \int_a^{a+\delta_1} \Phi dx\right) + A_2 \left(\int_o^{\delta_2} \Phi dx - \int_a^{a+\delta_2} \Phi dx\right) + \cdots\right] \quad - 4.4$$

When δ_1, δ_2, δ_3, etc. are small, we can express these integrals as a Maclaurin series; thus, neglecting all terms other than the first, equation 4.4 simplifies to

$$V_b' - V_a' = 2k_1 (\Phi(o) - \Phi(a)) \left[\delta_1 A_1 + \delta_2 A_2 + \cdots\right] \quad - 4.5$$

In a similar way by considering situations when γ and δ are small equation 4.3 simplifies to

$$V_c' = k_2 \gamma \Phi(o) (A_1 + A_2 + A_3 + \cdots) \quad - 4.6$$

Now δ_1 δ_2 δ_3 etc. depend firstly on the value of the magnetic field and secondly upon the spectroscopic parameters of the line in question.

We can separate this double dependancy by putting:-

$$\delta_1 = \beta_1 \delta$$

$$\delta_2 = \beta_2 \delta$$

$$\delta_3 = \beta_3 \delta \quad \text{etc}$$

where β_1, β_2, β_3, etc are functions of the spectroscopic parameters and δ is the shift that would be produced in a given magnetic field if the Landé splitting factor for that line component were unity. Thus equation 4.5 becomes

$$V_b' - V_a' = 2k_1(\Phi(o) - \Phi(a))\ \delta\ [\beta_1 A_1 + \beta_2 A_2 + \beta_3 A_3 + \cdots] \qquad - 4.7$$

Now the factors $(\beta_1 A_1 + \beta_2 A_2 + \cdots)$ and $(A_1 + A_2 + A_3 + \cdots)$ are known from tables for the majority of spectral line components, and for simplicity in future will be referred to as f_1 and f_2 respectively.

By dividing 4.7 by 4.6 and rearranging we obtain

$$\delta = \frac{V_b' - V_a'}{V_c'} \cdot \frac{k_2}{k_1} \cdot \frac{\gamma}{2} \cdot \frac{f_2}{f_1} \cdot \left(1 - \frac{\Phi(a)}{\Phi(o)}\right)^{-1}$$

Initially it was intended to make $\Phi(a)/\Phi(o)$ small compared to unity. A series of measurements showed the results were not satisfactory due to the small difference signal level. This resulted in a very poor signal to noise ratio.

As soon as it was realised that it was not feasable to have $\Phi(a)/\Phi(o)$ small, some results were taken measuring this quantity on a two shot basis. Although some reasonable results were obtained by

this method, it was not altogether satisfactory since the discharge could not be relied upon to pinch in a similar manner twice in succession.

The problem was overcome by also recording the signal $V_b' + V_a'$ which, from equations 4.1 and 4.2, is given by:-

$$V_b' + V_a' = 2k_1 f_2 \int_o^a \Phi dx$$

In order to proceed further, it is necessary to make some assumptions as to the form of Φ, in order that the integral may be evaluated. Roberts, in the course of measuring line widths, has shown that the spectral lines emitted from the Z pinch we are considering are dispersive, provided that there is no appreciable reabsorption.

The profile of the Fizeau interferometer was shown in Chapter 2 to be very nearly an Airy function. The Airy function can be expressed as an infinite sum of Lorentz or dispersion profiles (Mewe and De Vries, 1964)

$$\text{i.e. } A(x) = \frac{\tanh(\pi w)}{\pi w} \sum_{n=-\infty}^{\infty} \frac{1}{1 + \left(\frac{x+n}{w}\right)^2} \qquad - 4.9$$

It can be shown from this that

$$\int_o^a A(x) = C \int_o^{\infty} \frac{1}{1 + \left(\frac{x}{w}\right)^2}$$

where a is half the fringe spacing as before, and C is a constant.

Furthermore if we convolute a dispersion profile with an Airy function the result is an Airy function with a different width.

Thus the profile Φ can be considered as an Airy function and

$$\int_0^a \Phi dx = \Phi(o)\int_0^\infty \frac{1}{1 + (\frac{x}{w})^2} = \Phi(o).\frac{\pi}{2}.w$$

where it must be remembered that w is the half half width of the dispersion profile as a fraction of half the fringe spacing a.

Thus

$$V_b' + V_a' = \pi k_1 f_2 w \Phi(o) \qquad - 4.10$$

Dividing this equation by equation 4.6 and rearranging we have

$$w = \frac{V_b' + V_a'}{V_c'} \cdot \frac{\gamma}{\pi} \cdot \frac{k_2}{k_1} \qquad - 4.11$$

The half half width of the Airy function w* will be different from w except in cases where w and w* are small.

Beyer-Helms (1963) has shown that

$$\sin \pi w^* = \sinh \pi w \qquad - 4.12$$

but $\sin \pi w^* = \frac{1 - R_{eff}}{2\sqrt{R}}$

where R_{eff} is the effective reflectivity of the interferometer plates.

In other words we may express the Airy function in the form

$$A(x) = \frac{\Phi(o)}{1 + \frac{\sin^2 \pi x}{\sin^2 \pi w^*}}$$

or

$$A(x) = \frac{\Phi(o)}{1 + \frac{\sin^2\pi x}{\sinh^2\pi w^*}}$$

Hence $\Phi(a) = A(a) = \Phi(o) \quad \frac{\sinh^2\pi w}{1 + \sinh^2\pi w}$

therefore $\frac{\Phi(a)}{\Phi(o)} = \tanh^2\pi w$ - 4.13

Thus from equations 4.7, 4.11 we have

$$\delta = \frac{V_b' - V_a'}{V_c'} \cdot \frac{k_2}{k_1} \cdot \frac{\gamma}{2} \cdot \frac{f_2}{f_1} \left[1 - \tanh^2 \left(\frac{V_b' + V_a'}{V_c'} \cdot \frac{k_2}{k_1} \cdot \gamma\right)\right]^{-1} \quad -4.14$$

It is not difficult to show that

$$H = \frac{4\pi mc^2}{e} \cdot \frac{1}{2ts} \delta \quad - 4.15$$

where H is the magnetic field, t the interferometer plate separation and s is the fringe spacing.

Hence

$$H = \frac{4\pi mc^2}{e} \cdot \frac{1}{2ts} \cdot \frac{V_b' - V_a'}{V_c'} \cdot \frac{k_2}{k} \cdot \frac{\gamma}{2} \cdot \frac{f_2}{f_1} \left[1 - \tanh^2 \left(\frac{V_b' + V_a'}{V_c'} \cdot \frac{k_2}{k_1} \cdot \gamma\right)\right]^{-1}$$

- 4.16

4.3 Points Arising From Equation 4.16

Two points which arise from the approximations made in the derivation of this formula require further attention.

Firstly, it was stated earlier that the spectral line profiles

are dispersive provided that there is no appreciable reabsorption. There is however likely to be some reabsorption particularly when the discharge is run at high currents.

When there is reabsorption the profile can be described by

$$\Phi(x) = 1-\exp\left(-\frac{\tau_o}{1 + (x/w)^2}\right)$$

(See Notes on optical thickness in section 5.9)

This profile is somewhat different to a straightforward Lorentz profile. The two are compared in fig 4.3.

A computer program was written for an Elliot 803 computer to determine what errors were likely to result in assuming a dispersion profile. The program, which is not reproduced here, essentially shows that the integration error introduced is less than 7% even when τ_o is as large as 20.

The second point which arises from the derivation of equation 4.10 is concerned with the assumption that the shifts are small. This is primarily because the value of V_c' will not be the true value of the peak height, $V_b' - V_a'$ not being nearly so sensitive to large shifts as V_c' and $V_b' + V_a'$ not being affected at all.

This is most easily explained with the aid of fig 4.4 which shows how much greater the percentage change is for V_c'.

In order to overcome this difficulty we can either ensure that

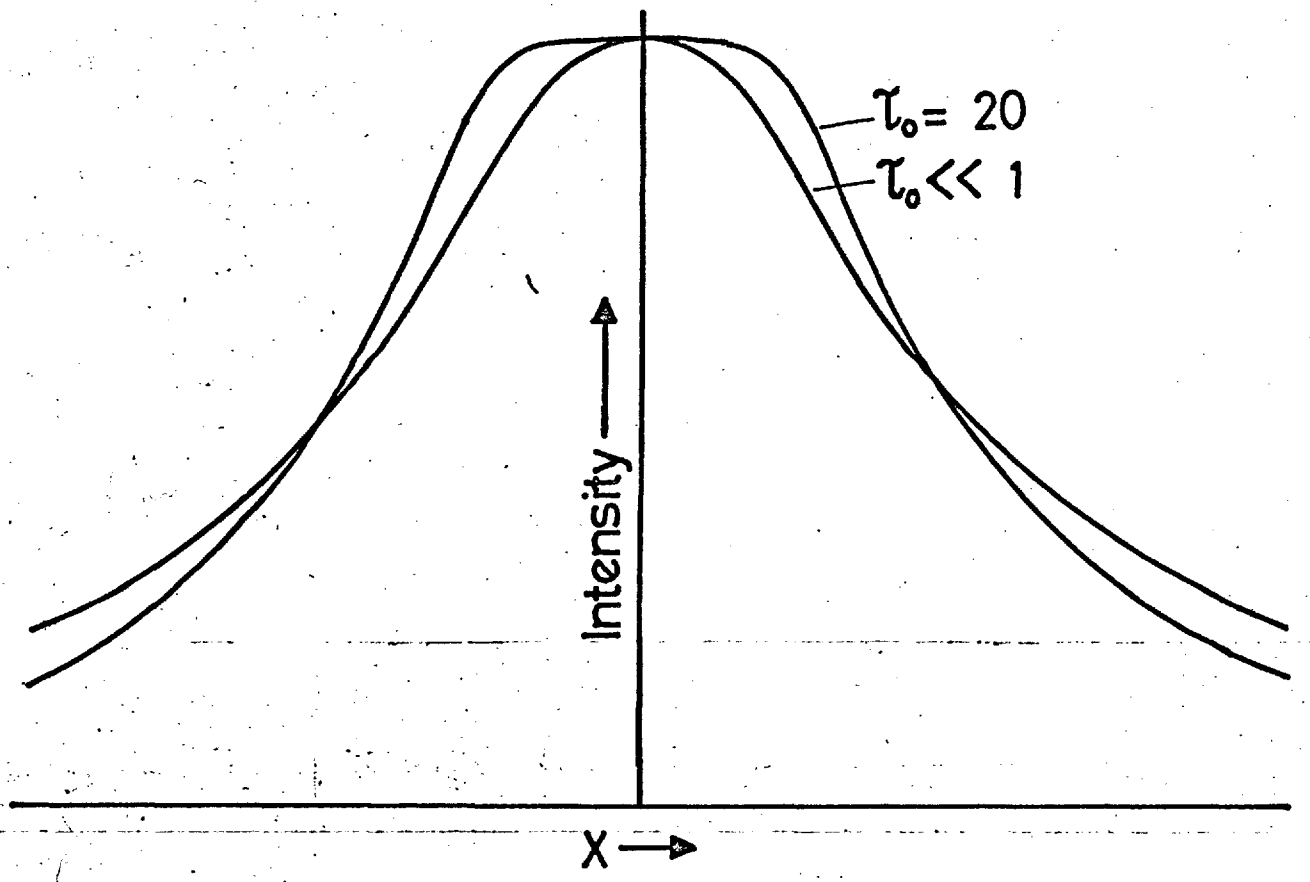

Fig 4.3 OPTICALLY THICK AND DISPERSION PROFILES WITH EQUAL WIDTHS AND PEAK INTENSITIES

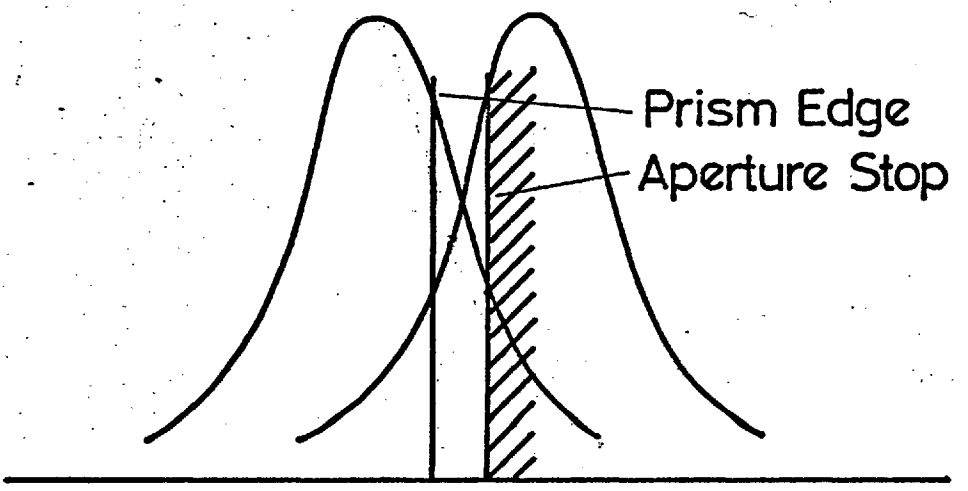

Fig 4.4 TO SHOW ERROR IN THE PEAK HEIGHT SIGNAL WHEN THE SHIFT IS LARGE.

the shift is small or correct for this error mathematically. Fig 4.5 shows how this error varies with change in V_c' due to a change in the width as the shift is kept constant. Plotted with this curve is the sensitivity of the instrument, which can effectively be represented by $(1 - \frac{\Phi(a)}{\Phi(o)}) \int_o^\delta \Phi dx$.

The sensitivity is plotted against the dispersion of the interferometer, which is varied by changing the separation of the interferometer plates. This is a more relevant way of changing the dispersion in this case than by changing θ, since by changing θ one only has a relatively small range capability, due to the restrictions imposed by the sampling arrangement.

It is quite clear from fig 4.5 that the error introduced by the incorrect measurement of the peak height of the profile is considerable over a large range of conditions. Furthermore, the sensitivity is greatest over regions where the error is large. It is for this reason that it was considered not feasable to operate the instrument with no peak recording error.

It is also impractical to attempt an analytical expression allowing for this error when more convenient methods are available. Imperial College's IBM 7090 computer offers an ideal way of correcting the results numerically, using equation 4.16 as a basis.

The program that was written for this purpose is described

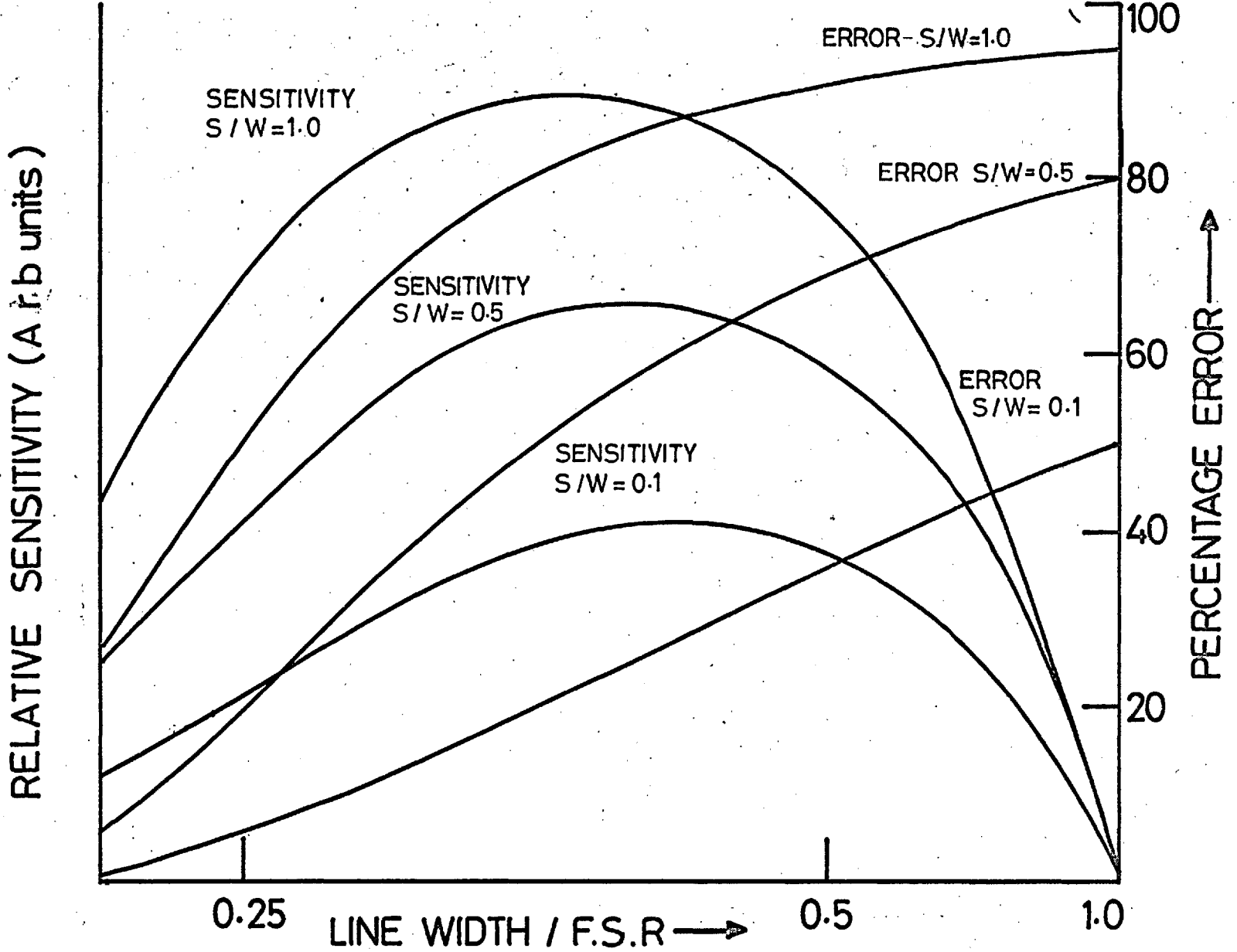

Fig 4.5 SENSITIVITY AND ERROR CURVES FOR DIFFERENT SHIFT TO WIDTH RATIOS PLOTTED AGAINST LINE WIDTH / FREE SPECTRAL RANGE

more fully in Appendix II but consists basically of a reiteration process. The width of the line is first of all calculated using equation 4.9; the field is then calculated using this value of width. This value of the field is used to artificially shift the line and a corrected value of the peak height is calculated. The corrected peak height value is used to calculate a new width which in turn is used to calculate the field. The process is continued until successive values of field are within any limits of each other. A careful study of the reiteration process shows that successive field values will oscillate asymetrically about the limiting value. If the initial results are subject to a large error, it is found that nine iterations are required to bring the result within 5% of the limiting value. This is satisfactory as regards computer time and the situation may be improved by the inclusion of a 'damping factor' in the iteration process.

References

Beyer-Helms, F.	Zeits. für angewandte Physik XV, 4, 330, 1963.
Mewe and De Vries	Rijnhvizen Report 64-17 Jan 1964
Roberts, D.E.	Thesis, University of London, 1967.

Chapter 5

Design, Construction and Operation of the Instrument

5.1 The Instrument

The design of this instrument for measuring magnetic fields is based upon a design by D. D. Burgess for an instrument to measure the ratio of the shift to width of a spectral line. An essential difference between the two instruments is that, in order to measure shifts directly, a third recording channel has been added. (See chapter 1). A two channel instrument was proposed by J. Cooper for measuring magnetic fields when the line width can be assumed to be constant. The three channel system of the final design is essentially a combination of these two ideas.

A general schematic layout and photograph of the instrument are shown by fig 5.1 and fig 5.2.

The radiation emerges from the plasma via a fused quartz window, and passes through a quarter wave plate, P, chosen for the wavelength used. It is then focussed onto the entrance slit of the Hilger constant deviation monochrometer by means of lens L_4. The light of selected wavelength emerges from exit slit and is collimated by the lens L_1. The fringe pattern produced by the wedge is focussed by the lens L_2 into the plane containing the edge of the wedge and aperture stops. The prism divides one fringe into two about its maximum. One side is focussed on photomultiplier 3 after reflection

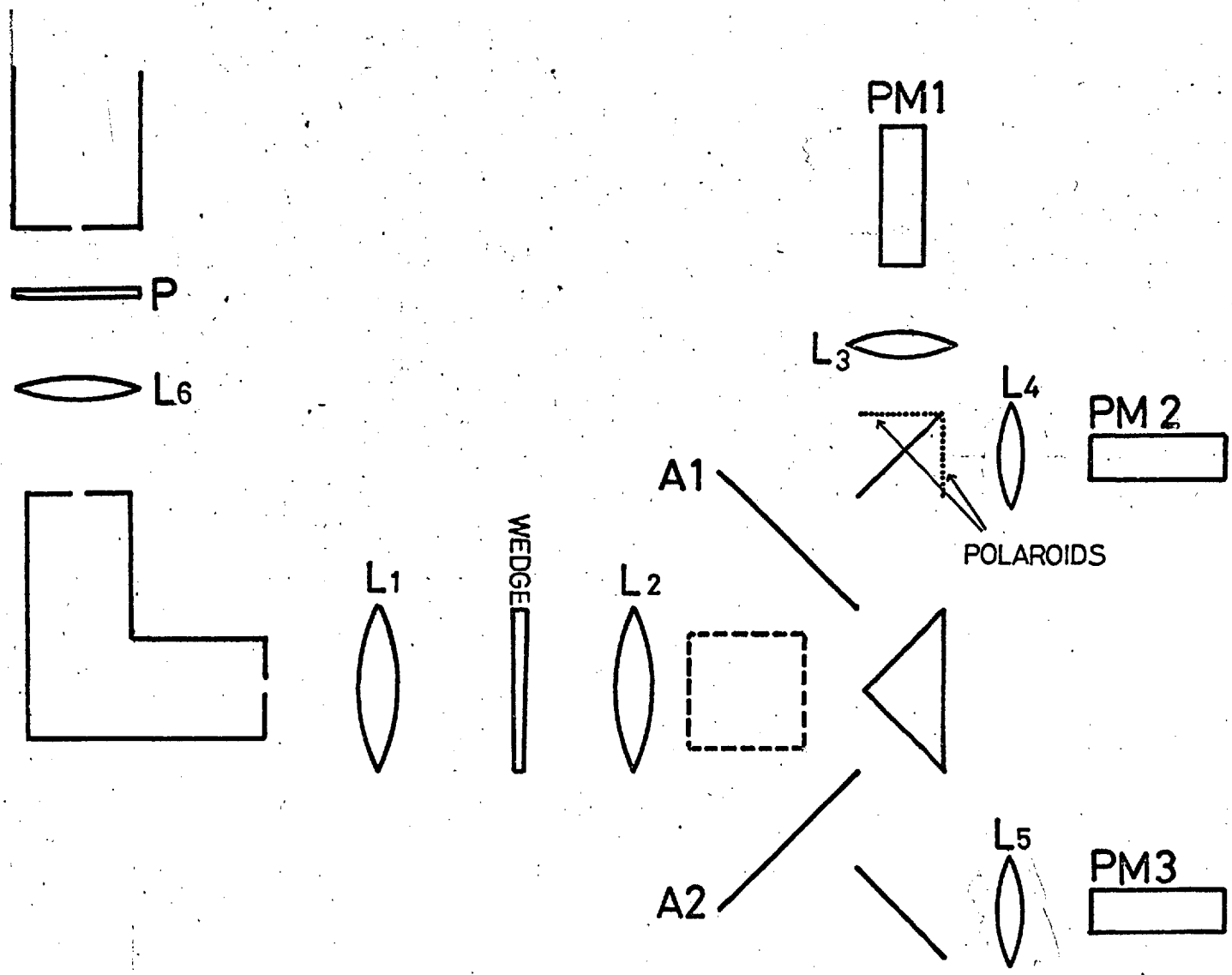

Fig 5.1 SCHEMATIC DIAGRAM OF THE ZEEMAN SHIFT INSTRUMENT

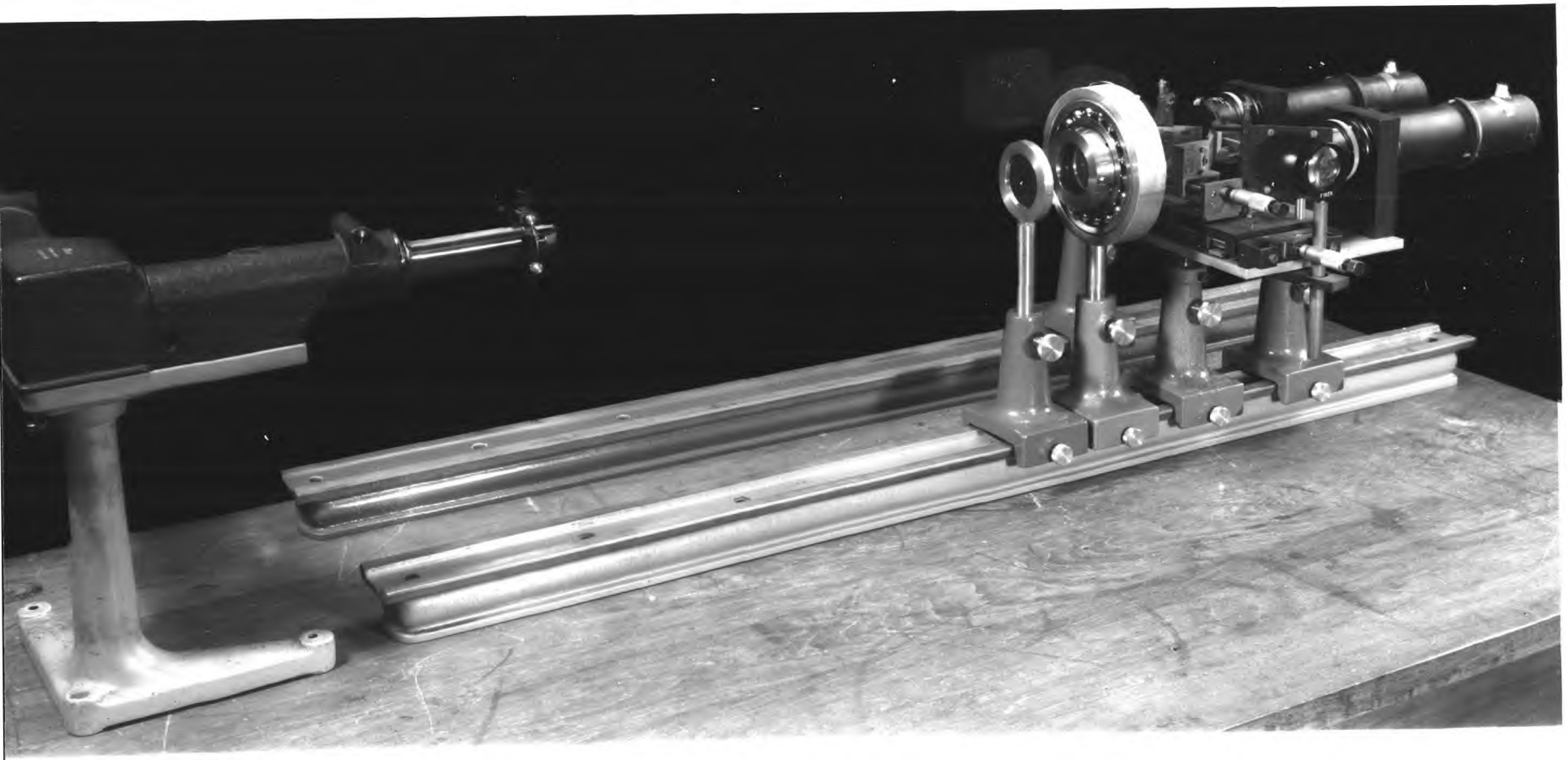

Fig 5.2 The Zeeman Instrument

from a fully silvered mirror and the other side of the fringe is split by a stack of glass plates to be focussed onto photomultipliers 1 and 2.

5.2 Sampling Arrangement

This is constructed in such a way that the prism can be moved backwards and forwards in the fringe image plane, the aperture stops A_1 and A_2 moving with the prism but being capable of independant adjustment by means of micrometer screw heads.

The photomultipliers remain in a fixed position together with the two mirrors and the lenses L_4, L_5 and L_6. These lenses are arranged so that the light collected by them is focussed to a point on the photocathode. This procedure is normally frowned upon since it has a tendancy to 'burn a hole' in the photocathode if high light intensities are used. However, the intensity falling on each photocathode with this arrangement is not high and should not have any serious effect on the photocathode. The reason for the focussing is that when the fringe is shifted, or its form changed in any way, the same spot on the photocathode will be illuminated, and, since the sensitivity of the photocathode varies considerably over its area,then only in this way can a truely representative signal be received.

A similar effect could be obtained using a diffusing screen which would effectively result in the whole of the photocathode

being illuminated all of the time. This arrangement, however, involves a greater loss of light than the focussing arrangement.

5.3 The Interferometer Mount

The original interferometer mount consisted of a dural case with steel spring mounted adjustment screws, which was fastened directly to the saddle bar of the optical bench. This worked satisfactorily when the plate separation was ~ 25μ. However, for this experiment larger values of plate separation were more convenient (~ ·5 mm), and at these separations temperature changes in the darkroom resulted in quite large alterations in the fringe pattern. Attempts were made to stabilize the temperature by increased ventilation but this was not satisfactory. Finally, a new mount was designed on a similar principle to a temperature compensated clock pendulum. The case was made of stainless steel and the retaining screws were made of brass. The dimensions of the mount were such that expansion of the stainless steel was counteracted by the greater expansion of the brass screws.

Optical requirements dictated (see section 5.4) that the interferometer should be rotatable. This was acheived by placing the mount inside a large diameter double ball race, which proved to be of smooth enough action to allow the mount to be rotated without disturbing the fringe pattern appreciably. A diagram of the final version of the mount is shown in fig 5.3.

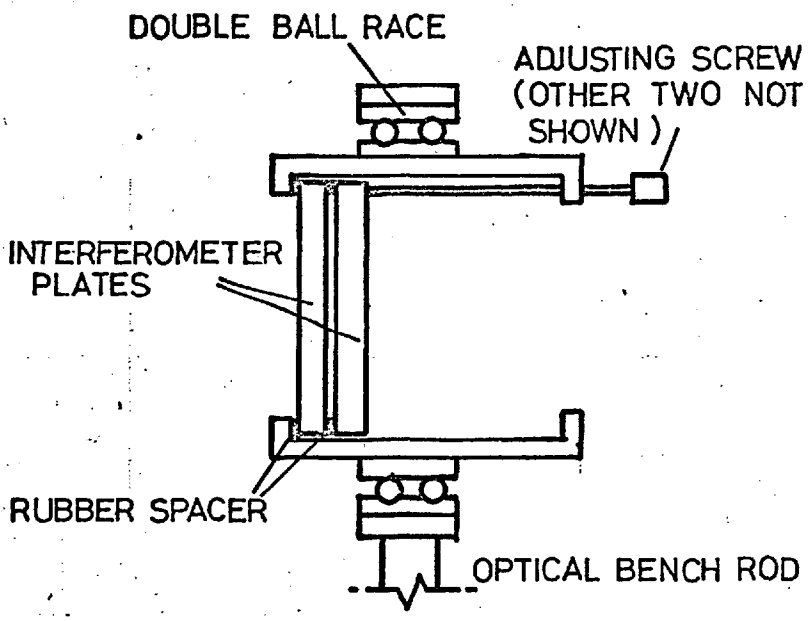

Fig 5.3 CROSS SECTION OF WEDGE MOUNT

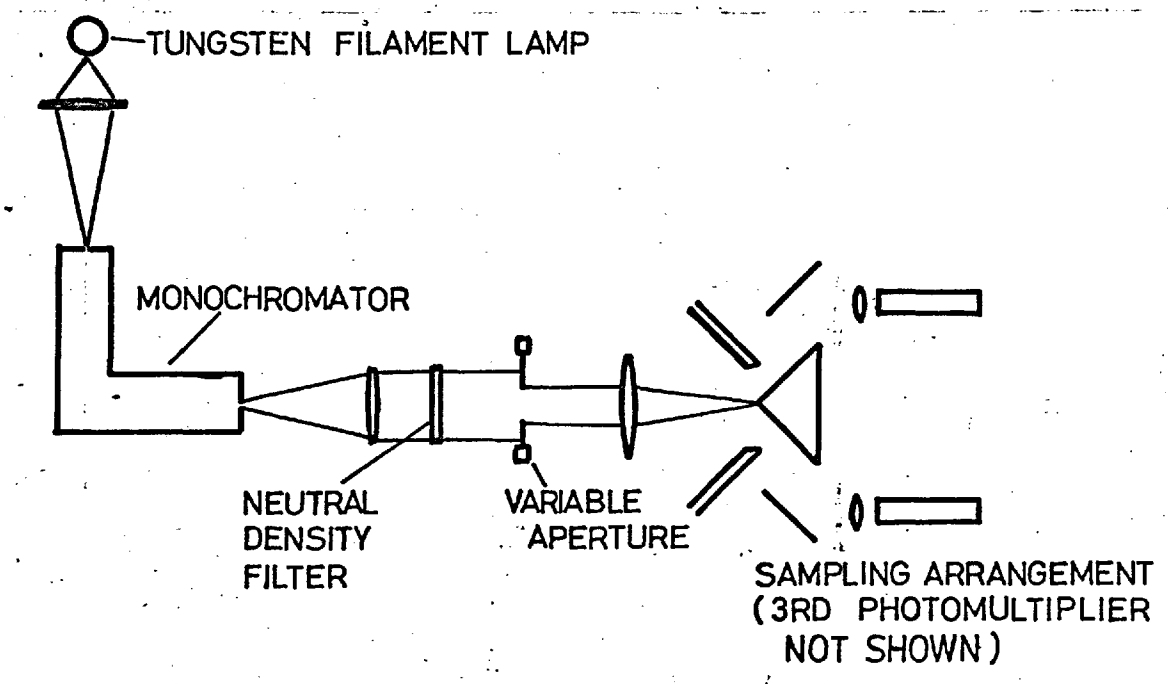

Fig 5.4 APPARATUS FOR MEASURING k_1/k_2

5.4 Optical System

The passage of light through the variety of optical components contained in this system resulted in some rather complex polarisation states of the light incident on the photomultipliers. In order to analyse this, it was necessary to test each component separately and to determine its polarisation properties.

Firstly, the window of the plasma tube was tested in situ for strain birefringence. This was made from fused quartz but was found to be of such a small diameter that the birefringence was not noticeable.

The quarter wave plate consisted of a single layer of brown mica or muscovite cemented between two glass plates. The one used for much of this work was bought commercially from Ealing Optical Co. but satisfactory results were obtained by selecting pieces of mica of the correct thickness, using a micrometer dial gauge.

The Hilger constant deviation monochrometer was, not unexpectedly, polarisation sensitive, but was found to be optically inactive. The polarisation sensitivity was not a serious difficulty and is taken account of when the photomultipliers are balanced.

One of the two main sources of the elliplicity of the light

reaching the photomultipliers was in fact the dove prism image rotator. This was made of glass and the birefrigence could only be explained by assuming that internal strains were present, these probably being introduced in the production of this large piece of glass. A three mirror image rotator was also tested, and, although it was slightly better, it was not completely satisfactory. It was finally decided to dispense with an image rotator as such and to rotate the interferometer in its stead. A further advantage in removing the image rotator is that the light loss will be reduced by about 10%.

The second source of ellipticity was in the beam splitter mirror, M_1. This initially was a semi-silvered mirror. Partially transmitting metallic mirrors, however, produce a large amount of ellipticity in the reflected and transmitted beams. This mirror was replaced satisfactorily by a stack of glass plates, although this sets the angle at which the polaroids in front of the photomultipliers must be orientated. A multilayer dielectric polarisation beamsplitter mirror would have been more effective but one was not readily available.

Surprisingly, the alluminised front of the prism did not introduce any appreciable degree of ellipticity, probably because a very thick coating had been evaporated. Had this not been the

case some slight difficulty may have been encountered in the production of a suitable dielectric multilayer.

Some results were taken with this modified system and they were found to be satisfactory. The lens L_3 was useful for two reasons; firstly in that it focussed the light through the image rotator thus allowing for a much smaller aperture prism, and secondly by choosing focal lengths and positioning the components correctly, this lens can be used to magnify or diminish the fringes as desired. However, the most convenient working magnification was found to be unity, and since the image rotator has been excluded, the lens L_3 is unecessary provided that a small degradation in the fringes can be tolerated. This degradation corresponds to a further finesse given approximately by $\frac{x}{d\,\alpha_{max}}$ where d is the distance of the fringe object plane to the sampling frame, α_{max} is the maximum acceptance angle and x is the fringe spacing. Under working conditions this corresponds to a finesse of greater than 50 which is very much larger than the resultant finesse due to other causes derived in chapter 2.

5.5 Electronics

The photomultipliers used were EMI types 9524 and 9526, the 9526 being a quartz envelope version of the 9524. These photomultipliers were by no means ideal for the purpose due to their relatively high noise level, but have the important advantage of being relatively inexpensive. The EHT supplies were provided

by a single Isotope Developement D332 power supply via 3 - 1 MΩ potentiometers; one potentiometer for each photomultiplier.

The output from the photomultiplier is fed by coaxial cable into a 2.2 KΩ load mounted on the front of a tektronix oscilloscope. Signal integration is achieved by the cable capacitance and an additional capacitor placed across the load resistance. Integration time of ·5 μsec was used most frequently although this could be changed to suit the conditions.

Three recording channels were required, two of these, i.e. the sum and difference signals, were photographed from the traces of a dual beam oscilloscope type 551, and the third channel, i.e. the line peak signal, was photographed from a single beam oscilloscope type 541. Parallel triggering for these oscilloscopes was obtained from the bank timing units.

5.6 Spectral Lines Chosen

Fig 5.6 shows a photograph of the argon spectrum taken with a medium glass spectrograph. It is quite obvious from this plate that there is an abundance of spectral lines from which to choose. However, the two most suitable lines were found to be the 4806 Å line of multiplet 6 and the 4401 Å line of multiplet 1. These two lines were selected because they were:-

a) well separated from neighbouring lines

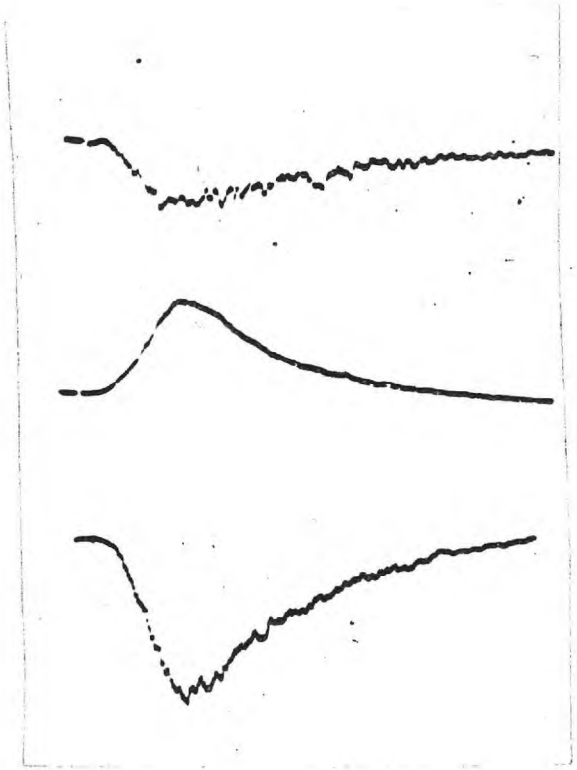

Fig. 5.5 Photograph of Oscilloscope Traces.

Tube Volts = 1 KV.

Mag. Field Volts = 1 KV.

Pressure = .15 torr

Time - 20μsec/cm.

Sensitivity

Upper - 0.05 volts/div.

Middle - 0.5 volts/div.

Lower - 0.05 volts/div.

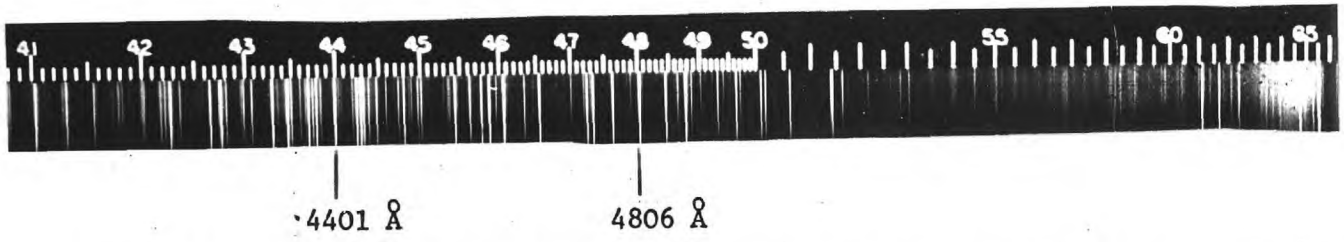

Fig 5.6 Photograph of Argon Spectrum Showing the two Spectral Lines of Interest

b) reasonably intense.

c) described by Russell-Saunders coupling.

This last criterion is only essential if the experimental values of the constants for the line are not known.

The relavent properties of these two lines are summarised in table 5.1 and a diagramatic representation of the transitions is shown in fig 5.7.

In a magnetic field of value H, the energy of a particular level, w, is changed by an amount hwMg.

$$w = w_o + hwMg \qquad - 5.1$$

where h - Planks constant

w - Larmor precession frequency

M - magnetic quantum number

g - Lande splitting factor

where $$g = 1 + \frac{J(J + 1) + S(S + 1) - L(L + 1)}{2J(J + 1)}$$

The intensities of the various components are given by (Condon and Shortley, 1935)

$$I_\sigma = A(J \pm M)(J \mp M + 1)$$

for $J \rightarrow J$ transitions

Table 5.1

The Relevant Characteristics of the Two Lines

4806 Å and 4401 Å

Line Wavelength	4401	4806
Approx. Rel. Intensities	7	20
Multiplet No.	1	6
Upper Level Designation	$4p\ {}^4P^o_{5/2}$	$4p\ {}^4P^o_{5/2}$
Lower Level Designation	$3d\ {}^4D_{7/2}$	$4s\ {}^4P_{5/2}$
U.L. obs. g	1·599	1.599
U.L. calc. g	1·600	1.600
L.L. obs. g	---	1.598
L.L. calc g	1·428	1.600
No. of σ components	12	2

Moore (1941)

and $I_\sigma = B(J \mp M + 1)(J \mp M + 2)$

for $J \rightarrow J + 1$ transitions

and $I_\sigma = C(J \pm M)(J \pm M - 1)$

for $J \rightarrow J - 1$ transitions

when viewed along the field direction. A, B and C are constants, the values of which are irrelevant to the present context, since only one line is considered at once.

The relative splittings and intensities are indicated in fig 5.7 using these equations.

5.7 Operation of the Instrument

The apparatus was contained in a dark room with the exception of the two oscilloscopes whose front panels form part of one wall. Despite the fact that the wedge had been designed to be temperature compensated, it was found desirable to allow conditions in the darkroom to reach equilibrium after switching on the electronics. A period of $\frac{1}{2}$ - 1 hour was found to be quite sufficient to allow the wedge to reach equilibrium. Fringes were first obtained using a low pressure mercury lamp placed directly behind a suitable aperture. These fringes were adjusted such that the required fringe spacing was obtained using 5461 Å mercury line after correction for the differing wavelength. The fringes were then aligned with the prism edge, and the aperture stop A adjusted to the required value

Fig 5.7 Zeeman Patterns of Two Spectral Lines

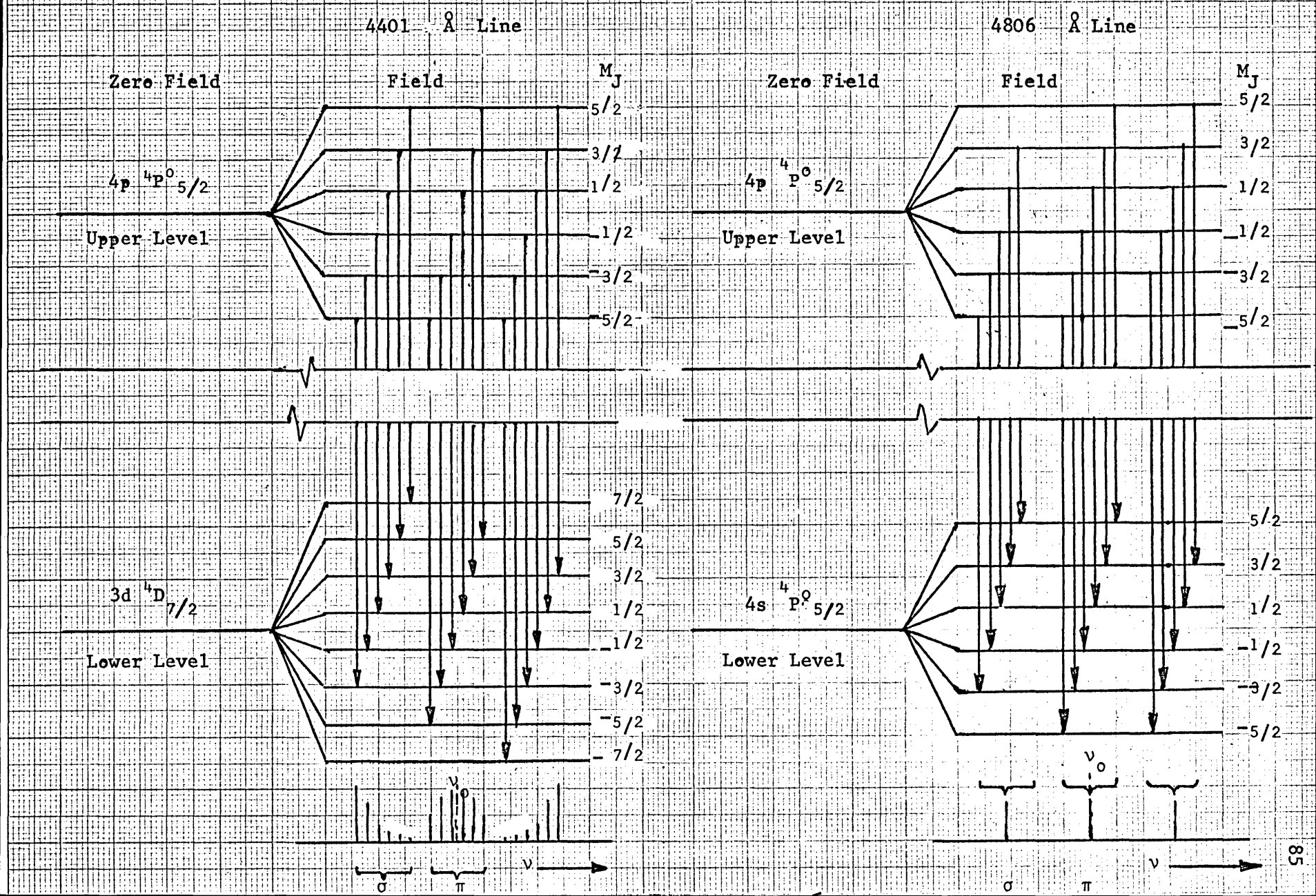

using its micrometer screw drive. The mercury lamp was removed and the required Ar II line selected on the monochrometer, from a pulsed argon Geisler. The Geisler was pulsed at a rate of about 5 p.p.s. by simple overvolt method. The rise in current at each flash was used as a trigger for the two oscilloscopes. This method of triggering was found to be more reliable and convenient than using the internal trigger facility of the oscilloscope.

The aperture stop B was then closed down to less than 1 mm. The signal from photomultiplier C was then used to set the beam splitter edge in the centre of the fringe. The voltage applied to photomultiplier A was then adjusted until exactly the same signal is received from p.m. A and B. This can be done very accurately using the differential amplifier plug-in unit of the tektronix oscilloscope.

The instrument was then ready for use. Before any recording was taken, however, two further checks were carried out. Firstly, the quarter wave plate was rotated to a 'neutral' position such that it should not produce any signal on the difference channel. The discharge was initiated and the absence of signal on the difference channel was confirmed. The second check was done on two consecutive discharges by rotating the $\frac{\lambda}{4}$ plate 45^{o} either side of the 'neutral' position. It should be confirmed that the two difference signals should be equal, but of opposite sign. If

confirmation from these two checks is not obtained then this indicates that, either the correct orientation of the $\frac{\lambda}{4}$ plate had not been chosen, or one photomultiplier was not being operated within its linear region. Many other possible faults can explain the failure of operation in these conditions, and several of these were encountered on commencing this work. However, the two mentioned above were the most common and troublesome, the latter particularly so.

After each discharge the argon Geisler tube was used to check that the beam splitter prism edge was still in the centre of the fringe. It soon became apparent that such a high frequency of checking was not necessary, as the fringes remained essentially stationary for periods of at least ten minutes, during which time six recordings were possible. To ensure a reasonable margin of confidence, a check was made every three discharges.

At the end of a set of results the fringe spacing was again checked using the mercury green line and the reading on the micrometer, used to control the position of aperture stop B, noted.

The interferometer plate separation was measured using microscope with a micrometer eye-piece, the plates being viewed through a hole drilled in the side of the mount for that purpose.

5.8 Determination of k_1/k_2

In section 5.7 we dealt with the operation of the instrument.

Before any meaningful results can be taken it is necessary to measure the ratio k_1/k_2 (see chapter 4)

The essence of this method must be to allow the same intensity of unpolarised light to fall on photomultipliers B and C and then to determine their respective responses. Initially attempts were made to devise a satisfactory method of simultaneous illumination, because of the better accuracy of a null method using a differential amplifier. It soon became clear, however, that it is not at all easy to produce two beams of unpolarised light of equal intensity without having two detectors of known relative response. Since finding the relative response of two detectors is the object of this experiment, an "impasse" had been reached.

The optical arrangement for measuring k_1/k_2, which was finally used, is shown in fig 5.4. Light is provided by a tungsten filament lamp supplied from a 12 volt car battery. The part of the spectrum around 4806 Å is selected by means of the monochrometer and the light collimated by the lens L_1. Neutral density filters and a variable aperture serve to vary the intensity of the light which is focussed into the plane of the aperture stops by means of the lens L_2. The outputs from the photomultipliers are fed, in turn, directly into a sensitive galvanometer. The EHT voltages are adjusted to produce a convenient value of k_1/k_2. This procedure was repeated several times as a check against fluctuations

in the lamp supply, although any fears of this proved to be groundless.

5.9 Uniformity of Illumination of the Wedge

Several conditions were mentioned in chapter 3 which restrict the use of the Fizeau interferometer. One further point which must be mentioned arises from the uniformity of illumination of the wedge. If the wedge is not uniformly illuminated then any shift which occurs across the wedge will be recorded as a greater or smaller shift by the photomultipliers, depending upon the sign of the intensity gradient.

It is therefore absolutely essential to ensure that the wedge is uniformly illuminated and considerable time and care was spent in adjusting the optics of the system until good uniformity was achieved.

5.10 Further Considerations Concerning the Optical Opacity of the Plasma.

In chapter 4 consideration was given to the effects of reabsorption on the profile and what error this resulted in. Reabsorption will also affect the position of observation within the plasma, in so far as radiation being emitted at the far end of the discharge tube will not contribute equally with emission from the near end. The recorded signals will thus be the result

of an integral along the axis taking account of the optical depth. The situation is further complicated by the fact that, if the plasma is very opaque and consequently viewing is restricted to a position near the electrode, the values of n_e and T_e, and hence τ, vary rapidly.

The optical path for 10% reabsorption of the total line intensity has been calculated by Burgess (1965). Using the conditions given in chapter 9, and also those given by Roberts (1967), we find that the optical path will lie between 0·5 cm and 10 cm. These values assume that both n_e and T_e are constant up to the electrode. It has been shown by Burgess in the case of an unstabilised pinch that n_e falls off rapidly as we near the electrode, and Haines (1961) has predicted a rapid fall off in temperature. Since the conditions within the plasma are such that we are working near the minimum value of optical path shown in Burgess's graphs, then a decrease in either n_e or T_e will result in a large decrease in τ_o. It is therefore reasonable to suppose that minimum distance of viewing into the plasma is of order as the electrode disturbances, i.e. ~ 2 cm.

If we assume that, apart from this region near the electrode, the plasma is uniform, then light emitted within the plasma will decay as Lambert's Law

$$I = I_0 \exp(-x/d)$$

where d is a characteristic length

For 10% absorption then

$$\frac{I_0}{I} = \frac{10}{9}$$

and $x = L$

where L corresponds to the value of L_s given by Burgess for the optical path for 10% reabsorption.

Thus the average viewing position is given by

$$x_m = d \ln 2$$

$$= L \frac{\ln(2)}{\ln(1.1)}$$

$$\simeq 6.5 L$$

Thus the mean position of viewing will lie somewhere between the limits 5.5 cm and 100 cm from the electrode, depending upon the conditions.

The rather naive approach above takes no account of the variation of τ across the line profile. This could have an effect on the measurement of the field only if the magnetic field varied with z. However since the constancy of the field with z has been checked experimentally (chapter 6) then this final consideration is likely to be of little consequence.

In conclusion we can see that under the worst conditions of

n_e and T_e the minimum mean distance of viewing will exceed 5 cm for the line centre, and will exceed this at all other parts of the profile. Thus it can be reasonably assumed that the electrodes will have little effect on the results.

5.11 The Conditions Studied

Burgess (1966), Roberts (1967), et al. have described situations where the electron density in a linear pinch reaches a maximum value as the pressure is varied. A preliminary survey with the Zeeman instrument indicates that a transition was taking place in the region of 0.300 torr. A study of time variation of the intensity of the 4806 Å line indicated that the interesting range of pressures lies up to 0.350 torr. Pressures greater than this value did not produce any noticable difference in the time profile. The range of pressures chosen was from 0.15 torr to 0.35 torr in .50 torr steps; the lower limit in pressure was determined by the inability of the discharge to fire reliably at lower pressures.

The ranges of voltages to which the two condenser banks were charged were determined, in a similar manner to the pressure, by the condenser banks. Stabilising fields of nominally 5 and 10 K gauss were found convenient. With both these values of field, the discharge bank voltage range of 1 Kv to 3 Kv was found to produce widely varying situations. At the lower voltages the discharge showed little signs of any pinch phenomena whereas

at the higher voltages there were signs of a very pronounced pinch.

5.12 Presentation of Results Obtained with the Zeeman Instrument.

Fig 5.5 shows a photographic recording taken at .15 torr pressure with a nominal 10 K gauss stabilising field and the tube capacitor bank changed up to 3 K volts. The upper trace corresponds to the line centre intensity and the middle and lower traces to the difference and sum signals respectively. Figs 5.8 and 5.9 show a plot of magnetic field with time obtained from such photographs. A compression of the magnetic field is noticeable at higher currents, reaching a maximum somewhat before the pinch. Fig 5.8 shows the magnetic field at .15 torr pressure and with 5 K gauss stabilising field, for discharge voltages of 1 Kv, 2 Kv and 3 Kv, and fig 5.9 shows the magnetic field as its nominal value is changed from 5 to 10 K gauss, keeping the tube volts constant at 3 K volts. Of particular interest is the amount of field trapping that is observed and the extent to which the field expands after the pinch, when the various initial conditions are varied. These quantities represented by the factors $B_{max}/B_{average}$, and B_{max}/B_{min} are shown in table 5.2 for the whole range of conditions studied.

Table 5.2 also lists the values of the time taken to the maximum value of field and the time taken to maximum light output. These quantities are of interest when a comparison is made with

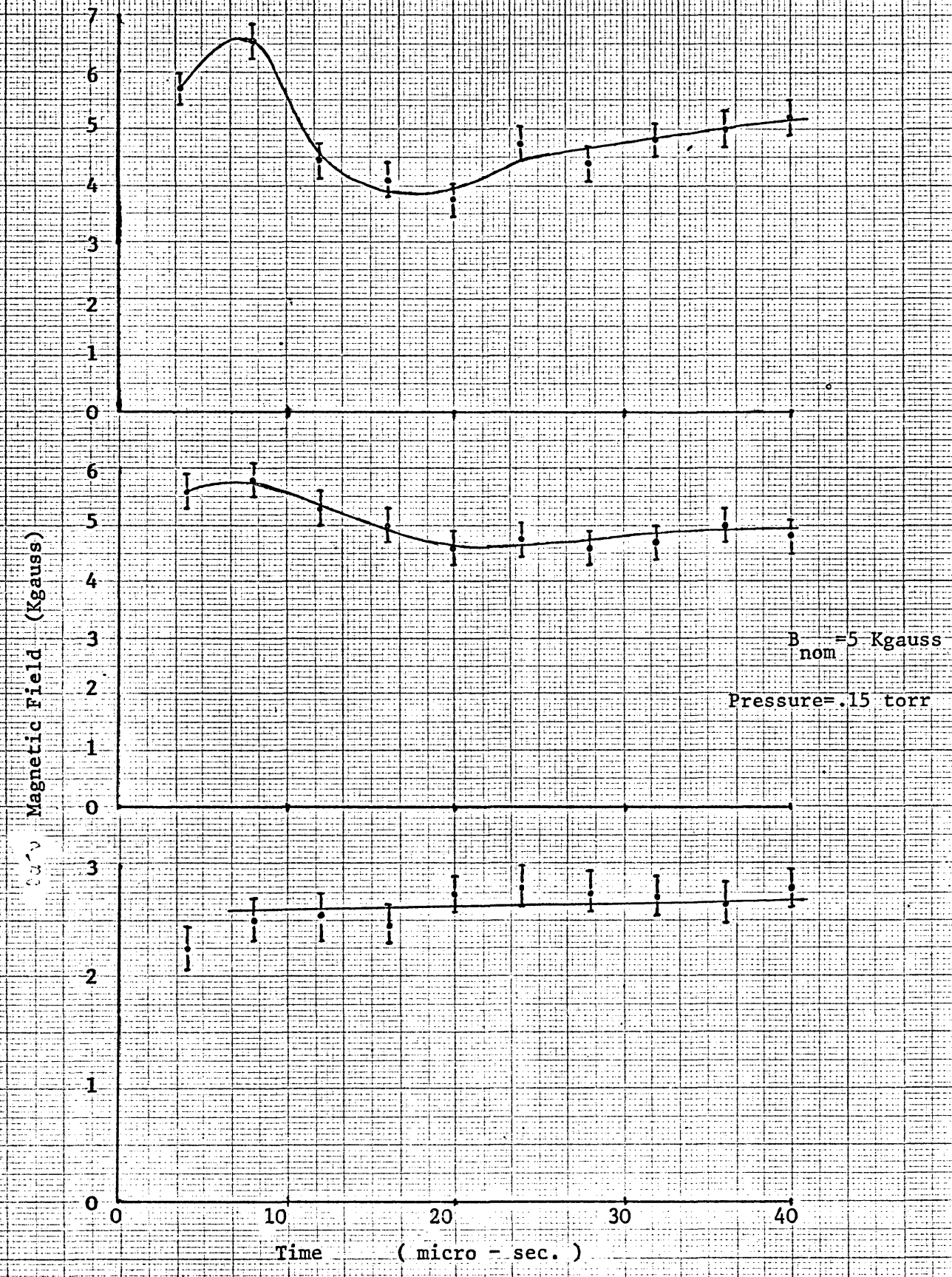

Fig. 5.8 Variation of Mag. Field with Time for Three Values of Current.

Fig. 5.9 Variation of Mag. Field with Time for Two Values of Stabilising Field.

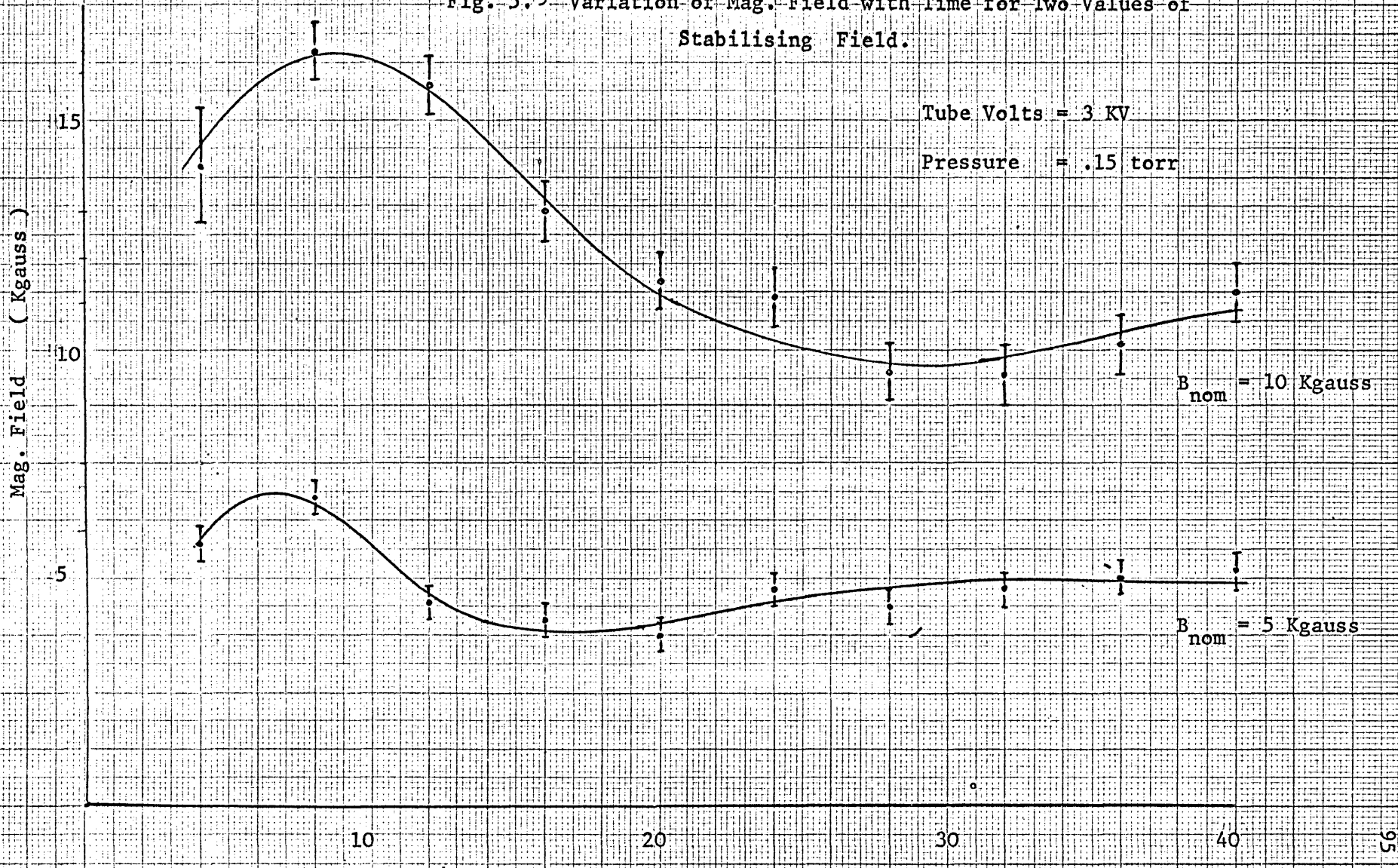

Table 5.2

Field Compression and Characteristic Times of the Discharge

Pressure torr	Mag. Volts Kv	Tube Volts Kv	B_{max}/B_{min}	B_{max}/B_{min}	τ_p μsec	τ_{Bm} μsec
.150	1	1	1.2	1.1	32	40
		2	1.4	1.2	17	20
		3	2.2	2.0	15	15
	2	1	1.0	1.0	42(24)	---
		2	1.4	1.25	36(12)	15
		3	2.0	1.7	36(10)	12
.25	1	1	1.0	1.0	40	---
		2	2.0	1.4	24	16
		3	2.2	2.0	16	12
	2	1	1.0	1.0	40	---
		2	1.3	1.1	32	20
		3	1.8	1.7	21	16
.35	1	1	1.0	1.0	38	---
		2	2.0 *	1.8 *	28	
		3	3.0 *	2.2 *	20	
	2	1	1.00	1.00	32	---
		2	1.20	1.05	28	28
		3	2.0	1.3	24	24

* indicates that error on these values is large (~ 30%)
Figures for τ_p in parentheses indicate the arrival of the "shock".

the theoretical predictions derived in chapter 10.

5.13 Discussion of the Results

The final equation derived in chapter 4 gives the magnetic field in terms of known constants and measured quantities. The errors may be conveniently classed into two groups, firstly those which will affect the absolute value of field measured, and not the relative values measured during one discharge, and secondly those which will affect both readings. In the first group enter the quantities t, s, γ and k_2/k_1 given in equation 4.10. The quantities k_2/k_1 and γ are a greater source of error than t and s, since they appear twice in the equation in such a way that the error is additive. Even after very careful alignment the aperture stop C could not be set to better than 0.001" which corresponds to an error in γ of 7%. The factor k_2/k_1 could be measured more accurately (2%) but slight changes in temperature and vibration would cause the value to become uncertain to approximately 5%. These two quantities alone introduce an error in order of 26% into the absolute value of the field.

When one considers the effects of the second group of errors the errors in k_2/k_1 and γ are only of second order importance and introduce an error of less than 1% in the relative value of field. The most serious source of error in this group is due to the uncertainty introduced into the oscilloscope traces

by shot noise.

When the two nearly equal signals from photomultipliers A and B are subtracted then a signal of approximately one tenth of either A or B results. Because shot noise is random, the noise levels on signals A and B add incoherently. Thus of the three traces recorded, the difference signal has by far the smallest signal to noise ratio, and consequently is the main contributor to the error. Observation of the photographs shows that the shot signal to noise ratio lies typically within the range of 0.1 to 0.05. We would therefore expect that the most pessimistic values of error are correspondingly 10% to 5%.

In chapter 10 a quantitative discussion of some of the results presented in this chapter, and the correspondence to results given in chapter 9, will be given. Furthermore, the agreement with theory is discussed. It therefore remains in this chapter to state in a simple qualitative manner the trends and findings of the results.

In section 5.10 it was mentioned that a noticeable change occurred in the form of the discharge as the pressure was changed from .150 torr to .350 torr. The photographs showing the line peak intensity for 10 K gauss nominal field and tube volts of 3 Kv in fig 5.10 illustrate this point suitably. It is a little

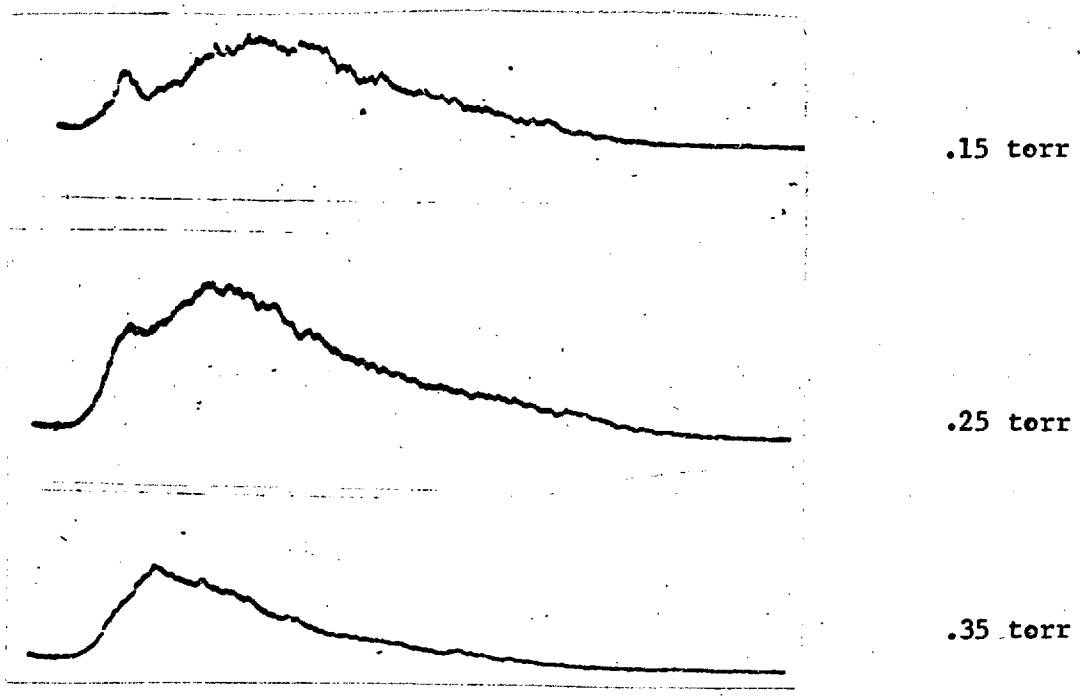

Fig 5.10 Characteristic Light Output at Different Pressures.

surprising therefore that the compression of the field varies so little as the pressure is changed. The reason for this could possibly be due to the fact that as pressure is increased, the conductivity rises and, according to the model in chapter 10, this could easily offset any slowing down of collapse due to the increased pressure. On the whole, predictions of the modified snow plough model given in chapter 10 agree reasonably well with the measured values of compression. This model does not give any indication concerning the reason for the two peaks in intensity although a qualitative account based on the shock model is given. The design of the pinch would seem to be fortuitous in that conditions may be varied easily over a sufficient range such that, in some, no field compression is apparent, and in others quite considerable compression is experienced. Thus as the discharge voltage is increased from 1 Kv to 3 Kv this change is very apparent. The highest recorded value of field compression is approximately 3, which occurs at a pressure of .3 torr, and with 5 K gauss stabilising field and 3 Kv charge on the discharge condenser bank. The asterisk against this and some other readings indicates that the value given is most probably lower than the true value, although a larger error is involved. This arises because at high pressures and high discharge currents the very large range in light intensity between the pinch and afterglow renders it very difficult to obtain accurate values of both on

the same trace. When the apertures are open sufficiently to give a reasonable reading in the afterglow, at the pinch the photomultipliers overload; conversely when the light throughput is reduced to prevent overloading at the pinch, the noise problem in the afterglow becomes severe.

In contrast to the results obtained in chapter 9, the values of field compression do not seem particularly sensitive to changes in magnetic field. The reason for this will become apparent later, sufficient to say that the compression not only depends upon the nominal value of the field but also on the velocity with which the pinch collapses. It will be seen from table 5.2 and from the results obtained in chapter 9 that despite the fact that the collapse is less extensive at high fields, the plasma attains a higher velocity.

The results in Table 5.2 are interesting in that in one or two cases, predominantly at low pressures, the time to maximum field is larger than the time to the first maximum in light output which may reasonably be assumed to correspond to a pinch. This is contrary to what is predicted on a simple model although an assumption that the initial peak is due to a shock front travelling in front of the current carrying piston would explain it (see chapter 10). As the appearance of this first peak becomes less and less like a shock compression, so does the time

to maximum value of magnetic field come more nearly into line with theoretical predictions.

Finally it should be stated that the value given in table 5.2 are the average values obtained from at least three sets of measurements. The spread in the readings is sometimes much greater than can possibly be attributable to experimental error. This occurs because the several spark gaps that are used in the production of the stabilising field do not fire consistently, particularly at low operating voltages, with the result that the stabilising field may vary over a considerable range and is very often below its nominal value at low operating voltages.

References

Burgess, D.D. Thesis, University of London, 1965.

Condon, E.V. and Shoritey, G.H. Theory of Atomic Structure, Cambridge University Press, 1965.

Cooper, J. Private Communication

Haines, M.G. Proc. Phys. Soc, LXXV11, 643, 1961.

Moore, C. Atomic Energy Levels, N.B.S. 1941.

Roberts, D.E. Thesis, University of London.

Chapter 6

Magnetic Probes.

6.1 Introduction

The chief disadvantage associated with all types of probes is that they disturb the plasma. Of the various types of probe that are available for measuring magnetic fields a simple coil probe is probably the best, and, despite the prime disadvantage, it provides a useful check on the Zeeman instrument. This chapter is concerned basically with the work done with magnetic probes. A very simple theory is presented which is adequate, provided that it is applied with care. The theory is followed by description of the probe used, the experimental procedure and results. The chapter concludes with a comparison of the results obtained with the optical and probe methods.

6.2 Theory of Magnetic Probes

If a coil of n turns and effective area A is placed in a changing magnetic field, B, then the voltage, V, produced across the ends of the coil is given by

$$V = - n A \frac{dB}{dt} \qquad - 6.1$$

The minus sign being indicative of Lenz's Law.

In order to obtain the highest sensitivity it is therefore

desirable to have a large n and large A. These requirements, however, directly conflict with other specifications, namely that the number of turns should be small, to minimise the inductance of the coil, and that the area should be small so that the probe produces little disturbance to the plasma. A compromise is thus necessary.

The voltage V in equation 6.1 will, in general, be a function of time and before any interpretation of measurements can be made the effect of different circuit elements must be considered. An extensive treatment of the theory of coil probes is given by Frayne (1963) but a much simplified treatment which will be presented here is sufficient to indicate the general properties.

An equivalent circuit can be drawn for the probe with its measuring circuit. This is given in fig 6.1. We shall assume for simplicity that the transmission line is terminated by its characteristic impedance R and therefore may be neglected.

Thus we have

$$V(t) = L\frac{di}{dt} + ir + V_o(t) \qquad -6.2$$

where $V_o(t)$ is the potential difference generated across R .

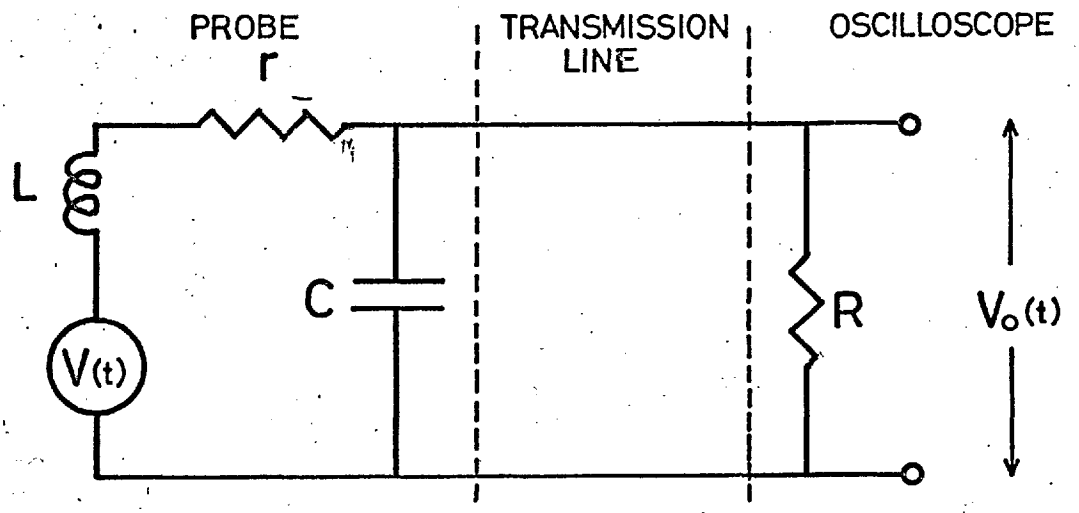

Fig 6.1 EQUIVALENT CIRCUIT FOR PROBE ASSEMBLY

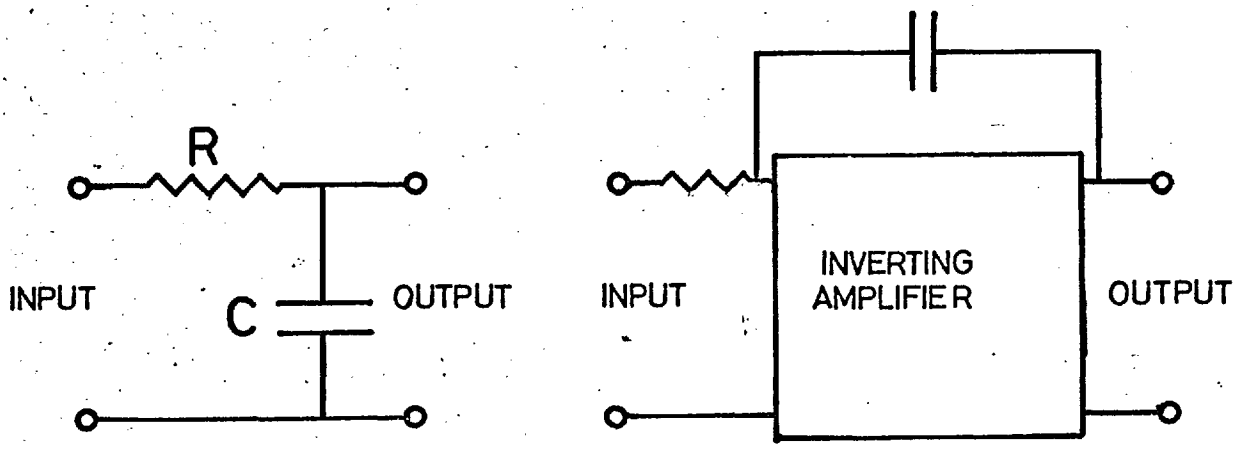

a) Simple R-C b) Miller

Fig 6.2 TWO TYPES OF INTEGRATOR

Splitting the current i into two parts and remembering that

$$\frac{dq}{dt} = i$$

then $q_2 = CV_o(t)$

or $i_2 = \frac{dq_2}{dt} = C\frac{dV_o(t)}{dt}$

and $i_1 = \frac{V_o}{R}$

hence $i = i_1 + i_2 = C\frac{dV_o(t)}{dt} + \frac{V_o}{R}$

Substituting into equation 6.2 yields

$$LC\frac{d_2V_o(t)}{dt^2} + \left(\frac{L}{R} + Cr\right)\frac{dV_o(t)}{dt} + V_o(t)\left(1 + \frac{r}{R}\right) = V(t) \quad - 6.3$$

The solution of this equation is non-trivial and is strongly dependent on the form of V(t). In order to continue further without assuming any form of V(t) it is necessary to make some approximations.

The capacitance C arised because of inter-winding capacitance in the coil itself and the leads up to the transmission cable. The resistance r is due mainly to the coil, and L will be the coil self inductance. A typical set of values for these quantities are

$L = 5\ \mu H$

$C = 50$ pf

$R = 150\ \Omega$

$r = 5\ \Omega$

thus

$$LC = 2.5 \times 10^{-16} \qquad Cr = 2.5 \times 10^{-10} \qquad \frac{L}{R} = 3.3 \times 10^{-8}$$

and $\frac{r}{R} = \frac{1}{30}$

The inductive time constant is thus of greatest importance. Furthermore if we are prepared to neglect the r/R term then equation 6.3 becomes

$$V_o(t) = V(t) - \frac{L}{R}\frac{dV_o(t)}{dt} \qquad - 6.4$$

Two extreme cases are of interest, namely when $\frac{L}{R}$ is large and when $\frac{L}{R}$ is small compared to a characteristic time of V(t). In the first case 6.4 becomes

$$V_o(t) = \frac{R}{L}\int_o^t V(t)dt$$

$$= \frac{nAR}{L} B$$

assuming that B = 0 initially.

This is the situation in the Rogowski coil. To achieve this L must be made large, but this usually entails violation of the

other conditions. The second case, i.e. when $\frac{L}{R}$ is small, is of more interest in the present situation. We can expand $\frac{dV_o(t)}{dt}$ as a power series of $\frac{dV(t)}{dt}$

Thus we have

$$V_o(t) = V(t) - \frac{L}{R}\frac{dV(t)}{dt} \qquad - 6.5$$

neglecting all powers in $\frac{dV(t)}{dt}$ higher than the first.

We can see from equation 6.5 that if V(t) is too swiftly varying then account must be taken of the rate of change of V(t). It is therefore not difficult to see that it is desirable to make L as small as possible and R as large as possible. In which case

$$V_o(t) = - n A \frac{dB}{dt} \qquad - 6.6$$

It was stated earlier that it is desirable to have L small. The reason for this is now apparent.

In the final stages of this calculation the capacitance C was assumed to be small, as indeed in practice it is kept. The value of C, however, in much the same way as L, is dependent on the dimensions of the coil and to some extent minimising the inductance will almost certainly have a similar effect on the capacitance.

In order to obtain a measure of the magnetic field from the potential $V_o(t)$ it is necessary to carry out some integration process. This can be done in one of two ways. Firstly, an electronic integrator may be included in the circuit and the integrated signal of $V_o(t)$ displayed directly on the oscilloscope, or secondly, the signal may be integrated afterwards, either numerically or graphically. Of these two methods the first involves less tiresome work than the second, although the latter may very likely be more accurate. If a simple resistance-capacitance integrator circuit is used (fig 6.2a) then unless a very large time constant is used then some error will be introduced. This error is cumulative and consequently very undesirable. A large time constant will reduce the error in this integration to a negligibly small fraction but this involves making both R and C large with very serious consequences regarding the sensitivity. A superior method is to use a Miller integrator, the scheme of which is shown in fig 6.2b. This type of integrator is far superior to the simple circuit with regards to linearity and does not suffer from the disadvantage of reducing the output.

Unfortunately, a Miller integrator was not available at the time and a simple R-C integrator was used initially. The sensitivity was such, however, that accurate results could not be obtained. It was decided therefore to carry out the integration

graphically afterwards. This method was chosen in preference to the construction of a suitable amplifier for a Miller integrator because, for the limited number of results taken, it was considered less time consuming.

6.3 Construction of the Probe

Frayne (1963) has shown that in order that the readings from the coil should be representative of the magnetic field at the centre of the coil, the ratio of the length of the coil to the diameter should be 0.72. However Herzog and Tischler (1953) have shown by experiment that a better space resolution is obtained when $\frac{L}{D} = 0.67$.

In the present context neither of the above considerations are of particular consequence since the probe is constructed to measure B_z and it is assumed that B_z is independent of z. The probe was in fact constructed with these figures in mind but no particular care was taken in achieving the exact ratio of value quoted above. Fig 6.3 shows a photograph of the probe tip and fig 6.4 is a sketch of the probe assembly.

The coil consisted of 60 turns of 50 s.w.g. wire on a "perspex" former. The resistance per unit length of this wire is quite high because of its small diameter, and consequently a connection was made to stouter 36 s.w.g. wire immediately next

Fig 6.3 PHOTOGRAPH OF A PROBE TIP

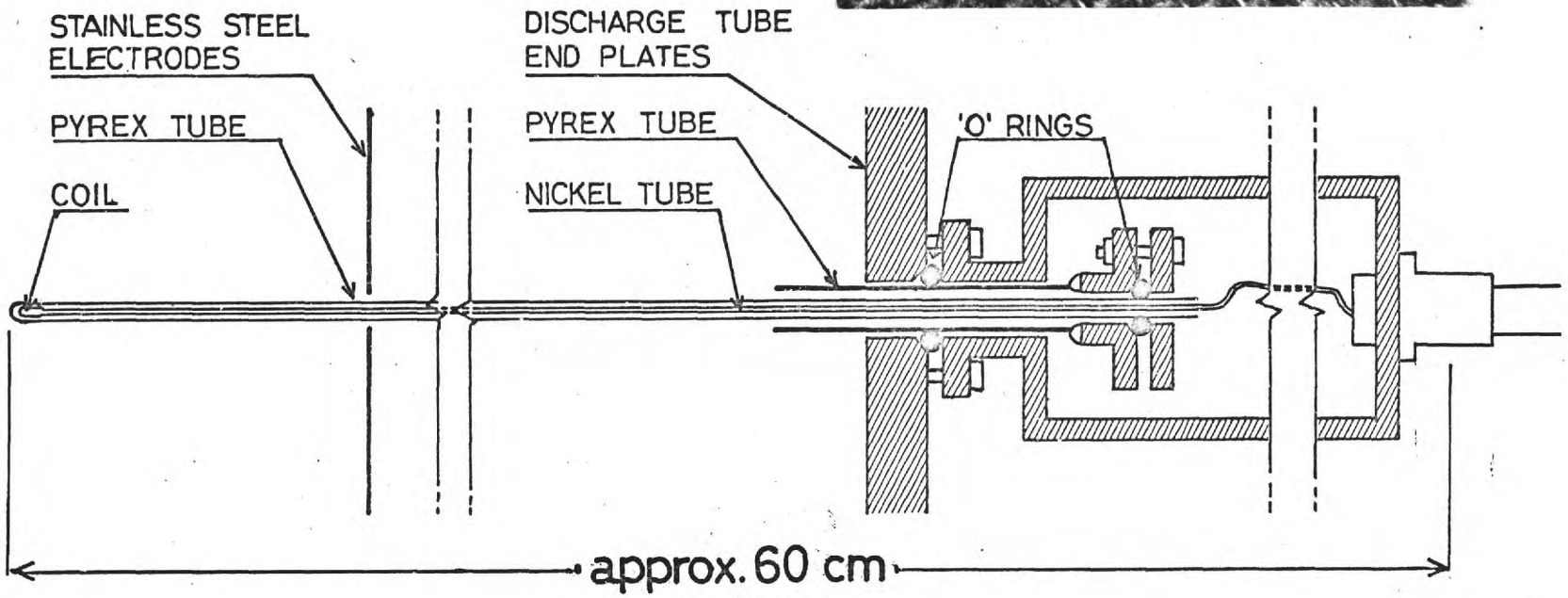

Fig 6.4 PROBE ASSEMBLY

to the coil. The resistance of the probe including the immediate feeding wires was 5Ω of which 4Ω was attributable to the coil. The 36 s.w.g. feeding wires were threaded through a 0.66 x 0.76 mm nickel tube which acted as an electrostatic screen. The coil was potted with perspex cement and the coil and the nickel tube were contained in a 4 mm O.D. pyrex tube. This 4 mm tube was arranged to be capable of sliding over distance of approximately 10 cm within a 12 mm O.D. pyrex tube which made a vacuum joint by means of an O ring to the outer part of the electrode assembly of the tube. The smaller diameter tube protruded through a ¼" diameter hole in the electrode itself and its position was adjustable along the axis of the tube in order to check on the uniformity of the field.

Connection to the oscilloscope was made by 150Ω twin feeder cable, this being terminated by a 150Ω resistor immediately before the oscilloscope input terminals.

6.4 Calibration of the Probe

Equation 6.6 shows that the voltage output is directly dependent on the area-turns of the coil. It is therefore necessary, to obtain quantitatively correct results, that the turns of the probe are known. It is not a sensible proposition to measure the dimensions and calculate its area-turns when a

practical approach is much easier and is likely to be more accurate.

The system used, shown in fig 6.5, consisted of a pair of Helmholtz coils 8 cm diameter and 8 cm apart driven by a small capacitor bank of 20 μF which was changed up to 2000 Volts. A standard coil of 3 cm and of 3 turns was placed, concentric with the probe, at the centre of the Helmholtz system. A current is discharged through the coil using a simple spark gap arrangement and the outputs from the standard coil and the probe were monitored simultaneously on a double beam oscilloscope. From the relative outputs of the two coils and knowing accurately the dimensions of the standard coil, an accurate determination of the area turns of the probe is obtained, provided that the time constants of both coils are small compared to the period of the discharge. Although the inductance of the standard coil is larger than the probe, 10 μH, the time constant is still very much smaller than the period of the discharge which was 800 μsec.

In this way the area-turns of the probe was found to be $.260 \pm .002$ cm^2 turns.

6.5 Operation and Results obtained with the Probe

The quarter period of the magnetic field bank is approximately

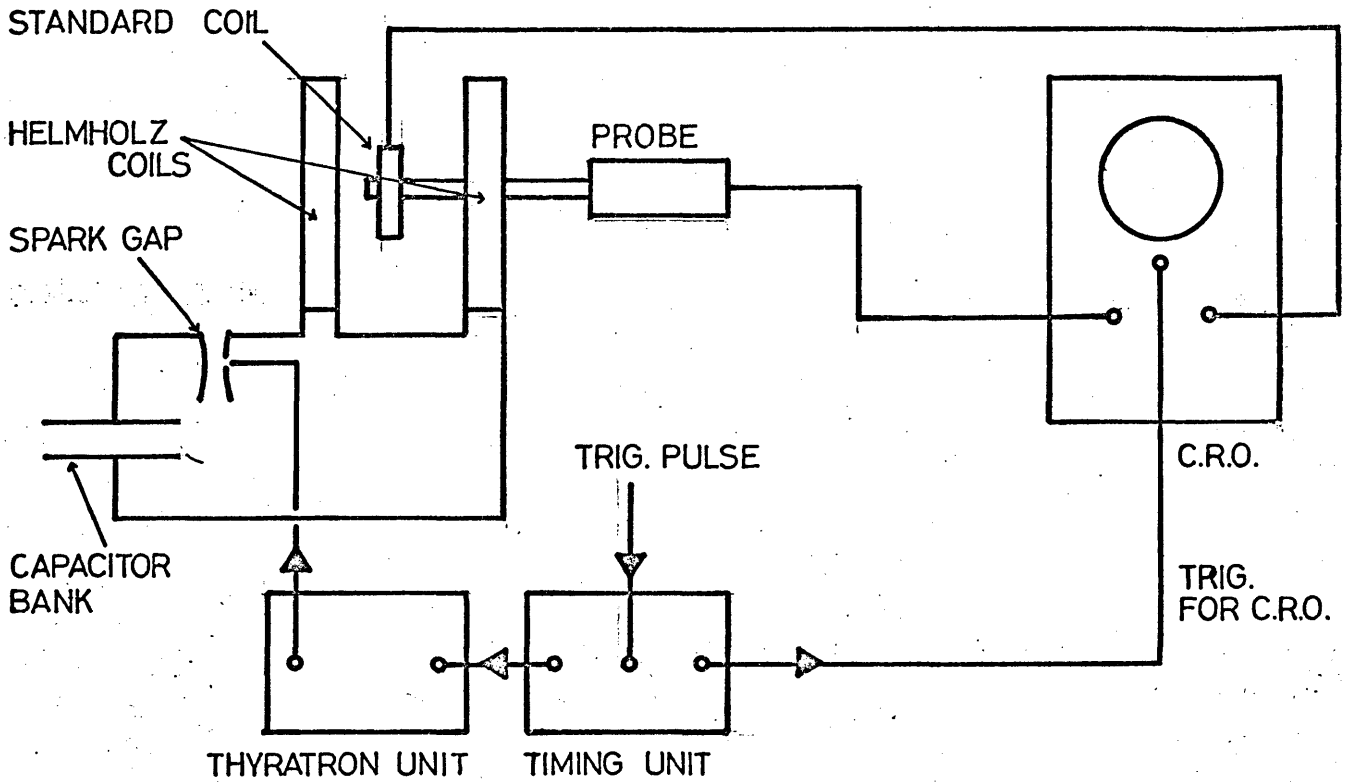

Fig 6.5 SCHEMATIC DIAGRAM OF APPARATUS FOR CALIBRATION OF THE PROBE

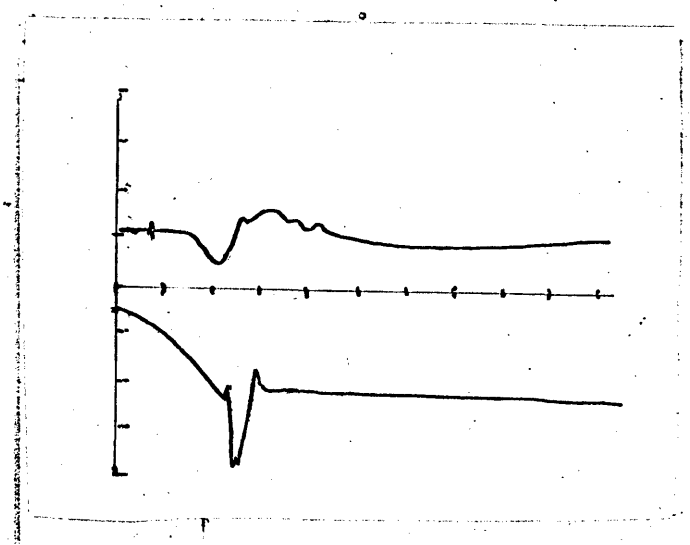

Upper beam:
20μsec/div,
1 volt/div

Lower beam:
·2msec/div,
0·5 volt/div

Fig 6.6 PHOTOGRAPH OF PROBE TRACE
B_{noM} = 10Kgauss Tube Volts = 2KV
Pressure = ·25 torr

250 μsec whereas the quarter period of the discharge bank varies with conditions, but a typical value being 25 μsec. We see from this that two different time scales are involved. We require, firstly, to record the absolute value of the field and, secondly, to note the variations in the field due to the discharge current. To facilitate this measurement the probe output was displayed simultaneously on the two beams of a Tektronix 555 oscilloscope. The two beams of this oscilloscope can be swept at different speeds, the start of the sweep of one being capable of being delayed by a variable amount after the start of the sweep of the other. Fig 6.5 shows a photograph of a set of results obtained by the probe.

Probe measurements were taken at various points along the axis of the discharge tube, mainly as a check that the assumption of axial symetry in chapter 5 is valid. This was confirmed within the limits of the movement of the probe which were 1 cm from the electrode to approximately 11 cm from the electrode.

The differential output shown in the photograph in fig 6.6 was projected onto graph paper and integration was carried out graphically.

Figs 6.7 and 6.8 show the integrated results under two conditions namely at .150 torr with 5 K gauss nominal stabilising

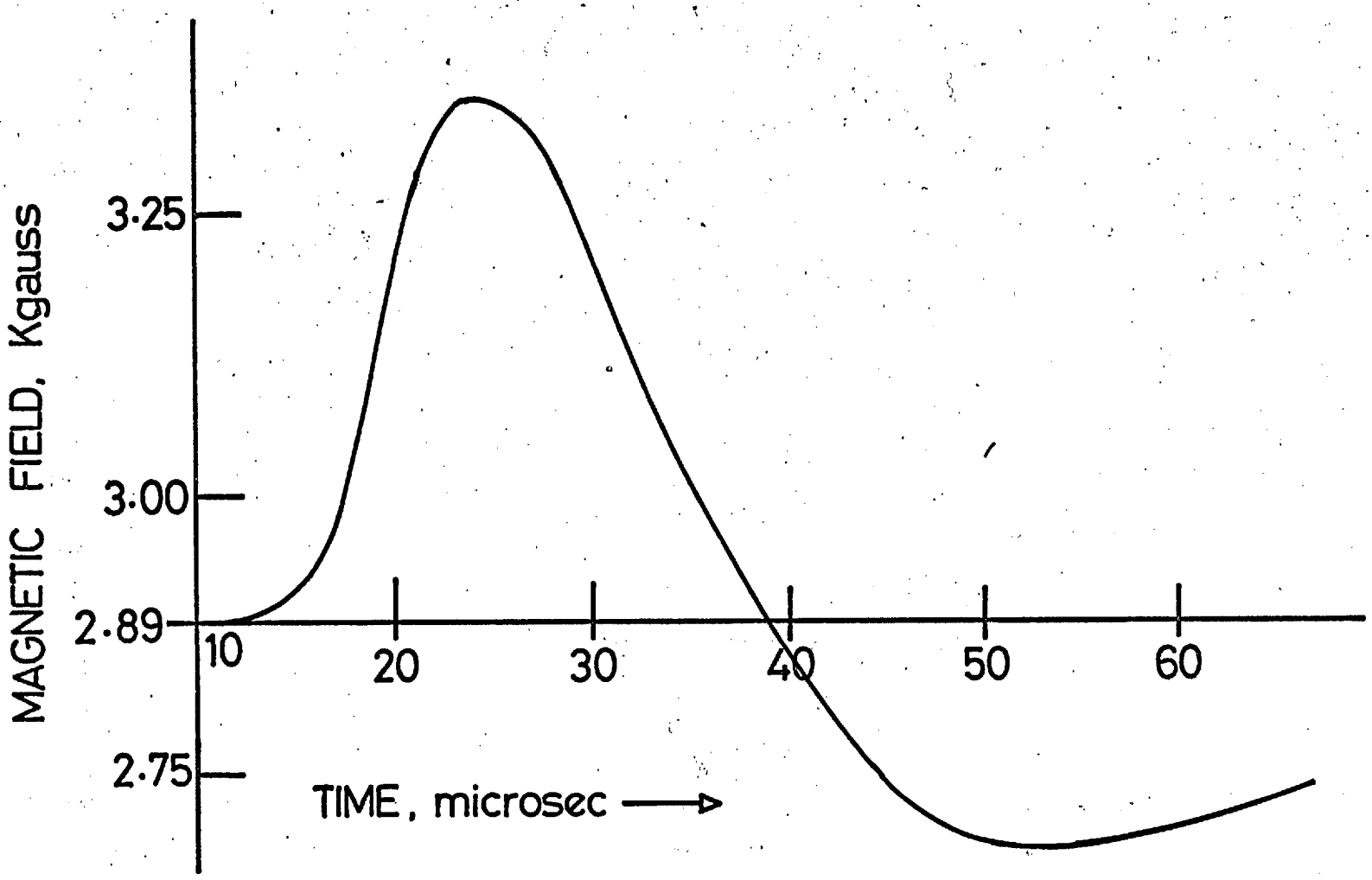

Fig 6.7 MAGNETIC FIELD VS. TIME FROM PROBE MEASUREMENT

Fig 6.8 MAGNETIC FIELD VS. TIME FROM PROBE MEASUREMENTS

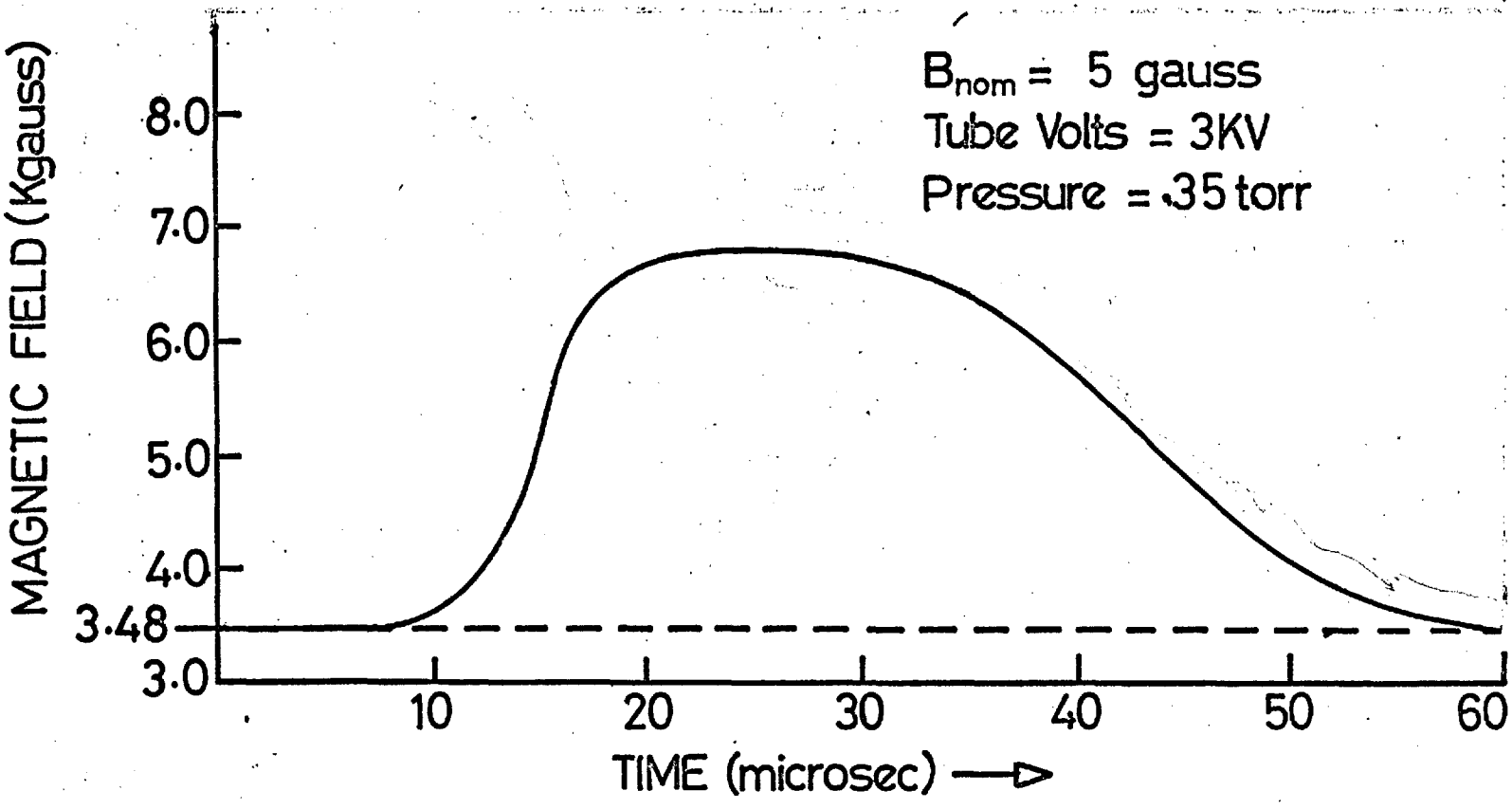

field and at .300 torr with 5 K gauss nominal stabilising field.

As with the Zeeman instrument results, the presence of field compression is very apparent, together with the rarefaction as the plasma expands from the axis. The form of the results are in very good agreement with the Zeeman instrument. The absolute value of the field agrees reasonably well with the previous results, although they are generally lower, and confirm that the magnetic field bank is not firing correctly. Generally, the compression results agree within the limits of experimental error, although the results obtained with the probe do seem to be consistently rather higher. The higher values of field compression obtained with the probe cannot easily be explained on the basis of its affect on the plasma; indeed one would expect that the reverse would be so. The reason would seem to be connected with the low absolute values of field measured by the probe.

The observation that the firing of the banks seemed very sensitive to changes in temperature and humidity, and was, at times, extremely erratic, would also seem to have some bearing on the above point, in so far as the two sets of measurements were taken at different times of the year.

This explanation of the relatively small differences

between the two results is for the most part conjecture and no systematic procedure was carried out to verify it. However, traces showing the magnetic field without the crowbar do indicate that some spark gaps appear not to break down until sometime during the second half cycle. This means that under normal operation these capacitors would most likely be shorted as a result of the crowbar pulse and not contribute to the magnetic field.

Finally we can see that although it has not been possible to draw any conclusions with regard to the affect of the probe on the plasma, this experimental data offers a worthwhile check on the operation of the Zeeman instrument.

References.

Frayne, P. Thesis, University of London.

Herzog and Tischler Rev. Sci. Inst. 24, 1000, 1953.

Chapter 7

The Ruby Laser

7.1 Introduction

The previous six chapters of this thesis have been concerned with the measurement of magnetic fields in a stabilized linear pinch. In chapter 9 an attempt will be made to correlate these measurements with some simple models of the mechanisms involved in the pinch. It becomes apparent after studying these models that a knowledge of the form that the plasma takes during the initial stages of the discharge would help considerably in deciding which plasma model, if any, is applicable under a particular set of conditions.

Previous spatially resolved measurements on this discharge have been obtained on a shot-to-shot basis. This is not altogether satisfactory since the discharge is not exactly reproducible. The ideal diagnostic would allow for both spatial and temporal plotting of the particular parameter that is to be measured without any disturbance of the plasma. Such a diagnostic nethod as this is proposed at the end of chapter 8 but for the remainder of the experimental part of this thesis we will confine ourselves to a method which achieves time resolved spatial plotting of electron density. The

several methods for doing this, discussed in chapter 8, each require a very intense source of light, preferably one which can be switched on and off in a time short enough for the plasma not to have moved. Such a source of light is a Q-switched laser, the most common type being the ruby laser. In our application, the ruby laser has the further advantage over other Q-switched lasers, in that the light output is in the visible region of the spectrum and will affect a photographic plate directly without the necessity of image convertors.

7.2 Simple Theory of the Three Level (Ruby) Laser.

In 1917 Einstein introduced the concept of stimulated emission as applied to spectral lines. With the advent of this concept, the laser became conceivable. However, it was not until 43 years later that Maiman succeeded in producing the first working laser. Since that time very large effort has been put into the field of lasers with the result that there are a very large number of different types of lasers, and laser materials, which can be bought commercially.

The population of a state within a material above $0^{o}K$ is determined by four processes apart from the temperature. These are:-

1) Absorption of radiation

2) Spontaneous emission of radiation

3) Stimulated emission of radiation

4) Non radiative effects.

The actual number of transitions which are produced depends upon a) Some property of the material b) The number of electrons in the originating states, and in cases of absorption and stimulated emission c) The radiation density.

The constants for absorption and stimulated emission are the same, and thus whether light of a particular reequency will be absorbed or amplified depends upon the population ratios of the associated states. Thus if the upper level is more highly populated than the lower, amplification may take place.

Consider now the energy level diagram for the Cr^{++} ion replacing an $A\ell^{++}$ ion in an $A\ell_2O_3$ lattice (saphire), Fig 7.1.

The ^2E level is a metastable state and there is only a very small spontaneous decay rate from it. The ^2E level is in fact split into two and we have two transitions to the ground state called R_1 and R_2

where $R_1 \equiv 6943$ Å

and $R_2 \equiv 6929$ Å

However, for the purposes of calculating the rate equations it is convenient to consider these two as one.

Fig 7.1 shows the energy level diagram for the ruby laser. The quantities n_1, n_2 and n_3 represent the populations of the respective levels and ρ represents the radiation density at the relavent frequency. The non-radiative transition coefficients between levels 3 and 1 and 2 and 1 are small compared to the radiative transitions and have therefore been neglected. The rate equations are thus

$$\frac{dn_3}{dt} = \rho\, B_{13}\, n_1 - \rho\, B_{31}\, n_3 - n_3\, A_{31} - n_3\, s_{32}$$

$$\frac{dn_2}{dt} = n_3\, s_{32} - n_2\, A_{21}$$

$$\frac{dn_1}{dt} = -\rho\, B_{13}\, n_1 + \rho\, B_{31}\, n_3 + n_3\, A_{31} + n_2\, A_{21}$$

where B_{13} is absorption coeff. level $1 \rightarrow 3$

B_{31} stimulated emission coeff. level $3 \rightarrow 1$

A_{31} - spontaneous emission coefficient level $3 \rightarrow 1$

A_{21} - spontaneous emission coefficient level $2 \rightarrow 1$

s_{32} - non-radiative coefficient level $3 \rightarrow 2$

Furthermore it has been assumed that $\rho(\nu_{21}) = 0$

Because of the large values of $\rho(\nu_{13})$ that are involved, A_{31} can be neglected with respect to $\rho\, B_{31}$. Also, since $n_1 >> n_3$

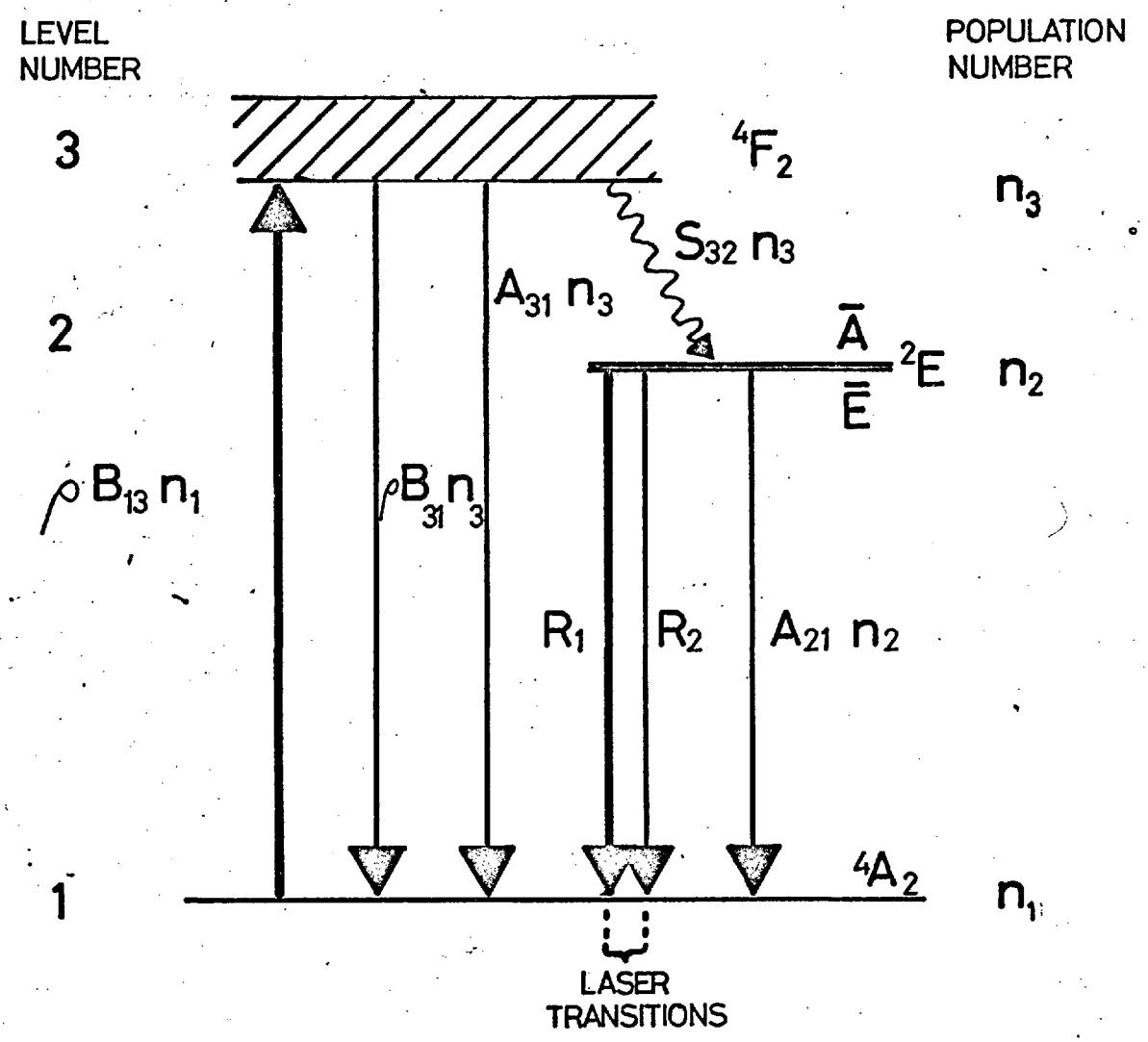

Fig 7.1 ENERGY LEVEL DIAGRAM OF RUBY (NOT TO SCALE.)

then $\rho\ B_{31}\ n_3 << \rho\ B_{13}\ n_1$

Thus we have

$$\frac{dn_3}{dt} = \rho\ B_{13}\ n_1 - n_3\ s_{32} \qquad - 7.1$$

$$\frac{dn_2}{dt} = n_3\ s_{32} - n_2\ A_{21} \qquad - 7.2$$

$$\frac{dn_1}{dt} = - \rho\ B_{13}\ n_1 + n_2\ A_{21} \qquad - 7.3$$

For the steady state conditions i.e.

$$\frac{dn_3}{dt} = \frac{dn_2}{dt} = \frac{dn_1}{dt} = 0$$

then from 7.1

$$\rho\ B_{13}\ n_1 = n_3\ s_{32}$$

The population inversion is represented by the ratio of n_2/n_1 which is given by

$$n_2/n_1 = \rho\ \frac{B_{13}}{A_{21}} \qquad - 7.4$$

When concerning ourselves with the practical laser we are interested in the gain per unit length α. This is a function of temperature, doping and population inversion (D'Haenens, 1962).

Maiman (1960) gives for 0.05% doped ruby at room temperature

$$\alpha = \frac{0.4(n_2 - n_1)}{N_o}\ cm^{-1} \qquad - 7.5$$

where N_o is the total number of chromium ions.

In order to sustain oscillations within the optical resonator the net gain per transit through the ruby must be at least equal to the net average loss per path. If we assume that α is constant along the length of the ruby and that most of the losses arise from the high transmission of the optical resonator mirrors then

$$e^{-\alpha l} = \sqrt{R_1 R_2}$$

where R_1 and R_2 are the reflectivities of the mirrors and l is the length of the ruby.

$$\alpha = \ln(1/(R_1 R_2)^{\frac{1}{2}})/l \qquad - 7.6$$

which in the present case where $l = 5\text{cm}$ $R_1 = .98$ $R_2 = .60$ then

$$\frac{n_2 - n_1}{N_o} \simeq \frac{1}{10}$$

or $$\frac{n_2}{n_1} \simeq 1.2$$

Thus quite small overinversions are sufficient to overcome appreciable losses within the optical resonator.

7.3 Spatial Variation of Light Output from the Laser

Since the output from the laser is to be used to expose a photographic film, it is of interest what the radial distribution

of the population inversion is. This will depend upon the diameter of the crystal, its doping and the distribution of the pump radiation. Devlin (1962) has shown that if the ruby rod is uniformly illuminated then there exists a region within the ruby of radius R_o/n where the energy density of radiation is essentially constant. In this case R_o is the radius of the ruby rod and n is its refracture index. The inversion within the ruby has been measured along the axis and at the walls, Danen (1965), but the results from this are inconclusive when an attempt is made to correlate them to Devlins calculations. However they do indicate that as the pump energy is increased a further flattening of the over-inversion takes place

At very high pumping energies the saturation effects due to superadiance will produce a further flattening of the radial distribution. However this is of no consequence when the experimental system is considered since the superadiance limit will not be reached until

$$\frac{n_2}{n_1} \simeq 12.0$$

whereas the total overinversion which the Kerr cell will sustain is (see section 7.9)

$$\frac{n_2}{n_1} \simeq 6$$

In conclusion therefore one can expect at least a region of radius R_o/n or 0.6 R_o to be reasonably uniform, which seems to have been corroborated by experimental results, which in general show a reasonably uniform distribution.

7.4 Transverse and Longitudinal Modes of the Ruby Laser

Rigrod (1963) reported some transverse mode patterns of the He-Ne laser operating at the 1.153μ transition. The results he obtained, although not directly applicable to the ruby laser, do show the type of mode patterns one might expect. The particular pattern which is predominant depends upon the diffraction properties of the optical resonator. The light from each of the antinodes is of the same frequency and bears a constant phase relationship to the other antinodes. Thus the interference pattern produced by the Mach-Zehnder interferometer (see chapter 8) will be affected by transverse modes only to the extent of becoming amplitude modulated by them, but since there is no frequency difference between different antinodes there will be no fringe shifting.

The competition between different longitudinal modes of a laser was first reported by Bennett (1962) who again used the 1.153μ line of the He-Ne laser. The formation of these various longitudinal modes is best shown with the aid of fig 7.2.

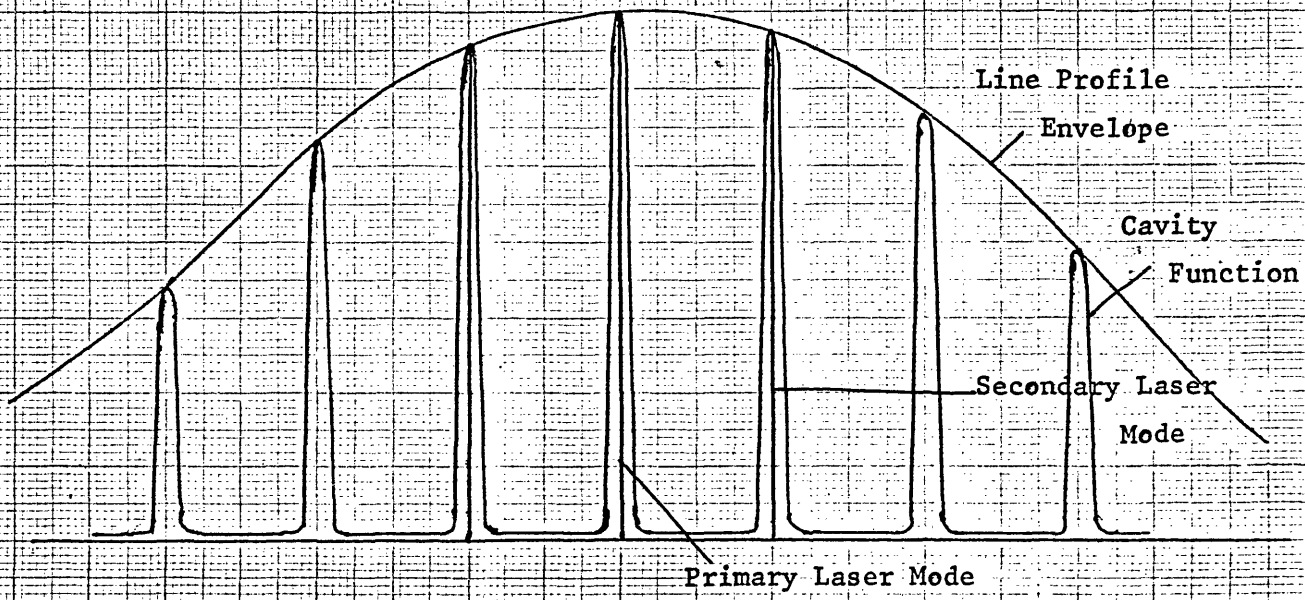

Fig 7.2 Longtitudinal Modes of a Laser.

Fig 7.3 Spacial Beat Frequency

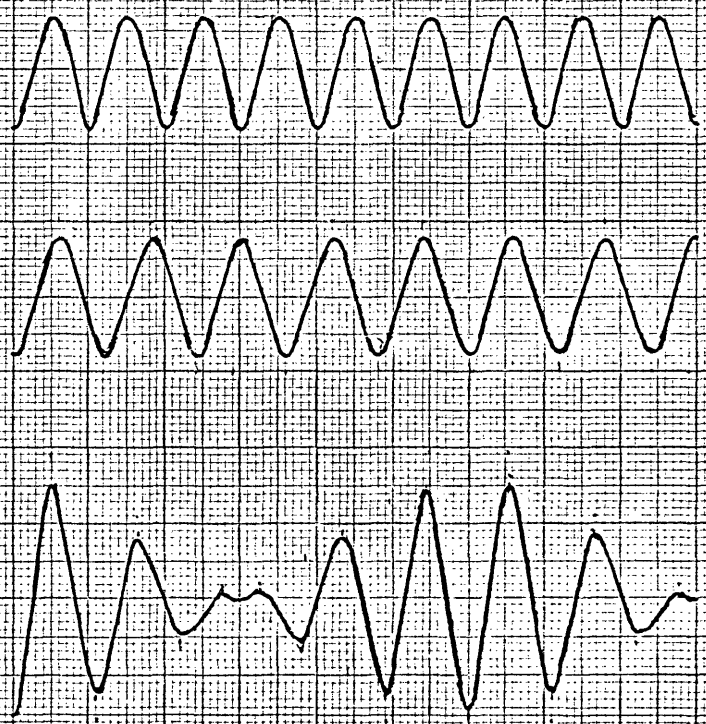

As we may see from chapter 2 the free spectral range of the resonator is $\frac{\lambda^2}{2L}$. When L = 40 cm and λ = 6900 Å this corresponds to a wavelength separation of 0.005 Å.

As we will see in chapter 8, the fringe pattern which is displayed spacially by the Mach-Zehnder, can be considered as the Fourier transform of the illuminating radiation. In order to be used to measure large electron densities, without ambiguity, it is necessary to have a large number (~100) of fringes across the plates and in order to facilitate setting, about 1,000 fringes are required before they interfere. Fig. 7.3 illustrates this point. Suppose we have two wave trains of frequencies f_1 and f_2 which are superposed.

The beat frequency produced is $f_1 - f_2$ and the number of wave maxima from one beat node to the next is $\frac{1}{2}\frac{f_1 + f_2}{f_1 - f_2}$

$$= \frac{\lambda}{\Delta\lambda} = \frac{6900}{0.005} \simeq 1.4 \times 10^6$$

This is considerably in excess of the figure of 1,000 quoted as a requirement above.

7.5 Q-Spoiling Techniques

The uncontrolled relaxation oscillations in a ruby are not suitable in this experiment unless some form of time resolving device, such as a framing camera, is incorporated. However,

because of the low sensitivity of photographic emulsions at this ruby wavelength (6943Å) large powers are necessary to produce adequate exposures. In order that the laser may be used in conjunction with a framing camera a large mean intensity is required from the laser. This is possible, but these lasers are very expensive and one was not available for the present work. The low power laser which was available consisted of a 5cm x 0.6cm pink ruby with 0.02 % Cr^{++} doping. This gives sufficient total light output to expose a photographic emulsion but in order to yield time resolved measurements it must be used in a giant pulse mode.

Various methods of Q spoiling are available. These may be conveniently separated into two groups, active and passive. The latter category, which includes saturable dyes, can be discounted as the primary method of Q switching in the present application since no accurate control of the timing of the giant pulse is possible. The three most common, active Q switches that are used are a) Kerr cell

b) Pockles cell

c) A rotating mirror

The Kerr cell and the Pockles cell can both be considered as 'fast' Q switches, where the change from a low Q resonator to a high Q resonator is achieved quickly with respect to the

time taken for the laser pulse to grow. The rotating mirror may be regarded as a 'slow' Q switch where the change from a low Q resonator to a high Q resonator takes a long time compared to the rise time of the laser pulse. Although the rotating mirror Q-switch introduces very little loss into the resonator during the high Q period, it does however have the disadvantage that slight movement in the stationary mirror will produce some time jitter in the production of the pulse. Furthermore laser action is likely to be initiated in some off axis mode, making alignment more difficult. These two disadvantages together with the difficulty in making a mechanically stable rotating mirror and timing apparatus were the reasons for not using the rotating mirror. The choice between the Kerr cell and the Pockles cell is not nearly so clearly defined, and the actual choice of the Kerr cell was one of convenience, since much of the electronics had already been designed and built.

A theoretical treatment of both fast and slow Q switches has been carried out (Arrechi, 1964; Hellworth, 1964; Wagner, 1963; Frantz, 1964; Vulsteke, 1963). In the next section, however, we consider only the action of the 'fast' Q switch system this being applicable to the Kerr cell.

7.6 Q-Spoiling Dynamics

A rigorous solution to the dynamics of the production of

giant laser pulses is extremely complex since it involves cross coupling between the different modes which can be propagated. Useful results however can be obtained much more easily by the use of certain simplifying assumptions with regard to the mode structure of the laser.

We will consider a Q-switching system with single mode operation where the spacial distribution of photon density is uniform; then we can write down fairly simple rate equations. (Hellworth, 1961).

$$\frac{d\Phi}{dt} = \left\{(n_2 - n_1)\,\sigma c + \frac{\gamma(t)}{\tau}\right\}\Phi + s \qquad - 7.8$$

and

$$\frac{d(n_2 - n_1)}{dt} = -2\,(n_2 - n_1)\,\sigma c\Phi + R \qquad - 7.9$$

where σ is the absorption cross section

and $\alpha = (n_2 - n_1)\sigma$ (Maiman, 1961)

$\gamma(t)$ = time varying loss term (due to Kerr cell)

c is the velocity in the ruby

Φ is the photon density

τ is the decay time of the optical resonator.

S and R are spontaneous decay rate and the pump rate respectively. The pump rate, R, because of the large value of Φ and $\frac{d(n_2 - n_1)}{dt}$ involved in the production of a giant pulse, can usually be neglected.

Equations 7.8 and 7.9 have been solved numerically (Wagner, 1963). Solutions for the 5cm x 0.6 cm ruby have been obtained by M. H. Key(1966). These are reproduced in graphical form in figs 7.4, 7.5, 7.6 and 7.7.

A very simple analytic solution can be obtained concerning the form of the rise of the pulse, if the decay of radiation in the resonator is neglected. Hence we have for the population densities

$$n_2(t) = n_2(o) - \Phi(t) \qquad - 7.10$$

and

$$n_1(t) = n_1(o) + \Phi(t) \qquad - 7.11$$

If we now assume that in equation 7.8 that for $t < 0$

$$\gamma(t) = \infty$$

and this changes instantaneously to

$$\gamma(t) = 0 \text{ when } t > 0$$

Furthermore if we write the spontaneous decay rate, S, as

$$\delta = n_2(t)\, A_{21}$$

then 7.8 reduces to, for $t > 0$

$$-\frac{1}{2c\sigma}\frac{d\Phi}{dt} = \Phi^2 + \left(\frac{A_{21}}{2c\sigma} - \frac{n_2(o) - n_1(o)}{2}\right)\Phi - \frac{n_2(o)\, A_{21}}{2c\sigma}$$

Fig 7.4 COMPUTED ENERGY OUTPUT

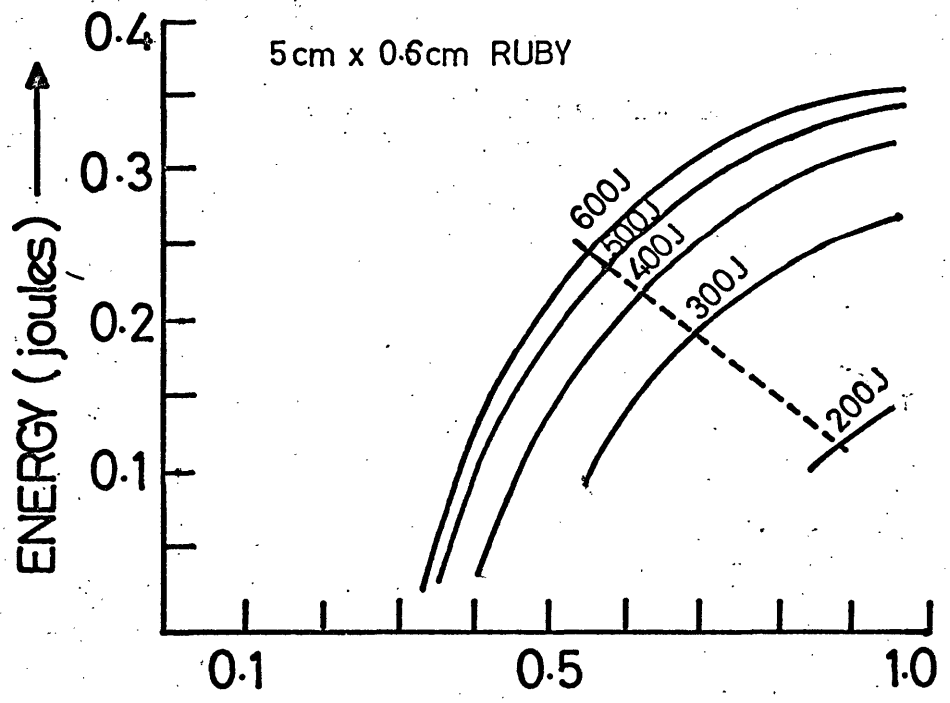

Fig 7.5 COMPUTED POWER OUTPUT

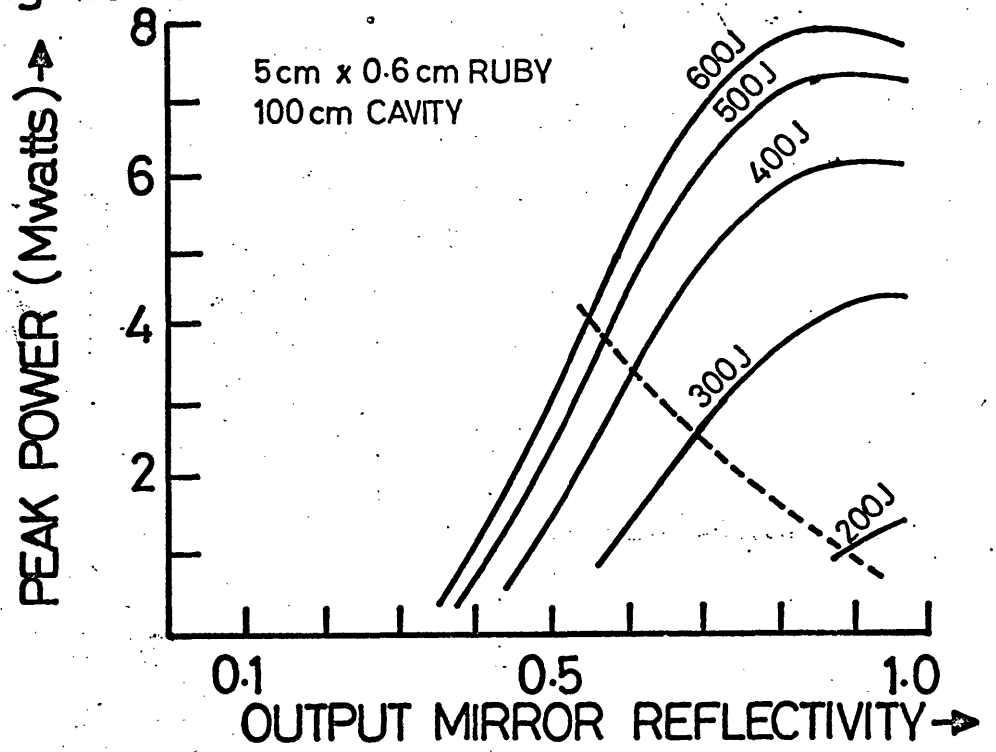

Fig 7.6 COMPUTED ENERGY OUTPUT

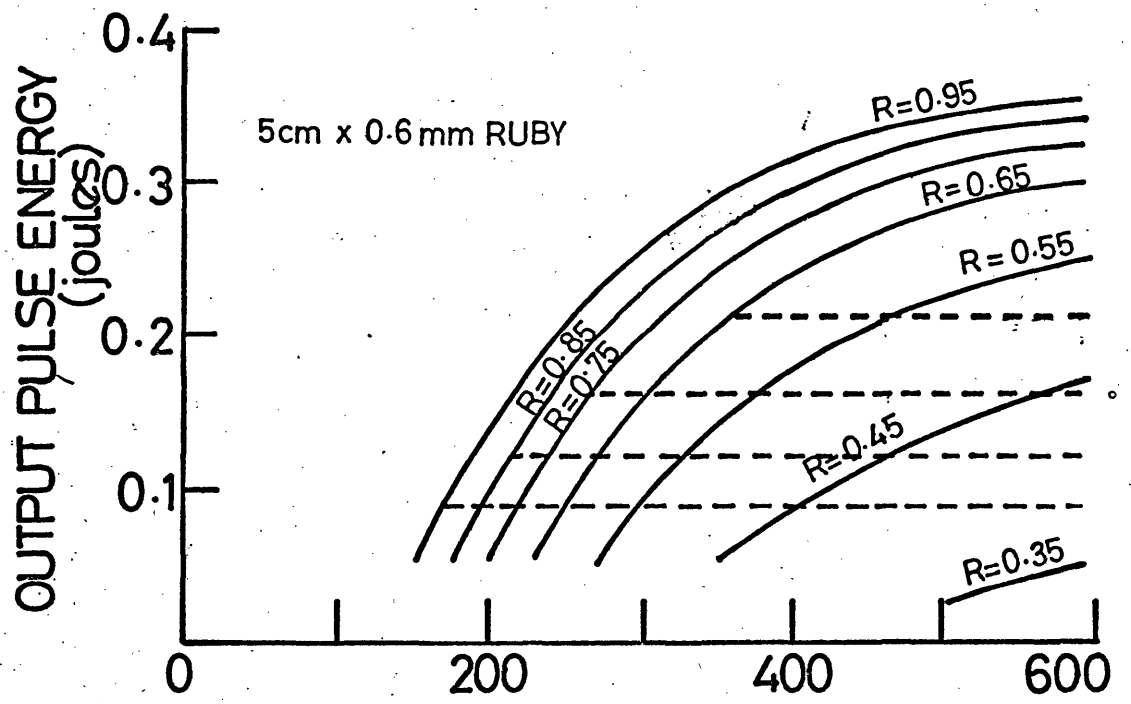

Fig 7.7 COMPUTED PULSE WIDTHS

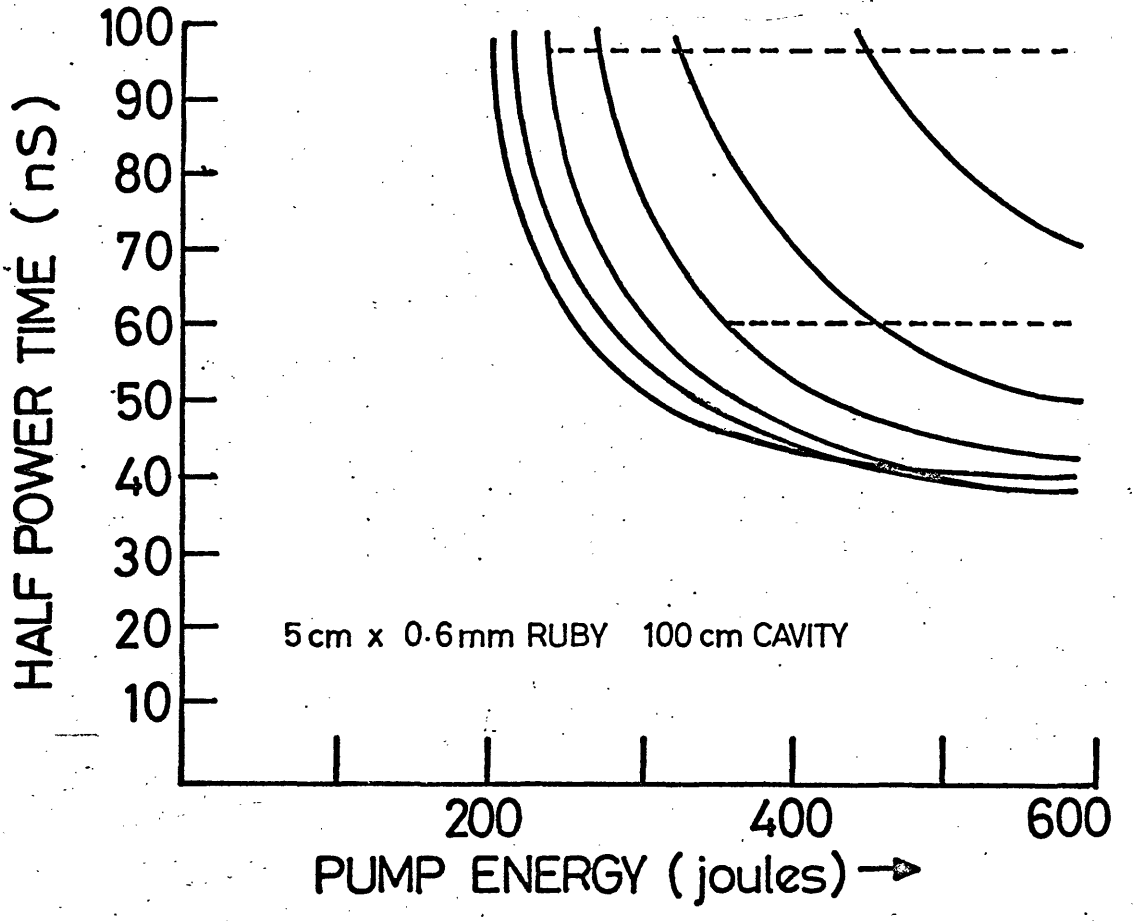

It has been pointed out by Frantz (1964) that a solution to this takes the form

$$\Phi = \frac{n_2(o) - n_1(o)}{2} \cdot \frac{1 - e^{-t/\tau'}}{1 + Ae^{-t/\tau'}}, \qquad - 7.12$$

if $\frac{A_{21}}{2c\sigma} << n_2(o) - n_1(o)$

where $\tau' = \frac{1}{c\sigma\{n_2(o) - n_1(o)\}}$

and $A = \frac{\{n_2(o) - n_1(o)\}^2 c\sigma}{2\, n_2(o)\, A_{21}}$

From equation 7.12 we can define a rise time of the pulse

$$T_R = 4.4\tau'$$
$$\simeq 9 \text{ nsec.}$$

The result of this simple theory is not in very good agreement with experiment, where the rise time has been measured to be ≃ 30nsec. (see section 7.10).

More detailed numerical calculations give a much more accurate result, simply because the effect of losses and transit time have been neglected in the simple theory.

From fig 7.7 we see that with 400 joules pump energy and R = .6, the half power time i.e. the time taken between the half intensity point on the rise of the pulse, is ~60 nsec. From

experiment the shortest half power time obtained was ~80nsec (fig 7.15). However this final discrepancy could easily be accounted for by the fact that the efficiency of the reflecting cavity is known only approximately.

7.7 Design and Operation of the Ruby Laser

The original cavity for the laser consisted of six small flash tubes, arranged in series, clustered around the 5cm x 0.6cm ruby. This system, however, was extremely difficult to trigger and consequently a second cavity was constructed which used one flash tube at one focus of an elliptical cavity. The ruby was placed along the other focus. The cavity had a major diameter of 7cm, a minor diameter of 5cm and a length of 10cm. The ruby was clamped at one end by means of a spring arrangement to an alloy protractor used for measuring its orientation. The other end was free to rotate. The flash tube, English Electric type XL93, had a 3in. arc length and 9mm bore. This large size was in fact unnecessary considering the size of the ruby crystal but it was decided that the system should be designed to accept a larger ruby crystal with the minimum of modification, should the small ruby prove inadequate. The ellipical cavity itself was constructed of duralumin, the inside of which was highly polished. Insulation of the flash tube was originally achieved using 'pyropholite', a machinable asbestos type material

with reputedly good electrical characteristics. Unfortunately the 12 Kv trigger pulse tracked across the 'pyropholite' causing it to crack. The electrical energy of the condenser bank was then discharged through this crack resulting in damage to the cavity walls and to the flash tube, the damage being serious enough, to the flash tube, to crack the quartz envelope. As a result of this unfortunate incident it was decided to enclose the flash tube in a further quartz tube which acts as both an insulator and a guide tube for the cooling air. A photograph of the laser is shown (complete with Kerr cell) in fig 7.8 and a cross sectional drawing of the cavity is shown in fig 7.9

The mirrors used in the optical resonator were of multilayer dielectric type, on fused quartz substrates, with reflectivities of .98 and .60. These figures give reasonable values for pulse width and power output. The flash tube was driven from a capacitor bank consisting of 14, 27μf, 5Kv capacitors through a 520μH choke consisting of 10 gauge copper wire on a 'tufnol' former. Owing to the fact that the changes only developped 3Kv the maximum stored energy was 1.7 kilojoules. Of this 1.7 kilojoules about 50% was lost due to the resistance of the leads and the inductance windings and approximately another 30-40% was lost within the cavity, mainly due to the fact of the bad missmatch in the size of the ruby and flash tube. These losses

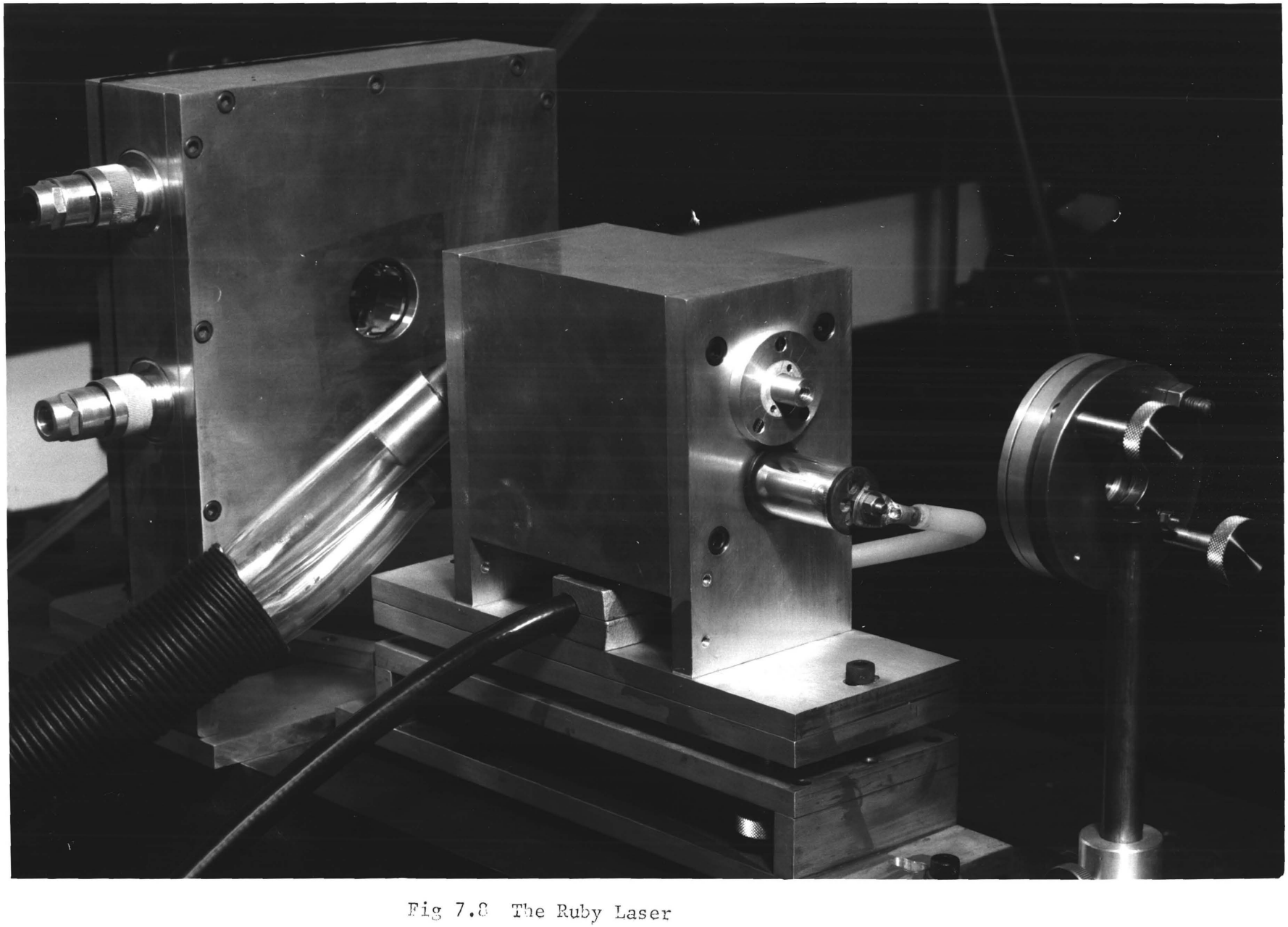

Fig 7.8 The Ruby Laser

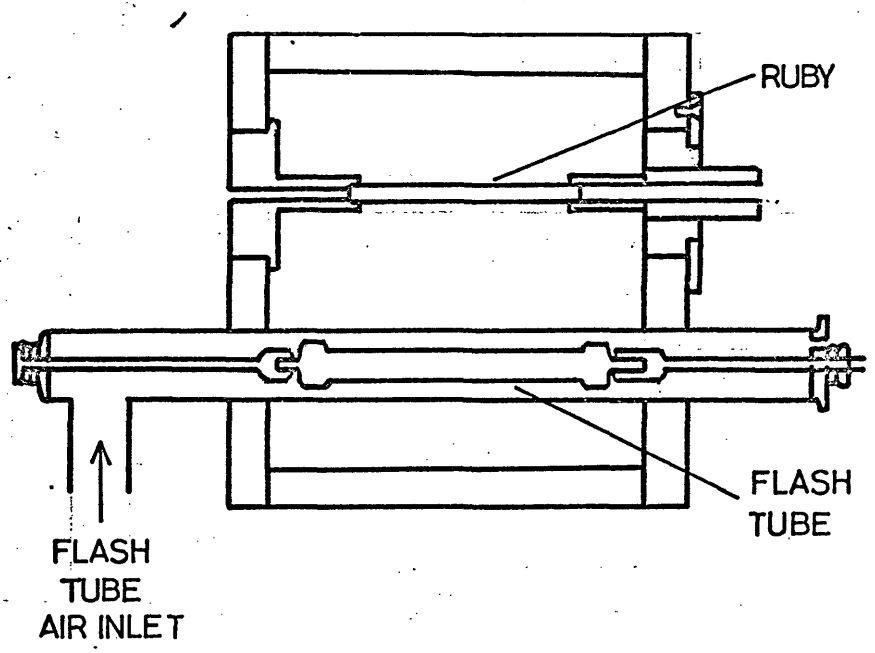

Fig 7.9 LASER CAVITY (NOT TO SCALE)

resulted in the maximum energy available for pumping being in the order of 500 Joules.

Triggering was achieved by using a high voltage relay to connect across the flash tube a small capacitor (0.01μf) charged up to 12 Kv. The speed of discharge of this capacitor was such that the 520 μH inductance effectively isolated this small capacitor from the main discharge bank.

Alignment of the optics was originally carried out using an auto-collimator. The reflection from the back mirrors was aligned with the reflection from the front surface of the laser rod and this was then used to align the front mirror. This procedure worked perfectly adequately when alignment of the laser with some other component was not critical but a different method had to be employed when critical alignment with other components was necessary. The arrangement found most convenient for doing this is described in chapter 8.

7.8 Threshold and Power Output

The relaxation oscillations of the ruby laser were observed using a R.C.A. photomultiplier type 7102. This photomultiplier was also used to determine the threshold pump energy for the .98, .60 resonator which was found to be ~190 joules. This is considerably higher than the theoretical estimate of ~100

joules (fig 7.5), but the mathematical model used for this calculation is rather crude and neglects extraneous losses within the cavity. The photographs (figs 7.10 and 7.11) show the relaxation oscillations slightly above, and well above threshold, respectively.

The power output from the laser was measured using a small cell containing copper sulphate solution (see fig 7.12). The cell was constructed of perspex with thin glass end windows. A column of saturated copper sulphate solution, .6cm long, will absorb approximately 90% of any incident radiation at 6943Å and, provided the cell has a small enough thermal capacity a detectable temperature rise will ensue when laser light is incident. The temperature rise was measured using a Cu-constantin thermocouple and a sensitive lamp and scale galvanometer. Calibration of the unit was achieved by passing an electric current through a small coil of resistance wire placed in the cell. If the current is passed for a short enough time compared to the time taken for the cell to respond, then the system may be treated in a similar way to the ballistic galvanometer. In this case

Power $\propto$ max. galvanometer defl.

The validity of this relationship was checked by passing various currents through the heating coil and, within the

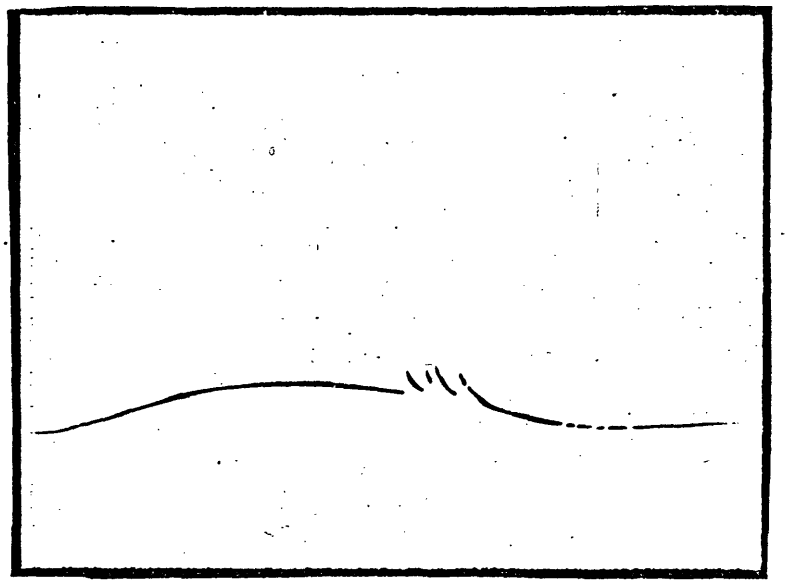

Fig 7.10 Laser Output near Threshold.

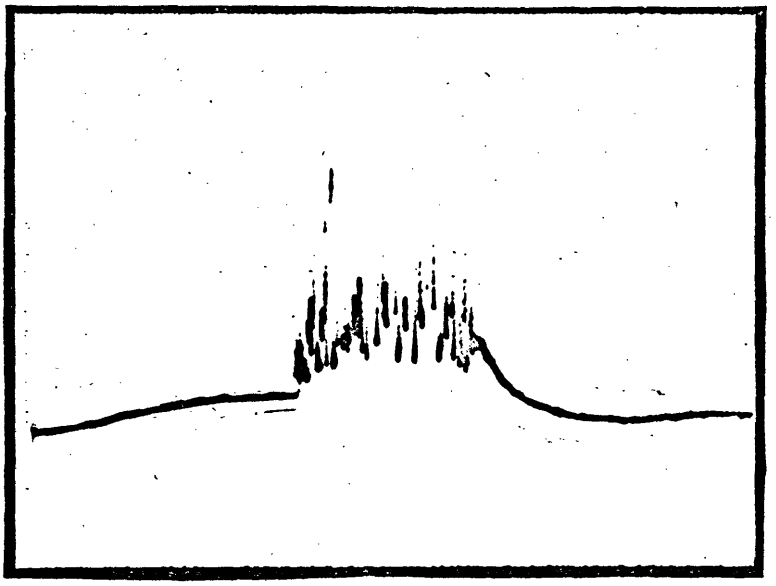

.2 msec

Fig 7.11 laser Output well above Threshold

(Not to the same intensity scale)

experimental limits, was found to be true.

At 500 joules pump energy the ~~power~~ energy output was found to be 10 ± 4 millijoules whereas the power output at 190 joules pump energy was undetectable with this apparatus.

7.9 The Kerr Cell

If an electric field is applied to an isotropic dielectric material, the material becomes birefrigent. This effect is known as the Kerr electro-optic effect. When a liquid is placed in an electric field it behaves optically as though it were a uniaxial crystal with the optic axis in the direction of the electric field. Thus light passing through the liquid is split up into an E and an O ray, each one moving with different velocity. Thus, on emergence from the cell, there will be a phase difference between the two polarisations and there will be a change to the resultant polarisation state.

The optical path difference between the two rays is given by

$$\partial = B_k \frac{\ell V^2 \lambda}{d^2}$$

where ℓ is the length between the plates and d is their separation

λ is the wavelength

V is the potential difference across plates, and

B_k is the Kerr constant.

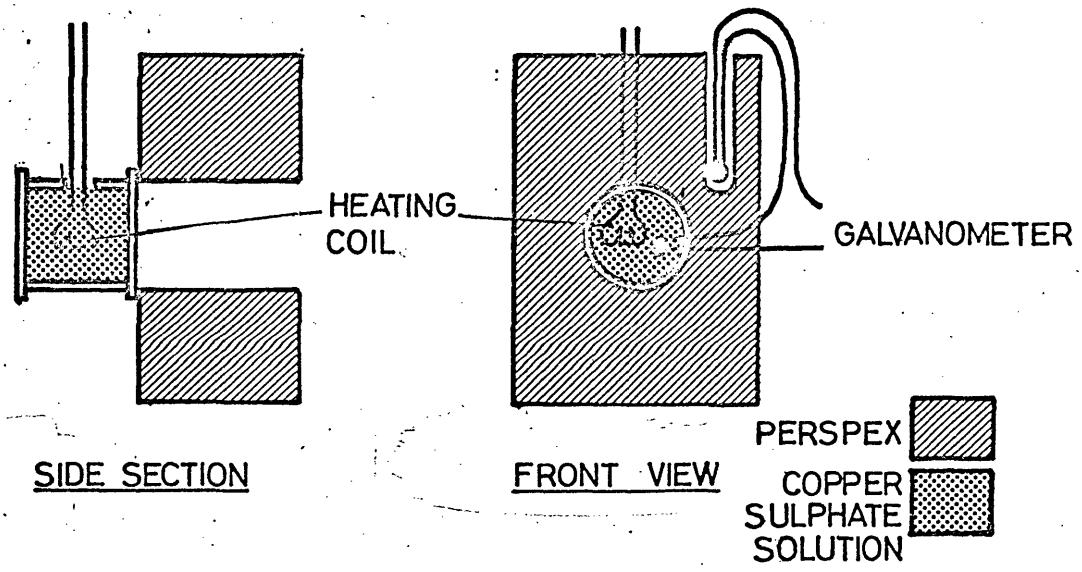

Fig 7.12 COPPER SULPHATE CELL

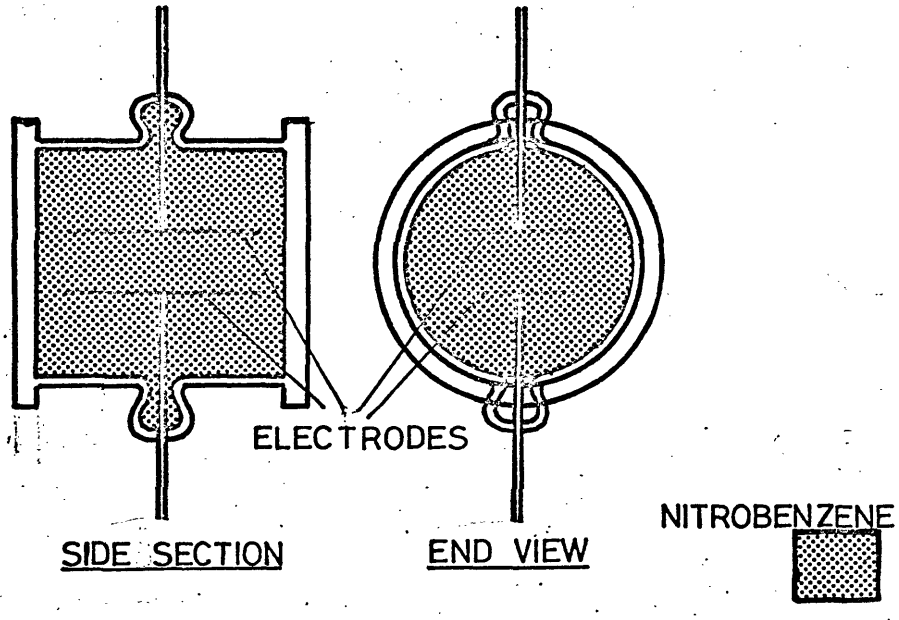

Fig 7.13 KERR CELL

The most commonly used substance in Kerr cells is nitrobenzene, the values of B_k for which vary slowly with wavelength, Cotton (1931), and has a value of 1.97×10^{-10} c.g.s. units at 7000 Å.

The Kerr cell used was similar in construction to the one designed and used by M. H. Key. Fig 7.13 shows a drawing of it, the plate dimensions being 1cm x 4cm with a separation of 0.8cm.

It is possible to use the Kerr cell as a Q spoiling device for the ruby laser in separate modes known as $\lambda/4$ and $\lambda/2$ switching.

a) $\lambda/2$ switching

Here in the low Q conditions, light of one particular polarisation is rotated by the Kerr cell until on emerging it is polarised at right angles. This polarisation is removed from the resonator using a nicol prism. In the high Q condition, zero field is applied to the Kerr cell, and no rotation takes place, the nicol prism transmits all the light (Fig 7.14a)

b) $\lambda/4$ switching

In this case the voltage on the Kerr cell in low Q condition is arranged to produce a path difference of $\lambda/4$ between the E and O rays. The emergent beam is then circularly

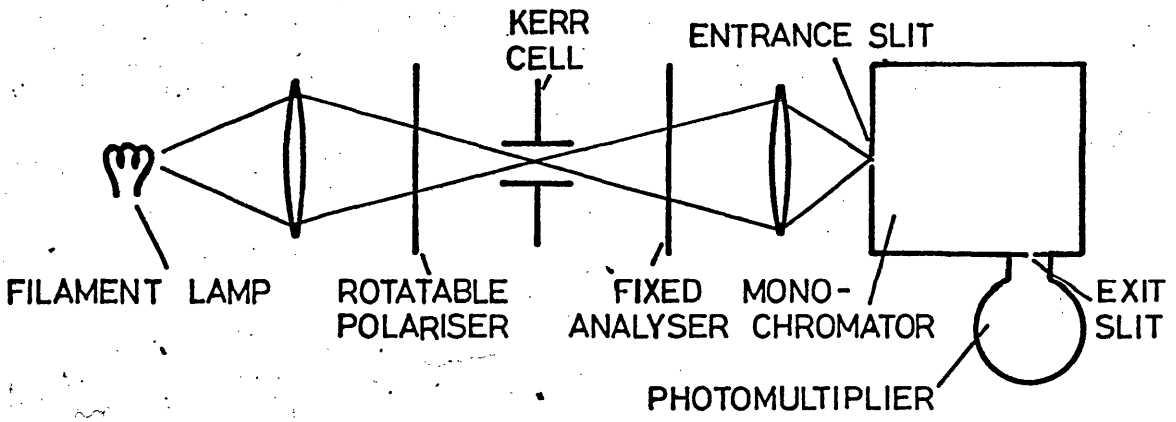

Fig 7.14a DIAGRAM FOR $\lambda/2$ SWITCHING

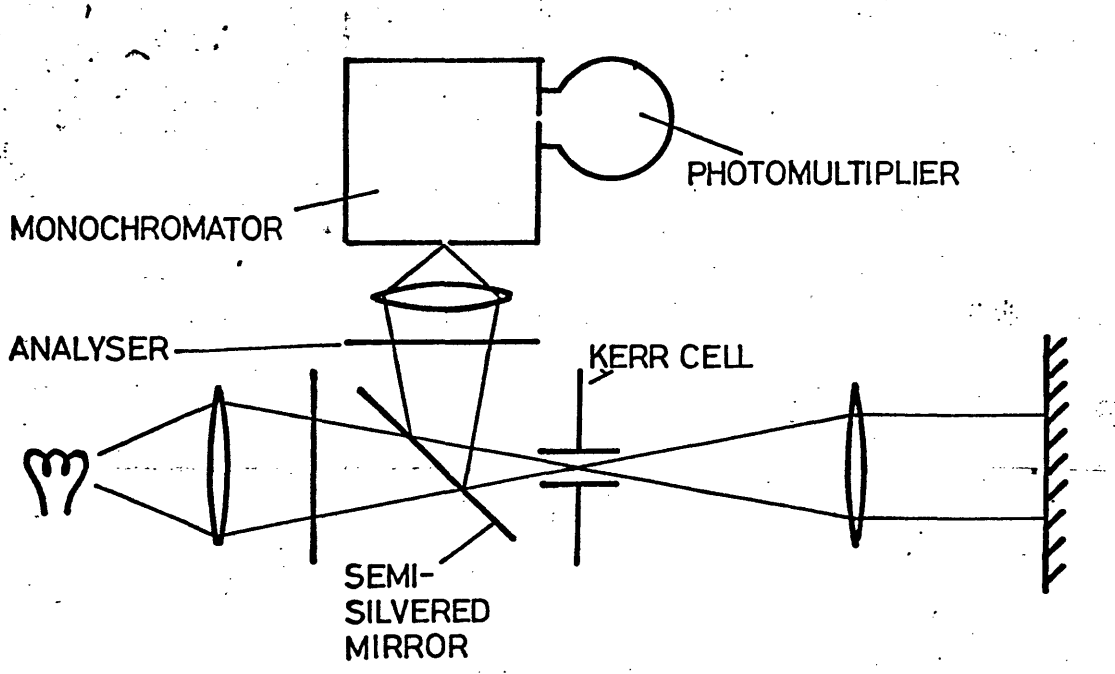

Fig 7.14b DIAGRAM FOR $\lambda/4$ SWITCHING

polarised. This light is then reflected off the resonator mirror and back through the Kerr cell. After the second transit through the Kerr cell the light is polarised at right angles to the original direction. A ruby crystal is anisotropic, and the amplification is 5 times greater when the light polarised along the C axis than along the other two axes. Thus if the crystal is cut with the C axis at right angles to the crystal axis and correctly with respect to the Kerr cell, the threshold will be increased in the low Q condition by approximately ~~5~~ (fig 14b) 5+5 : 5+1

The Kerr cellwas tested for operation in both these modes. If the value of the Kerr constant, given previously, is used then we find that $\lambda/4$ switching should take place at 14.4 Kv, whereas the value was found to be 16.0 Kv. The discrepancy ceases to become quite so surprising when one considers the large variations in the published values of the Kerr constant. Grant (1963) gives the Kerr constant in nitro-benzene at 7000 Å to be 3.64×10^{-10} c.g.s. units, almost twice as great as the value given by Cotton!

The only explanation that can be put forward is that purity standards in the manufacture of the nitrobenzene must vary considerably.

One rather important point does emerge from this discussion, and that is that since the pulsing apparatus is only operable up to 16.5 Kv, $\lambda/2$ switching is just not possible with this Kerr cell. This did not prove to be a very serious disadvantage since the degree of overpopulation in the ruby required to make $\lambda/4$ switching ineffectual, could not be obtained with this set up. Furthermore since $\lambda/2$ switching necessitates the introduction of a further component into the resonator thereby increasing the spurious loss, it was considered better to use $\lambda/4$ switching.

7.10 Performance of the Q poiled Laser

The introduction of the Kerr cell into the optical resonator increased the laser threshold by 45%; this resulted further in the power output at 500 joules pump energy being reduced by a factor of greater than 3.

The production of giant pulses was carried out successfully although to some extent erratically. The majority of pulses obtained had a form rather similar to that shown in fig 7.15a. The pulse has a rather ragged trailing edge presumably caused by the poor optical quality of the ruby. However occasionally a pulse would appear with a form similar to that shown in fig 7. 15b, which closely fitted the ideal computed shape. It can only be assumed from this that, if certain lateral modes are suppressed

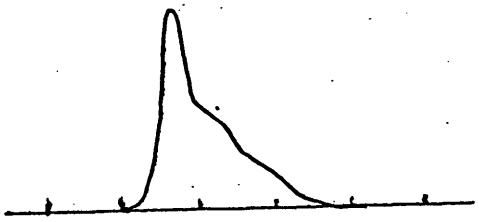

Amplitudes not to the same scale

200 nsec/cm

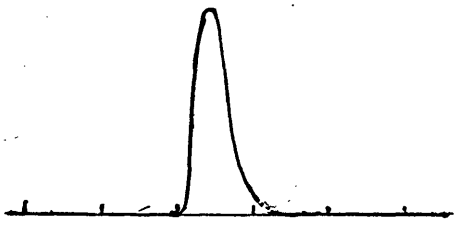

Fig 7.15 Q- Spoilded Laser Output

due to slight mialignment, the optical quality, along the path pertaining to the remaining mode or modes, was good enough to produce the predicted pulse form.

This effect however was not pursued further since it was also established that the pulse, even when of the type shown in fig 7.15a, was of sufficient intensity to produce adequate exposure of the photographic film. Since this requirement was the most important one it was considered that, for the purposes of measuring electron densities, it was quite adequate.

References

Arechi, F.T. Potenza, G. Sona, A. Il Nuova Cimento XXXlV

Bennett, W.R. Phys. Rev. 126, 580, 1962.

Cotton, A. and Rabinovitch, J. Annual Tables of Constants and Numerical Data, (1931)

Daneu, V. Sacchi, C.A. Svelto, O. Applied Optics, 4, 7, 863, 1965.

Devlin, G.E. McKenna, J May, A.D. Sharvlow, O Applied Optics, 4, 7, 863, 1965.

D'Haenans, I.J. Asawa, C.K. J.A.P. 33, 11, 3201, 1962.

Frantz, M. Applied Optics, 417, 1964.

Grant Kamal Proc. IEEE 51, 1364, 1963

Hellworth, R.W. Advances in Quantum Electronics Columbia Univ. Press, 1961.

Hellworth, R.W. Hughes Research Lab. Report, 300, 1964.

Key, M.H. Thesis, University of London, 1966.

Maiman, T.H. Nature, 187, 493, 1960

Maiman, T.H. Phys. Rev. 123, 4, 1145, 1961.

Rigrod Applied Phys. Letters, 2, 51, 1963.

Vulsteke, A. J.A.P. 34, 1615, 1963.

Wagner, W.G. and Lengyel, B.A. J.A.P. 34, 7, 2040, 1963.

Chapter 8

The Mach Zehnder Interferometer

8.1 Introduction.

It is required to produce accurate spatially resolved distributions of electron density. This is essential in understanding the dynamics of the stabilised linear pinch and is of considerable help in correlating the results obtained from the magnetic field measurements to calculations which are given in Chapter 9.

The requirements for obtaining spacial plots of number density, and some restrictions, were mentioned in chapter 7. This chapter concerns itself with the selection of a suitable method for carrying out these measurements, followed by an analysis of the system chosen, i.e. the Mach-Zehnder interferometer. The preliminary theory to the Mach-Zehnder interferometer is irrelavent at this stage and is contained in appendix 1V.

8.2 Methods Available to Obtain Spacial Plots of Electron Densities.

Apart from the methods which rely on observing the plasma from shot-to-shot, there are four techniques which are suitable for obtaining spacial plots of electron densities, these being

1) Shadow graphs

2) Schlieren photography

3) Interferometry

4) Holography

Of these four, holography is unique in that it does not yield directly either the refractive index or a derivative of the refractive index, but is capable of yielding results in either and both of these forms. For this reason holography, although not strictly a method in itself, is superior to any one of the first three methods but suffers from one serious disadvantage. Since a hologram is in essence a photograph of the fourier transform of the object (Gabor (1949), Leith and Upatnieks (1962)) a very great deal of information must be stored on the photographic plate, necessitating the use of very fine grain photographic plates. Unfortunately fine grain photographic plates are very slow, particularly at the ruby wavelength, 6943 Å, where normally fast emulsions have a very poor response. The power output from the ruby laser described in chapter 7 is not sufficient to produce a reasonable exposure of these fine grain plates, although more powerful lasers, which have been made, would.

It can be shown that to a rough approximation the shadow method measures the second derivative of the refractive index

whilst the Schlieren method measures the first derivative (Beams, 1954), and interferometric methods measure the refractive index directly (Ladenburg, 1954). A direct comparison of the shadow method with the other two methods is only possible when the second derivative of the refractive index is small, since when this quantity is large an analysis of the resulting photograph is extremely difficult. Unfortunately shadow methods are of greatest use when there are rapid variations within the system; where phenomena such as turbulence are clearly visible (Jahoda, 1964). However, this method does not lend itself easily to a quantitative determination of the refractive index.

A comparison between Schlieren and interferometric methods is much more readily obtained. Consider the Schlieren system in fig 8.1. An image of the slit S1 is produced by the two Schlieren lenses L_1 and L_2 in the plane of the knife edge, K.E. The object under study is placed between the two lenses and the knife edge is arranged such that the image of S_1 is cut off. The only rays of light which reach the screen, are rays which have been refracted upwards by the object. Thus an intensity distribution which is dependent on the nature of the object is produced. In practice the knife edge only partially obscures the image of S_1 since, if the image is completely obscured, only the variations in the object which produce upward deflections

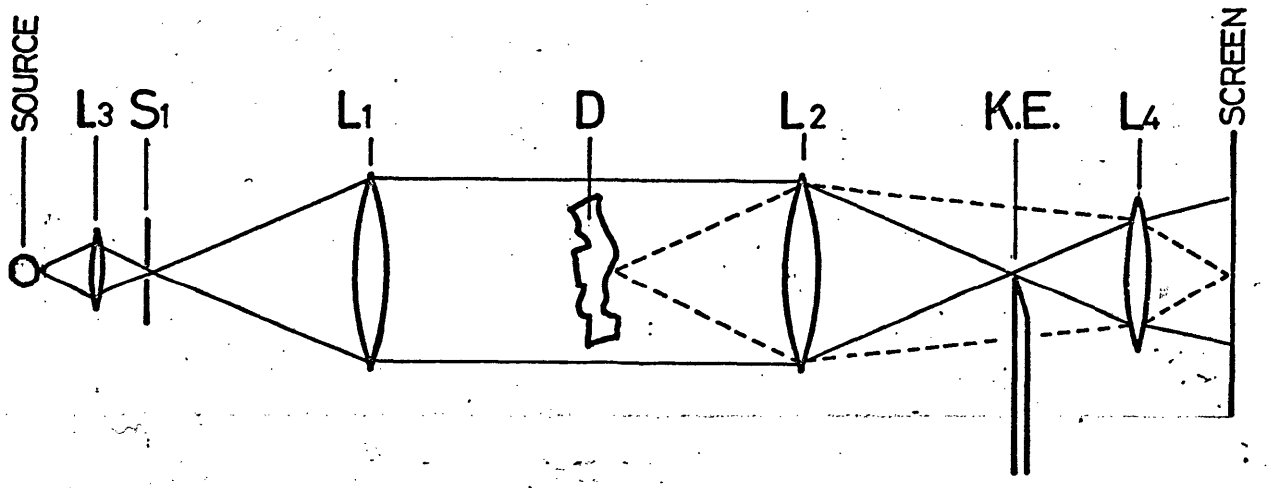

Fig 8.1 A SCHLIEREN SYSTEM (SCHEMATIC)

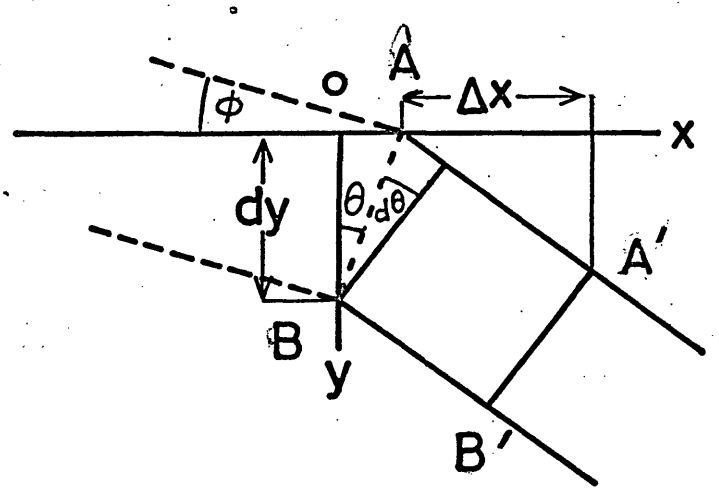

Fig 8.2 DIAGRAM SHOWING THE DEVIATION OF RAY DUE TO dn/dy

would be recorded.

It can be shown that change in intensity ΔI is given by (Leipman, 1947)

$$\frac{\Delta I}{I} = \frac{\epsilon f}{a}$$

where I is the average intensity, f is the focal length of the lens L_2 and a is the width of the image of the slit that is unobstructed by the knife edge. ϵ is the angle through which the ray is deflected due to the disturbance. This can be seen by reference to fig 8.2. If the optical path between AB and A'B' is $\Delta\ell$ then

$$AA' = \frac{\Delta\ell}{n}$$

and

$$BB' = \frac{\Delta\ell}{n+dn}$$

hence

$$\Delta\Theta = \frac{1}{n}\ \frac{dn}{dy}\ d\ell \sin\Phi$$

or

$$\epsilon = \int_0^{\ell} \frac{1}{n}\ \frac{dn}{dy} \sin\Phi\ d\ell$$

A reasonable value of f/a is $\sim 10^4$ and if we assume that the minimum detectable value of $\frac{\Delta I}{I}$ is $\frac{1}{10}$ then we find that for the discharge in question

$$\frac{dn}{n} > 3 \times 10^{-6}$$

To obtain this a value of sin Φ has been assumed to be near unity.

For an interferometric method then the path difference is given by

$$\Delta = \int_0^{\ell} (n - n_0)\, d\ell$$

Thus using the same value for ℓ as above and assuming the wavelength of the observing light to be 7000 Å

then

$$\frac{dn}{n} > 7 \times 10^{-8}$$

These simple calculations show that an interferometric method is more sensitive than the schlieren method by a factor of approximately 50. Thus, provided that sensitivity is the only criterion then an interferometric method is to be desired. There are further disadvantages in the schlieren method, although these are more of a practical nature. The sensitivity of the instrument depends upon the ratio $f/_a$ being large. Furthermore, the image of the slit s, must be very good. This implies that the lenses or mirrors used must be virtually free from spherical aberation and, for lenses used with non-monochromatic light, chromatic aberation. The polishing of lenses to this quality is difficult and although the interferometer

mirrors must be polished to about the same tolerance, the cost of the lenses is much higher. A further disadvantage which, in many cases, will be more important than the two already mentioned, is that only a small proportion of the total light can be used to expose the photographic plate if the sensitivity is to be kept high (i.e. with a small). Interferometers, however, can use up to 50% of the available light. Finally, it is not difficult to see that, since the schlieren method depends upon the derivative of the refractive index, the interpretation of results obtained by this method are likely to be rather more difficult than results obtained by interferometric methods.

In conclusion we see that unless the refractive index and refractive index gradients are high, then an interferometric method is likely to be more useful and accurate than either shadow or schlieren methods. If the refractive index gradients are high then it is possible that an interferometric method may be totally unacceptable because of a very large number of fringe shifts and the difficulty of interpretation. In these cases shadow or schlieren methods are to be preferred.

8.3 Choice of Interferometer.

Of the two types of interferometer, i.e. multiple beam and two beam interferometers, only the two beam type is applicable in this case because of the large path differences associated

with multiple beam interferometers in this application. The two two beam interferometers which could be of use are the Twyman-Green and the Mach-Zehnder.

Electron density measurement made with the He-Ne laser show that there is likely to be a sufficiency of fringe shifts rather than a dearth, with a consequence that the simple path Mach-Zehnder is to be preferred to the double path Twyman-Green. The factor 2 in sensitivities between these two instruments is not to be considered a serious difference as the factor of 50 involved between the schlieren and interferometric methods. The Mach-Zehnder interferometer has the added advantage that it is more compact than the Twyman-Green, although the latter involves less components.

8.4 Theory of the Mach Zehnder Interferometer.

The Mach-Zehnder interferometer consists of two beam splitter and two fully reflecting mirrors usually arranged to be at the corners of a rectangle or parallelogram. It will be assumed, for the purposes of this initial theory that these mirrors will be perfectly flat and of zero thickness. A diagram of a rectangular interferometer is shown in fig 8.3. The two beam splitters M_1 and M_4 have coordinates (o, o) and (a, b) and the fully reflecting mirrors M_2 and M_3 have coordinates (a, o) and (o, b)

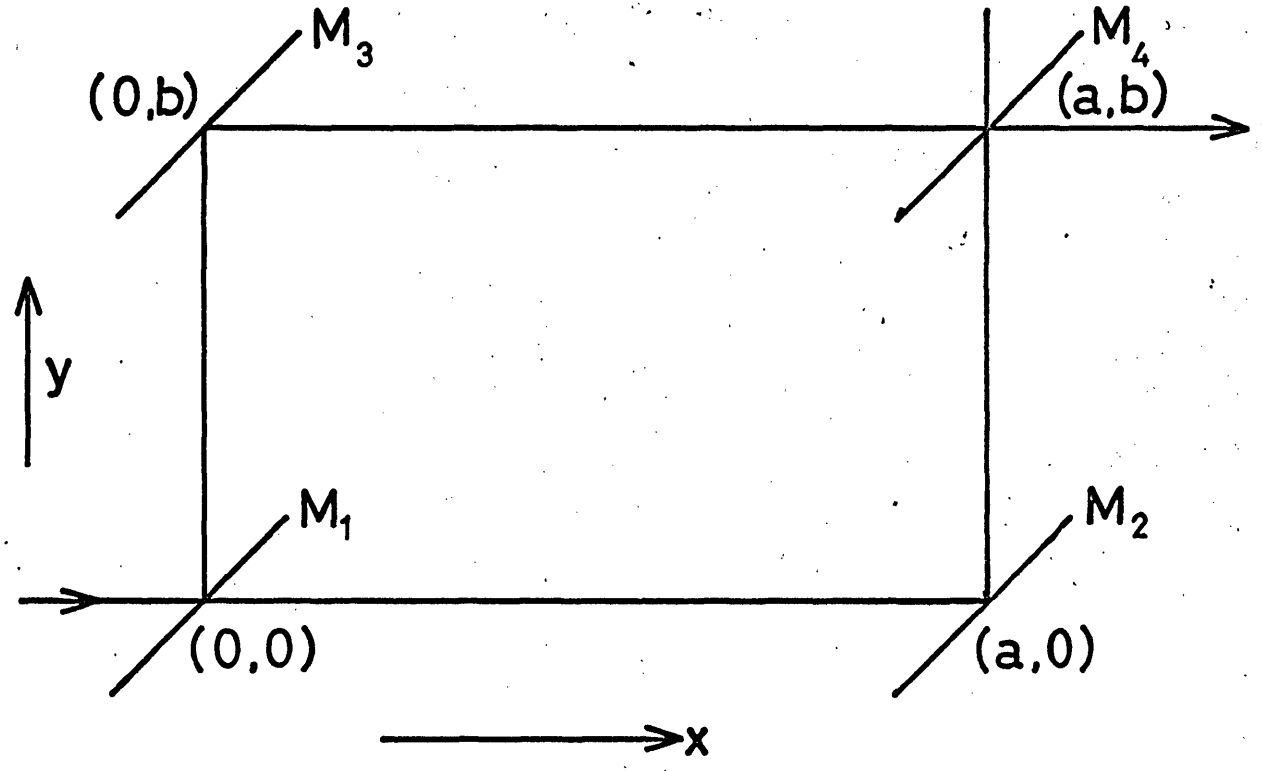

Fig 8.3 SCHEMATIC DIAGRAM OF MACH ZEHNDER SHOWING COORDINATES OF THE MIRRORS

respectively. Light is incident in the positive x direction at (o, o) and is split into two beams which are recombined by M_4, the output light being viewed in the x direction from (a, b). If each of these plates are accurately positioned and are parallel to one another then a uniform bright field will be viewed at the output. Slight deviations from parallelism by one or more of the mirrors will produce fringes with a $(\text{cosine})^2$ intensity distribution with orientation dependent upon the orientation of the mirrors. The analysis of the system (by normal geometrical means) when more than one mirror is misaligned becomes extremely confusing and involved. In order to reduce the algebra to a reasonable length a vector notation will be used.

Let the normals to the mirrors M_1, M_2, M_3, M_4 be $\bar{n}_1$, $\bar{n}_2$, $\bar{n}_3$ and $\bar{n}_4$ respectively. The vector representing the incident ray is denoted by $\bar{r}$ and the positional vector of the observation point by $\bar{x}_o$.

Then we find that for rotation of the mirrors M_3 and M_4 the path difference, Δ, is given by

$$\Delta = 2\bar{r}.A.\bar{x}_o \qquad - 8.1a$$

where A is a dyadic of the from

$$A = \bar{n}_3\,\bar{n}_3 - 2(\bar{n}_3.\bar{n}_4)\,\bar{n}_3\,\bar{n}_4 + \bar{n}_4\,\bar{n}_4 \qquad - 8.1b$$

This equation is derived in appendix IV.

The form of this dyadic shows us that the path difference is dependent only upon the directions of $\bar{n}_3$ and $\bar{n}_4$ and not on the direction of $\bar{n}_3 \times \bar{n}_4$. Thus the path difference will be constant along the direction $\bar{n}_3 \times \bar{n}_4$.

We may simplify this equation further if we say that the angle between $\bar{n}_3$ and $\bar{n}_4$ is α then we can write $\bar{n}_4$ as the sum of two vectors, one in the $\bar{n}_3$ direction and one, $\bar{s}$, in the $\bar{n}_3 \times (\bar{n}_4 \times \bar{n}_3)$ direction

$$\bar{n}_4 = -\bar{n}_3 \cos\alpha + \bar{s} \sin\alpha \qquad - 8.2$$

Substituting this into equation 8.1b we have

$$A = \{\bar{n}_3 \bar{n}_3 - 2\cos\alpha\, \bar{n}_3(-\bar{n}_3 \cos\alpha + \bar{s}\sin\alpha) - (\bar{n}_3\cos\alpha + \bar{s}\sin\alpha)(\bar{n}_3\cos\alpha + \bar{s}\sin\alpha)\}$$

$$= \sin\alpha\,\{\bar{n}_3\bar{n}_3 \sin\alpha + \cos\alpha(\bar{n}_3\bar{s} - \bar{s}\bar{n}_3) + \bar{s}\bar{s}\sin\alpha\} \qquad 8.3$$

The resulting equation, obtained by substituting this into equation 8.1a, can be further simplified if we make use of the fact that variation in the direction $\bar{n}_3 \times \bar{n}_4$ has no effect upon the path difference, then we can say

$$\bar{x}_o = x\,(\bar{n}_3 \cos\beta + \bar{s}\sin\beta)$$

where x is a scalar

thus remembering that $\bar{n}_3.\bar{n}_3 = \bar{s}.\bar{s} = 1$ and $\bar{n}_3.\bar{s} = \bar{s}.\bar{n}_3 = 0$

$$\Delta = 2 x \sin\alpha \; \bar{r}.\,(\bar{n}_3 \sin(\alpha + \beta) - \bar{s}\cos(\alpha + \beta))$$

The fringe spacing w

$$w = x_n - x_{n-1}$$

is given when

$$\Delta_n - \Delta_{n-1} = \lambda$$

$$\text{thus } w = \frac{\lambda}{2 \sin\alpha \; \bar{r}.\bar{t}} \qquad - 8.5\text{ a}$$

$$\text{where } \bar{t} = \bar{n}_3 \sin(\alpha + \beta) - \bar{s}\cos(\alpha + \beta) \qquad -8.5\text{ b}$$

Normally one will either use the interferometer with horizontal or vertical fringes. These two cases will now be discussed further.

8.5 Vertical Fringes

Vertical fringes are referred to as fringes which are perpendicular to the plane of the centres of the interferometer mirrors or fringes which are produced when $\bar{n}_3 \times \bar{n}_4$ is vertical. In this condition we have that the plane of $\bar{t}$ will contain $\bar{r}$. Furthermore for minimum fringe width $|\bar{r}.\bar{t}| = 1$.

$$\text{and } w_{v\,min} = \frac{\lambda}{2 \sin\alpha} \qquad - 8.6$$

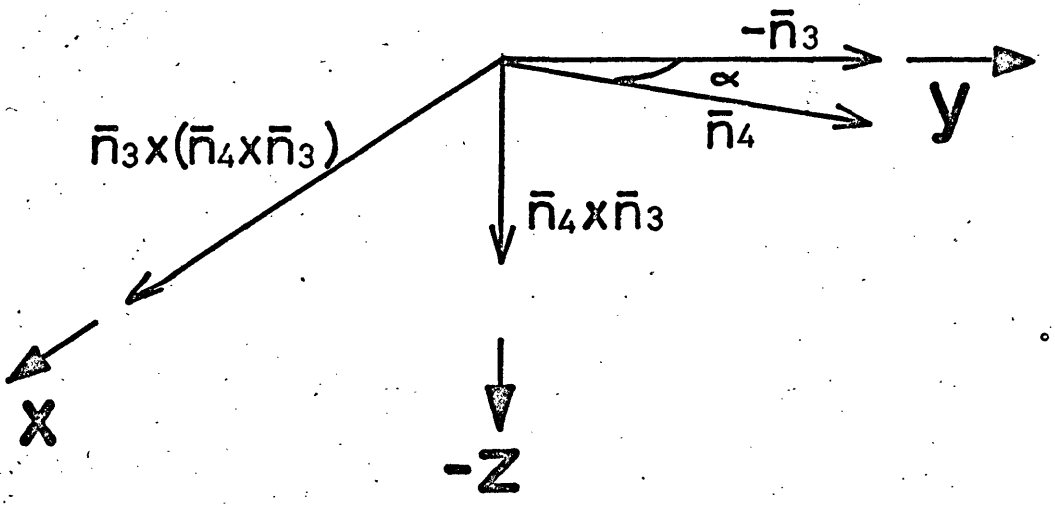

Fig 8.4 DIAGRAM SHOWING DIRECTIONS OF $\bar{n}_3$, $\bar{n}_4$ AND $\bar{s}$

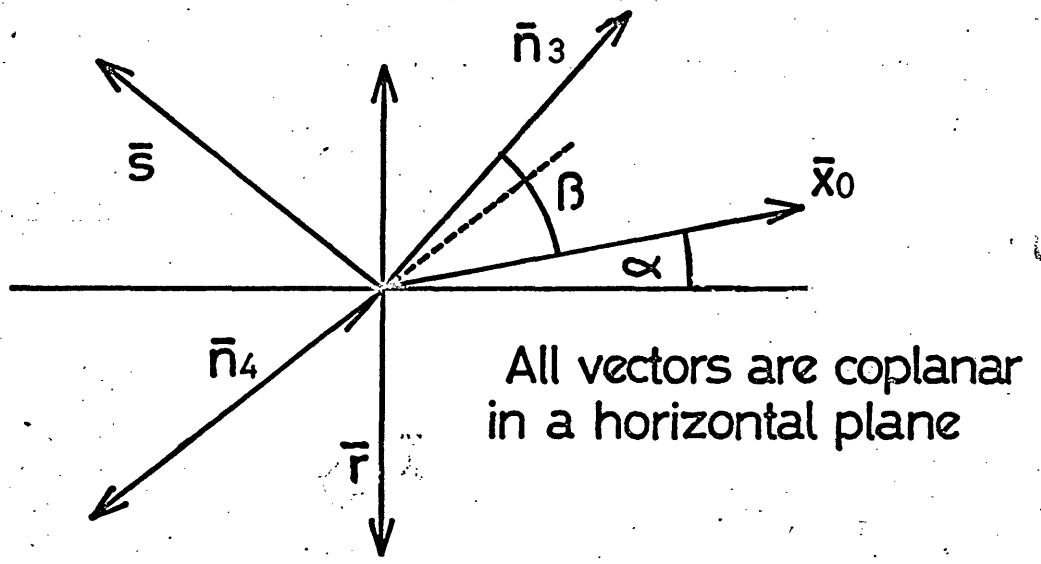

Fig 8.5 DIAGRAM SHOWING DIRECTION OF MINIMUM FRINGE WIDTH, $\bar{x}$, FOR VERTICAL FRINGES

For this condition to occur the plane of viewing must be inclined at an angle of β to $\bar{n}_3$ since $\bar{x}_o = x(\bar{n} \cos \beta + \bar{s} \sin \beta)$. However, $\bar{r}$ is the normal to a plane which makes an angle of $\alpha + \beta$ to $\bar{n}_3$ (see fig 8.5) and since α is small we can see that for perpendicular viewing the error in assuming that equation 8.6 holds is very small.

8.6 Horizontal Fringes

Horizontal Fringes occur when the vector $\bar{n}_3 \times \bar{n}_4$ is horizontal. Since now $\bar{n}_3$, $\bar{s}$ and $\bar{r}$ are not coplanar, the absolute value of the scalar product, $|\bar{r}.\bar{t}|$, must be less than unity, with the consequence that for a given value of α the fringe width, w, will always be greater than $w_{v\ min}$. Fig 8.6 shows a somewhat simplified case where it is assumed that $\bar{n}_4$ is in the plane of the centres of the interferometer and makes an angle Φ with the plane which has $\bar{r}$ as its normal. $\bar{n}_3$ is now coplanar with $\bar{n}_4$ and the vertical axis, and makes an angle α with the horizontal plane. The fringe width will now be a minimum when $\bar{t}$ is in the horizontal plane and makes an angle Φ with the $-\bar{r}$ direction, where the angle Φ is the angle of incidence of $\bar{r}$ on to the interferometer plates.

Hence $|\bar{r}.\bar{t}| = \cos \Phi$

and we have that

$$w_{h\ min} = \frac{\lambda}{2 \sin \alpha \cos \Phi} \qquad - 8.7$$

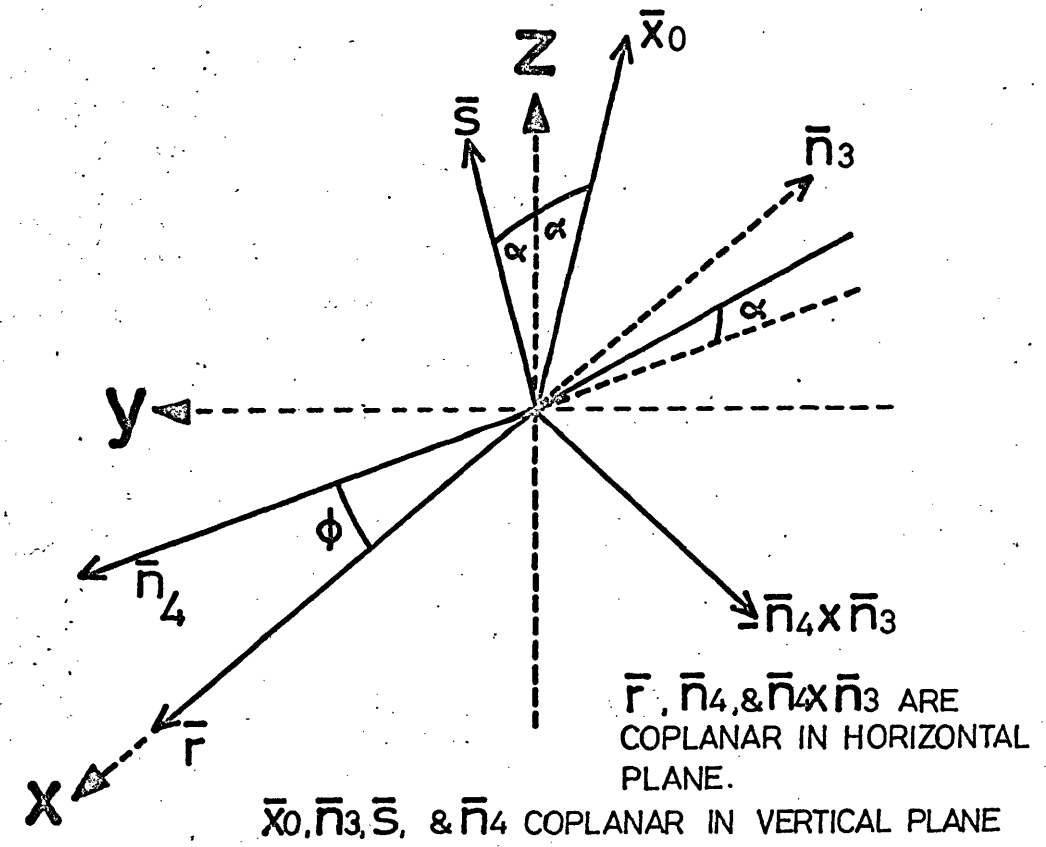

Fig 8.6 DIAGRAM SHEWING DIRECTION OF MINIMUM FRINGE WIDTH, $\bar{x}$, FOR HORIZONTAL FRINGES

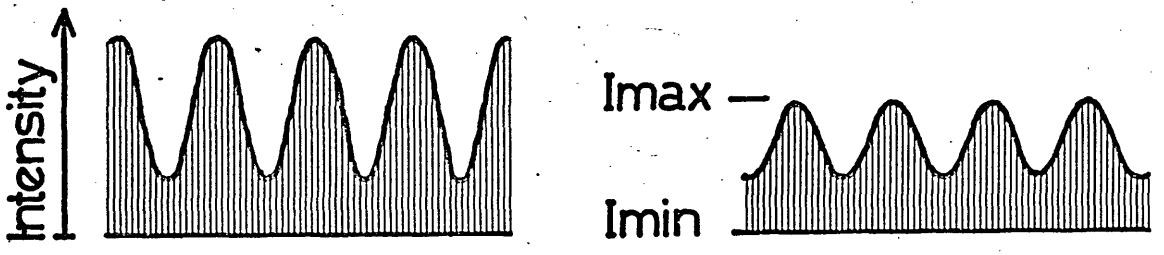

Fig 8.7 VISIBILITY OF FRINGES

$$\bar{t} = \bar{n}_3 \cos\alpha - \bar{s} \sin\alpha$$

therefore using equation 8.5 b we have

$$\beta = 90^\circ - 2\alpha$$

Thus the plane of viewing for minimum fringe width is the plane through $\bar{x}_o$ and $\bar{n}_4 \times \bar{n}_3$ where $\bar{x}_o$ is in the plane of $\bar{n}_3$ and $\bar{s}$ but orientated at angle α to the vertical towards $\bar{n}_3$. However since α is small there will be very little difference if a plane through the vertical and $\bar{n}_4 \times \bar{n}_3$ is chosen as the viewing plane.

8.7 Fringe Localisation

Since any practical source must have a finite size the fringes will become degraded as the viewing plane is moved further from the exit mirror of the interferometer. This degradation can be avoided using focussing optics since there is a plane of best focus. The position of the fringe localisation is dependent upon the orientation of the mirrors.

In the vertical fringe case, with only one mirror rotated, the plane of localisation will be a plane parallel to the plane of best viewing, (given in section 8.5) but passing through the axis of rotation of the rotated mirror. If two mirrors are rotated, the plane of localisation may lie anywhere before the final mirror. Reference to fig 8.8 shows that the distance of

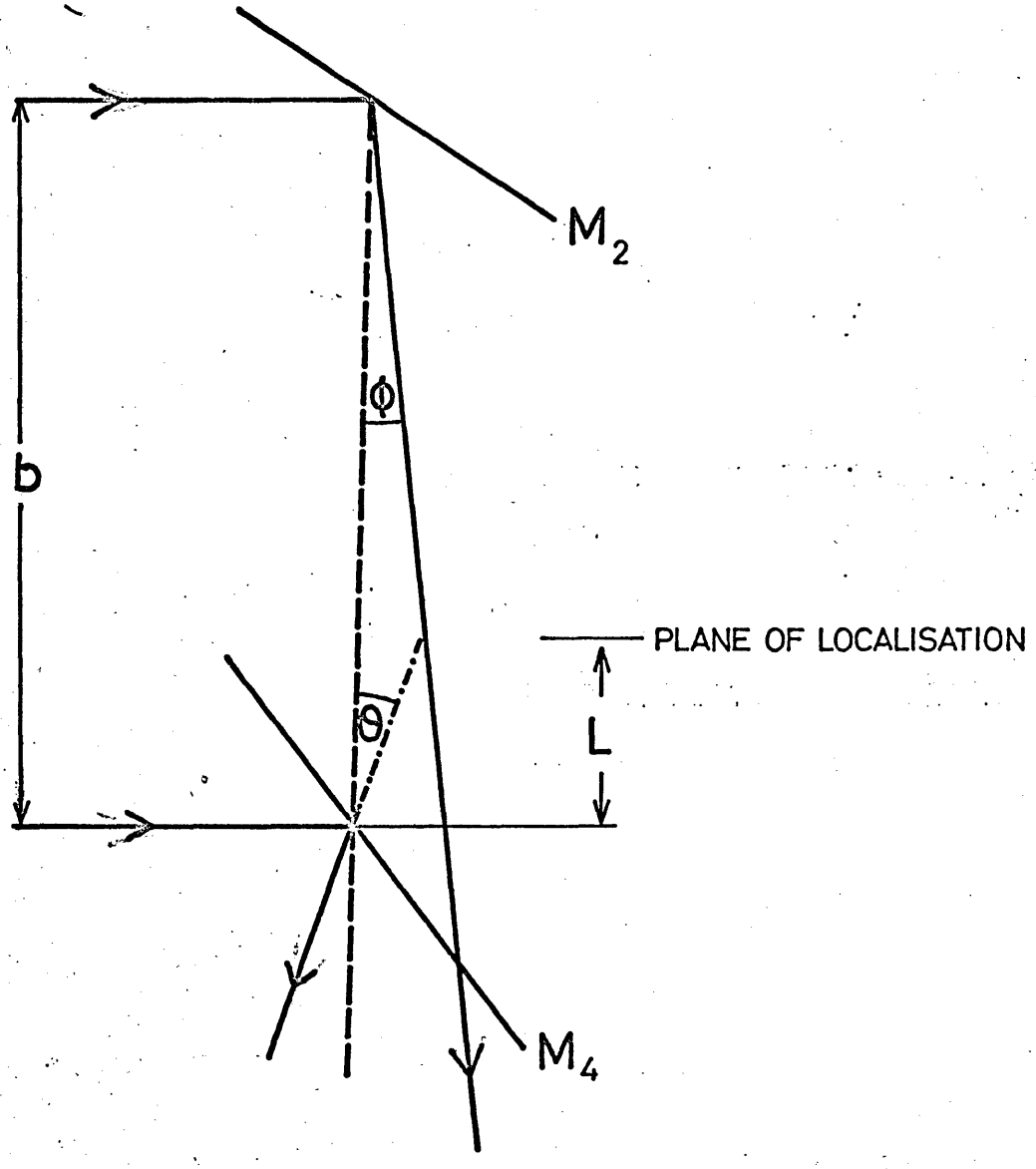

Fig 8.8 SHOWING PLANE OF LOCALISATION OF FRINGES

the fringes from the final mirror is, in the case where M_4 and either M_2 or M_3 are misaligned

$$L = b\left(1 + \frac{\sin \Theta \cos \Phi}{\sin (\Phi - \Theta)}\right) \qquad - 8.8$$

where a is the distance between the two mirrors $\Theta/2$ is the angle M_4 makes with its undisplaced position. $\Phi/2$ is the angle M_2 or M_3 make with their undisplaced positions.

If a third mirror is rotated then the position of localisation can occur beyond the last mirror. It will be noticed that the fringe localisation is dependent upon the absolute rotation of the mirrors whereas the fringe width is only dependent upon the difference in rotation. Thus it is possible to obtain any fringe width with the fringes localised in any planes by suitable adjustment of the mirrors.

8.8 Fringe Visibility.

No mention has yet been made of the visibility of fringes that will be viewed, although a high value of this quantity was assumed desirable in sections 8.5 and 8.6.

Under ideal situations, the fringes obtained will be of a $(\text{cosine})^2$ distribution with a maximum intensity equal to the intensity of the incident light. Imperfections will degrade

these fringes by decreasing the maximum intensity and effectively adding a constant intensity to the fringes. The degradation is best described by the visibility, V, given by

$$V = \frac{I_{max} - I_{min}}{I_{max} + I_{min}} \qquad - 8.9$$

Thus for perfect fringes, the visibility is unity and for no fringes the visibility is zero.

The overall visibility of fringes will be due to several effects, some of these associated with the source of light used with the interferometer and some associated with the interferometer itself. The visibility is dependent upon the source in two ways; firstly, because of its physical size and, secondly, because of its spectral distribution.

Bennett (1951) has shown that for vertical fringes the source should be a circle with radius ρ given by

$$\rho = \tan \Phi_L \qquad - 8.10$$

where f is the focal length of the collimating lens and Φ_L is given by

$$\cos \Phi_L = 1 - {}^{K}/_{N} \qquad - 8.11$$

where N are the number of fringes specified with a clarity defined

by K. Bennett does not directly relate K to the visibility but it can be shown that

$$V = \frac{\sin 2\pi K}{2\pi K} \qquad - 8.12$$

Thus if we specify a visibility of 0.8 then

$$K \sim \frac{1}{6}$$

The value of N will depend to some extent on the conditions to be measured but except on very rare occasions, no more than 100 fringes will be required. Thus

$$\Phi_L \sim \frac{1}{17}$$

or $\rho \sim f/_{17}$

In the present case the collimating lens has a focal length of 36 in, which gives

$$\rho \sim 5 \text{ cm}$$

Thus in order to obtain 100 fringes with a minimum visibility of 0.8, then the source size must not exceed a 10 cm diameter circle. Where a laser is used as a source this restriction is of little consequence since the output beam from a laser, even unfocussed, is unlikely to approach this diameter.

A similar relation can be obtained in the case of horizontal fringes although in this case the optimum source shape is not a circle but approximates to a line source whose actual shape and dimensions depend upon the interferometer angle.

The limitations of spectral purity of the source are also unrestrictive when one is dealing with lasers. Consider line profile given by a(w), the visibility of the fringes produced by this source is directly related to the fourier transform of it. This fact is usually used as a way of investigating the spectra of certain sources but in this case we are interested in the effect of the source on the fringes and not vice-versa.

The fourier transform of a(w) is f(x) given by

$$f(x) = \int_{-\infty}^{\infty} a(w)\, e^{-iwx}\, dw$$

If a(w) is taken to be dispersive

$$a(w) = A \frac{1}{1 + \left(\frac{w-w_o}{\gamma/2}\right)^2}$$

then it can be shown that (Ditchburn 1952)

$$f(x) = B\, e^{-\gamma x/2} \cos w_o x$$

where $B = \gamma \sqrt{2\pi A}$

Thus when $w_o = 5 \times 10^{14}$ sec^{-1} ($\lambda = 6000$ Å) and in order to obtain 100 fringes with a minimum visibility of 0.8 we find that

$$\gamma/2 = \frac{\ln(1.25)}{2} \times 10^{13}$$

or $\Delta\lambda \simeq 13$ Å

where $\Delta\lambda$ is the half-half width of the spectral line. This is far in excess of the laser line width (0.03 Å).

Throughout the analysis so far, we have considered that the interferometer consists of perfectly flat infinitely thin mirrors. This perfect situation is not attainable practically with a consequence that the interferometer will contribute some degradation of the fringes. The two main contributions to poor fringe visibility are unequal reflectivities of the mirrors and surface irregularities of the plates.

The contribution due to unequal reflectivities is not particularly restrictive in that with reasonable care the overall effective reflectivities of the two arms can be made very nearly equal. The visibility is given by

$$V = 1 - (R_a - R_b)$$

where $R_a = \sqrt{R_1 R_3}$

and $R_b = \sqrt{R_2 R_4}$

are the effective reflectivities of the two arms of the interferometer.

Unlike the reflectivities however, the flatness of the mirrors may become quite restrictive. Overall bow in the mirrors will produce a bending of the fringes but irregularities which are much smaller than the fringe width will result in a loss of visibility. Equation 8.12 can be used to determine the required tolerance on the mirrors. If the mirrors are flat to $K\lambda$ then the visibility due to this effect will be given by equation 8.12. Thus, for mirrors flat to $\lambda/10$, then

$$V \simeq 0.95$$

Therefore, although the visibility of the fringes can be reduced by many different effects, the only one which is likely to have any influence in the present experiment will be due to surface irregularities, but, providing the plates are flat to some small fraction of a wavelength, little difference will be noted in the visibility.

References

Beams, J.W. — Gas Dynamics and Combustion of High Speed Aerodynamics and Jet Propulsion. Physical Measurements Vol 1X, A2, Princetown Univ. Press, 1954.

Bennett, F.D. — J.A.P. 22, 2, 1951.

Ditchburn, R. W. — Light, Blackie, 1952.

Gabor, D. — Nature, 161, 777, 1948.

Jahoda et al. — J.A.P. 35, 2351-63, 1964.

Landenburg, Bershader — Gas Dynamics and Combustion of High Speed Aerodynamics and Jet Propulsion. Physical Measurements Vol IX, A3, Princetown Univ. Press, 1954.

Leipman, H.W. Puckett, A.E. Introduction to Aerodynamics of a Compressible Fluid, Wiley, 1947.

Leith, E. and Upatnieks, J. J. Opt. Soc. Am., 53, 1377, 1963.

Chapter 9

Measurement of Electron Densities

9.1 Introduction

The Mach-Zehnder interferometer is capable of measuring very small refractive index changes. These small variations in the refractive index can be used to determine certain plasma parameters, in particular the electron density. The first part of this chapter deals briefly with the dependence of the refractive index on these parameters and how these results are utilised in the case of the Mach-Zehnder. In common with most other branches of physics, there is only a limited range of validity, within the framework of the theory. This range of validity is discussed in some detail. The chapter continues with the experimental work carried out with the Mach-Zehnder followed by a discussion of the results obtained.

9.2 The Refractive Index of a Plasma.

The dielectric constant of a plasma can be obtained from the dispersion relation (Denisse and Delcroix, 1963). This is a very long equation but however, can be much simplified by some assumptions.

For a transverse wave propagating in a plasma with a longi-

tudinal magnetic field assuming that there is no attenuation i.e. the collision frequencies are all small then we find that there are two solutions for the dielectric constant

$$\varepsilon_1 = 1 - \frac{w_p^2}{(w + w_L)(w - \Omega_L)}$$

and

$$\varepsilon_{11} = 1 - \frac{w_p^2}{(w - w_L)(w + \Omega_L)}$$

where

$w_p = \frac{(4\pi n_e q_e^2 c^2)^{\frac{1}{2}}}{m_e}$ - plasma frequency

w - frequency of the radiation

$w_L = -\frac{q_e B}{m_e}$ - electron cyclotron frequency

$\Omega_L = \frac{q_i B}{m_i}$ - ion cyclotron frequency

If w corresponds to the optical region of the spectrum and B always has some reasonable value then

$$w >> w_L >> \Omega_L$$

and we find that the two values of the dielectric constant become the same

$$\varepsilon = 1 - \frac{w_p^2}{w^2} \qquad - 9.1$$

Physically this means that there is no coupling between the two rays and consequently there is no Faraday rotation.

Now since from Maxwells equations the refractive index, μ, is given by

$\mu = \sqrt{\mu^* \varepsilon}$ where μ^* is the permeability of the medium

If w_p/w is small compared to unity then we have

$$\mu = 1 - \tfrac{1}{2} \frac{w_p^2}{w^2} \qquad - 9.2$$

neglecting all higher powers in w_p/w.

In the Mach-Zehnder, where one arm has a constant refractive index and the other arm contains the plasma, we are only concerned with differences or changes in the refractive indices of the two arms. This can be expressed in the form of the path difference, Δ, which can be written

$$\Delta = \int_0^L (\mu(x,y,z,t) - \mu_o)\, ds \qquad - 9.3$$

where μ_o is either the initial refractive index or the refractive index in the other arm.

In order to obtain any quantitative measurements from any interferograms it is necessary to either assume symetry along at

least one axis, or assume some form to the relavent parameter. In this case, where we are considering a linear pinch viewed in the z - direction, we assume that μ is not a function of z. Thus we have

$$\Delta = (\mu(x,y,t) - \mu_o)L$$

Thus the phase difference δ will be given by

$$\delta = \frac{2\pi L}{\lambda} (\mu - \mu_o)$$

when $\delta = 2\pi$ then

$$(\mu - \mu_o) = \tfrac{1}{2} \frac{w_p^2}{w^2} = \frac{\lambda}{L}$$

or

$$n_e = \frac{2\pi}{L} \cdot \frac{m_e}{q_e^2} \cdot \frac{1}{\lambda} \qquad - 9.4$$

Thus when $\lambda = 6943 \times 10^{-8}$ cm and the inter electrode distance, L = 38 cm the electron density will be given by

$$n_e = N \times 0.855 \times 10^{16} \text{ electrons/cc} \qquad - 9.5$$

where N is the number of fringe shifts.

The minimum value of electron density, we will be able to measure, if we assume that the smallest measurable value of N is $\frac{1}{10}$, will therefore be less than 10^{15} electrons/cm^3. This

is adequate for most purposes encountered.

9.3 Other Contributions to the Refractive Index

In addition to the effect of free electrons on the refractive index there are four further contributions which should be taken into account, Griem (1964).

a) Contribution of heavy charged particles. This gives a similar relation to that obtained for the electron contribution but because of the very large mass of the ions, one may consider this negligible in comparision. For A II where $N_+ \simeq n_e$ then $\frac{(\mu - 1)e}{(\mu - 1)i} \sim 10^{-5}$

b) Contribution of bound electrons. When the probing wavelength has a greater energy than the energy of the bound electron below the ionisation limit, then this bound electron can be considered as free and able to contribute to the refractive index. For argon at 20,000°K and $n_e = 10^{17}$ cm^{-3} then the total error that will be measured in the electron density, due to both neutral and singly ionised components is given by

$$\frac{\Delta n_e}{n_e} \sim 2 \times 10^{-3}$$

Of these two components the contribution due to the neutral atoms is far greater than that due to the singly ionised species simply because of the difference in ionisation energies.

c) Contribution of line radiation coincident with the probing frequency. At the probing wavelength 6943 Å the only emission line which is likely to produce any effect whatsoever is the 6942 Å NII line, which will exist as an impurity within the plasma. This is not a particularly strong line however, and since nitrogen exists only in very small proportions its contribution to the electron refractive index is very small. For an impurity concentration of 1/100 and at 20,000°K and $n_e = 10^{17}$ cm^{-3}

$$\frac{(\mu-1)_{line}}{(\mu-1)_e} < \pm 10^{-4}$$

The sign taken depends upon which side of the line centre the probing frequency is on.

d) Contribution of line radiation non-coincident with the probing frequency. A fairly large contribution to the refractive index can be produced by resonance lines, despite their remoteness. This arises because of their very large ground state populations. Under conditions specified previously the total error due to resonance lines is

$$\frac{(\mu - 1)_{res}}{(\mu - 1)_e} = - 8.8 \times 10^{-3}$$

of which by far the greatest proportion is due to the first ionisation stage, simply because of its greater abundance.

The typical values are due to Wheeler (1965).

The total error from all these sources will thus be

$$\frac{\Delta n_e}{n_e} \sim 6 \times 10^{-3}$$

Thus under the conditions specified the total effect on the refractive index due to causes other than free electrons is somewhat less than 1%. Although this represents a systematic error it is small compared to the experimental error of ~5% discussed in section 9.6.

9.4 Error in the Electron Density Measurement Due to Refraction of the Probing Ray

Whereas the errors mentioned in section 9.3 do not directly introduce any limit to the electron densities that can be measured, the deviation of the probing ray, by large refractive index gradients, does.

This error may be derived using the equation derived in chapter 8 for the deviation of ray of light in a refractive index gradient. If we assume that the ray is normal to the direction of the gradient and that the gradient is constant along a path length ℓ, then we have that the angular deviation is given by

$$\theta = \frac{\ell}{\mu} \frac{d\mu}{dy}$$

where y is the direction orthogonal to the probing ray.

If the angle Θ is small then the ray after leaving the plasma can be considered to have diverged from a point half way in the plasma. Fig 9.1 shows the deviated ray and its resultant wave front.

If the distance of the viewing plane to the centre of the disturbance is L then the shift in the fringe position, represented by CB is given by

$$CB = \frac{BD.\sin\Theta}{\sin(\alpha+\Theta)}$$

but since both Θ and α are small, and in order that this fringe shift must be small, then

$$\Theta < \alpha$$

consequently

$$s = CB = \frac{BD\,\Theta}{\alpha}$$

$$= \frac{L\Theta.\Theta}{2\alpha}$$

$$= \frac{\ell^2.\,L.\mu'^2}{2\mu^2\alpha}$$

where μ' is taken as the derivative of the refractive index.

Now since $\mu \simeq 1$ and the unshifted fringe width is given

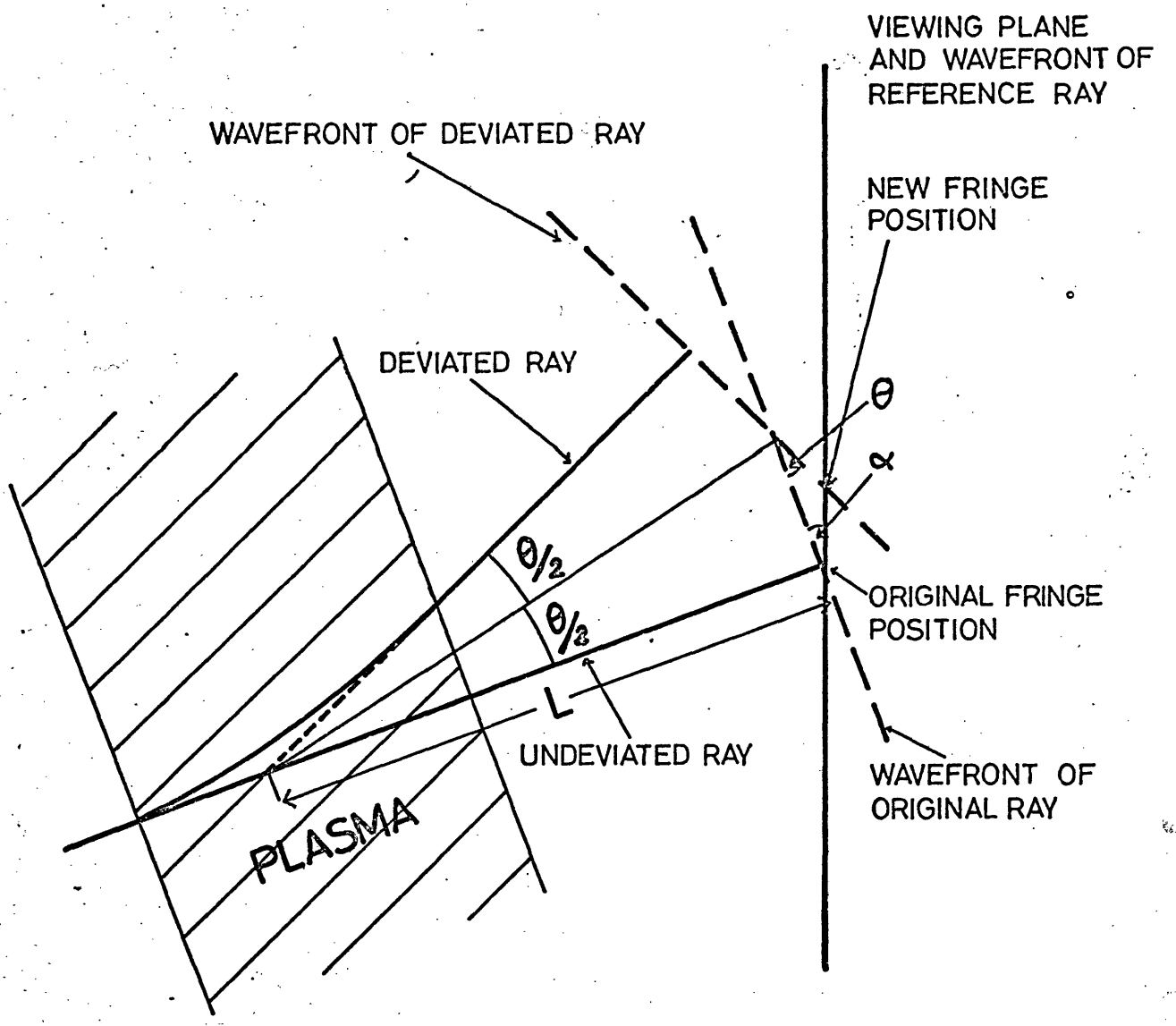

Fig 9.1 TO SHOW THE EFFECT ON FRINGE POSITION OF LARGE REFRACTIVE INDEX GRADIENTS

by w, where

$$w = \frac{\lambda}{2\alpha}$$

then

$$\frac{s}{w} = \frac{\mu'^2 \ell^2 L}{\lambda} \qquad - 9.6$$

Thus the criterion that the shift due to the deviation of the ray should be negligible is that

$$\frac{\mu'^2 \ell^2 L}{\lambda} < 1$$

For $\ell = 38$ and $L = 100$, we find that 10 fringe shifts/cm is the maximum allowed without violation of this condition. Thus under some conditions, this requirement is clearly not fulfilled, and a correction must be made to the number of fringe shifts by an amount indicated by equation 9.6.

9.5 The Construction of the Apparatus

Many Mach-Zehnder interferometers that have been constructed have been relatively sophisticated, in some cases involving complex mechanisms for varying the spacing and the orientation of the mirrors. In the present instant however, because the interferometer is to be used with a laser, much less stringent requirements are necessary, with a subsequent simplification in design. This simplification in design arises because of the long coherence length of the radiation emitted by the laser,

allowing interference fringes to be obtained with much larger path differences than was hitherto possible. It was decided therefore that it was quite adequate if the mirrors could be positioned to within a few millimetres, and consequently each mirror support was made separate and all four were supported on a rigid TT structure around the plasma discharge tube.

Fig 9.2 and 9.3 show the interferometer in position around the discharge tube, the mirrors labelled M_1 - M_4 corresponding to the notation used in chapter 8. Thus M_1 and M_4 are beam splitters and M_2 and M_3 are fully reflecting mirrors. The mirror mounts were designed to facilitate rough alignment when the interferometer angle is 45°. This in no way prevents the use with other interferometer angles; the TT form of the support allowing the interferometer angle to be reduced to 20°. For reasons of cost and convenience the TT form support arrangement was constructed out of heavy gauge steel channel which was machined flat to within about 0.001" along the top face and one side. The small side arms were machined flat along the top and at one end to allow for a good fit to the main piece; they being bolted rigidly in position.

Because of the resilience of the steel channel, vibrations were readily transmitted to the interferometer plates resulting in the rapid movement of the fringes. This problem was overcome

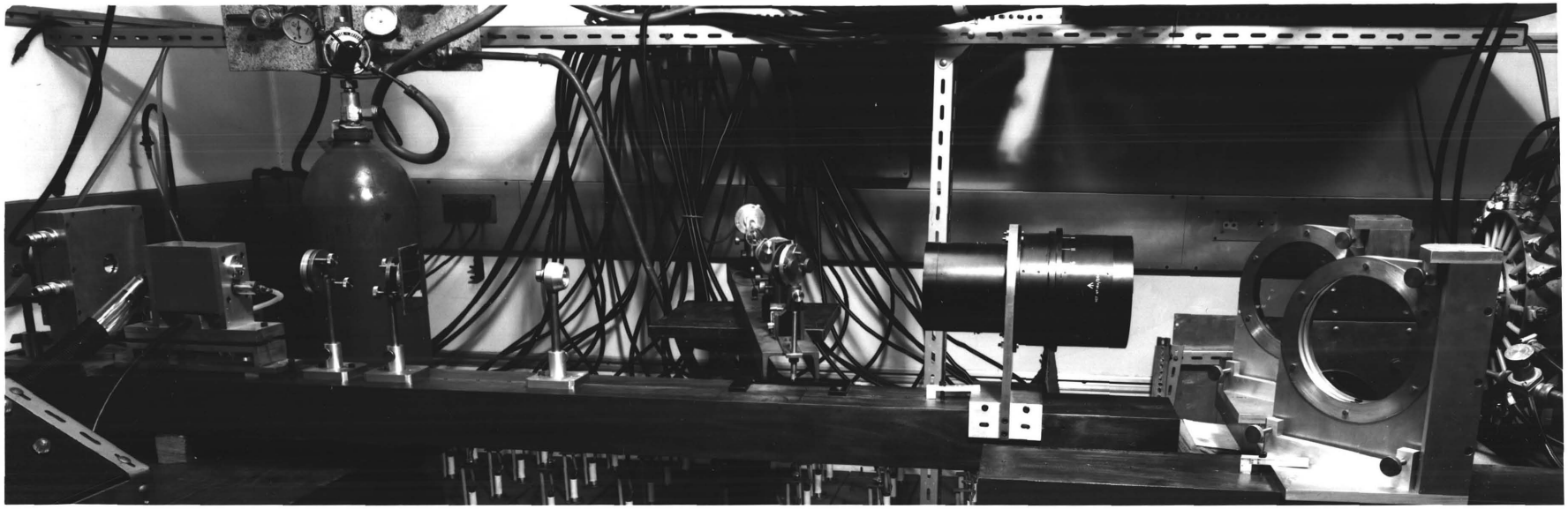

Fig 9.2 Two Views of the Apparatus

Fig 9.3

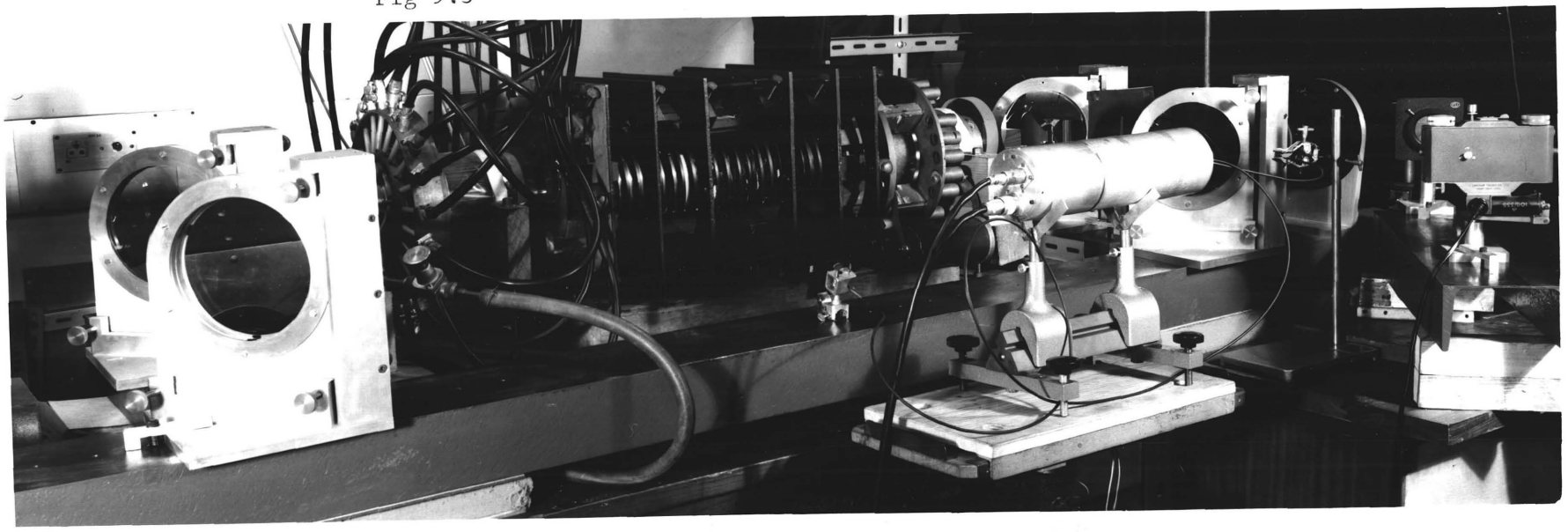

by supporting the whole assembly on anti-vibration mountings, which consisted of small sheets of polyurathene foam, sandwiched between two pieces of hardboard. This method proved very successful, since it reduced the fringe movement to an undetectable level. The medium and long term stability of this arrangement was tested using a He-Ne laser to produce fringes. These were then photographed with various exposure times. The results from this were very encouraging; the slight degradation in the fringes after several minutes exposure, being easily explainable by the instability of the laser.

Fig 9.4 shows a diagram of the system with the ruby laser and associated optics. The ruby laser, microscope lens and collimating lens are mounted on another steel channel which is not supported on anti-vibration mounts. The large telescope lens for focussing the light after passage through the interferometer is mounted on the TT section of the interferometer as is a fully aluminised mirror which deflects the light through approximately 135° to be collected by the lens of a 35 mm camera. The position of the camera and telexcope lenses are arranged such that in focus fringes of a reasonable size are obtained on the film.

The discharge tube was modified to allow viewing over nearly the whole section of the tube. In the original electrodes, a thin

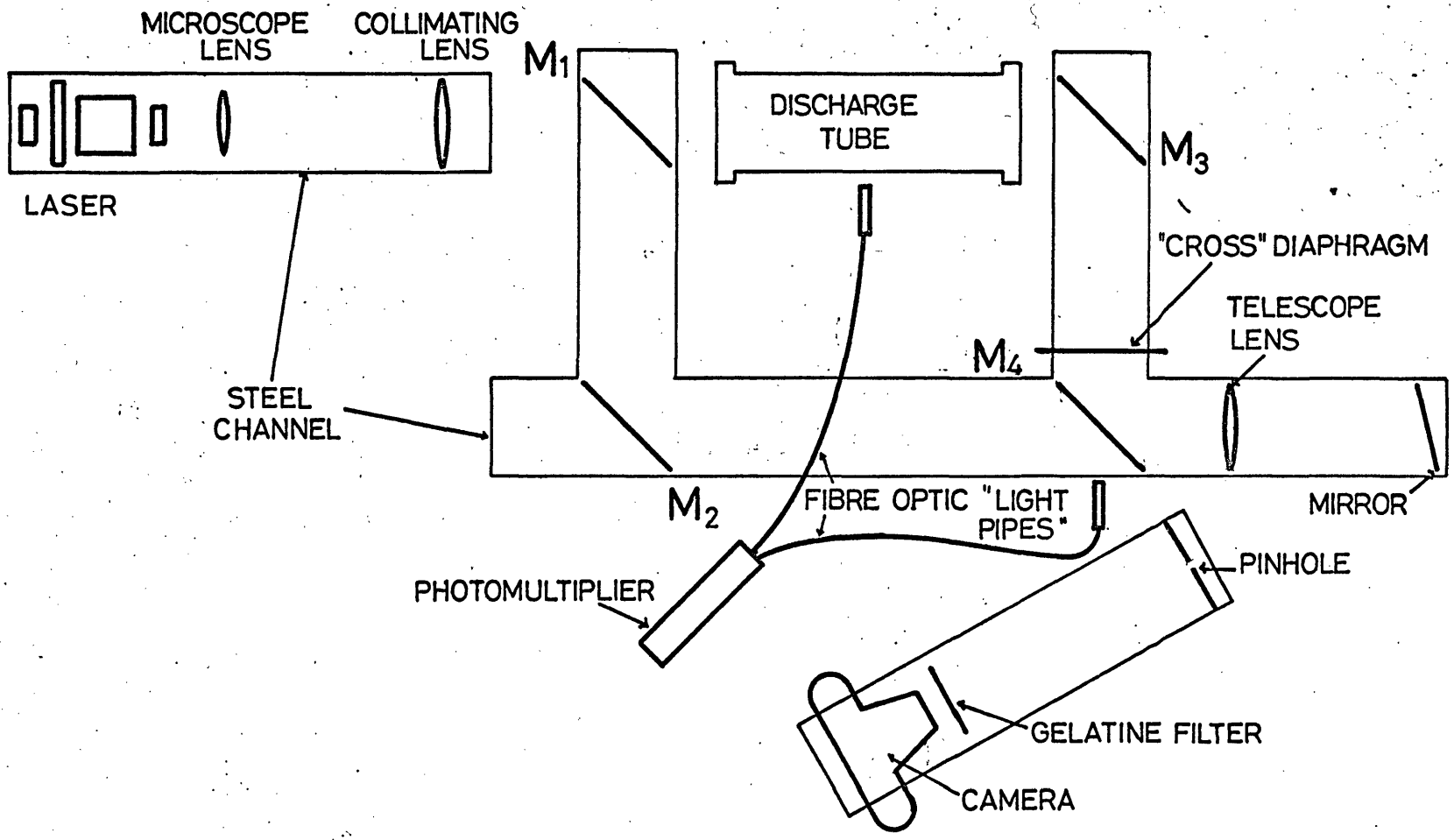

Fig 9.4 SCHEMATIC DIAGRAM OF INTERFEROMETER SYSTEM

cross was cut in order to limit the effects of eddy currents produced by the stabilising magnetic field. The electrodes were reconstructed so that the thickness of the cross was increased to approximately 1/4" thus allowing at least two fringes to be viewed across the tube with reasonable ease. The electrode segments were supported individually on brass bars which could be adjusted with the electrodes in position, upon removal of the end windows. This was a considerable improvement on the old electrode design which required that the electrodes be removed in order to adjust them. The end windows consisted of 1" thick 5" diameter optical glass polished to within $\lambda/4$. A sketch diagram of the new electrode assembly is shown in figure 9.5

Photographic emulsions which are sensitive to 6943 Å are unfortunately sensitive to a very much greater extent in the blue and green regions of the spectrum. Some safe guards were therefore necessary to prevent light which was emitted from the plasma (predominantly in the blue and violet parts of the visible spectrum) from reaching the photographic plate. This was achieved by two devices, one of which was a gelatine filter, Wratten 29. This strongly attenuates any radiation with a wavelength shorter that 6100 Å, and was placed directly in front of the camera lens where it was easily ensured that no light was reflected off the back of the filter in to the camera. The second procedure used

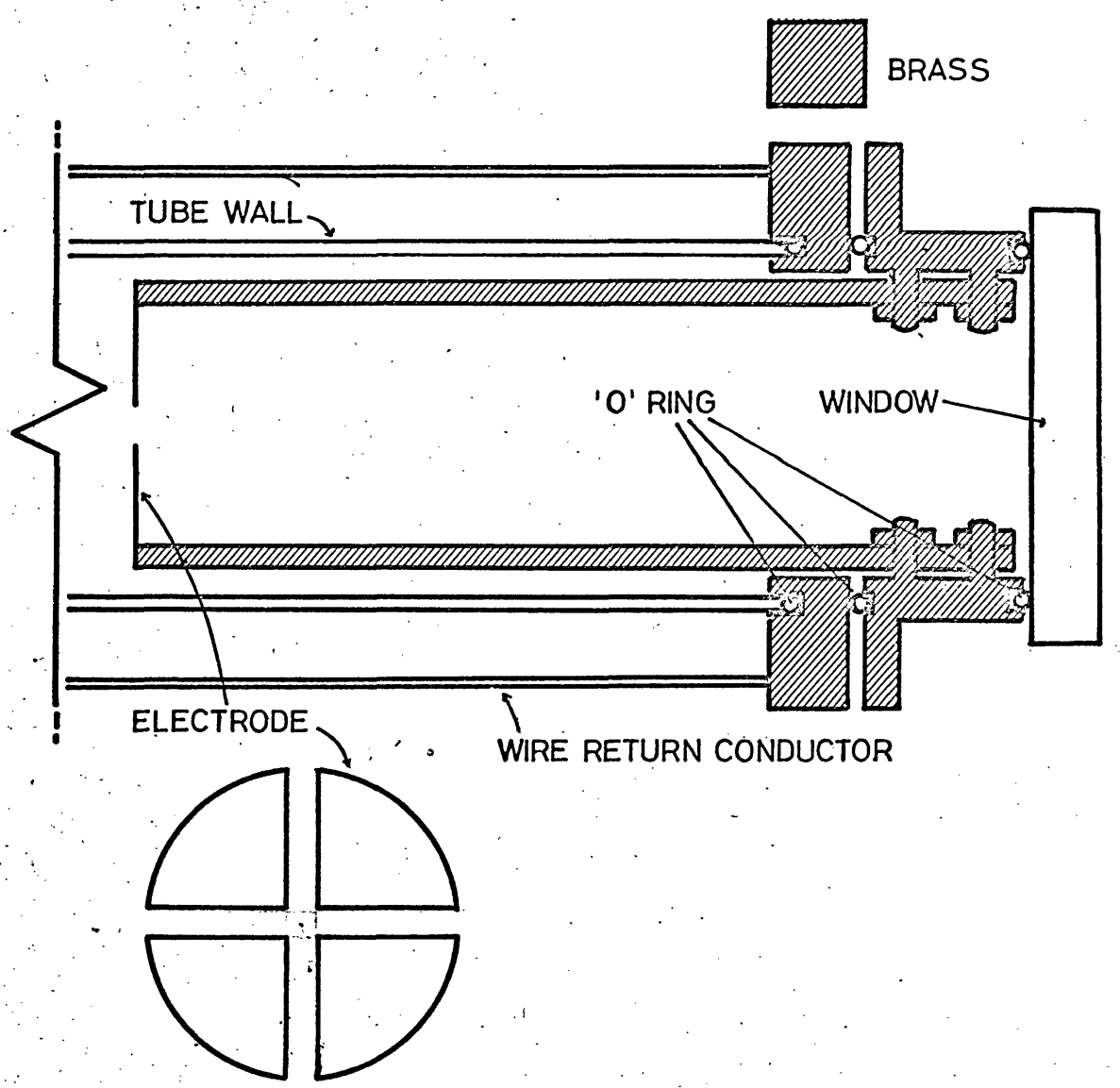

Fig 9.5 SECTION THROUGH ELECTRODE ASSEMBLY AT 45° TO THE VERTICAL

to reduce the plasma light consisted of a screen with a cross cut in it of the same dimensions as the cross in the electrodes. This was placed between mirrors M_3 and M_4 in the interferometer and carefully positioned to allow unobstructed passage of the laser beam. These two devices proved to be more than adequate and no 'fogging' of the film could be detected even at very high discharge intensities. The electronics associated with this apparatus were unfortunately more complex than the system described briefly in the introduction. Fig 9.6 shows a block diagram of the modified system. Because of the large time constant of the ruby laser flash tube circuit it was necessary to trigger the magnetic field approximately 1msec after the initiation of the flash tube current. Breakdown in the flash tube was achieved by overvolting to approximately 12 Kv. This method of triggering, although very simple, suffers seriously from time jitter, and consequently it is necessary, in order to attain a consistent performance, to trigger the rest of the electronics from the rise of the current through the flash tube. This was conveniently done by passing the cable through a ferrite ring on which is wound a few turns of wire. The wire forms the secondary of a transformer and the output across its ends is sufficient to trigger the next stage in the electronics.

The capacitor bank supplying power to the ruby laser consisted

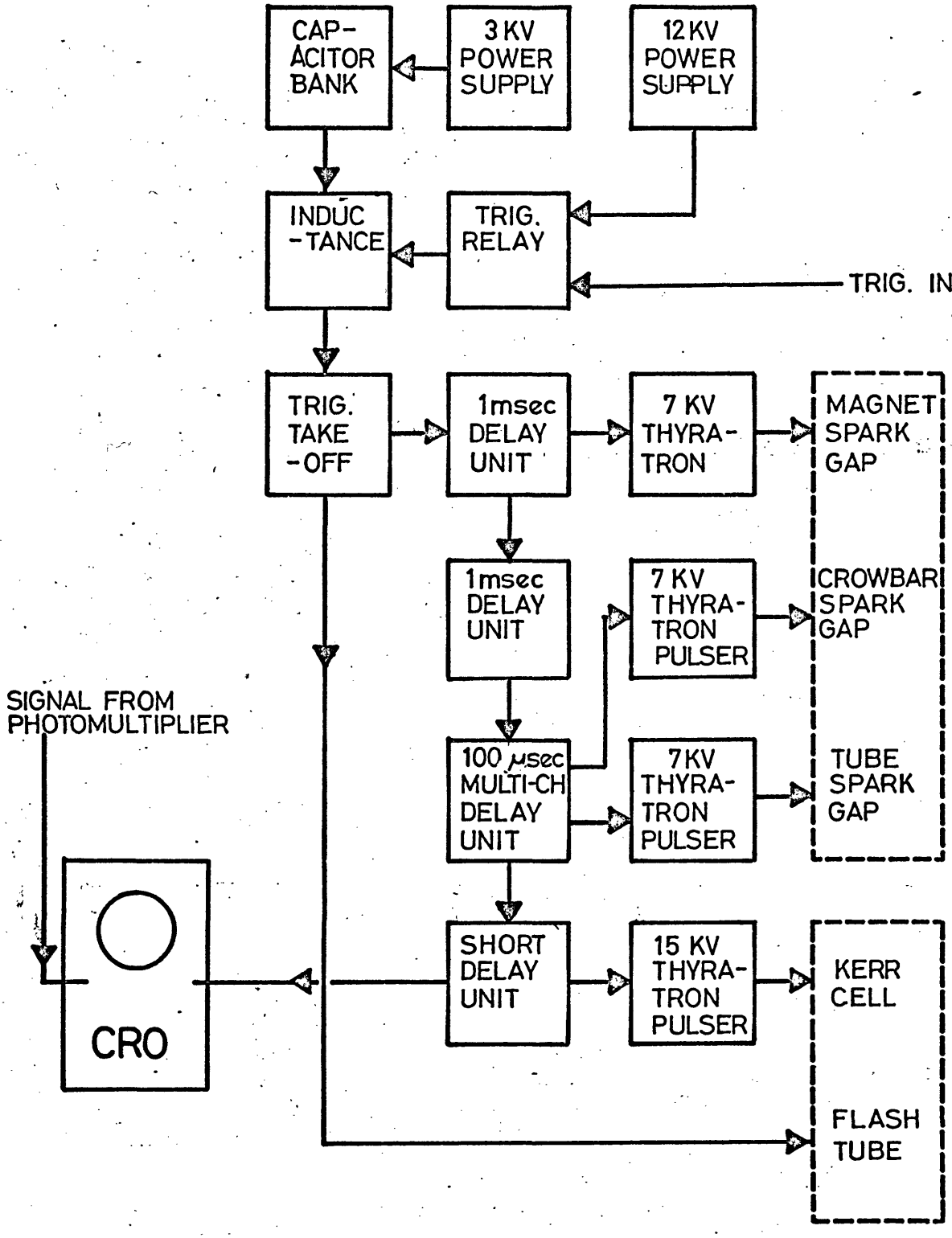

Fig 9.6 BLOCK DIAGRAM OF ELECTRONICS

of 14, 27μF capacitors which were capable of being charged up to 5 Kv although the available power supply would only deliver 3 Kv. This gave a stored energy of 1.7 Kilo-joules of which about half was dissipated in the cables and the inductance. Thus roughly 900 joules could be supplied to the flash tube. The inductance consisted of 90 turns of 10 s.w.g. insulated copper wire, wound on a 'tufnol' tube former of approximately 8 in. diameter giving an inductance of 520μH.

9.6 Alignment and Operation of the System

It has been mentioned already that because the interferometer is to be used with a laser, fringes can be obtained with large path differences between the arms of the interferometer. It is therefore not necessary to go to great lengths to obtain white light fringes, where the path differences must be small, when not noticeably worse fringes may be obtained by measuring the distance between the mirrors with a ruler! Alignment is further simplified using a He-Ne laser. In order to facilitate the alignment of the system, two screens were constructed which could be located accurately with respect to the machined faces of the channels. A small hole is punched in each screen in such a position that the beam from the laser, when passing through both holes, is parallel to, and in the same vertical plane as in the steel channel. The He-Ne laser beam was first aligned with the channel

holding the ruby laser and arranged to be incident on the centre of the mirror M_1 at the required angle. (see fig 9.7). The screens were then replaced behind the interferometer and the other mirrors adjusted until both parts of the beam pass through both pin holes. This rough alignment is sufficient to be able to detect fringes if the beam is spread out to fill the whole of the aperture. However, before this is done it is necessary to align the ruby laser mirrors, firstly with themselves and secondly with the interferometer. In order to do this the screens are moved back on to the channel holding the ruby laser and by means of mirrors the beam is shone through the pinholes in the opposite direction to that previous. The reflections from the ruby laser mirrors are then used to align them. Finally it is necessary to position the microscope lens accurately, this is done by shining the He-Ne laser beam through the pinholes in the original direction and then adjusting the position of the microscope lens.

Initially it was found necessary to use an auto collimator to make final adjustments in the orientation of the ruby laser mirrors. However, practice at alignment with the He-Ne laser very quickly made this unecessary. Final adjustments to the interferometer mirrors were made by observation of the fringes produced.

The Kerr cell thyratron unit was designed to produce an

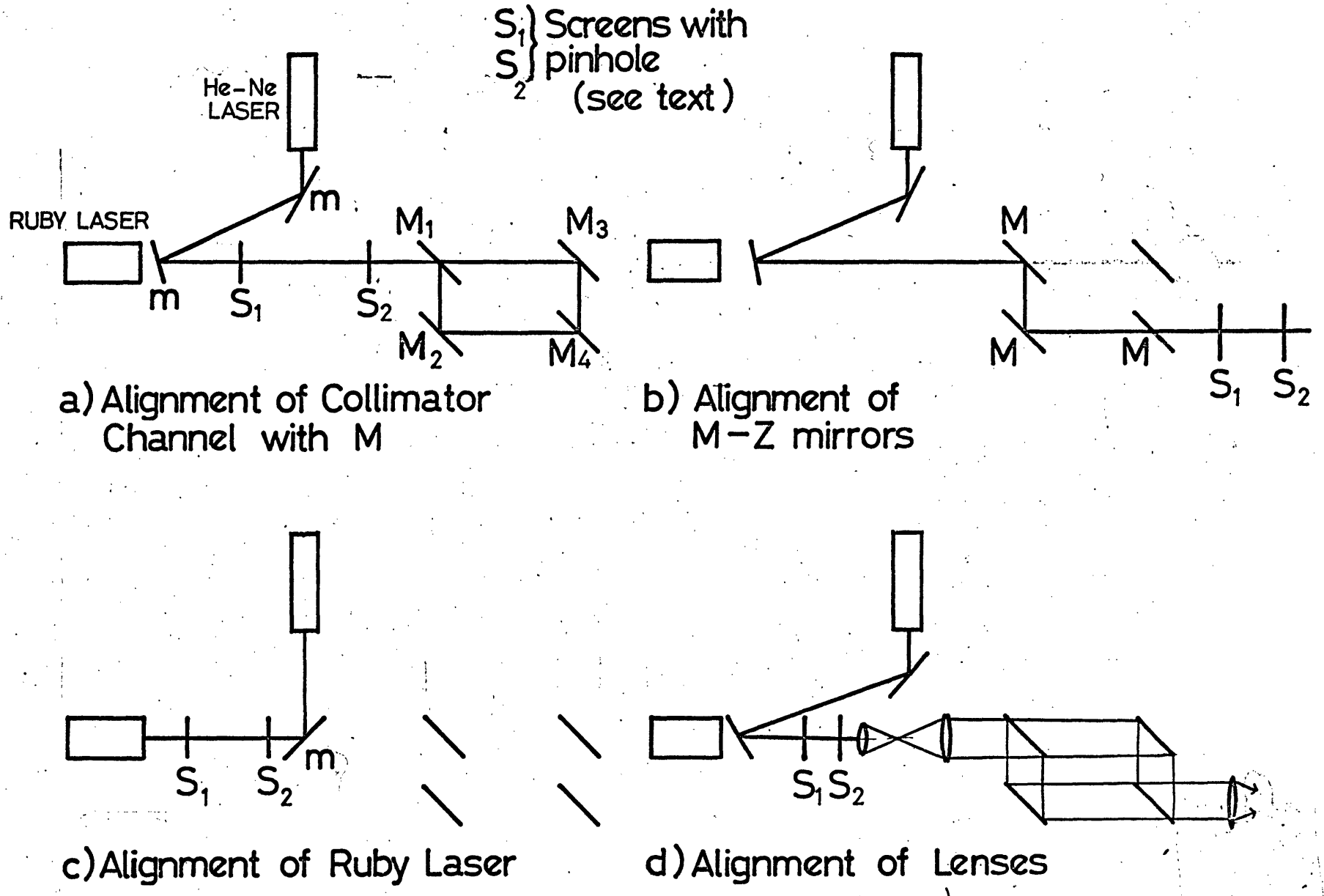

Fig 9.7 ALIGNMENT PROCEDURE (SCHEMATIC)

output marker pulse, which was originally used to detect the position of the laser pulse in respect to the discharge. This procedure was found unsatisfactory because of the uncertainty as to whether the ruby pulse actually occurred at that time or not. It was decided, therefore, in order to overcome this uncertainty and to elliminate any timing errors in the oscilloscope, that one photomultiplier would be used to view both the light output from the plasma and the light output from the laser. This was done conveniently using two fibre optic bundles, each of which were terminated by tubes to reduce the angle of acceptance and hence increase the discrimination. Suitable filters were placed in front of these bundles, the values and types of which were determined experimentally.

9.7 Results Obtained with the Interferometer

It was mentioned in chapter 4 that the characteristics of the discharge are apt to change with time, this change being particularly dependent on the quality and age of tube walls. Although the tube walls had not been altered since the last magnetic field measurements were taken, the electrodes had. It was therefore necessary to determine whether or not the changes in the electrode structure have any effect on the discharge characteristics. To this end measurement of the axial light output was made during the same discharge as the

interferogram was taken. The axial light output thus corresponds to the sum signal of the Zeeman instrument and in much the same way, the general form was consistent from shot to shot, although the plasma was not exactly reproducible. In order to facilitate correlation with the calculations given in chapter 10 the waveform of the discharge current was monitored simultaneously with the light output. Fig 9.8 shows two interferograms taken, at different times during the discharge. Results were taken to cover a wide range of conditions.

Pressure .15 to .35 torr

Magnetic field nominally 5 K gauss and 10 K gauss

Tube volts 1 Kv to 3 K volts

To display the results of all of these conditions fully would require far too much space. Consequently, the results taken under 4 different conditions are shown in graphical form in figs 9.9 to 9.12. These conditions were selected because they are fairly representative and indicate the trends which were noticed.

Firstly in almost all cases the first appearance of n_e is at the walls of the discharge tube. This might be expected since most descriptions of a pinched discharge make this preliminary hypothesis. The case where this does not appear to be so

Before the Pinch

Tube Volts = 3KV

Mag. field Volts = 2 KV

Pressure = .35 torr

At the Pinch

Fig 9.8 Interferograms of the Plasma

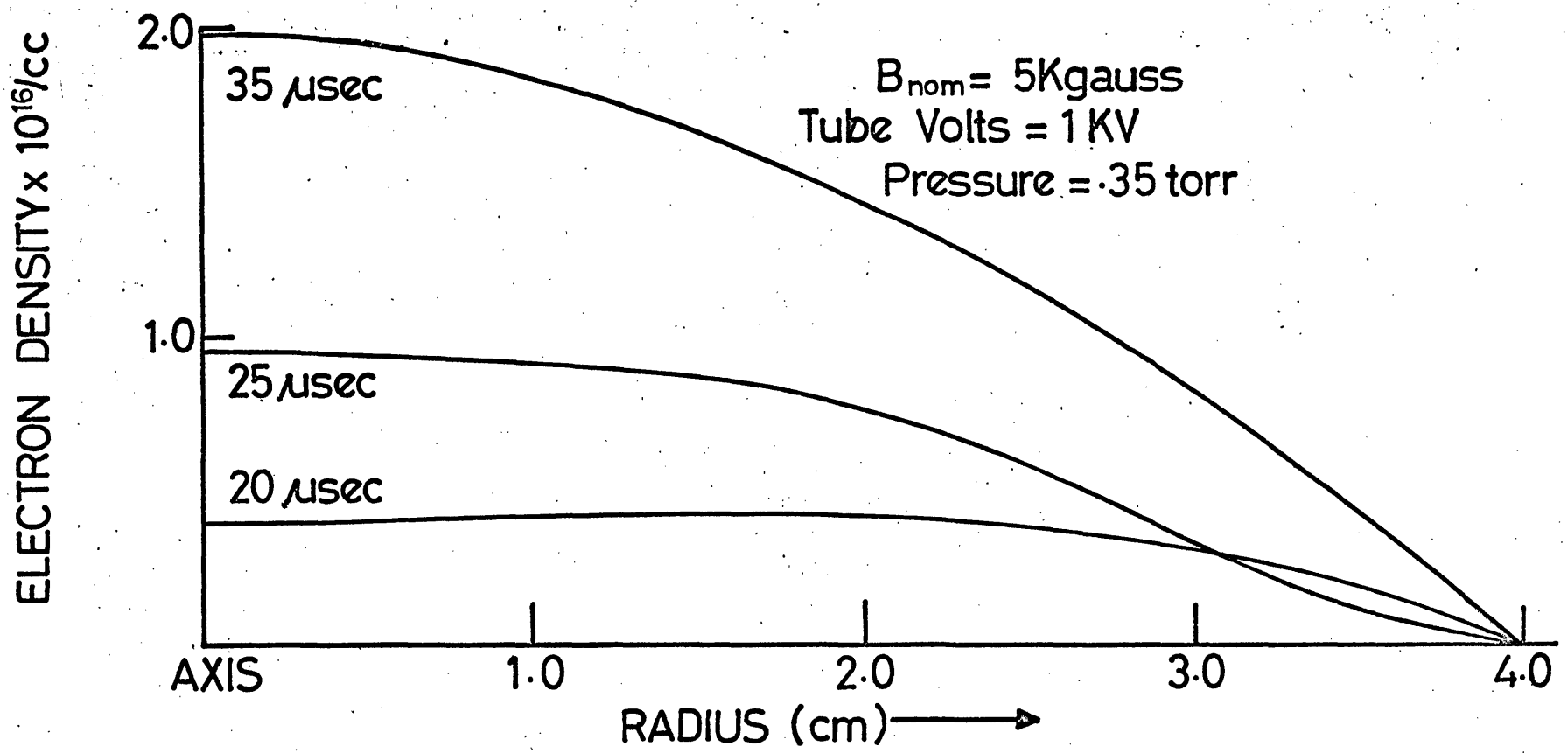

Fig 9.9 SPATIAL VARIATIONS OF ELECTRON DENSITY AT VARIOUS TIMES DURING THE DISCHARGE

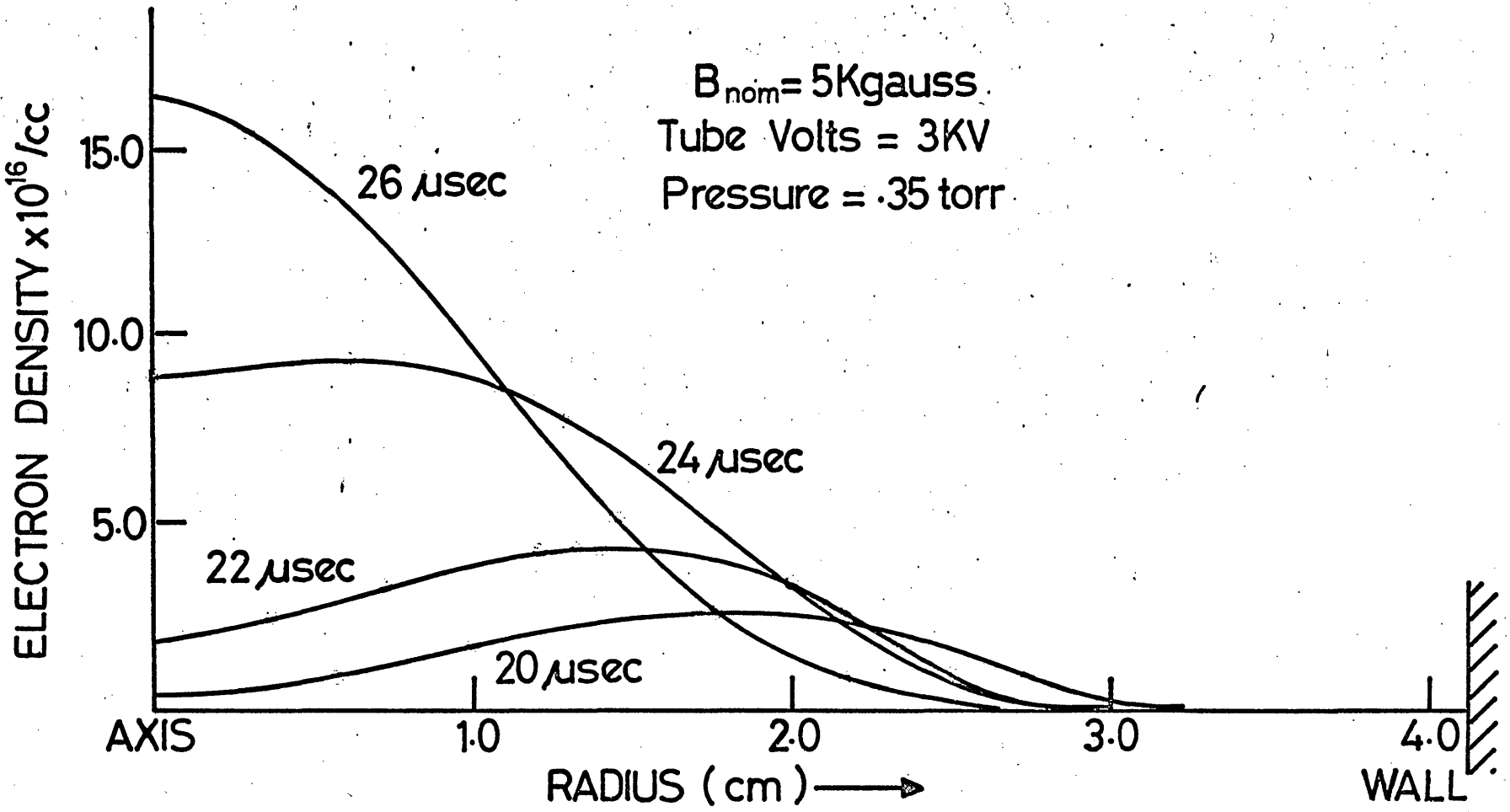

Fig 9.10 SPATIAL VARIATIONS OF ELECTRON DENSITY AT VARIOUS TIMES DURING THE DISCHARGE

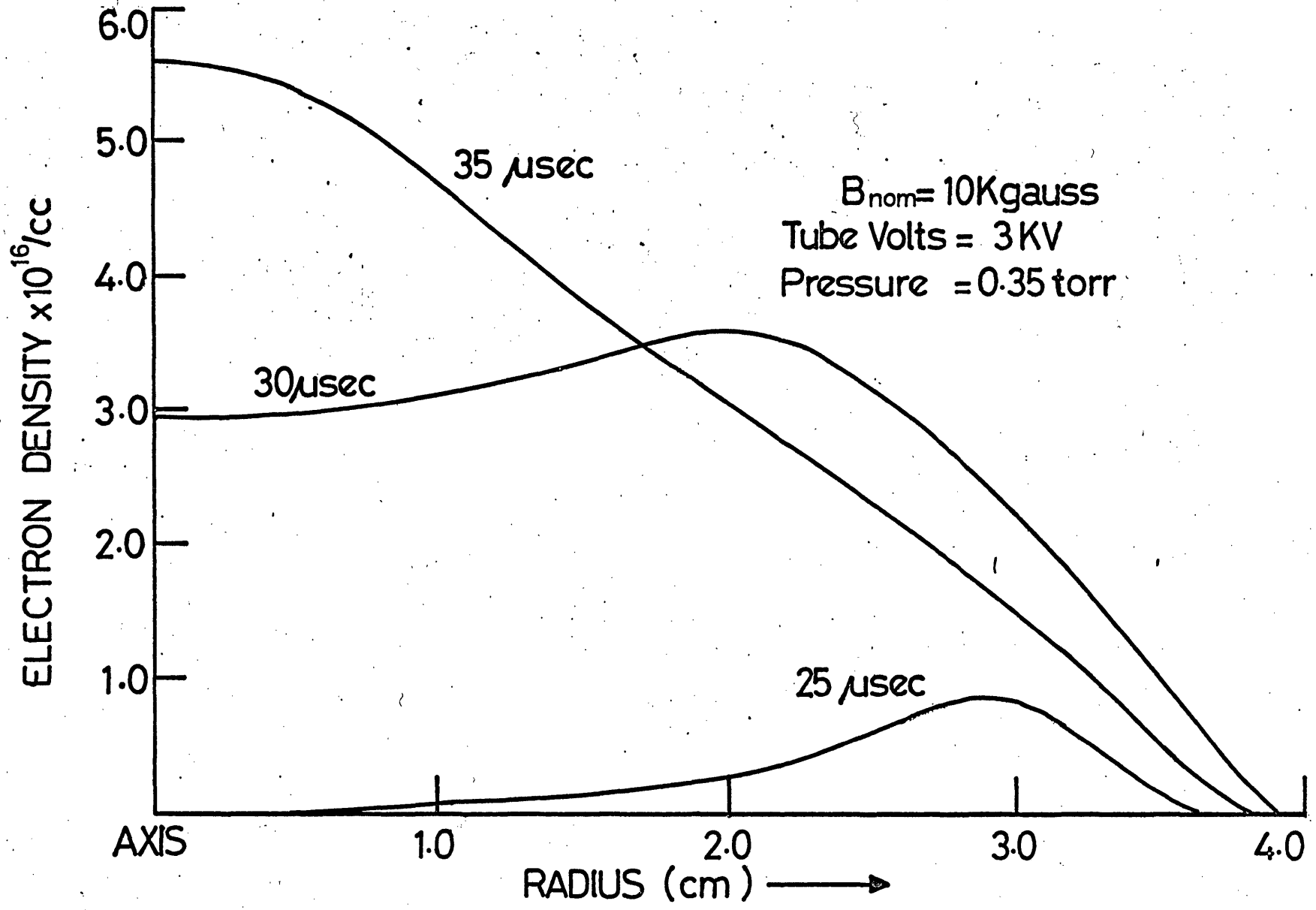

Fig 9.11 SPATIAL VARIATION OF ELECTRON DENSITY AT VARIOUS TIMES

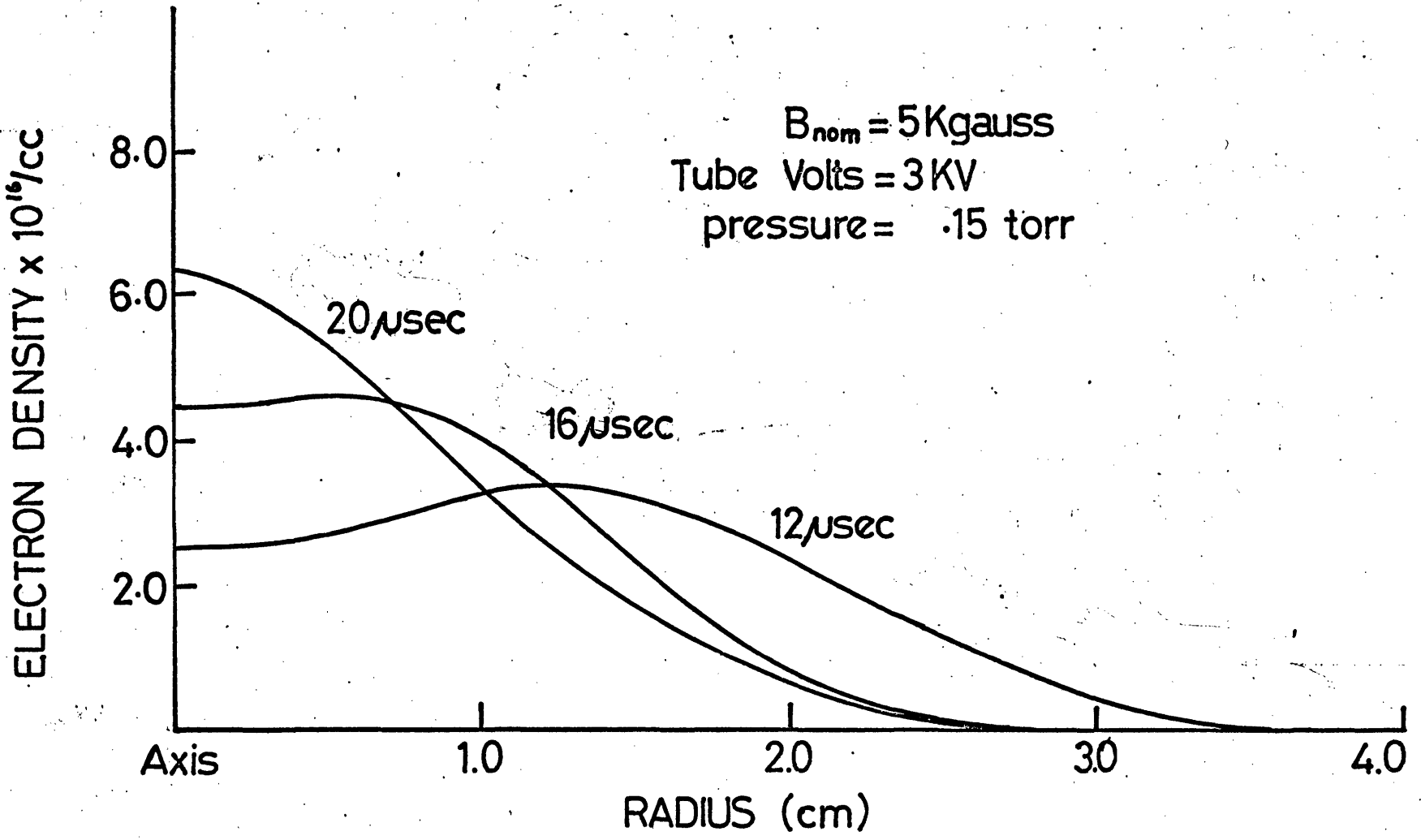

Fig 9.12 SPATIAL VARIATION OF ELECTRON DENSITY AT VARIOUS TIMES

is the extreme case; magnetic field nominally 5 KG

tube voltage 1 Kv

Pressure .35 torr

From the graphs, the electron density appears reasonably uniformly over the tube, but falling off towards the tube walls. The density then rises all over the tube but to a greater extent near the centre. This results in a very flat topped distribution in n_e which seems similar to what one might expect in a glow discharge. The transition from the collapsing shell type discharge to the glow discharge type is apparent in the intermediate conditions. Thus, although in all other conditions shown the maximum in n_e is first seen at the walls of the tube, it will be noticed that, physical movement of the shell towards the centre only occurs to a very limited extent as the pressure and magnetic field are increased. The condition

Pressure 350 μ

Magnetic field 10 KG nominal

Tube volts 3 Kv

illustrates this quite well, although the position of the peak value of n_e moves inwards, the actual value of the density remains roughly constant after the peak value has passed. A feature which the form of this discharge has in common with its unstabilised counterpart is that the time taken to pinch increases

at higher pressures. The time to pinch is also dependent on the values of the magnetic field and the discharge current, each affecting the speed of collapse as one would expect. A complete treatment of these effects is beyond the scope of what was intended for this work but the correlation of the results obtained, with the theory, is discussed later.

One effect which is not apparent in the unstabilised case, is the diameter of the half value of n_e, at the pinch, is virtually independent of pressure (see table 9.1). This indicates that the final diameter is not determined by the kinetic pressure of the plasma, as is the case with the unstabilised pinch, but largely determined by the magnetic pressure due to the trapping of the stabilising field. This fact is assumed in the next chapter when a simple model to describe the dynamics of the stabilised pinch is discussed.

Table 9.1

Conditions	Pressure μ of Hg	Peak Density x 10^{16} electrons/cm^3	Half width of pinched columb(cm)
B = 5Kgauss	150	6.4	1.10
Tube 3Kv	250	13.3	0.95
	350	16.3	1.10
B = 10Kgauss	150	3.0	1.85
Tube 3Kv	350	5.6	2.30
B = 5Kgauss	150	1.3	3.10
Tube 1Kv	250	1.8	2.95
	350	2.1	2.90

The discharge is more sensitive to changes in the voltage applied to the magnetic field condenser bank than in changes in the voltage to the discharge tube condenser bank although when $V_B/V_T \sim 1$ (V_B voltage applied to magnet bank and V_T voltage applied to discharge bank) the change in n_e produced by variations of either is not very great. This may be explained by considering the stability conditions for the plasma. Very crudely when $B_\Theta >> B_z$ the plasma is grossly unstable and large fluctuations in n_e can be expected for relatively small fluctuations in B and I. When $B_L >> B_\Theta$ the plasma is grossly stable and small variations of B_z and B_Θ have very little effect due to the near absence of any pinch. The conditions in this discharge are such that

$$B_{\Theta_{max}} < 0.6\ B_L$$

i.e. the discharges vary from a marginally stable to stable conditions. The fact that V_B has a greater effect than V_T can be explained by the fact that as the current tends to increase the pinch diameter would tend to decrease thereby increasing the inductance of the circuit. The increased inductance acts so as to oppose the increase in current. The current in the magnetic field windings is, however, very little affected by the conditions within the discharge.

9.8 Errors in the Results

Phenomena which are likely to cause any error in the results have been mentioned in previous sections but two further comments must be made regarding the results presented here.

Firstly because the plasma is not exactly reproducible care must be taken from inferring too much from the sequence of interferograms. A particularly severe case of this is shown in the condition

pressure 350 μ

magnetic field 10 K gauss nominal

tube volts 3 Kv

If one considers a point ½" from the tube walls, then the variation of n_e with time would require that the plasma be capable of carrying out some unusual contortions. What is more likely is that the discharges producing the three interferograms are more different than would be supposed from the light output traces.

Secondly, a difficulty arises when $V_B/V_T \sim 1$ and in the early stages of the discharge in that it is not possible, in all certainty, to say that at any particular point the density is zero. If this is not possible then, although the variation

in n_e may be correct, the position of the horizontal axis may be wrong. Where this doubt exists an estimate of the axis position is made by using the results that D. E. Roberts obtained with the He-Ne laser.

References

Denisse and Delcroix — Plasma Waves Interscience, 1963.

Griem, H. — Plasma Spectroscopy, McGraw-Hill, 1964.

Wheeler, C.B. and Dangor, A.E. — Imperial College Internal Report, 1964.

Roberts, D.E. — Thesis, University of London, 1967.

Chapter 10

A Simple Approach to the Mechanisms Involved in the Linear Pinch

10.1 Introduction

In this chapter an attempt has been made to explain some of the results presented in this thesis.

An exact analysis of the linear pinch is, of course, impractical and recourse must be taken to various simplified models. The four which are commonly employed are the snowplough, free particle, shock and adiabatic models. In the snowplough model, originally proposed by Rosenbluth (1954) and later discussed by several authors, e.g. Anderson *(1958), Nation (1960), it is assumed that when a particle is hit by a collapsing magnetic 'piston' the particle then travels along with the front. The free particle model, however, allows the particles to move freely in a radial direction. In order that this can be so, the mean free path of the particle must be large. In the linear pinch under discussion the densities are relatively large $\sim 10^{17}$ electrons/cc and the mean free paths correspondingly short. The free particle model is thus not a particularly apt description in the present case and will not be considered further. The shock model, however, is a compromise between the free particle and the snowplough

* This paper contains many references

models. In the shock model, a particle after coming into contact with the magnetic piston is allowed to move in a limited distance in front of the piston.

The adiabatic model for the pinch is not valid, as was pointed out by Nation (1960) because, in the initial stages of the discharge, shock waves will be produced with the consequent violation of the adiabatic criterion. We therefore only consider the shock model and the particular case of this, 'the snowplough model'.

The snowplough model would seem at first to represent an unrealistic situation since the front produced by the piston action would be of infinite density and zero temperature. This situation, however, does not seriously affect the predictions made by this model with regard to such quantities as the time taken to the first pinch (Anderson, 1958).

A very brief resume is given of the two models as applied to an unstabilised linear pinch. We then describe the modifications made to the snowplough model in order to include the effect of the stabilising field. The relatively unsatisfactory results obtained at high discharge currents are discussed. In an attempt to improve the results in these cases a further modification to the snowplough model is presented.

In conclusion, a discussion of the predictions of the original and modified models is presented together with a comparison with experimental results.

10.2 The Snowplough Model

The snowplough model was originally proposed by Rosenbluth (1954) and has been discussed by various authors since.

Although the mathematics for this model has been carried out many times previously a short description will be attempted here by way of an introduction to the later work. The assumptions made are

a) The current flows in a thin shell which acts as a magnetic piston in compressing the gas.

b) When a gas atom is struck by the shell, it sticks to the shell and travels in with it.

c) The resistance of the shell is negligible

A corollary of b) is that the kinetic pressure of the plasma is neglected.

The equation of motion is obtained from the principle that the force acting on any system is equal to its rate of change of momentum

$$F_r = \frac{d}{dt}\left(M \frac{dr}{dt}\right) \qquad -10.1$$

where r is the radius and M is the mass of gas effected. This is given by

$$M = \pi\rho\ (R^2 - r^2) \text{ per unit length} \qquad - 10.2$$

where R is the radius of the discharge tube.

The force is produced by the self magnetic field of the current sheath which exerts a pressure of

$B^2/2\mu_o$ on the shell

(M.K.S. units will be used throughout this chapter)

The force per unit length on the shell will be

$$F_r = - \frac{\pi\mu_o I^2}{4r} \qquad - 10.3$$

If we put $y = r/R$ then the snowplough equation reduces to

$$\frac{d}{dt}\left[(1 - y^2)\frac{dy}{dt}\right] = - \frac{\mu_o I^2}{4\rho R^4} \cdot \frac{1}{y} \qquad - 10.4$$

Whether or not this equation can be solved analytically depends on the form of I. Anderson (1958) et al consider that the current rises linearly with time, whilst Curzon and Howard (1963) obtained a solution for a particular sinusoidal variation.

A more accurate approach is to use experimental values of current and to solve the equations numerically. This was carried

out by Curzon, Churchill and Howard (1963) and although this method is more acceptable the results obtained with it do not differ greatly from the simple model.

Considering the simplifying assumptions which are made in this model, the agreement between it and experiment is remarkable. Several other modifications than those mentioned above can be made which will improve the agreement and some of these will be mentioned later in this chapter.

10.3 Shock Model

The Shock Model proposed by Allen (1957) is physically more acceptable because, in the frame of reference of the piston, all particles are not brought to rest but are allowed to move in front of the piston, creating a shock wave. A particle will thus have three degrees of freedom and consequently the ratio of the specific heats, γ, will be 5/3.

Reynolds (1961) has shown that the ratio of piston to shock velocity is given by

$$\frac{u}{v} = \frac{\gamma+1}{2(1-\frac{1}{M})} \qquad - 10.5$$

where M is the Mach number of the shock.

When $\gamma = 1$ and M is large this reduces to the snowplough model,

and when the particles have 1 degree of freedom, i.e. move only inwards, as in the free particle model, $\gamma = 3$ and the velocity ratio is 2.

The experimental results given by Reynolds show that for hydrogen and deulerium a value of γ between 1 and 5/3 is required. This is allowed for by assuming that ionisation and dissociation will increase the number of degrees of freedom and consequently reduce the value of γ. This procedure gives a much better fit between experiment and theory over a wide range of conditions although experimental error was rather large. Reynolds also points out that at low piston velocities the experimental results agree well with the snow plough model. In view of the difficulties of solving the equations for anything more complicated than a simple two dimensional case, and because of the good agreement with the snowplough model at low piston velocities, (which are usual with the present apparatus) it was decided to modify the snowplough equation to include the influence of a stabilising magnetic field.

10.4 The inclusion of a Stabilising Magnetic Field.

The snowplough model discussed in section 10.3 assumes that the collapsing shell will be of zero thickness and consequently of infinite density. This is not at all satisfactory when one considers the effect of the stabilising magnetic field, and in effect

a finite thickness must be assumed. Furthermore, it is necessary to make some assumption as to the structure of this front. An estimate of the thickness and structure of the front can be obtained from results in the last chapter. Since the structure changes with different conditions a very much simpler case of a rectangular structure has been assumed, although the thicknesses obtained experimentally have been used. One further assumption that is made in order to simplify the mathematics is that the conductivity of the plasma remains constant throughout the discharge. This is clearly not so, since in the initial stages the conductivity must be very low, but the effect on the field compression is likely to be very small since, as we shall see later, most compression occurs when the pinch is well under way. Therefore the assumption that σ is constant is probably quite reasonable.

These assumptions together with the associated distribution of B_θ and B_z are shown diagrammatically in Fig. 10.1. The pressure exerted on the plasma now becomes

$$\frac{-B_\theta^2}{2\mu_o} + \frac{B_z^2(\text{inside})}{2\mu_o} - \frac{B_z^2(\text{outside})}{2\mu_o} \qquad - 10.6$$

The negative sign indicates a pressure tending to reduce y
Thus the snowplough equation (10.4) is modified to

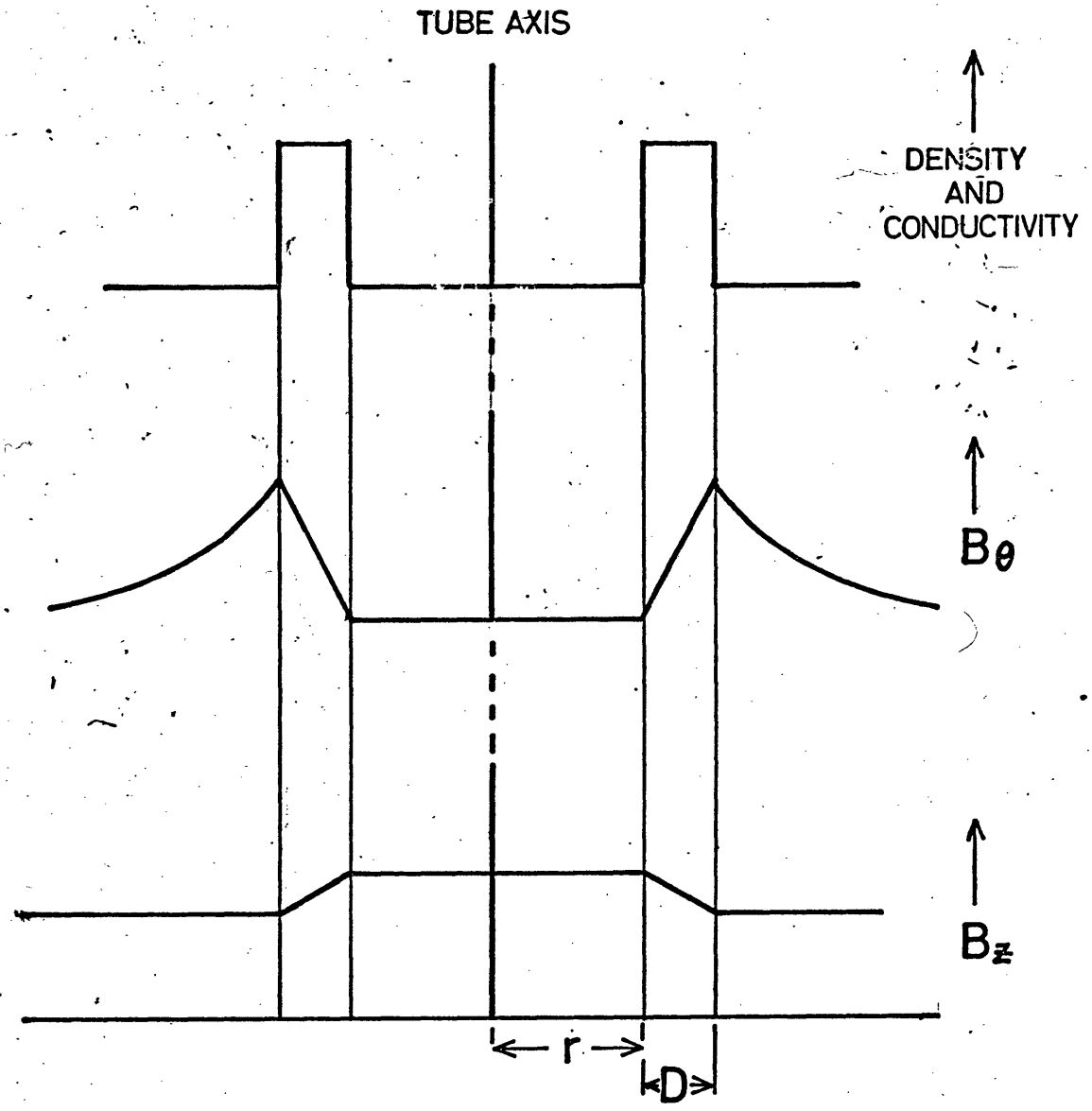

Fig 10.1 ILLUSTRATING THE ASSUMPTIONS MADE CONCERNING THE DENSITY, CONDUCTIVITY, B_θ AND B_z

$$\frac{d}{dt}\left[(1-y^2)\frac{dy}{dt}\right] = \frac{-\mu_o I^2}{4\rho R^4}\cdot\frac{1}{y} + \frac{B_1{}^2 y}{2\mu_o} - \frac{B_o{}^2 y}{2\mu_o} \qquad - 10.7$$

where

$B_1 = B_z$ (inside)

$B_o = B_z$ (outside)

Before proceeding further it is convenient to consider how B_1 and B_o are determined.

From Maxwells equations

$$\frac{1}{\mu_o}\nabla \times \underline{B} = \underline{j} \qquad - 10.8a$$

if the displacement current is neglected

also

$$\nabla \times \underline{E} = -\frac{\partial \underline{B}}{\partial t} \qquad - 10.8b$$

and Ohms Law is

$$\underline{j} = \sigma(\underline{E} + \underline{V} \times \underline{B}) \qquad - 10.8c$$

If we now assume that the Hall effect is negligible (see Appendix V) then we need only consider the azimuthal component of the current density as contributing to B_z. Thus 10.8a becomes

$$j_\theta = \frac{1}{\mu_o}\left[\frac{\partial B_r}{\partial z} - \frac{\partial B_z}{\partial r}\right]$$

Axial symetry gives that $\frac{\partial B_r}{\partial_z} = 0$

consequently

$$j_\Theta = -\frac{1}{\mu_o} \frac{\partial B_z}{\partial r} \qquad - 10.9a$$

Similarly from 10.8b we obtain

$$\frac{\partial B_r}{\partial t} = -\frac{1}{r} \frac{\partial}{\partial r} (rE_\Theta) \qquad - 10.9b$$

and from 10.8c

$$j_\Theta = \sigma(E_\Theta - V_r B_z) \qquad - 10.9c$$

(for right handed set of axes.)

Ellimination of j_Θ and E_Θ from these three equations results in

$$\frac{\partial B_z}{\partial t} = \frac{1}{r} \frac{\partial}{\partial r} \left[\frac{r}{\sigma\mu_o} \frac{\partial B_z}{\partial r} - r B_z \frac{\partial r}{\partial t}\right] \qquad - 10.10$$

The second term of equation 10.10 may be considered to trap the flux by the inward sweep of the plasma ($\frac{\partial r}{\partial t}$ is negative). The first term, the term containing σ, may be looked upon as the flux leakage term, since it is essentially $\nabla^2 \underline{B}$ when the azimuthal and axial dependencies are ignored.

Following the assumptions made earlier we now put a form to the radial distribution of B

$$B = \frac{-(B_1 - B_o)r}{D} + C \qquad - 10.11$$

within the region of the conducting shell.

thus

$$\frac{\partial B_z}{\partial t} = -\frac{1}{\mu_o \sigma D} \cdot \frac{B_1 - B_o}{r} - \frac{1}{r} B_1 \frac{\partial r}{\partial t} - \left(\frac{B_1 - B_o}{D}\right) \frac{\partial r}{\partial t} \qquad - 10.12$$

If we consider now a point on the inner side of the shell then B_z and the rate of change of B_z will be the same on either side of the transition. But within the central region B_z is no longer dependent on r and consequently the partial derivatives in 10.12 may be replaced by total derivatives

$$\frac{dB_1}{dt} = -\frac{1}{\mu_o \sigma D} \cdot \frac{B_1 - B_o}{r} - \frac{1}{r} B_1 \frac{dr}{dt} - \left(\frac{B_1 - B_o}{D}\right) \frac{dr}{dt} \qquad - 10.13$$

In order to obtain B_o we must make one further assumption, either that the flux through the field coil is constant or that B_o remains constant at the value of the initial field. Bezbatchenko (1957) assumed that the former was true and this assumption was initially adopted here. However, as a check, computations were carried out for both cases and the difference was found to amount to only 0.1% variation in any parameter.

If the flux is constant through the coil then

$$B_o = B_{av} \frac{R_c^2}{R_c^2 - r^2} - \frac{B_1 r^2}{R_c^2 - r^2} \qquad - 10.14$$

where R_c is the coil radius

Now if $y = r/R$ is written as y_1 and $B_1 = y_3$

then equation 10.7 becomes

$$\frac{d}{dt}\left[(1-y_1^2)\frac{dy_1}{dt}\right] = \frac{-\mu_o I^2}{4\rho R^4} \cdot \frac{1}{y_1} + \frac{y_3^2 y_1}{2\mu_o} - \frac{1}{2\mu_o} \cdot \frac{(a\,B_{av} - y_3 y_1^2)^2}{(a-y_1^2)^2} \quad - 10.15$$

where $a = R_c^2/R^2$

Although the current I usually differs widely from sinusoidal with the unstabilised pinch, the effect of the stabilising field is to reduce the 'violence' of the pinch thereby reducing the inductive effect of the plasma.

Thus $I = I_o \sin wt$ - 10.16

to a good degree of accuracy.

Substitution of 10.16 into 10.15 defines the right hand side specifically.

Equations 10.13 and 10.15 cannot be solved analytically, and consequently recourse must be taken to numerical methods. However, before any numerical method can be applied it is necessary to remove the double derivative in 10.15 by the substitution

$$y_2 = \frac{dy_1}{dx}$$

where $x = wt$

We now have the equations

$$\frac{dy_1}{dx} = y_2 \qquad - 10.17a$$

$$\frac{dy_2}{dx} = \frac{-bd \sin^2 x}{y_1} + by_3^2 y_1 - \frac{b(a\,B_{av} - y_1^2 y_3)^2 y_1 + 2y_1 y_2^2}{(a - y_1^2)^2} \qquad -10.17b$$

$$\frac{dy_3}{dx} = \frac{-c(y_3 - B_{av})}{y_1} - y_2\left[\frac{y_3}{Ry_1} - \frac{(y_3 - B_{av})}{D}\right] \qquad - 10.17c$$

where $b = \frac{1}{R^2 \mu_o \rho w^2}$

$$c = \frac{1}{D\, w\, \mu_o\, \sigma\, R}$$

$$d = \left(\frac{\mu_o I_o}{2\pi R}\right)^2$$

These equations have been solved under various conditions using the Runge-Kutta method of integration developed by Merson (lance, 1960). The computations were carried out on an IBM 7090 computer. The program is described briefly in Appendix IV.

10.5 Comparisons between experimental results and computations.

Experimental results indicate that at peak discharge currents of 30 KA the magnetic field compression is negligible when B_{nom} = 10 K gauss, but rises typically to around 2.1 as the current is

increased up to 90 KA, and the stabilising field reduced to 5 K gauss. These initial computations predict that the field compression will be negligible at 30 KA current (~1%) but only rising to approximately 1.3 at 90 KA. The agreement is thus not very good, although several interesting points do arise from these calculations.

Firstly, as the conductivity rises, the field compression reaches a maximum value and then falls off. This can be understood readily if it is remembered that the compression depends not only on the conductivity but also on the rate at which the sheath moves towards the axis. As the conductivity is raised beyond a certain point its effect on slowing the plasma down is greater than any direct increase in compression, with the result that the compression falls.

A second feature of the results is that, as the pinch becomes more and more controlled by the stabilising field then the time to maximum compression gets earlier in relation to the pinch time. As the discharge current is increased the stabilising field has less influence and the maximum compression occurs at the pinch. If the discharge current is increased further the stabilising field is insufficient to prevent the discharge reaching the axis and the equations 10.17 are not strictly valid.

It will be noticed in the results presented in chapters 5 and

6 that it often happens that, after the pinch, the magnetic field is reduced below the initial value. This is not predicted by these computations, although the reason for this is easily seen.

When the plasma reaches its mimimum radius, then this radius is determined by

a) The stabilising field compression

or b) The kinetic pressure of the plasma.

If the stabilising field is controlling the plasma then the approach to the minimum radius will be relatively slow (see fig 10.3) and the compression at this time will be small. This results in a more or less stable configuration and since the B_z pressure is very small, no expansion of the plasma will take place until the discharge current drops considerably.

If the kinetic pressure is controlling the plasma then the approach to the axis is much faster, and consequently the field compression is greater. As the plasma is brought to rest, however, the trapped field escapes. This results in a further heating of the plasma. The pressure now causes the plasma to expand rapidly to the walls of the tube. Because of the plasma's relatively high conductivity, this will result in a rarefaction of the field within the plasma.

Thus we would expect that the rarefaction of the magnetic

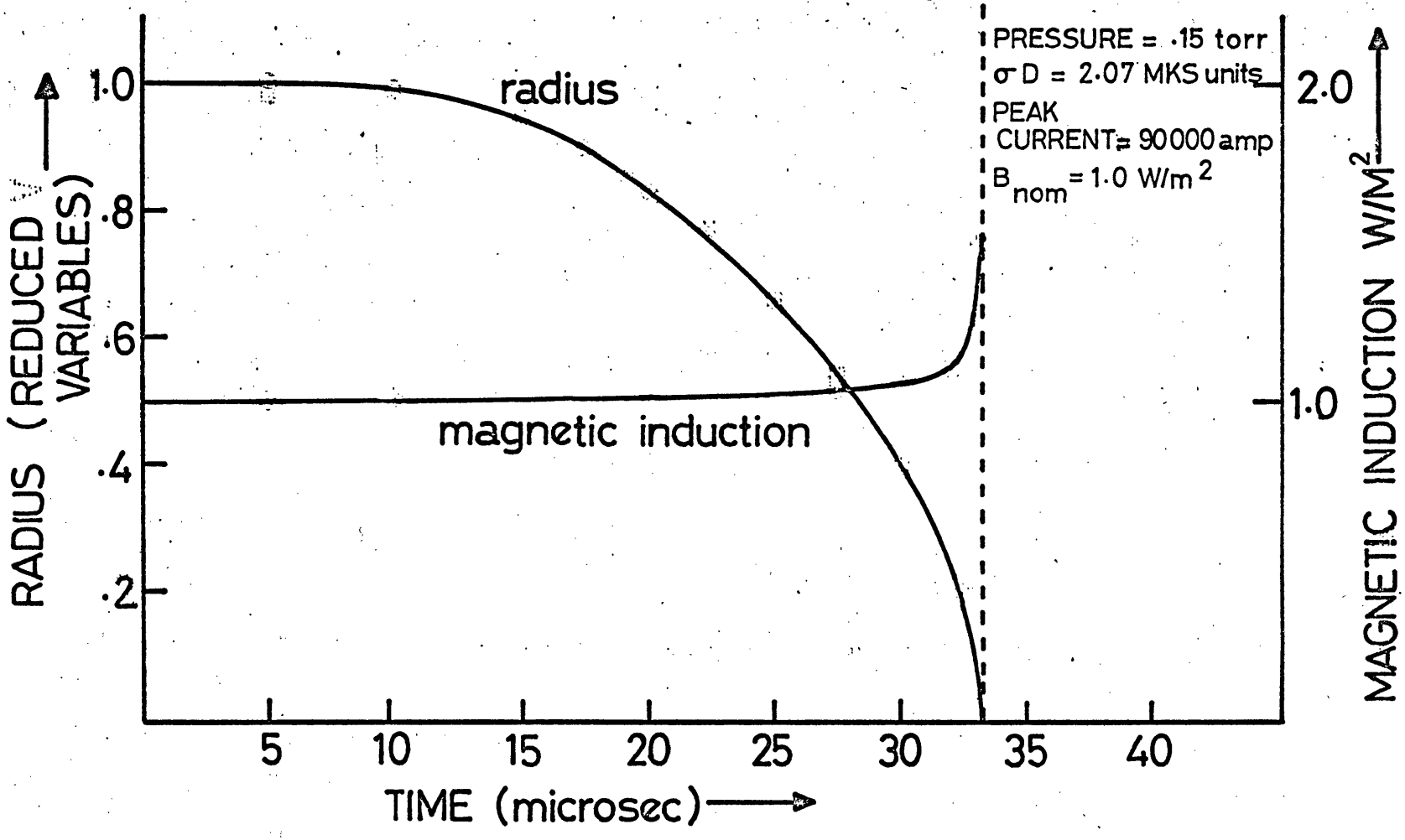

Fig 10.2 MAGNETIC INDUCTION AND RADIUS VS. TIME (COMPUTED RESULTS)

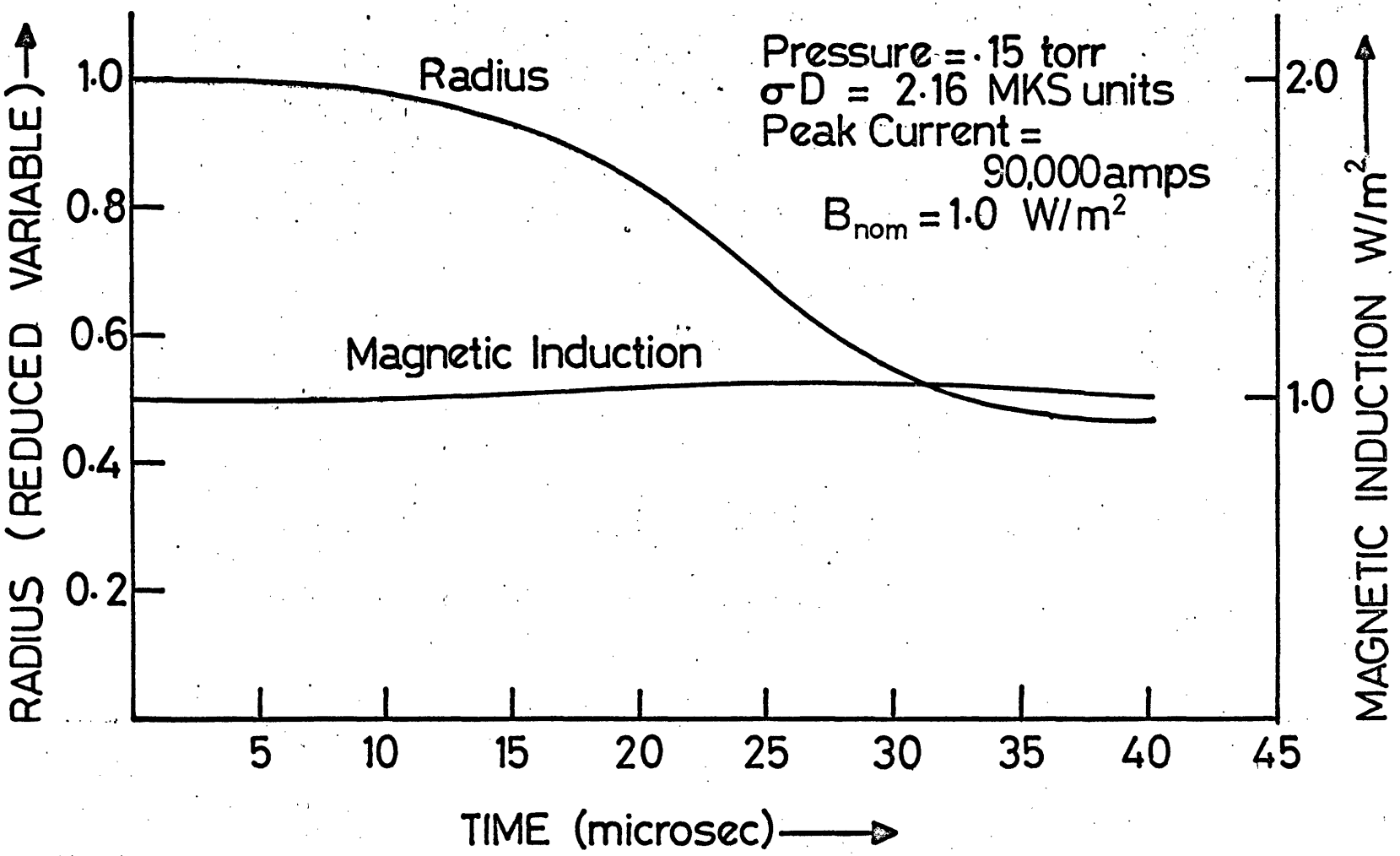

Fig 10.3 MAGNETIC INDUCTION AND RADIUS VS. TIME (COMPUTED RESULT)

field to be an indication that the pressure contributes significantly to the later stages of the pinch.

Figs 10.2 and 10.3 show some results under the conditions B_{nom} = 10 K gauss and tube volts = 3 Kv at .15 torr pressure. The only parameter which has been varied in these two graphs is the value of the conductivity. We see that an increase in σ of only 5% has a very pronounced effect. In Fig 10.2 the stabilising magnetic field is not capable of preventing the discharge reaching the axis and since the plasma reaches the axis with a large velocity, the magnetic field compression is appreciable.

Fig 10.3, however, shows the situation when the conductivity is increased by 5%. The motion of the plasma is dominated by the stabilising field and very little compression results.

10.6 Modifications to the Original Model

An important modification was suggested by Curzon (1967), where account is taken of the fact that a non zero mass is involved in the initial acceleration phase of the plasma.

The left hand side of equation 10.4 can thus be written

$$\frac{d}{dt}\left[(m_o + \pi\rho(R^2 - r^2))\frac{dr}{dt}\right]$$

m_o can be considered as arising from a thickness ρ near the walls

of the tube as shown in fig. 10.6

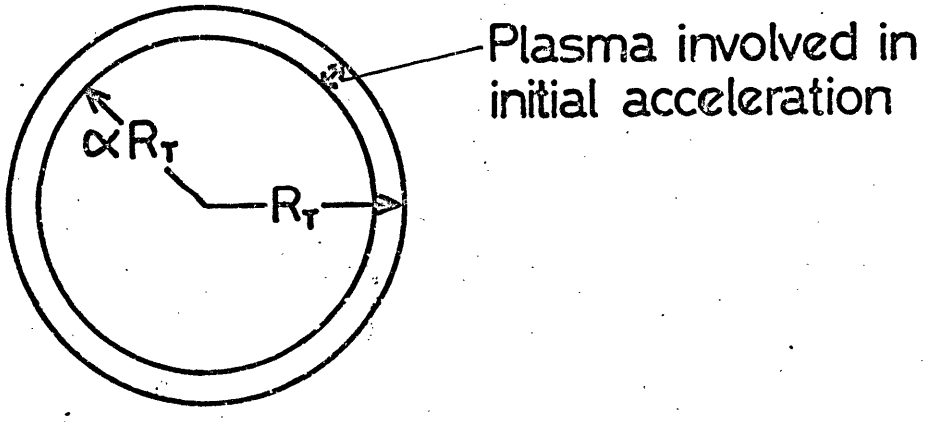

Fig 10.6 INITIAL MASS ASSUMPTION

thus $m_o = \pi\rho(R^2 - \alpha^2R^2)$ per unit length.

In reduced variables the left hand side of 10.4 thus becomes

$$\frac{d}{dx}\left[(\beta - y_1^2)\frac{dy_1}{dx}\right]$$

where $\beta = 2 - \alpha^2$

The effect of the inclusion of an initial mass is shown in fig 10.4 where the radius - time graph is plotted against the corresponding previously calculated result. In the initial stages of the discharge, when the current is low, m_o has a very significant effect, and the acceleration of the plasma towards the centre is greatly reduced. Since the discharge current does not reach a maximum until well after the pinch the initial effect is counteracted by the larger acceleration near the time of maximum compression.

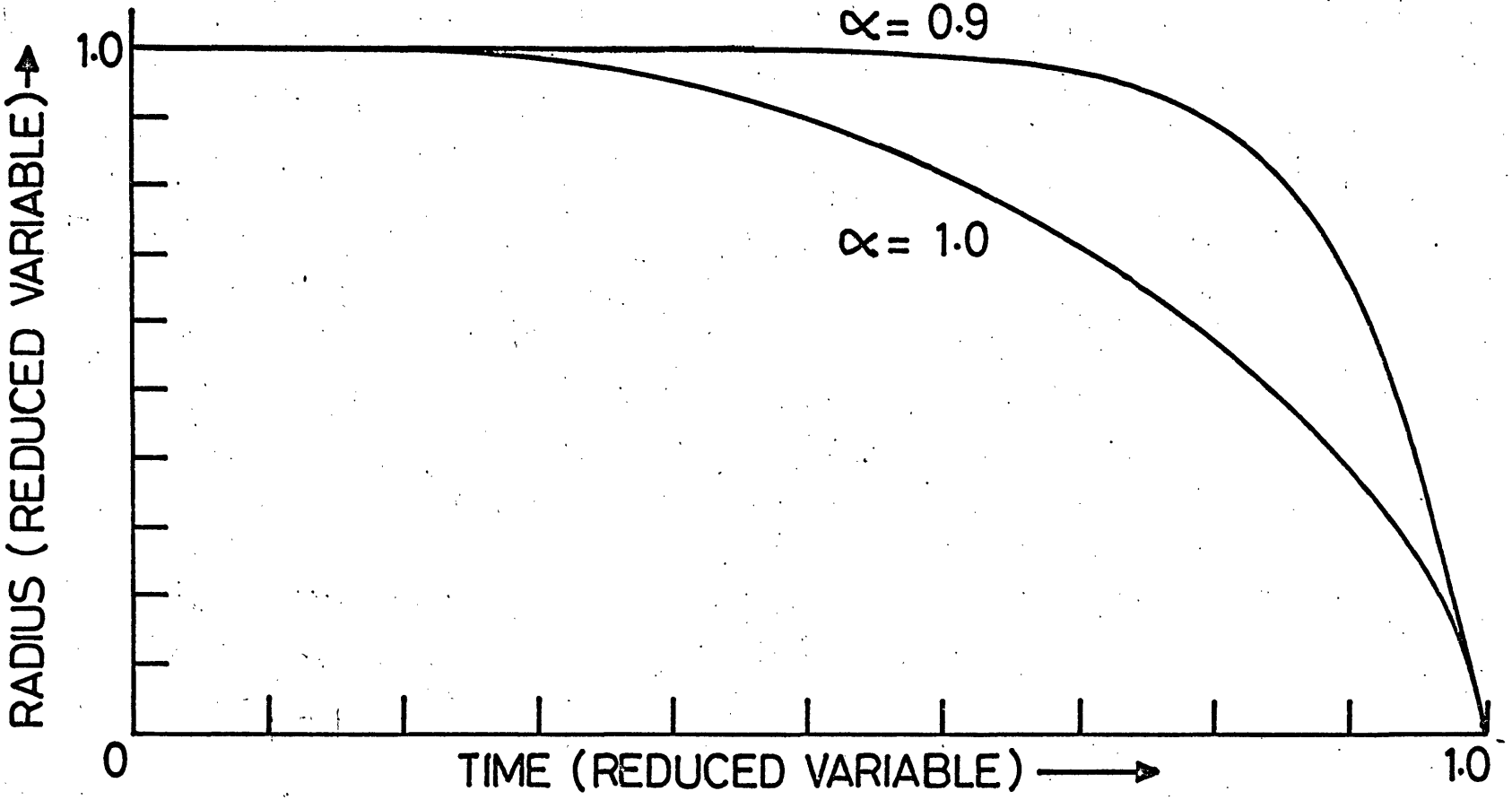

Fig 10.4 ORIGINAL AND MODIFIED SNOW PLOUGH MODELS

The overall effect is a rather more 'square' radius-time graph.

10.7 Results with the Modified Program

Fig 10.5 shows the radius-time graph and the magnetic induction-time graph for the conditions B_{nom} = 0.5 w/m^2 Tube volts = 3Kv and pressure = .15 torr. It is apparent that very much greater magnetic field compressions are obtained on this model. In the particular example given, the field compression = 2.16. This is in good agreement with experiment. On one or two occasions, at higher pressures, the experimental values of compression were as high as 3. Values as high as this were not obtained from the calculations.

Also in good agreement with the experimental results is the time taken to the pinch. We see from table 5.2 that the experimentally obtained result is 15 μsec, whereas the calculated result is 15.8 μsec. In general the results obtained for times to pinch agree well with experiment, there being a very distinct increase in the times, as

a) The nominal magnetic field is increased

b) The discharge current is decreased

and to a lesser extent, as

c) The filling pressure is increased.

Each of these trends might be expected from a simple qualitative treatment.

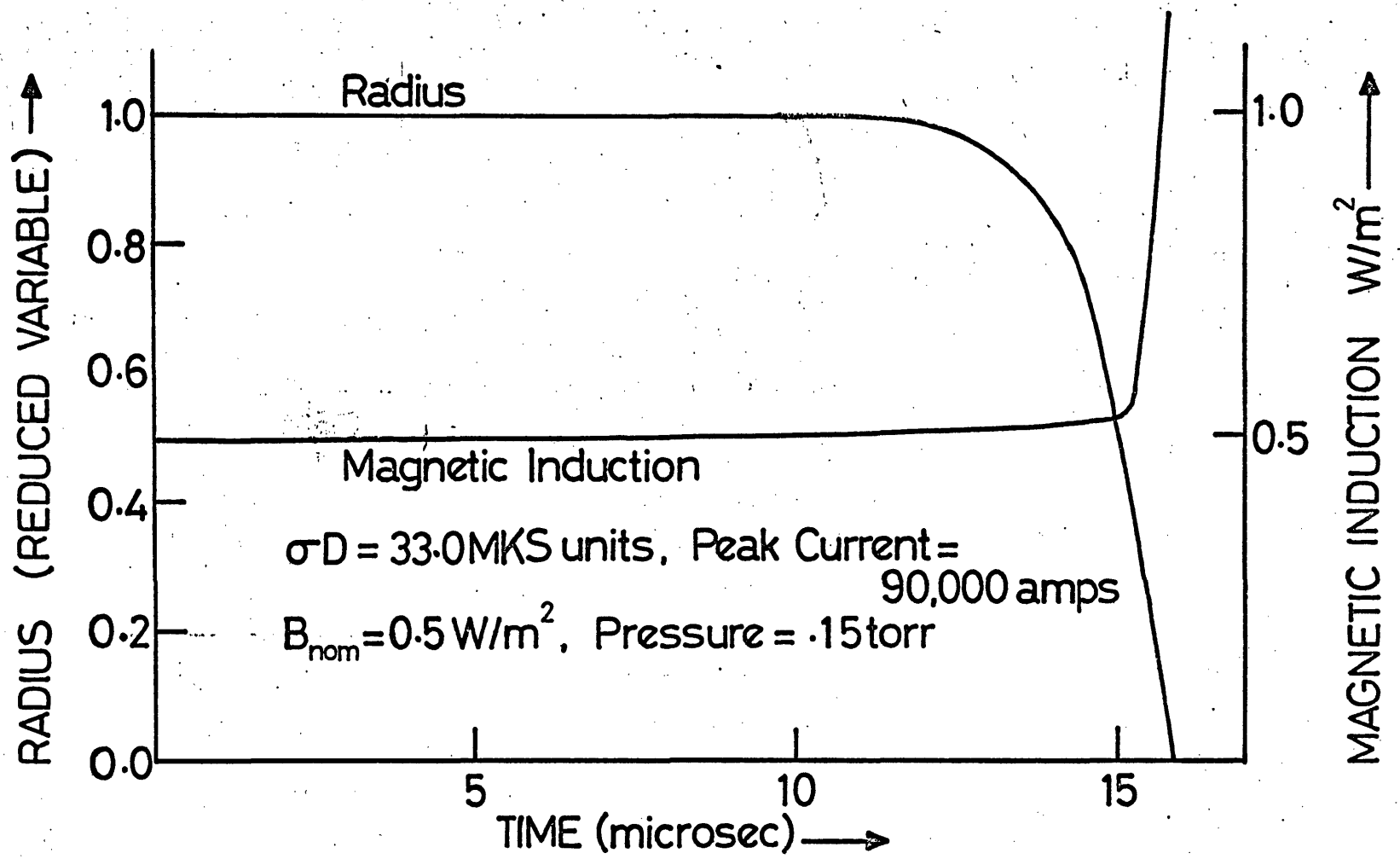

Fig 10.5 MAGNETIC INDUCTION AND RADIUS VS. TIME (COMPUTED FROM MODIFIED MODEL)

One point that is not quite so easily understood is the very distinct change in the value of the conductivity-sheath thickness product, by the modified model as compared to the original model. We can see from equation 10.12 that the conductivity only appears as a product with the sheath thickness and although, in the computing, it was the conductivity which was varied, only the product has any significance. Furthermore, since the conductivity is well defined, the sheath thickness should be considered as the more uncertain quantity. Table 10.2 plots some calculated values of this thickness with the corresponding experimental results presented in chapter 9 for a temperature of 25000°K.

Table 10.2

Values of Sheath Thickness (cm) when T = 25,000°K

Pressure = .15 torr Tube volts = 3Kv

Nom. Mag. Induction w/m^2	Calculated (Original)	Calculated (modified)	Experiment
0.5	1.5	3.0	2.1 ± 0.1
1.0	.45	0.3	1.8 ± 0.1

This table shows the very pronounced difference between the two models. In the original model the variation in the value of the

sheath thickness does not differ as widely as with the modified model. In the original case the values are both below the experimentally obtained values whereas this is not so with the modified calculation.

The degree of agreement at 0.5 w/m^2 stabilising magnetic induction is quite good, if one remembers that the value of temperature used is an average value, and that a 20% change in this would bring either of the two calculated values within the experimental value.

With a stabilising induction field of 1.0 w/m^2 the degree of agreement is not nearly so good. This is partly explained by the fact that the temperature assumed is far too high, although to account for variation fully would require a drop in the temperature to approximately 10,000^{o}K. Temperatures such as this, under these conditions, have not been measured. It therefore seems likely that the model that has been used to describe the pinch is not truely applicable under such conditions.

In conclusion we can see that the results from the modified program are in much better agreement with experiment than the original model. The field compressions, obtained from both models, are in much better agreement at low values of stabilising field than at high. This is probably due to inapplicability of these models to a grossly stable plasma.

References

Allen	Proc. Phys. Soc. B. 70, 24, 1957.
Anderson, O.A. et Al.	Phys. Rev. 110, 6, 1375, 1958.
Bezbatchenko, A.L. Golovin, Yavlinsky, N.A.	I.N. Ivanov, D.P. Kirillov, V.D. J. Nucl. Energy II. 5, 71, 1957.
Curzon, F.	Private communication
Curzon, Churchill and Howard	J. Nucl. Fusion, 3, 293, 1963.
Curzon and Howard	Proc. Phys. Soc. 81, 349, 1963.
Lance, G.N.	Numerical Methods for High Speed Computing Iliffe, 1960
Nation, J.	Thesis, University of London, 1960
Reynolds and Quinn	J. Nuclear Energy part C., 3, 1961.
Rosenbluth, M.N.	Infinite Conductivity Theory of Pinch. Los Alamos Report, LA 1850, 1954.

Chapter 11

Concluding Remarks

In the first part of this thesis there is described a new method for measuring magnetic fields in a plasma. The method has been shown to work satisfactorily and the advantages, to be gained by using it, have been pointed out. The instrument described is very versatile and, although it is not as accurate as a conventional magnetic probe, it represents a useful contribution to diagnostic technique. One of the major reasons for the lower accuracy of the Zeeman instrument is because of the versatility of the instrument; if some reduction in the flexibility of the instrument could be tolerated, then a considerable increase in the accuracy could be obtained. This may be achieved in part by the use of fixed apertures and a fibre optic system. The stability of the disperser could be further increased by using an etalon rather than an interferometer; this would also facilitate the quick operation of the instrument. The error introduced by shot noise is likely to be, in the limit, far more restrictive than any other source of error. The high noise level arises because of the low photon efficiency of the photomultipliers. Photomultipliers are available which have a much higher photon efficiency, but these are quite expensive. Semi-conductor devices are available which have a much higher

efficiency but these are very insensitive and require extremely sophisticated amplifiers to produce a measurable signal.

It was hoped at the commencement of this work that this spectroscopic method for measuring the magnetic fields could be used to determine how much disturbance a conventional probe makes to the plasma. Although some differences can be noted from the results, no definite conclusions can be drawn from these, except that any disturbance is less than the accuracy of the results.

The electron density measurements have proved useful in so far as spatial distributions have been obtained on this apparatus with greater accuracy than hitherto. The interferometer proved very successful, fulfilling every condition that was required of it. Although many interferometers have been designed previously which involve much more sophisticated mountings, the present system provides a very useful instrument for situations where all but the highest precision and stability is required.

The results obtained with this instrument show clearly the effect of the stabilising field on the collapse stages of the discharge. When a relatively low stabilising field is used a definite collapsing front is observable. This is assumed in the various models described in chapter 10. As the magnetic field is increased

the pinch becomes much less pronounced until, eventually, a situation is reached where the discharge could be more suitably explained as a glow discharge. Such situations as this are clearly shown in the Mach-Zehnder results. The extension of the equations derived in chapter 10 to such conditions as this is clearly not valid although the agreement is reasonable. This reasonable agreement probably arises because in both cases the plasma is dominated entirely by the magnetic field.

In general, the calculations presented in chapter 10 and the experimental results presented in chapters 5,6 and 9 are in good agreement. The original model used, although predicting reasonable values for the time to pinch, was not capable of producing sufficient field compression. The reason for this appeared to be that the plasma did not approach the axis with sufficient velocity. The modification presented in chapter 10 shows one way in which higher velocities would be predicted, whilst at the same time making the physics of the situation more acceptable. This modification, however, is not the only one which could be used to explain the initial anomoly.

If we assume that some gas particles escape past the piston in the later stages of the pinch then this would reduce the inertia of the plasma with a resultant increase in velocity near the axis.

Computations, taking account of this effect, have not been carried out on the stabilised pinch. However, Taylor (1967) has carried out some calculations in the absence of the stabilising field and has found that higher velocities are produced, together with slightly shorter pinch times. The shock model for a collapsing pinch has been used to explain some discrepancies in the results of the snowplough model. In this situation, also, it is not difficult to see how the inclusion of a shock wave could result in the prediction of greater field trapping. It has been mentioned in chapter 10 that in most conditions the shock wave will travel faster than the driving piston. Since ionisation is produced in the region behind the shock front, this would result in the conducting sheath becoming thicker as it nears the axis, with a consequent rise in the mean velocity. Experimental evidence for this last point is inconclusive. The axial light emission at low pressures indicates that some plasma reaches the axis well before the main compression. If this were due to a shock wave preceeding the main pinch, then one would expect that some evidence of the driving piston would be noted before the first pinch occurs. The interferograms do not show this, the first pinch having expanded well away from the axis before any definite signs of the main pinch occur.

We can see, therefore, that although the experimental results have been explained to a reasonable degree of accuracy, the modification

made to the computation is not the only one which could explain the original discrepancy. Indeed, a combination of these modifications would probably give a more acceptable explanation.

Three proposals for future work arise from this thesis. Firstly, refinements of the Zeeman instrument in the way mentioned should increase the accuracy of the instrument sufficiently so that a determination of the perturbation of the plasma by the probe could be made.

The Mach-Zehnder interferometer offers a very accurate way of measuring the electron density of the plasma, with a consequence that the plasma could be a very useful source for quantitative spectroscopy: in particular for the measurement of stark broadening of spectral lines.

Finally, the use of the Mach-Zehnder interferometer is limited to the case of relatively non-violent pinches by virtue of the fact that $\int n_e dl$ becomes too large. One may overcome this by viewing the plasma side on. This means that many fringes will be caused without the plasma being present, due to the imperfections in the walls of the tube. If, however, a double exposure hologram were taken, the first exposure of the tube, and the second exposure

of the tube and plasma, then what results on the photographic plate is an interferogram of the difference between the two exposures, i.e. the plasma. This would prove a useful extension to the work presented in this thesis.

References

Taylor, T.B. Thesis (to be published).

Acknowledgements

This work was carried out whilst the author was a member of the Plasma Physics Group, Imperial College. To Dr. Latham I offer my thanks for his help and supervision throughout this period. My thanks are also extended to the other members of the academic staff in the Plasma Physics Group, in particular C.B. Wheeler, Dr. A. Folkierski, and A.E. Dangor.

I am grateful to Mr. P. Daly and Mr. B. Boreham who constructed much of the apparatus and to Mr. Nyman who built most of the electronics.

To Dr. D.E. Roberts, who read the manuscript, I am very grateful. I am also indebted to Dr. M.H. Key for allowing me to reproduce figs 7.4-7.7, to Dr. D.D. Burgess for allowing me to reproduce fig 3.2 and 3.3 and for his help in the initial stages of this work, and to R.M. Dunnett who allowed me to use subroutines 'merson' and 'check' mentioned in appendix IV.

I would also like to thank Miss P. Grubb who patiently typed the manuscript.

Finally, I would like to thank S.R.C. who provided the money for three years of this project and the bank manager of the National Provincial Bank (South Kensington) who provided it for the last three months.

Appendix I

A Computer Program for Calculating the Instrument Profiles of the Fizeau and Fabry Perot Interferometers.

In chapter 3 we saw that the phase difference δ_p of the p^{th} reflected ray was given by

$$\delta = \frac{2\pi t}{\lambda} \frac{[\sin 2\ (p-1)\theta\ .\ (1-\alpha^2/2) - 2\ \sin^2(p-1)\theta\ .\ (\alpha - \alpha^3/6)]}{\theta + \theta^3/3}$$

The value of δ was computed for each value of p from 1 to 50 and at the same time two cumulative sums were taken (see chapter 3)

these are

$$S_1 = \Sigma\ R^{p-1} \cos \delta$$

and

$$S_2 = \Sigma\ R^{p-1} \sin \delta$$

The intensity is then obtained from S_1 and S_2 by

$$I(t,\alpha) = (1 - R)^2\ (S_1^2 + S_2^2)$$

Assuming that the transmission is given by $(1 - R)^2$.

The values of $I(t,\alpha)$ were computed for 100 values of t, spaced evenly between N - 0.5 and N + 0.5 (where N is an integer).

This intensity distribution was carried out for several values of α between $-\alpha_m$ and $+\alpha_m$. Direct integration of corresponding values of $I(t,\alpha)$ was carried out using Simpsons rule, no weighting being given to any value of α. The fact that no weighting has been applied means essentially that we have a rectangular distribution of intensity with α. Although this will not be true at very small angles, it is considered an adequate assumption, since, at these small angles, the effect of α should be small.

When the Fabry Perot profile is being computed the formula given already for δ is not suitable, since the computer is required to evaluate $^0/_0$. Instead of this, the standard form of δ is used.

i.e. $\delta = \frac{2\pi t}{\lambda} \cos \alpha$

(This also saves considerably on computing time).

Apart from this difference the computational method is identical with the Fizeau case.

A flow diagram for the program is given on the next page.

Flow Diagram for the Computer Program given in Appendix 1

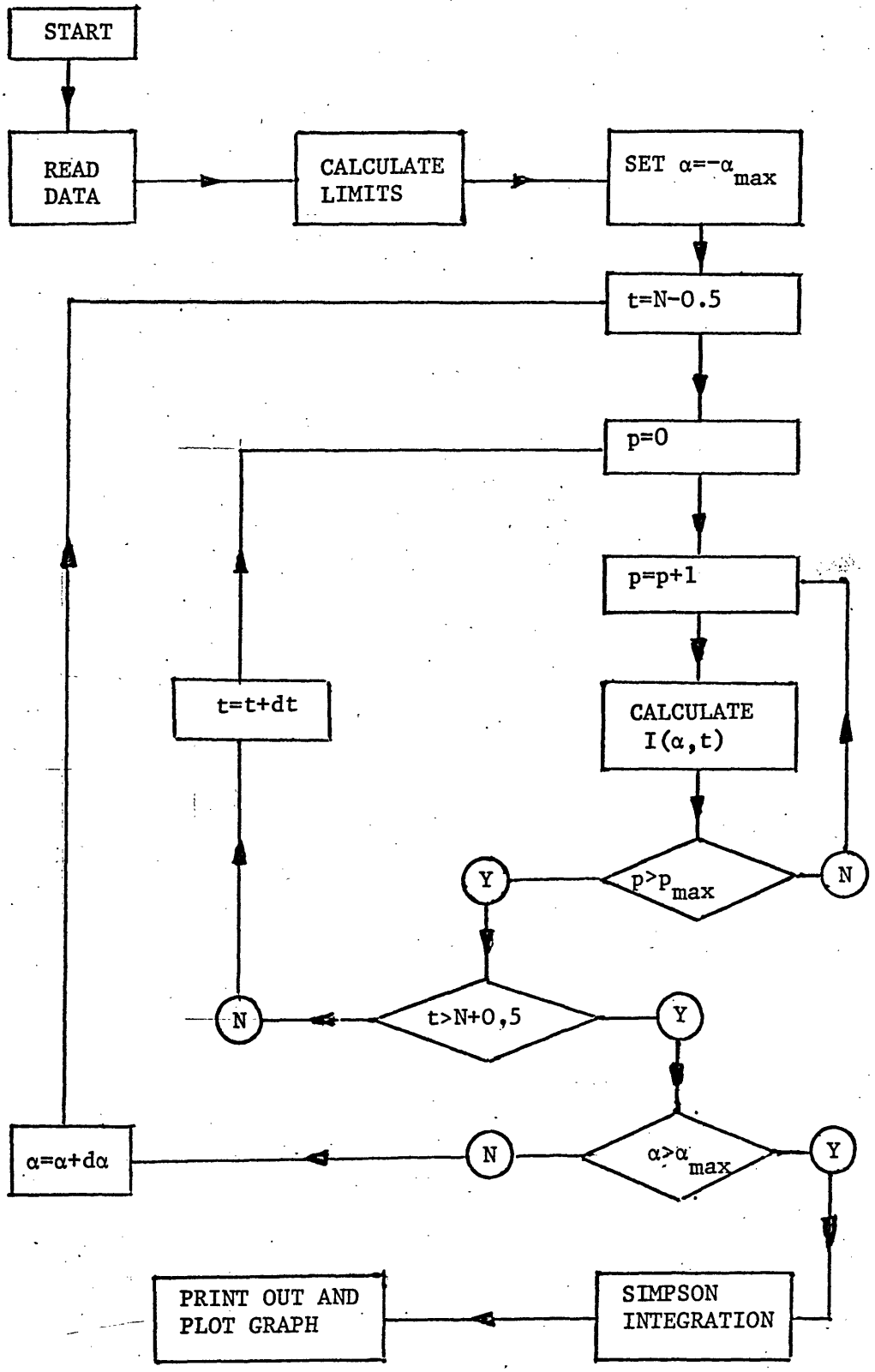

Appendix II

A Computer Program to Calculate the Magnetic Field in a Plasma from Experimental Data.

This program uses the formula given by equation 4.16 for the magnetic field. This formula, if applied directly however, involves some considerable error if the shift is large for the reason pointed out in chapter 4. An iterative process is used to correct for this error.

After calculating the values of the various constants used in the equations, the line width is determined using equation 4.11. Using this value of line width the value of the magnetic field is calculated. This value for the magnetic field will determine how much the profile is shifted as a fraction of an order. This can be done using equation 4.15. If we now assume a dispersive profile which is shifted by an amount δ (equation 4.15), then a new value of the peak height signal can be determined. This is then used to recalculate the value of the line width. The whole process is repeated several times.

In the cases where the shift to width ratio is small, then very few iterations are required to produce an accurate answer. However on some occasions many iterations are required. The most

convenient limit to the number of iterations was found to be nine. On the very few occasions when this was not enough, the shift to width ratio was so large as to invalidate this procedure anyway.

In the situations where an accurate result is produced after very few iterations, it would be very wasteful on computer time to allow the full nine iterations to be carried out. An option was therefore included which allows the iteration to be terminated at a predetermined accuracy.

The various values of line width and magnetic field are stored until the completion of the calculation and all of them are printed out. This provides a check on whether the required accuracy has been achieved.

A flow diagram for this computer program is shown on the next page.

Flow Diagram for Computer Program given in Appendix 11

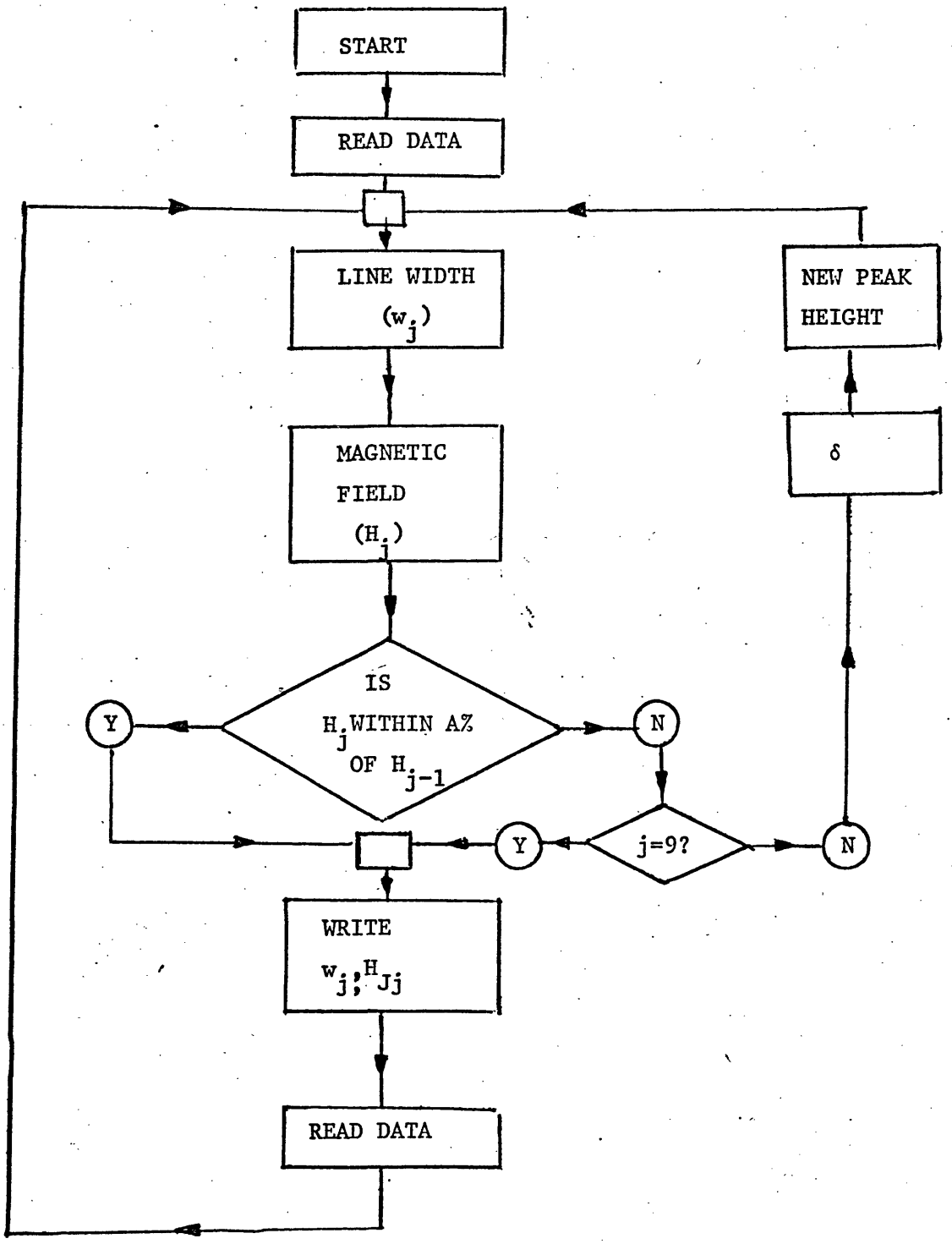

Appendix III

Derivation of the Path Difference Formula for the Mach-Zehnder Interferometer.

If $\bar{r}_{j-1}$ is a vector which represents ray incident onto a mirror, with a normal represented by $\bar{n}_j$, then the reflected ray will be represented by $\bar{r}_j$ given by

$$\bar{r}_j = \bar{r}_{j-1} - 2(\bar{r}_{j-1} \cdot \bar{n}_j)\,\bar{n}_j \qquad (1)$$

This can be seen more easily with reference to fig. 1.

Now consider the path from the source to some point $\bar{x}_o$. This is best done by paths from virtual sources, one source being due to the rays passing through one aim of the interferometer and the other source due to passage by way of the other arm. Consider fig 2. $\bar{r}_2$ and $\bar{r}_4$ are the two exit beams and S_a and S_b are the two virtual sources. If we now choose the origin at the fourth mirror then point $\bar{x}_2$ within the surface S_a will be given by

$$\bar{x}_2 = -\,d\bar{r}_2$$

and likewise for S_b assuming that the interferometer is symetrical

$$\bar{x}_4 = -\,d\bar{r}_4$$

The perpendicular distances from these planes passing through

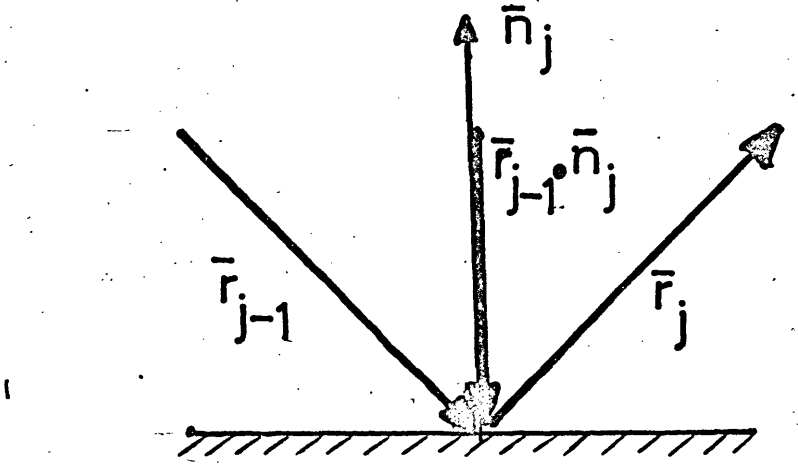

Fig 1 Reflection at a Mirror

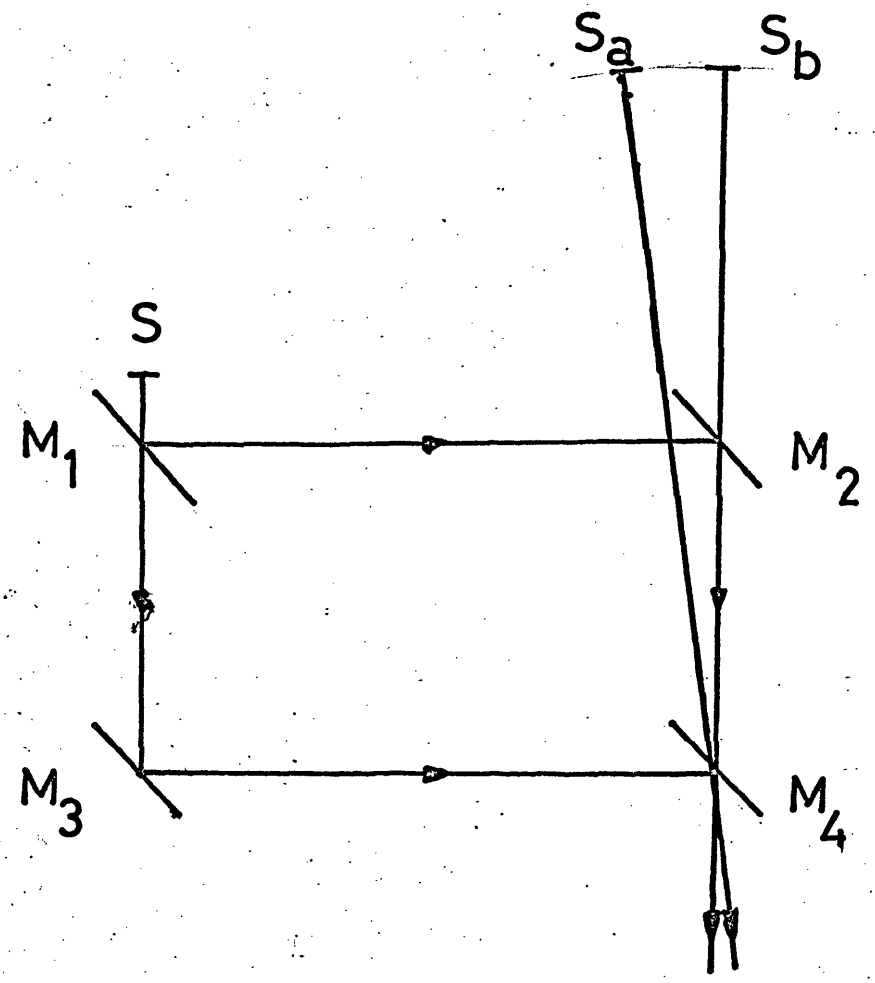

Fig 2. Showing Positions of S_a and S_b

the point x_o are given by

$$s_2 = (\bar{x}_2 - \bar{x}_o) \cdot \bar{r}_2$$

and $$s_4 = (\bar{x}_4 - \bar{x}_o) \cdot \bar{r}_4$$

respectively.

Thus the path difference Δ is given by

$$\Delta = s_4 - s_2 = (\bar{x}_4 - \bar{x}_o) \cdot \bar{r}_4 - (\bar{x}_2 - \bar{x}_o) \cdot \bar{r}_2$$

$$= d(\bar{r}_2 \cdot \bar{r}_2 - \bar{r}_4 \cdot \bar{r}_4) + (\bar{r}_2 - \bar{r}_4) \cdot \bar{x}_o$$

$$= (\bar{r}_2 - \bar{r}_4) \qquad (2)$$

Now if we make the assumption that M_1 and M_2 are parallel, Bennett (1951), then

$$\bar{n}_2 = -\bar{n}_1$$

and $\bar{r}_2 = \bar{r}$ where $\bar{r}$ is the incident ray.

Furthermore from (1)

$$\bar{r}_3 = \bar{r}_2 - 2\,(\bar{r}_2 \cdot \bar{n}_3)\,\bar{n}_3$$

and $$\bar{r}_4 = \bar{r}_3 - 2(\bar{r}_3 \cdot \bar{n}_4)\bar{n}_4$$

Substituting these equations back into (2) we have

$$\Delta = \{\bar{r} - [\bar{r} - 2(\bar{r} \cdot \bar{n}_3)\bar{n}_3] + 2\{[\bar{r} - 2(\bar{r} \cdot \bar{n}_3)\bar{n}_3] \cdot \bar{n}_4\}\bar{n}_4\} \cdot \bar{x}_o$$

$$= 2\overline{r} \cdot (\overline{n}_3\overline{n}_3 + \overline{n}_4\overline{n}_4 - 2\,\overline{n}_3(\overline{n}_3 \cdot \overline{n}_4)\overline{n}_4) \cdot \overline{x}_o$$

This is the result used in chapter 8 with

$$A = \overline{n}_3\overline{n}_3 + \overline{n}_4\overline{n}_4 - 2\,\overline{n}_3(\overline{n}_3 \cdot \overline{n}_4)\overline{n}_4$$

A is known as a dyadic and has the property that the resultant of a dot product with a vector, is itself a vector. This becomes apparent in chapter 8.

References

Bennett F.D. Journal of Appl. Phys. 22, 2, 1951.

Appendix IV

Computer Programs used in chapter 10.

The equations derived in chapter 10 are integrated using a modified Runge-Kutta method for numerical integration. The normal Runge-Kutta method unfortunately does not allow the error in the integration process to be determined. A modification by Merson (Lance, 1960) does allow a determination to be made of the error with only a slight increase in the complexity. This method will not be reproduced here since it has been adequately covered elsewhere (Dunnet, 1968).

The program was written in subroutine form to allow for ease of modification. The routines were as follows

a) Main Program - determination of initial constants and control of calculation
b) Subroutine WRI - Subroutine which writes out the desired information and stores it so that it may be plotted graphically at the end of the calculation.
c) Subroutine R.H.S. This subroutine determines the right hand side of equations 10.17a, 10.17b and 10.17c.
d) Subroutine UPSTAR - Subroutine determines initial conditions and starts off the integration process.

e) Subroutine MERSON - Calculates the next values of y_i ($i = 1 - 3$), knowing the previous values and the derivatives.

f) Subroutine CHECK - Determines the accuracy of the integration. If the accuracy is higher or lower than preset limits the integration step length is changed accordingly.

It will be noticed from equation 10.17b that the position $y_1 = 1$ is singular. This is, unfortunately, the situation at the start of the integration process. To overcome this, it is necessary to find a solution to these equations which applies when x is small, i.e. $y_1 \to 1$. An approximate solution for y_1 may be found using a Taylor series expansion

thus

$$y_1 = y_1(o) + y_1'(o)x + \frac{1}{2!} y_1''(o)\, x^2 + \ldots .$$

where $y_1'(o)$ and $y_1''(o)$ are the first and second derivatives of y_1 with respect to x when $x = o$

In the present situation

$$y_1(o) = 1 \text{ and } y_1'(o) = 0$$

therefore, neglecting higher derivatives than the second

$$y_1 = 1 + \frac{1}{2} y_1''(o)\, x^2$$

$$= 1 + \frac{1}{2} y_2'(o)\, x^2$$

$y_2'(o)$ is given by equation 10 and is indeterminate. This problem may be solved, as was pointed out by Taylor (1967), by repeated application of L'Hopital's rule. If we neglect the derivatives of y_3 (i.e. B_z) then we find

$$y_2'(o) = -\sqrt{bd/3}$$

Thus $y_1 = 1 - \frac{x^2}{2}\sqrt{bd/3}$

The calculation of y_1 by this method is sufficiently accurate to allow the integration process to be carried out.

The modification which was made, using the idea of an initial mass, removed any problem concerning the starting conditions since the point when x = 0 is no longer indeterminate. The modified program in this form provides a check on the accuracy of the integration with a Taylor expansion start, since with the program in this form both starting conditions may be used.

A flow diagram of the program is given on the next page.

References

Lance, G.N. Numerical Methods for High Speed Computers. Iliffe, 1960

Dunnett, R.M. Thesis (to be published)

Taylor, T.B. Thesis (to be published)

Flow Diagram for Computer Program given in Appendix 1V

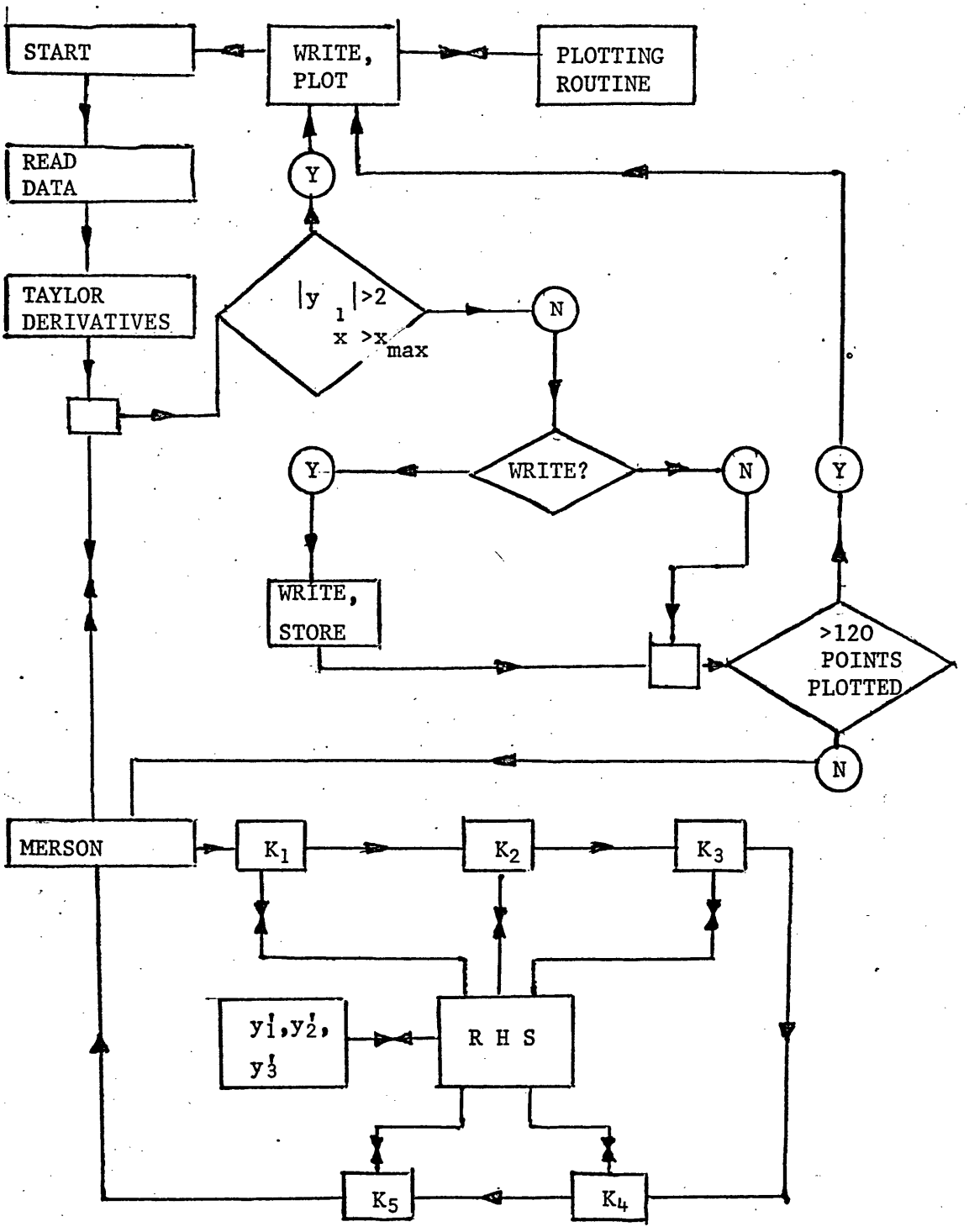

Appendix V

Plasma Conductivity

The equations relating the parameters of density, temperature and degree of ionisation to the electrical conductivity are well known. For the sake of easy reference a very simplified approach is reproduced here.

Assuming the Lorentz gas model and neglecting electron-electron collision, Delcroix (1960) shows that

$$\sigma_L = 2.457 \frac{n_e e^2}{m \nu_{av}}$$

where ν_{av} is the averaged collision frequency. The inclusion of electron-electron interactions is more difficult but Spitzer (1962) has calculated numerically that the total conductivity is

$$\sigma = 0.582 \sigma_L$$

Furthermore $\nu_{av} = 2.63 \, n \, T^{-3/2} \log \Lambda$

thus $\sigma = 1.54 \times 10^{-4} \, T^{3/2} \log \Lambda \text{ ohm}^{-1}\text{cm}^{-1}$

This value of conductivity applies only when there is zero magnetic field.

In the presence of a magnetic field the conductivity is represented by a tensor quantity

$$\begin{vmatrix} \sigma_\perp & \sigma_H & 0 \\ \sigma_H & \sigma_\perp & 0 \\ 0 & 0 & \sigma_{11} \end{vmatrix}$$

The tensor can be considered to be in cylindrical polar coordinates, since in this case the polar tensor and the cartesian tensor are identical.

σ_{11} is the same as σ given previously,

also $$\sigma_\perp = \frac{\sigma_{11}}{1 + w^2\tau^2}$$

and the Hall conductivity

$$\sigma_H = \frac{\sigma_{11}\, w\tau}{1 + w^2\tau^2}$$

Here w is the electron gyro-frequency and τ is the mean collision time

A typical case is when

$n_e = 10^{17}$ electrons/cc

$T_e = 25{,}000^\circ$ K

$B_z = 10$ K gauss

then $\sigma_\perp \simeq 0.96\ \sigma_{11}$

and $\sigma_H \simeq 0.2\ \sigma_{11}$

We thus see that the magnetic field produces only a very small anisotropy into the plasma.

References

Delcroix, J.L. Introduction to the Theory of Ionised Gases
Interscience, 1960.

Spitzer, L. Physics of Fully Ionised Gases
Interscience, 1962.

Publications

MEASUREMENT OF TRANSIENT STARK AND ZEEMAN SHIFTS USING A FIZEAU INTERFEROMETER.

(With D.D.Burgess)

Journal de Physique Supp. to No 3-4, 28, 1967

MEASUREMENT OF TRANSIENT STARK AND ZEEMAN SHIFTS USING A FIZEAU INTERFEROMETER

by D. D. BURGESS and T. A. HALL

Physics Department, Imperial College, London, Grande Bretagne.

Résumé. — Des déplacements de longueur d'onde des raies spectrales émises par un plasma peuvent être le résultat d'effets Doppler, Stark, Zeeman ou de combinaison de ces effets. Ces déplacements sont ordinairement transitoires et difficiles à détecter en présence d'un élargissement simultané de la raie. Une publication récente (Burgess et Cooper, 1965) décrit un instrument dérivant de l'interféromètre de Fizeau, destiné à la mesure du rapport déplacement/largeur de raies émises par des plasmas où l'effet Stark est dominant.

L'instrument a depuis été adapté à la mesure de champs magnétiques dans des plasmas en utilisant l'effet Zeeman. Sous sa nouvelle forme il est aussi adapté à la mesure des déplacements Doppler.

Nous résumons les avantages de l'interféromètre de Fizeau à ondes multiples dans de telles applications. L'instrument de Burgess et Cooper a été modifié par l'addition d'un troisième photomultiplicateur et d'un système polarisant. Avec le dispositif utilisé pour la mesure de champs magnétiques il est possible de séparer les effets de déplacements Stark simultanés et de mesurer la largeur de raie.

Nous discutons la correction des effets instrumentaux, et présentons des résultats de mesures de champs magnétiques piégés dans un pincement stabilisé en Z ; une comparaison est faite avec les résultats obtenus au moyen d'un laser à Argon par deux techniques différentes.

Abstract. — Shifts in the wavelength of spectral lines emitted by plasmas can be the result of Doppler, Stark or Zeeman effects, or combinations of these. Such shifts are usually transient and difficult to detect in the presence of simultaneous broadening of the line.

A recent publication (Burgess and Cooper 1965) described an instrument, based on the Fizeau interferometer, designed for the measurement of shift to width ratios of spectral lines emitted from Stark dominated plasmas. This instrument has now been adapted for the measurement of magnetic fields in plasmas utilising the Zeeman effect. In its new form it is also equally suited to the measurement of Doppler shifts.

The advantages of multiple beam Fizeau interferometers in such applications are summarized. The instrument described by Burgess and Cooper, has been modified by the use of a third photomultiplier and polarizing optics. With the arrangement used for measuring magnetic fields, it is possible to discriminate against the effects of simultaneous Stark shifts and also to measure the line width.

Correction for instrumental effects is discussed. Experimental measurements of trapped magnetic fields in a stabilized Z-pinch are presented, and compared with those obtained using two techniques an Ar II laser.

An instrument has been described recently by Burgess and Cooper [1] which is capable of measuring relatively very small shifts in wavelength of broadened spectral lines. This instrument was initially designed to measure the ratio of the shift to width for lines whose profiles are determined by electron impacts but with modification is capable of measuring Doppler and Zeeman shifts. This paper describes such a modification.

In order to detect a shift in wavelength of a spectral line it is necessary to monitor the intensity at two or more points on the line profile. This makes it desirable that the dispersive element should produce a linear dispersion, and since the shifts may often be small this dispersion must be high if the detector assembly is not to be small and delicate. Furthermore the line widths of interest in plasma diagnostics may vary considerably even in a single experiment, thus making variable resolution advantageous.

A multiple beam Fizeau fringe interferometer satisfies these requirements well. It has the further advantage over other dispersive systems that the dis-

persion can be varied, whilst keeping the ratio of resolving power to dispersion constant. This allows the profile sampling arrangement to be made very simple and rugged and still remain adequate under all conditions.

Both diffraction gratings and angled Fabry-Perot could be constructed to give sufficient dispersion and variable resolution, but neither are as versatile as the Fizeau fringe interferometer.

The light gathering power of a Fabry-Perot was shown by Jaquinot [2] to be $3.4/\beta$ better than an equivalent grating spectrometer with the same resolution, where β is the angle subtended by the slit height at the grating. Thus the light gathering power of most grating spectrometers is approximately 300 times less than an equivalent Fabry-Perot. Because of the lack of circular symetry in a Fizeau fringe interferometer its light gathering power is about π/N_R lower than a Fabry-Perot. This is still considerably better than most grating spectrographs and approximately the same as an angled Fabry-Perot, whose light gathering power is reduced because only a small part of a fringe is viewed.

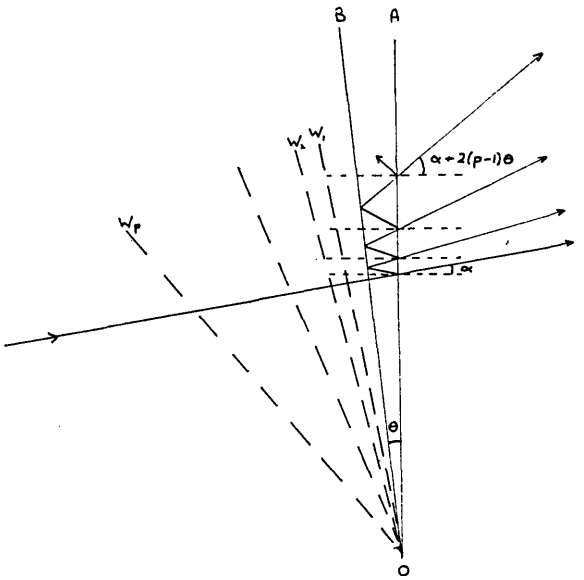

FIG. 1 — Illustrating the formation of Frizeau fringes.

Figure 1 illustrates the formation of multiple beam Fizeau fringes. Light is incident at an angle α to the reflecting plate AO which is inclined at an angle θ to a second similar plate. W_1, W_2, W_p represent virtual transmitted wave fronts. (The formation of fringes have been discussed by several authors [3] mainly in the context of surface studies, where large angles and small separations are usually used. For our requirements relatively large spacings and small angles are needed, and in this context the effects of importance are rather different).

The p-th transmitted front emerges at an angle $\alpha + 2(p-1)\theta$. If α, θ and p are small then the phase difference between the p-th and $(p+1)$-th front is given by

$$\delta_{p+1} - \delta_p = \frac{4\pi t}{\lambda} \cos\alpha .$$

This is independent of p, and the intensity distribution is given by the Airy formula, thus allowing much of the analysis given by Chabbal [3] for the Fabry-Perot to be used in this case.

In the use of Fizeau fringes several conditions concerning the maximum values of α, θ and p must be satisfied if the approximation is to be valid. Born and Wolf [2] show that the effective maximum value of p is given by

$$p = 1 : 4N_R .$$

For small α the Airy summation breakdown condition reduces to

$$\frac{2p^2\theta^2}{3} \cdot \frac{4\pi t}{\lambda} < \pi .$$

For a reflection finesse of 20 and a convenient fringe spacing 1 cm, this gives a maximum value of $t \sim 1.3$ cm which corresponds to a free spectral range at 5 000 Å of 0.1 Å. This is quite adequate, as Doppler widths even in Argon are larger than this for temperatures down to about 5 000 °C.

The restriction on α in the Airy breakdown condition is usually, for small plate separations, less limiting than that due to the broadening of the fringe produced by a finite solid angle of acceptance. Chabbal defines a scanning finess N_F

$$N_F = \frac{\lambda}{\alpha_{max}^2 t}$$

α_{max} is the maximum value of α and is set by the required resolution. Reducing it further than this is not desirable as the luminosity of the instrument is reduced.

The angle α leads to another important consequence in the case of Fizeau fringes, namely that the fringes are shifted along the wedge. This could produce grave systematic errors in the Stark shift measuring instrument but, as will be seen later, is only of secondary importance in the Zeeman instrument. This shift, however, can be overcome by ensuring that the

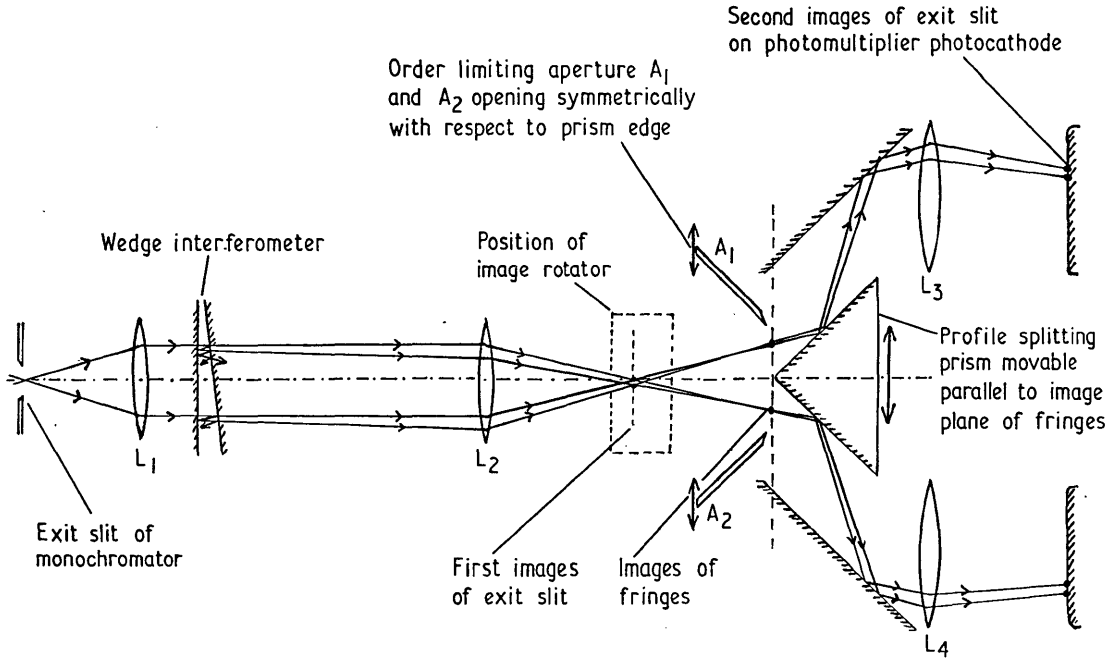

FIG. 2 — Schematic lay out of instrument.

standard source on which the instrument is set up subtends the same solid angle at the exit slit of the pre-monochromator as the source to be examined.

Figure 2 shows a schematic layout of the Stark shift instrument described by Burgess and Cooper. The diverging beam from the exit slit of the monochromator is collimated through the wedge by means of the lens L_1. The first images of the exit slit are produced within the image rotator by the lens L_2 which also produces an image of the fringes in the plane of the aperture stops A_1, A_2 and the prism edge. The profile is split into two by the prism which is fully reflecting on both front surfaces. The order limiting aperture stops A_1 and A_2 are designed to open symetrically with respect to the prism edge. Final images of the exit slit are produced on the photomultiplier cathodes by means of the lenses L_3 and L_4. This ensures that the area of the photocathode illuminated is independant of the position of the fringe on the wedge and this is desirable since the sensitivity of the cathodes may vary considerably over its surface.

At this stage one further point must be considered, which affects the Stark instrument, and that is the effect of order overlap. Figure 3 shows how the ideal difference signal, $2A$, is reduced by an amount $2B$. A correction curve has been plotted for $(2A - 2B)/2A$ against the ratio of line width to free

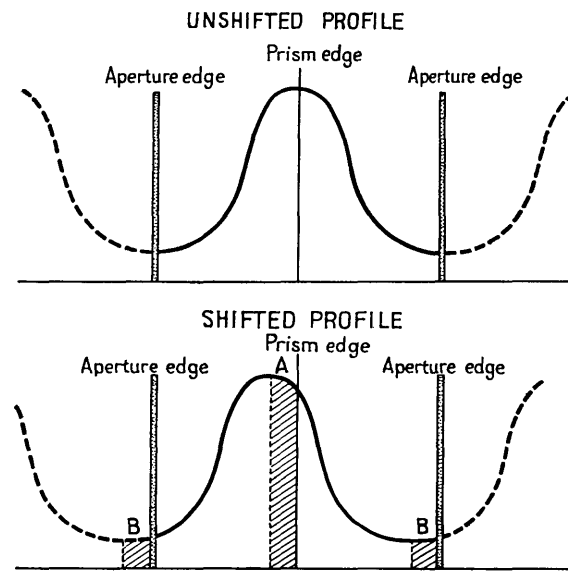

FIG. 3 — Effect of Order Overlapping.
Total area between aperture edges is constant equal to total area of single fringe without overlap. Change of intensity should ideally be A for each detector.
Hence ideal difference signal = 2A
Actual difference signal = 2A − 2B

spectral range, $W/\Delta\lambda_s$. Near the optimum value of $W/\Delta\lambda_s$, $(2A - 2B)/2A$ varies only slowly. With care

the residual error in the corrected difference signal should be less than 5 %.

The magnetic field measuring instrument is required to measure shift directly. This necessitates the use of a third photomultiplier, which then allows the shift and width of the σ components to be measured simultaneously. Further modifications to the Stark shift instrument can be seen from figure 4. These include independent aperture stops and the use of polarising optics.

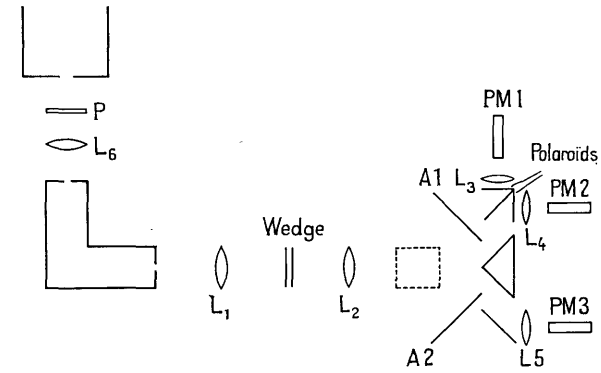

FIG. 4 — Schematic diagram of the Zeeman shift instrument.

Emitted spectral lines when viewed along the imposed magnetic field are split into two sets of contrarotating circularly polarised components shifted symetrically about the mean. A quarter wave plate, P, converts the circular polarisations into linear polarisations at right angles. Each polaroid in front of photo-multipliers 1 and 2 is adjusted to select opposite polarisations. Figure 5 shows the portion of each

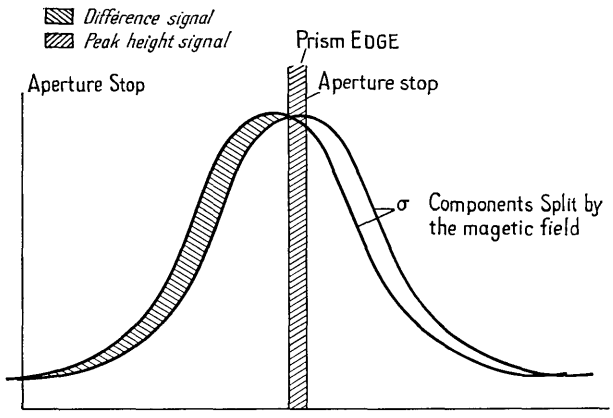

FIG. 5 — Fringe viewing arrangement.

fringe which each photomultiplier will view. Photomultiplier 1 views the component shifted to the red and photomultiplier 2 views the component shifted to the blue. Photomultiplier 3 records the intensity due to the central region of both components.

The signals from photomultipliers 1 and 2 are electronically added and subtracted. The sum, difference and peak height signals are recorded photographically from oscilloscope traces.

These recordings yield values of magnetic field and line width after allowance for instrumental effects and with the assumption of an appropriate line profile. In the experimental conditions of interest this profile is known both theoretically and experimentally to be closely dispersive in form.

The restrictions that applied to the Stark shift instrument apply equally to this version with the exception of the order overlap which is eliminated by the use of a third photomultiplier, and of the fringe shift due to varying α. This shifting of the fringe, together with any Stark shift present, only produce second order effects, since the photomultipliers record the splitting of the two components, and not just the shift of one.

A further second order effect arises due to the fact that as the profiles are shifted the third photomultiplier does not record the true peak height.

Both of these effects can be easily corrected for in the calculations, but usually introduce less than 3 % error.

A simpler version of the Zeeman instrument is possible when the line widths are small i. e. when the profile is basically the instrument function. This version requires only the peak height and the difference signal to be recorded, but the apparatus is essentially the same as the three channel system. The simpler version will not yield values of the line width.

The measurements of magnetic field that have been carried out up until the present time at Imperial College have been done on a stabilized pinch in argon. The Z-pinch consists essentially of two electrodes 10 cm in diameter and 40 cm apart contained in a pyrex tube. A discharge is produced between the electrodes by a 1 000 μF capacitor bank capable of operating at voltages up to 5 kV. The tube is surrounded by a single layer coil used to produce a uniform axial magnetic field of up to 30 kgauss when a 2 000 μF capacitor bank is discharged through it. The period of the magnetic field bank is very much longer than the discharge period and in the absence of plasma the magnetic field may be considered constant in time during the discharge.

Some typical results that have been obtained are shown in figure 6. Considerable magnetic field com-

pression occurs at the first pinch followed by a rarefaction as the pinch expands. Subsequent pinches produce little compression and the magnetic field settles down to a constant value.

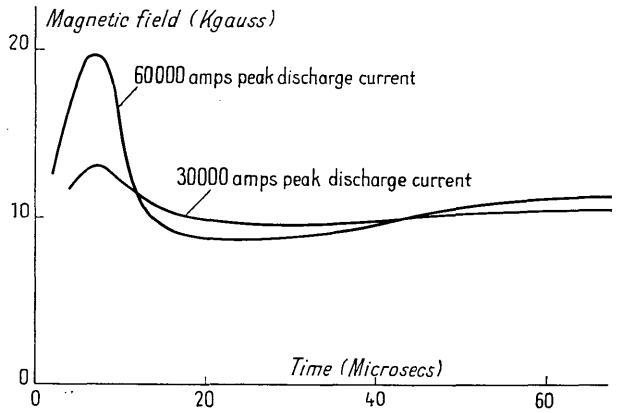

FIG. 6 — Axial magnetic field with time. Nominal value of applied field 11 k Gauss.

The value of the magnetic field before the pinch is susceptible to quite large errors because of the low light intensity and the consequent statistical noise at the photocathodes but as the light level rises the error falls rapidly to less than 5 %. The steady value of the magnetic field agrees well with the results obtained by Troughton at Imperial College who used an Ar II laser to measure resonance Faraday rotation. This value also is nearly identical with the value obtained using a search coil in the absence of plasma, as would be expected at this late stage in the discharge.

Bibliographie

[1] BURGESS (D. D.), and COOPER (J.), *Proc. Phys.*, 1965, **86**, 1333.
BURGESS (D. D.) and COOPER (J.), *J. Sci. Inst.*, 1965, **42**, 829.
[2] JAQUINOT (P.), *J. Opt. Soc. Amer.*, 1954, **44**, 10, 761.
[3] TOLANSKY, 1947, Multiple Beam Interferomtry (Pergamon).
BROSSEL (J.), *Proc. Phys., Soc.*, 1947, **59**, 224.
BORN and WOLF, 1964, Principles of Optics, 2nd Ed. (Pergamon).
CHABBAL (R.), *J. Rech. Bellevue*, 1953, **24**, 138.

RECENT DEVELOPMENTS IN THE APPLICATION OF THE MULTICHANNEL FABRY-PEROT TO PLASMA SPECTROSCOPY

JOSEPH G. HIRSCHBERG
University of Miami, Coral Gables, Florida, U. S. A.

Résumé. — L'interféromètre de Fabry-Pérot multi-canal par réflexion, s'est montré un instrument important pour l'analyse de la forme des raies spectrales quand une grande luminosité et une bonne résolution dans le temps sont nécessaires. Il a été appliqué à l'étude de plusieurs problèmes de physique des plasmas, par exemple la détermination de la température cinétique, dans une décharge « pinch » toroïdale dans un mélange d'hydrogène et d'hélium. Une nouvelle méthode utilisant des lentilles de Fresnel a été étudiée. Les mesures préliminaires indiquent que le nombre de canaux disponibles par cette méthode n'est limité que par la finesse de l'interféromètre.

Abstract. — The reflection multichannel Fabry-Perot has proven an important tool for the analysis of spectral line shapes where high luminosity and good time-resolution are required. It has been applied to several plasma physics problems, for example to determine kinetic temperatures in a toroidal pinch discharge in a mixture of hydrogen and helium. A new method utilizing Fresnel lenses has been devised. Preliminary measurements indicate that the number of channels available by this method is limited only by the finesse of the interferometer.

1. **Introduction.** — Until little more than a decade ago, the Fabry-Perot interferometer was generally thought of as wasteful of light and being of use only when maximum resolving power was needed. Two events, both connected with the Laboratoire Aimé Cotton in France, contributed heavily to reversing the situation. Multilayer dielectric reflecting mirrors with their extremely low absorption losses were developed, mainly at the Laboratoire mentioned, and Jacquinot pointed out the [1] geometrical luminosity advantages of the axially symmetric instruments. With the new mirrors, the Fabry-Perot is almost universally recognized as the most luminous of the direct-recording spectrometers.

In plasma physics, the shape and shift of spectral lines leads in many cases to important diagnostic data. In particular, the line breadth may give the Doppler temperature, the density, or even the magnetic field depending on the experimental conditions. Shifts may yield collective motions such as ion drifts or plasma rotation.

Two conditions often present in laboratory plasmas, however, serve to make accurate measurements difficult : 1) The intensity of the line-spectrum is generally low. This is especially the case in optically thin highly ionized hydrogenic plasmas, where only impurities radiate line spectra. The purer the plasma, and hence the more interesting, the weaker the spectrum. 2) The other difficulty is that since confinement is by far the most difficult problem in high temperature plasma physics, a large number of the interesting experimental situations are extremely rapidly changing, with characteristic times of tens and hundreds of nanoseconds.

The multichannel Fabry-Perot was chosen to satisfy the conditions of highest luminosity and speed, limited only by the photomultiplier characteristics.

2. **The Multichannel Fabry-Perot.** — When light from an extended monochromatic source falls upon a Fabry-Perot interferometer, fringes are formed at the focus of a lens behind the instrument. If the light is isotropic and the mirrors comprising the instrument are perfectly flat and parallel, the shape and position of the fringes are described by the well-known Airy formula for the transmission which yields the familiar expression for the Fabry-Perot fringe maxima :

$$n = 2\,\sigma\mu t \cos\theta\,, \qquad (1)$$

where n is the interference order number, σ the wave number of the radiation, and θ the angle of inclination from the normal.

In a multichannel device a convenient arrangement is N channels of equal wavenumber width, $\Delta\sigma$. Since the region of interest is near the axis, the cosine in (1) may be expanded, obtaining :

$$\sigma - \sigma_0 = \tfrac{1}{2}\,\sigma\theta^2\,, \qquad (2)$$

where σ_0 is the wavenumber of the radiation at $\theta = 0$.

Differentiating (2), and if we use a lens with focal